



Precise LEO Space Radiation Monitoring using the Space RadMon-NG Payload

**TU Delft**



Jasper Dijks

"To confine our attention to terrestrial matters would be to limit the human spirit."

- Stephen Hawking

Precise LEO Space Radiation Monitoring using the Space RadMon-NG Payload

by

Jasper Dijks

to obtain the degree of Master of Science

at the Delft University of Technology,

to be defended publicly on Friday the 24th of February 2023 at 10:00 a.m.

Student number:	5256003	
Project duration:	1 July 2022 – 24 February 2023	
Department:	Space Systems Engineering	
Faculty:	Aerospace Engineering	
Supervisor:	dr. A. Menicucci,	TU Delft, Space Systems Engineering
External supervisors:	dr. S. Danzeca,	CERN, BE-CEM-EPR (section leader)
	A. Zimmaro,	CERN, BE-CEM-EPR (PhD student)
Thesis committee:	prof. dr. J. Guo (Chair),	TU Delft, Space Systems Engineering
	dr. D. M. Stam (Examiner),	TU Delft, Astrodynamics & Space Missions

An electronic version of this thesis is available at <http://repository.tudelft.nl/>.

Front cover image with courtesy of the European Space Agency

Acknowledgements

During my internship at NLR in the first year of my MSc degree, I came into contact with the topic of radiation effects on space embedded systems. Since then, this topic has peaked my interest due to my background in physics. When I told one of the faculty professors my desire of wanting to do an internship at CERN, the perfect thesis opportunity arose of working with a space system at one of the largest research institutes in the world.

I would like to thank my thesis project supervisors dr. Alessandra Menicucci, dr. Salvatore Danzeca and Alessandro Zimmaro. Grazie mille per la vostra competenza e il vostro aiuto durante tutta la mia tesi. I would also like to show my gratitude to my colleagues and friends at CERN, making my internship an unforgettable experience. Best place in the world.

My sincere gratitude to my partner, family and friends for their love, support and visits throughout my thesis work. Both through harder and easier times. Ad astra.

*Jasper Dijks
Amsterdam, January 2023*

Summary

Space radiation has an enormous effect on the design considerations of space systems. It is one of the main causes of anomalies in spacecraft, meaning the environment in space needs to be accurately monitored and modelled. Total Ionizing Dose effects on electronics have been known for a long time, however in 1974 Single Event Effects were observed for the first time in digital electronics. This type of radiation effect was caused by a interaction of Galactic Cosmic Rays with the device. Small-scale radiation monitoring in space has previously been done by means of a RADFET sensor for Total Ionizing Dose, or by means of a Timepix sensor for measurement of higher energy particles. These devices were limited in terms of resolution, need relatively high bias voltages, have high power consumption and have high costs. CERN has developed a new type of radiation monitoring payload suitable for CubeSats, to make advances in space radiation monitoring. This device was originally based on the RadMon, a radiation monitoring device that is used in various facilities around CERN with the most famous one being the Large Hadron Collider tunnel.

CERN developed the Space RadMon-NG, a Commercial-Off-The-Shelf components based CubeSat payload. The payload contains a high resolution Floating Gate Dosimeter to measure the Total Ionizing Dose and a SRAM sensor to measure the High Energy Hadron fluence. At the start of the thesis research, there were still unanswered questions regarding this payload. The thesis research was performed at CERN on the Space RadMon-NG with the goal of answering the question: "How can the Space RadMon-NG payload make significant advances in space radiation monitoring compared to current state-of-the-art?".

To answer this question, a thorough literature review has been conducted, a deep analysis of the payload itself, multiple system-level tests at the CHARM facility at CERN, a separate temperature characterization test of the Floating Gate Dosimeter sensor at the Cobalt-60 facility and analysis of the payload data retrieved in orbit by the predecessor of the Space RadMon-NG in the CELESTA mission. The testing went mostly according to expectations and all requirements set before testing were verified in different campaigns. The biggest challenges encountered during the system-level testing at the CHARM facility were communication and cabling issues. For the temperature testing of the Floating Gate Dosimeter in the Cobalt-60 facility the biggest challenge was getting the set-up working and the condensation because of the temperature changes.

Based on the research performed, the following conclusions can be made. The payload has very good improvements to current state-of-the-art, both in terms of sensor performance and costs. The payload works extremely well in a mixed-field radiation environment, with sensor performances being within 2.5% of the references used. The Floating Gate Dosimeter shows good characteristics when under simultaneous influence of temperature variations and radiation, showing a performance of within 2.5% of the reference used when proper compensation is applied. The best compensation technique is based on the reference given by an identical sensor to the floating gate that is not susceptible to radiation but is affected by temperature variations. The CELESTA mission had a resolution that was too low for the orbit mapping of data, but validated the method of analysis for the Space RadMon-NG payload. The new payload is expected to measure a little over 5 Single Event Effects per sensor, per day based on OMERE simulations and the cross-sections measured.

Keywords: CELESTA, Commercial Off The Shelf, CubeSat Payload, Floating Gate Dosimeter, High Energy Hadrons, Space Radiation Monitoring, Space RadMon-NG

Contents

List of Figures	v
List of Tables	ix
Nomenclature	x
1 Introduction	1
1.1 The European Organisation for Nuclear Research.....	2
1.2 Research Design.....	3
2 Literature Review	5
2.1 Radiation Mechanisms	5
2.1.1 Particles	5
2.1.2 Particle Interactions	6
2.1.3 The Space Radiation Environment	9
2.1.4 Radiation Effects on Micro-Electronics	12
2.2 High Energy Hadron Fluence Measurement using SRAM	17
2.2.1 Cypress 90 nm SRAM Sensor	18
2.2.2 Multiple Cell Upset Bursts and Detection	18
2.2.3 On-line Burst Detection Algorithm	20
2.2.4 Alternating On-line Burst Detection Algorithm.....	22
2.3 Radiation Dose Monitoring with Floating Gates	23
2.3.1 Working principles	23
2.3.2 Layout	27
2.3.3 Operational Modes	29
2.3.4 Sensitivity	30
2.3.5 Comparison with RADFET.....	34
3 Space RadMon-NG Payload	35
3.1 System Engineering.....	35
3.2 Hardware Architecture	37
3.3 MCU Firmware Architecture	37
3.4 FPGA Design Architecture.....	38
3.4.1 Main Controller.....	39
3.4.2 MCU Controller.....	40
3.4.3 SRAM Controller	41
3.4.4 SRAM180 Controller	44
3.4.5 SPI Communication	46
3.5 Payload Operation	48
3.5.1 Power Consumption.....	48
3.5.2 I2C Communication	49
3.5.3 Interfacing with the Space RadMon-NG	50
3.6 State-of-the-Art Comparison	51
3.6.1 Current State-of-the-Art	51
3.6.2 Payload Differences	53
4 System-Level Testing	54
4.1 Radiation Tests CHARM	54
4.1.1 The CHARM Mixed-Field Facility	54
4.1.2 Preparation, Set-up and Installation.....	56

4.1.3	Dry Run CHARM	58
4.1.4	Radiation Runs CHARM	58
4.2	CHARM Campaign 1.....	59
4.2.1	Test Remarks	59
4.2.2	Burst Algorithm and Fluence Results	59
4.2.3	FGDOS and TID Results	62
4.2.4	Other Payload Results	65
4.3	CHARM Campaign 2.....	66
4.4	CHARM Campaign 3.....	68
4.5	Payload Communication	72
4.6	Conclusions and Implications.....	73
5	Floating Gate Dosimeter	75
5.1	Temperature Characterization Test.....	75
5.1.1	Background	75
5.1.2	Set-up.....	77
5.1.3	Dry Run Testing and Characterization.....	80
5.1.4	Cobalt-60 Thermal Radiation Testing	82
5.2	Results	85
5.2.1	Temperate Coefficient Evolution	85
5.2.2	Sensitivity Degradation	86
5.2.3	Total Ionizing Dose Compensation	89
5.3	Conclusions and Implications.....	92
6	CELESTA Mission.....	94
6.1	Space RadMon V1 Payload.....	94
6.1.1	Orbit Information and Environment.....	94
6.1.2	Orbit Mapping and Payload Results	95
6.2	Space RadMon-NG Payload Analysis Preparation	98
6.2.1	Mission Dose	99
6.2.2	Mission Flux and SEE Prediction.....	100
6.3	Conclusions.....	101
7	Conclusion	103
7.1	System-Level Testing	103
7.2	Floating Gate Dosimeter	104
7.3	CELESTA Mission	105
7.4	Research Questions	106
7.5	Future Work and Recommendations	107
	Bibliography	108
A	Arduino Code.....	113
A.1	Interfacing with Space RadMon-NG	113
A.1.1	SRM_NG_FPGA_TEST_BURST.ino	113
A.2	Reading FGDOS Chips and Temperature Sensor.....	118
A.2.1	read_FGDOS_Temp.ino	118
A.2.2	read_FGDOS_Temp.h	123
B	CELESTA Two-Line Element Sets.....	126

List of Figures

1.1	Spacecraft anomalies [29].	1
1.2	The CERN accelerator complex, layout in 2022 [39].	3
2.1	The Standard Model of particle physics. The graphic was taken from Quanta Magazine (2020) [47].	6
2.2	Illustration of the type of interactions between photons and matter. This figure is adopted from [36] without any changes.	7
2.3	Illustration of the type of interactions between charged particles and matter. This figure is adopted from [36] without any changes.	8
2.4	Illustration of the type of interactions between neutrons and matter. This figure is adopted from [36] without any changes.	8
2.5	Time averages radiation belt omnidirectional fluxes for protons (>10 MeV, top) and electrons (>0.5 MeV, bottom). This figure is adopted from [42] without any changes.	10
2.6	GLEs measured on Earth by NMs during the former solar cycles. This figure is adopted from [52].	11
2.7	GCR variation with the Solar cycle measured by NMs showing an inverse relationship. The figure has been adopted without change from [53].	12
2.8	Band diagram of a MOSFET with a positive gate bias. Illustrated are the main processes for radiation-induced charge generation. The figure was taken from [55].	13
2.9	Illustration of displacement damage. The figure was taken from [41].	14
2.10	Illustration of four effects of displacement damage due to energy levels introduced in the band-gap: a) increased thermal generation of carriers; b) increased carrier recombination; c) increased temporary trapping; d) reduction in majority-carrier concentration. This figure was taken from [63].	15
2.11	Charge generation and collection phases in a reverse-biased junction and the resultant current pulse caused by the passage of a high-energy ion. This figure was taken from [8].	16
2.12	Burst events seen at a low flux of $6.82 \cdot 10^6$ pp cm^{-2} . Figure was taken from [24].	19
2.13	Raw readings vs data corrected with the algorithm for bursts mitigation. Figure was taken from [24].	20
2.14	Example of a burst observation. Black pixels represent a high number of SEUs in nearby cells with neighbouring rows of the same block. White lines represent the boundaries between memory blocks. Figure was taken from [57].	20
2.15	Example of an SEU burst event involving several bit upsets on neighbouring rows and error bits located on the same column array. Memory Blocks are highlighted with different shades of grey. Figure was taken from [57].	21
2.16	Examples of a small cluster of bit upsets (a) and a burst event characterized by several single bit upsets following a rectangular geometrical shape (b). Figure was taken from [58].	22
2.17	SEU map of the SRAM die during irradiation with the alternate block detection algorithm. The rectangles correspond to the detection window at the location where a burst was recognized. Figure was taken from [58].	23
2.18	Cross section of a FG transistor and basic schematic of the sub-circuit. The figure has been adopted without change from [50].	24
2.19	The fraction of holes that escape initial recombination (charge yield) for alpha particles, protons, x-rays and a Cobalt-60 source. The figure was taken from [55].	25
2.20	Linearization of the sensor response. The black curve in the figure represents the characteristic (raw) response and the blue curve shows the response obtained by limiting the current by means of the charge injection. This figure was found in [14].	26
2.21	The working principle of FGDOS from Sealicon, found in source [56].	27

2.22	Electronic diagram of the $I-f$ converter used to turn the drain current into a frequency signal [32].	27
2.23	Schematic of the FGDOS chip developed at Sealicon.	28
2.24	Different operational modes on the FGDOS. The figure was taken from [16].	29
2.25	Sensitivity degradation of the FGDOS sensor. Taken from source [69].	31
2.26	Sensitivity degradation over the total dose. The red and blue symbols represent the first and the second run, respectively. Each recharge interval is represented by a specific symbol, as reported in the legend. Figure was taken from [14].	32
2.27	Frequency as a function of temperature. The highest curve shows the frequency variation of the twin MOSFET, which is the reference frequency. The lower curves show the frequency variation of the FG transistors for different amounts of charge stored in the FG. Figure was taken from [16].	33
2.28	S_t as a function of temperature. Increasing the temperature, the output signals become less sensitive to the variations in temperature. The same effect can be observed by increasing the charge stored in the FG. Figure was taken from [16].	33
2.29	TID measured by RADFETs (biased to 0 V and +5 V) and FGDOS. The radiation type used is a mixed field generated by the interaction between the 24 GeV proton beam and a copper target, labeled as Cu. Figure was taken from [12].	34
3.1	Flow chart for the Space RadMon-NG boards (physically) based on the interface control document of the Space RadMon-NG [68].	37
3.2	Flow diagram to depict the MCU and internal ADC implementation for the Space RadMon-NG.	38
3.3	Block diagram to depict the FSM of the main controller.	40
3.4	Block diagram to depict the FSM of the MCU controller.	41
3.5	Block diagram to depict the FSM of the SRAM controller.	44
3.6	Block diagram to depict the FSM of the SRAM180 controller.	46
3.7	Block diagram of the various signals in the SPI implementation. Figure was made using the block diagram view in Sigasi.	47
3.8	Block diagram to depict the FSM of the SPI protocol implemented.	48
3.9	Current consumption of the Space RadMon-NG in normal operation conditions. The start-up procedure is seen in the beginning ending with a measurement, then a 1 minute freeze and measurement on loop.	49
3.10	Diagram for the FSM seen from the outside of the system. Taken from the interface control document of the Space RadMon-NG.	50
3.11	Diagram of the interfacing setup with the Space RadMon-NG.	51
3.12	Cables schematic for the interfacing with the Space RadMon-NG using the power supply and Arduino.	51
4.1	3D render of the PS East Area Hall at CERN. From source [66].	55
4.2	Layout of the CHARM mixed-field radiation facility at CERN. From source [30].	55
4.3	Design of the the Arduino Feather M0 I2C shield PCB.	56
4.4	Harness manufactured for the communication of the Space RadMon-NG payload during testing in CHARM.	57
4.5	Illustration of the set-up that will be used for the testing at CHARM.	57
4.6	Dry run test set-up in the preparation room at CHARM.	58
4.7	Cypress compensated SEU count and raw SEU count over time.	60
4.8	Cypress compensated SEU count and raw SEU count over time from day 0.60 until day 2.25.	60
4.9	Cypress compensated SEU count and raw SEU count over time zoomed in on a compensated burst.	61
4.10	Particle fluence determined from the SEUs measured by the SRAMs over time from day 0.60 until day 2.25 compared to the RadMon V6 measurements.	62
4.11	FGDOS TID over time with sensitivity degradation included compared to RADFETs.	63
4.12	FGDOS recharge counts over time during campaign 1.	63
4.13	FGDOS TID over time with sensitivity degradation included from day 0.60 until day 2.25 compared to RADFETs.	64

4.14	FGDOS TID over time with sensitivity degradation included from day 0.60 until day 0.8 (around 5 hours from day 0.6) compared to RADFETs.	64
4.15	Temperature on the mezzanine board of the payload over time.	65
4.16	The various voltages from the voltage regulator in the payload over time.	65
4.17	The SRAM voltage of the payload over time.	66
4.18	The voltages in the payload over time.	67
4.19	The FGDOS recharges of the payload over time.	67
4.20	Reparations of the Space RadMon-NG payload in the buffer zone of CHARM.	68
4.21	The SEUs measured by the payload over time.	69
4.22	The HEH fluence measured for different cross-sections by the payload over time.	69
4.23	The RPD of the HEH fluence measured by the payload over time compared to the fluence measured by the RadMon V6.	70
4.24	The TID measured by the payload over time.	71
4.25	The RPD of the TID measured by the payload over time compared to the RadMon V6 RADFET.	71
5.1	Schematic of the test set-up that will be used for the FGDOS sensitivity test.	78
5.2	Design of the the Arduino Feather M0 SPI shield PCB.	78
5.3	Design of the FGDOS temperature test board PCB version 2.	79
5.4	Calibration curve of the thermal regulator to be used during the FGDOS temperature compensation experiments.	79
5.5	The set-up of the FGDOS testing used for the dry runs in the CERN BE-CEM-EPR laboratory.	80
5.6	The condensation on the FGDOS test PCB during the heating up from below 0°C.	81
5.7	Sensor frequency against the reference frequency from the twin NMOS during the dry run.	81
5.8	Sensor frequency against the temperature during the dry run.	82
5.9	Sensor frequency, reference frequency and temperature over time during the dry run with an induced recharge.	82
5.10	The set-up of the FGDOS testing used for the dry runs.	83
5.11	Calibrations using the ionization chamber of the dose rate on the active control board (left), passive control board (center) and active test board (right).	83
5.12	The ⁶⁰ Co testing timeline of the FGDOS. At the start of the final run, the board received a total amount of 82.5 Gy.	84
5.13	Sensor frequency, reference frequency and temperature over time during the dry run with an induced recharge.	85
5.14	Temperature sensitivity of the sensor over the temperature, split up in increasing and decreasing temperatures while being irradiated.	86
5.15	The temperature coefficient evolution over the TID received of the flat region between 40°C and 50°C, both for increasing and decreasing temperatures.	86
5.16	Sensitivity degradation of the sensor over the TID for the different boards. Note that the actual starting TID is 82.5 Gy and not 0 Gy.	87
5.17	Sensitivity degradation of the sensor over the TID for the different boards with degradation results from former tests as verification. Note that the actual starting TID is 82.5 Gy and not 0 Gy.	88
5.18	Relative percentage difference of the sensitivity degradation of the boards tested at ⁶⁰ Co and one of the former degradation curves. Note that the actual starting TID is 82.5 Gy and not 0 Gy.	88
5.19	Reference frequency of the twin NMOS in the FGDOS that can be used to analyze the influence of the temperature variations without any TID influence. Note that the actual starting TID is 82.5 Gy and not 0 Gy.	89
5.20	The TID measured by the different boards over time compared to the respective ionization chamber calibration. Note that the actual starting TID is 82.5 Gy and not 0 Gy.	90
5.21	Relative percentage difference of the TID received of the boards tested at Co60 and each respective ionization chamber calibration. Note that the actual starting TID is 82.5 Gy and not 0 Gy.	90

5.22	The TID measured by the test board over time compared to the test ionization chamber calibration with the different compensation methods. Note that the actual starting TID is 82.5 Gy and not 0 Gy.	91
5.23	Relative percentage difference of the TID received of the test board with different types of temperature compensation methods and the ionization chamber. Note that the actual starting TID is 82.5 Gy and not 0 Gy.	92
6.1	CELESTA HEH flux OMERE simulation from radiation belt particles as reference for the results.	95
6.2	Global schematic of the algorithm used for the trajectory determination of CELESTA and data mapping.	95
6.3	CELESTA trajectory data using the described algorithm in 3D ECI frame.	96
6.4	CELESTA trajectory data using the described algorithm in 3D ECEF frame.	96
6.5	CELESTA full ground track with data transmission position depicted as dots.	97
6.6	CELESTA SEL data of the two sensors during the mission in 2022.	98
6.7	CELESTA ground track with SEL rate data embedded.	98
6.8	Dose curve over shielding for the GOMX mission in OMERE.	99
6.9	Dose map for 1 mm shielding for the GOMX mission in OMERE.	100
6.10	HEH flux for the GOMX mission in OMERE.	100
6.11	Weibull fitting for Cypress SRAM cross section in OMERE.	101

List of Tables

2.1	Main sources of the natural space radiation environment. Taken from source [29].	9
2.2	Radiation effects overview with the parameters, relevant particles and typical units. This table was taken from source [61] with some minor adjustments.	12
2.3	Relevant technologies that are susceptible to TID effects. This table was taken over from the designated ECSS document [61].	14
2.4	Different type of SEEs with definition and destructiveness level, classified by soft or hard SEE. From source [44].	17
2.5	FGD-03F specification by Sealicon from source [56].	28
2.6	Characteristics of the FGDOS device in different modes.	29
2.7	Summary of the characteristics of the different operation modes. For autonomous mode, the error depends on the dose rate. Found in source [13].	30
2.8	Comparison of RADFET and FGDOS sensors in terms of main specifications. From source: [15].	34
3.1	Identification of key stakeholders and key requirements for the ISISPACE and GOMspace missions.	36
3.2	Requirements for the Space RadMon-NG payload that will be used for testing. The priority has been divided into essential (E) and conditional (C). The verification has been divided into test (T), analysis (A) and inspect (I).	36
3.3	Risk register for the Space RadMon-NG payload. Likelihood and consequence have been divided into high (H), moderate (M) and low (L).	36
3.4	Various bit configurations for the control register (0x00).	49
4.1	Overview of the radiation campaigns performed with the payload during the testing period. <i>*One of the voltage regulator was changed.</i>	59
4.2	On-board correction of the bursts happening in the Cypress SRAM in the Space RadMon-NG.	61
4.3	Various cross-section of the Cypress SRAM used on the mezzanine board on the Space RadMon-NG.	61
4.4	Requirements for the Space RadMon-NG payload that will be used for testing. The priority has been divided into essential (E) and conditional (C). The verification has been divided into Yes (Y), No (N). The asterisk means that it was not verified as a result of the test, but rather by analysis of previous tests and available data.	74
5.1	Various temperature ranges that can be encountered in space.	77
5.2	Sensitivities of the FGDOS sensors at the start of the temperature characterization test.	87
6.1	General orbit parameters of the CELESTA mission.	94
6.2	Prediction of the amount of SEEs in the SRAM of the payload for the GOMX-5 mission.	101

Nomenclature

Abbreviations

ACR	Anomalous Cosmic Ray	IoT	Internet of Things
ADC	Analog Digital Converter	LEO	Low Earth Orbit
ALICE	A Large Ion Collider Experiment	LET	Linear Energy Transfer
ASC	Analog Signal Conditioner	LHC	Large Hadron Collider
ASIC	Application Specific Integrated Circuit	LHCb	Large Hydron Collider beauty
ATLAS	A Toroidal LHC Apparatus	MCMC	Markov Chain Monte Carlo
BNC	Bayonet Neill–Concelman	MCU	Micro Controller Unit
CCD	Charge Coupled Device	MIP	Minimum-Ionizing-Particle
CELESTA	CERN Latchup Experiment STudent sAtellite	MIRAM	Miniaturized Radiation Monitor
CERN	European Organization for Nuclear Research	MISO	Master-In Slave-Out
CHARM	CERN High-energy AcceleRator Mixed-field	MOSFET	Metal-Oxide Semiconductor Field-Effect Transistor
CME	Coronal Mass Ejections	MOSI	Master-Out Slave-In
CMS	Compact Muon Solenoid	MPSoC	MultiProcessing System-on-Chip
CNN	Convolutional Neural Networks	NIEL	Non-Ionizing Energy Loss
COTS	Commercial Off The Shelf	NM	Neutron Monitor
CRC	Cyclic Redundancy Check	OBDH	On-Board Data Handling
CS	Chip Select	PCB	Printed Circuit Board
CSUM	University of Montpellier Space Centre	PIF	Proton Irradiation Facility
DD	Displacement Damage	POT	Protons-On-Target
DUT	Device Under Test	PS	Proton Synchrotron
ECEF	Earth Centered Earth Fixed	PSI	Paul Scherrer Institute
ECI	Earth Centered Inertial	PSU	Power Supply Unit
ESA	European Space Agency	R2E	Radiation to Electronics
EU	European Union	RADFET	Radiation-Sensitive Metal-Oxide Semiconductor Field-Effect Transistor
eV	Electron Volt	RHA	Radiation Hardness Assurance
FDIR	Fault Detection Isolation and Recovery	RPD	Relative Percentage Difference
FG	Floating Gate	SAA	South Atlantic Anomaly
FGDOS	Floating Gate Dosimeter	SATRAM	Space Application of Timepix based Radation Monitor
FPGA	Field Programmable Gate Array	SCK	Serial Clock
FSM	Finite State Machine	SCL	Serial Clock
GCR	Galactic Cosmic Ray	SDA	Serial Data
GEO	Geostationary Orbit	SEB	Single Event Burnout
GLE	Ground-Level Event	SEE	Single Event Effect
Gy	Gray	SEFI	Single Event Functional Interrupt
HEH	High Energy Hadron	SEGR	Single Event Gate Rupture
I2C	Inter-Integrated Circuit	SEL	Single Event Latch-up
IC	Integrated Circuit	SEP	Solar Energetic Particles
IEL	Ionizing Energy Loss	SET	Single Event Transient

SEU	Single Event Upset
SMD	Surface Mount Device
SPE	Solar Particle Events
SPI	Serial Peripheral Interface
SRAM	Static Random-Access Memory
TID	Total Ionizing Dose
TLE	Two-Line Element
ToT	Time-over-threshold
UV	Ultraviolet

Symbols

α	Temperature coefficient	f_{sens}	Sensor frequency
ϵ	Permittivity of the dielectric	I	Current
\mathcal{E}	Electric field	I_d	Drain current
\mathcal{E}_r	Constant depending on ionizing particle	L	Length
v_n	Voltage noise	m	Mass
ϕ	Particle fluence	N_{bits}	Number of bits
ϕ_{HEH}	High energy hadron fluence	N_{rech}	Number of recharges
ϕ_{ThN}	Thermal neutron fluence	Q_{col}	Collected charge
ρ_0	Resistivity of material at equilibrium temperature	Q_{gen}	Generated charge
ρ_T	Resistivity of material with temperature dependence	$R(\epsilon)$	Recombination rate
ρ_{ox}	Oxide density	R	Resistance
σ	Cross-section	R_E	Earth radius
σ_{HEH}	High energy hadron cross-section	S	Sensitivity
σ_{ThN}	Thermal neutron cross-section	S_D	Dose sensitivity
SEU_{tot}	Total number of SEUs	S_T	Temperature sensitivity
A	Area	T	Temperature
B_n	SRAM block	t	time
C	Capacitance	T_0	Reference temperature
c	Speed of light in a vacuum	t_{ox}	Oxide thickness
D	Dose	V	Voltage
e	Elementary charge	V_{cap}	Voltage over capacitor
E_{dep}	Deposited energy	V_{FG}	Floating gate voltage
f	Frequency	V_{init}	Initial voltage
f_0	Constant depending on ionizing particle	W_{e-h}	Energy needed for the creation of one electron-hole pair
f_{osc}	Oscillation frequency	x	Distance
f_{ref}	Reference frequency		

1

Introduction

Space radiation has an enormous effect on the design considerations of spacecraft systems and space missions. To meet this challenge, the space radiation environment must be understood and accurately modelled [10]. This understanding of the environment is of great importance for both the design considerations and the operation of space systems. It can also be used in the assessment of radiation effects on the avionics on-board the spacecraft or satellite [29]. Most spacecraft anomalies are caused by radiation, which can be re-partitioned in the different types of radiation effects as seen in Figure 1.1.

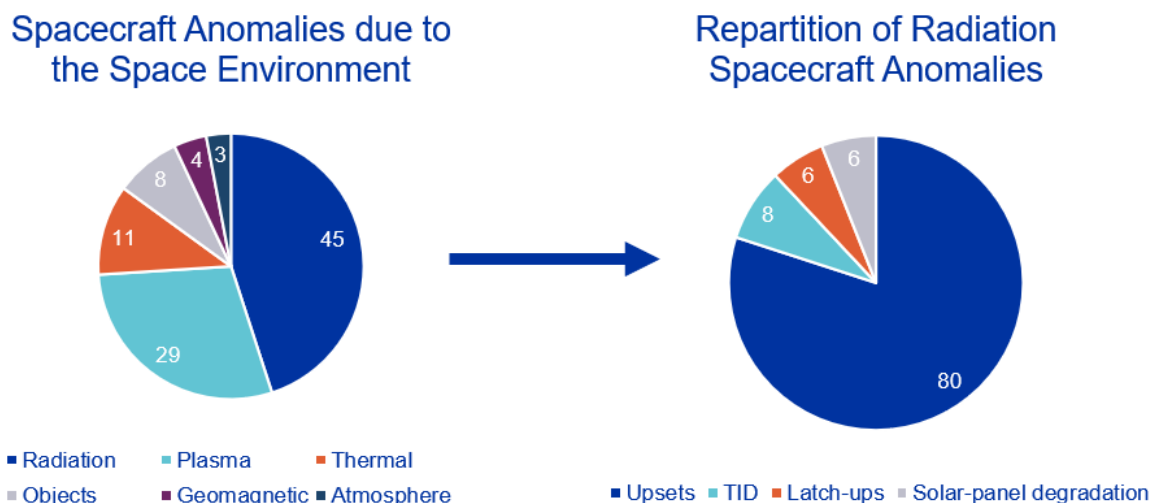


Figure 1.1: Spacecraft anomalies [29].

A second purpose of measuring the radiation environment in space is for the research of the physics of this radiation [37] and for space weather studies [67] [38]. A new class of anomalies in satellite operations have been first observed in 1974 when there was unexpected triggering in digital circuits. It was found that this was caused by interactions with Galactic Cosmic Rays (GCRs). The mechanism assumed responsible in this case was the charging of sensitive transistors to the turn-on voltage [9]. These effects were later named Single Event Effects (SEEs), since they could be caused by a single particle. Other mechanisms that can cause alterations to the performance and reliability of micro-electronic components used in radiation environments are Total Ionizing Dose (TID) or Displacement Damage (DD). These types of effects can come from different sources than GCRs, such as the Van Allen radiation belts containing electrons and protons or the Sun that emits protons, electrons and heavy ions and can cause solar events [7]. The effects do not play a major role on Earth since it is protected from space radiation by its magnetic field and atmosphere. Radiation monitoring might still be relevant on the surface

however, for cases like medical treatments or particle accelerators such as the ones at the European Organization for Nuclear Research (CERN).

Current monitoring devices that have been tested extensively in space are the Space Application of Timepix based Radiation Monitor (SATRAM) [33] and Metal-Oxide Semiconductor Field Effect Transistor (MOSFET) based devices such as the Radiation Sensitive MOSFET (RADFET) [4]. CERN has developed radiation monitoring devices for the Large Hadron Collider (LHC) and injection lines to monitor the TID which are currently based on RADFETs. They are now performing investigations on a new type of radiation sensor which utilizes a floating gate (FG) transistor as radiation sensitive part [12]. This device is called a Floating Gate Dosimeter (FGDOS) and was first developed by Sealicon (former iC-Málaga) with a characterization done at CERN [23]. This sensor will not only be further developed for accelerator applications, but also as radiation dose sensor for space applications. It will be one of the sensors used on the Space RadMon-NG payload [49]. This payload is the main scope of this thesis research.

There are however some challenges in this area. The first challenge has to do with the Static Random-Access Memory (SRAM) on the sensor board. In previous tests, this SRAM showed some peculiar behaviour where there were sudden error bursts in the device that could not be explained. These bursts make the measuring of SEEs unreliable and need to be detected. The second challenge is to prepare the FG sensor for the space environment in particular in terms of radiation and temperature variations. The influences of these environmental conditions on the sensor performance are not known yet. One of the things that was previously found in a constant dose rate test, is that there is some type of sensitivity degradation in the sensor. This has not been studied yet with radiation and temperature variations simultaneously. So far only an older type of FGDOS has flown once in space on a Lunar flyby mission [18], which showed a promising performance compared to OMERE simulations.

1.1. The European Organisation for Nuclear Research

The thesis work has been performed at CERN located in the canton of Geneva, Switzerland. CERN is one of the world's largest and most respectable institutes for scientific research. The main focus of the organization is to perform fundamental research on elementary particles. By the desire of understanding the universe and its building blocks, CERN is pushing technology to its limits or even further. CERN has build multiple particle accelerators and detectors that can reproduce and measure events that also occurred within a fraction of a second after the Big Bang. The most famous accelerator is the LHC, the largest particle accelerator in the world with a total length of 27 km. Particles are accelerated by a series of other machines before actually entering the LHC. In the LHC, the particles are accelerated in beams up until 6.8 TeV before they collide with each other. These particles created by these collisions are then studied by experiments located at the collision points around the LHC. These are: ALICE (A Large Ion Collider Experiment), ATLAS (A Toroidal LHC ApparatuS), CMS (Compact Muon Solenoid) and LHCb (Large Hadron Collider beauty). The experiments are explained in more detail below and the overall set-up of accelerators and detectors can be seen in Figure 1.2.

- ALICE: Detector designed to study strongly interacting matter at extreme energy densities. This can also result in so called quark-gluon plasma's.
- ATLAS: General purpose detector, which investigated a wide range of physics, from the search of the Higgs boson to exotic physics which could explain the dark matter mystery.
- CMS: Another general purpose detector with the same scientific goals as the ATLAS experiment, but with different technical solutions and a different magnet-system design.
- LHCb: Detector designed to study the beauty quark and focusing on the differences between matter and antimatter.

On 4 July 2012, the ATLAS and CMS experiments announced that they had independently observed a new particle in the mass region of around 125 GeV, compatible with the theoretical characteristics of the Higgs boson. On top of this extraordinary discovery, which implied in 2013 the Physics Nobel Prize to François Englert and Peter Higgs, the LHC experiments produced an incredible amount of scientific publications.

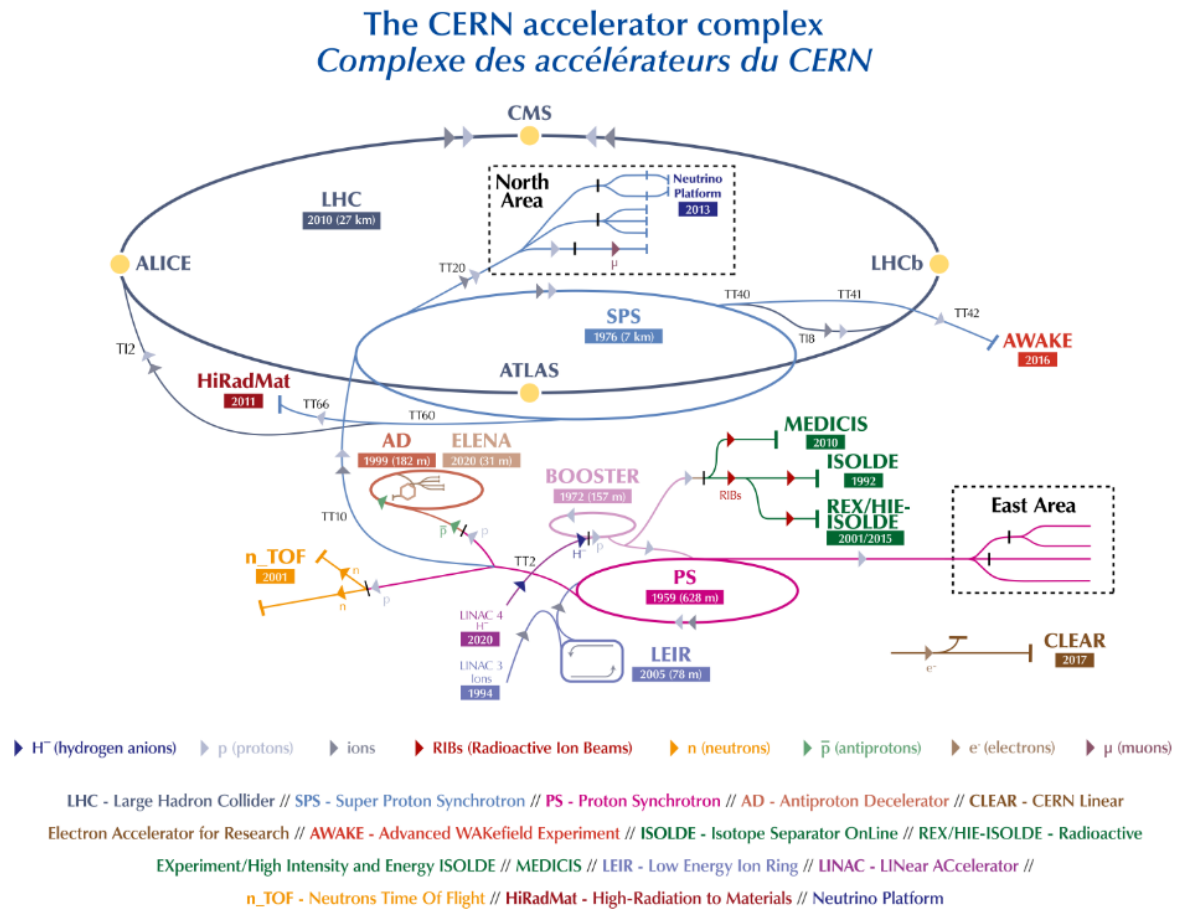


Figure 1.2: The CERN accelerator complex, layout in 2022 [39].

Since these experiments study very complex and rare events, building the accelerators and detectors was very challenging. One issue which is similar to space, or any other industry that encounters radiation, is to make the electronics required for the experiment radiation tolerant. A specific Radiation Hardness Assurance (RHA) procedure was created by CERN for systems to be used in radiation environments [25]. Because of the immense amount of electronics that CERN requires, there is a strong interest to move from Application Specific Integrated Circuits (ASICs) and radiation hardened systems to systems based on Commercial Off The Shelf (COTS) components. This is a very similar trend to what is happening in the space industry, hence the research performed at CERN has a great synergy with the research related to space flight. Before the start of this thesis research, CERN has already been working on its first satellite mission. This is the CELESTA mission, which was launched in July 2022, just after the kick-off of the thesis.

1.2. Research Design

This section will give an outline of the research design by introducing the main research areas, the research objective, research questions and the expected outcome of this thesis. The main topic of this research, as introduced in first part of this chapter, will be space radiation monitoring. This topic can be divided into three main research areas. The first one being the space radiation environment and effects, since this environment will be monitored and these effects (such as dose) will be measured while also affecting the sensor performance. The second area is radiation monitoring, which is more focused on the radiation sensitive part of sensor circuits and how radiation can be measured by means of physical mechanisms. This part will mainly focus on the High Energy Hadron (HEH) fluence and the FGDOS measurements. The last relevant research area is a combination of space embedded systems for the development of the payload itself and the test set-ups needed for characterizations and verifications.

To kick-off the research, a research objective is defined. This objective is set to guide the overall goal of the thesis and to give some direction to the research question. The objective is to allow for a increased resolution mapping of the near Earth radiation environment by performing a system analysis of the payload, verifying the firmware, characterizing the sensors and integrating results from previous missions. The final outcome of the thesis will be a flight ready declaration of the Space RadMon-NG payload hardware and firmware, that can ultimately return a more accurate radiation map of Low Earth Orbit (LEO). It will also come with a set of recommendations on how to optimize retrieving the results from the payload.

The research questions have been set up according to the Specific-Measurable-Attainable-Relevant-Time based principle, with each of the sub-questions leading to a kind of deliverable. In this way, the sub-questions each lead to a specific, measurable, attainable and realistic goal. Based on the combination of the initial thesis topic, the research objective and the literature study, the following main research question is proposed:

How can the Space RadMon-NG payload make significant advances in space radiation monitoring compared to the current state-of-the-art?

This main research can then be divided in the following sub-questions to break down the various activities to be performed and researched during the thesis. The questions will focus on the system study of the payload, state-of-the-art comparison, the system-level testing, the temperature characterization of the FGDOS sensor and an analysis of the CELESTA mission data.

- (i) What are the operational principles of the Space RadMon-NG payload and how does the system compare to current state-of-the-art?
- (ii) How does the payload perform when in a mixed-field radiation environment such as space and how can this performance be optimized?
- (iii) What are the characteristics of the FGDOS sensor when exposed to a space-like environment and how can the sensor be as accurate as possible?
- (iv) Which lessons can be derived from the CELESTA data and how can this data be used to define the data acquisition design of Space RadMon-NG?

By using these sub-questions as guidance of the thesis work, a final well formulated conclusion can be given to the main research question of this research with appropriate intermediate deliverables to stay on track. Each of the sub-questions will be addressed in a dedicated chapter: chapter 3 will contain an extensive analysis of the Space RadMon-NG and will do a state-of-the-art comparison; chapter 4 will focus on the system-level testing of the payload; chapter 5 will mainly focus on the FGDOS temperature characterization testing; chapter 6 will elaborate on the CELESTA mission, analyze data and set-up the new payload analysis. The conclusion and answers to the questions will be given in chapter 7, with additionally some future work proposals and recommendations.

2

Literature Review

This chapter contains the literature review for the thesis. It is mainly based upon the literature study conducted as preparation of the thesis. The literature review contains three main parts: radiation in the space environment and its effects, the HEH fluence sensors with Single Event Upset (SEU) bursts in a COTS SRAM device and the FGDOS for TID measurements.

2.1. Radiation Mechanisms

The basis of this project rests on radiation and the effects it can have on micro-electronics, specifically for space systems. To understand what these effects are, it is crucial to have a proper definition and understanding of radiation itself, building the knowledge of the topic from the ground up. This means knowing what particles are involved and what are the associated interactions of particles that can lead to the mentioned effects. This section will explain particles, the relevant particle interactions and a definition of the radiation environment that can be encountered in space. It will end with an explanation of what effects radiation can have on micro-electronics.

2.1.1. Particles

All matter in the universe is made of elementary particles. These elementary particles appear in two groups, namely quarks and leptons. The groups each contain six particles, which are related in pairs. The quarks contain the up - bottom pair, the charm - strange pair and the top - down pair. The lepton group contains the electron - electron neutrino pair, the muon - muon neutrino pair and the tau tau neutrino pair. The electron, muon and tau lepton all have an electric charge and a sizeable mass, while the neutrinos are electrically neutral with very little mass. All the quarks and leptons together are also known as fermions, which can contain a half-odd-integer spin. Spin is a fundamental characteristic of particles and described the total or intrinsic angular momentum of the particle.

In the universe, there are four fundamental forces at play. These are the strong force, the weak force, the electromagnetic force and the gravitational force. Each of these forces act on different ranges and have different strengths. The weakest force of them all is gravity, however it works on infinite range. The next one in line is the weak force, which is already much stronger than gravity but only acts on very short range (atomic level). The electromagnetic force is again a lot stronger than both the weak force and the gravitational force while also acting on infinite range. The strong force is the strongest of all fundamental forces, however also only acts on atomic level. Three of these force are a result from force carrier particles, named bosons. Bosons are particles that can contain integer spin. Discrete amount of energy is exchanged between matter by transferring bosons. The strong force is carried by the gluon boson, the electromagnetic force is carried by the photon boson and the weak force are carried by the W and Z bosons. Although not found yet in particle physics, it is hypothesized that the graviton boson is the particle carrying the gravitational force. One crucial particle, the particle that gives mass to all elementary particles, was discovered at CERN in 2012. This particle is called the Higgs boson. A key difference of this particle with the other elementary particles is the origin. Normally, a particle is de-

scribed as a wave in a field (such as light with a photon). However, in the Higgs boson case, the Higgs field came first which fills the entire universe giving mass to all elementary particles. The Higgs boson is a wave in this field and the discovery of the boson confirms the existence of the field. These theories all fit together in the so called Standard Model of particle physics. An illustration of the standard model with the elementary particles can be seen in Figure 2.1.

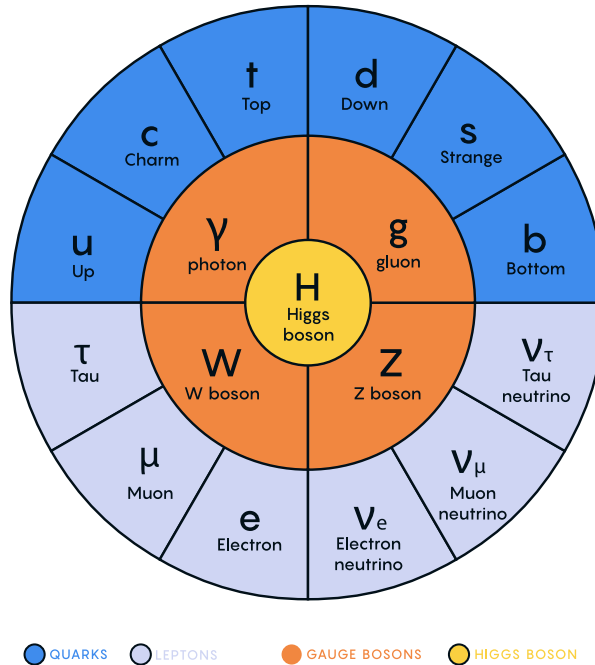


Figure 2.1: The Standard Model of particle physics. The graphic was taken from Quanta Magazine (2020) [47].

Bigger particles, like protons and neutrons, are made of these elementary particles. To be specific, the proton consists of two up quarks and one down quark, while the neutron consists of one up quark and two down quarks. These quarks are held together by the strong force (or the gluon boson). Since the proton has a charge of $+1e$ and the neutron does not contain any charge, it is believed that the up quark contains $+\frac{2}{3}e$ charge and the down quark contains $-\frac{1}{3}e$ charge. The groups that these bigger particles with three quarks belong to are called baryons. The proton and neutron are part of the nucleons category, while other baryons are part of the hyperons category. The second group of bigger particles are called mesons, which consist out of one quark and one anti-quark. This can again be divided into two categories, called pions and kaons. In general, baryons and mesons belong to the hadron type. The hadron is a particle which experience a strong nuclear force and containing two or three quarks. When there is a hadron with an energy higher than 20 Mev, it is referred to as a HEH.

A cluster of protons and neutrons (referred to as a nucleus) with a corresponding amount of electrons 'orbiting', can create a chemical element. It is important to note that the electrons are not really orbiting the nucleus, but are rather around the nucleus in a probability cloud. This probability cloud can be described with spherical harmonics, using the correct degree and order of the function. In total there are 118 chemical elements known. If such an element does not have the corresponding amount of electrons (one too much or too little for example), the element becomes charged and turns into an ion. Heavy ions are ions with a mass larger than the Helium-4 (^4He) element.

2.1.2. Particle Interactions

There are various types of particle interactions that can take place when a particle hits the lattice of matter. Out of the Standard Model, the photon, charged particles and neutron interactions will be considered. Particle interactions can be divided in these three categories. The effects resulting from these interactions in each category is elaborated below. Each category will give a brief explanation of the

particles involved and will show an illustration. Note that the illustrations are not physically representative, but rather used to understand the mechanism behind the interaction. After, the topic of energy loss will also briefly be touched upon. Most of the information given in this sub-section is taken from the thesis [30].

Photons

There are three kind of interactions that can happen as a results of matter being struck by a photon. A photon is a wave in the electromagnetic field and can contain quite some amount of energy. These possible photon interactions are listed below and the matching illustrations can be seen in Figure 2.2.

- Photoelectric effect: The energy of the photon is transferred to the electron it hits. When the energy of the photon is larger than the binding energy of the electron it hits, the electron can be ejected from its cloud.
- Compton effect: The energy of the photon is much larger than the binding energy of the electron. The photon collides with the electron and the energy of the photon is partially transferred to the electron, which is ejected from the cloud. The remaining energy stays with the photon, resulting in a change in the wavelength of the photon and scattering of the photon.
- Pair production: This interaction has the requirement that the trajectory of the photon is very close to the nucleus of the atom. The energy of the photon must also be over the threshold of $2m_e c^2$, where m_e is the mass of the electron and c the speed of light in vacuum. The photon loses all its energy and creates an electron-positron pair.

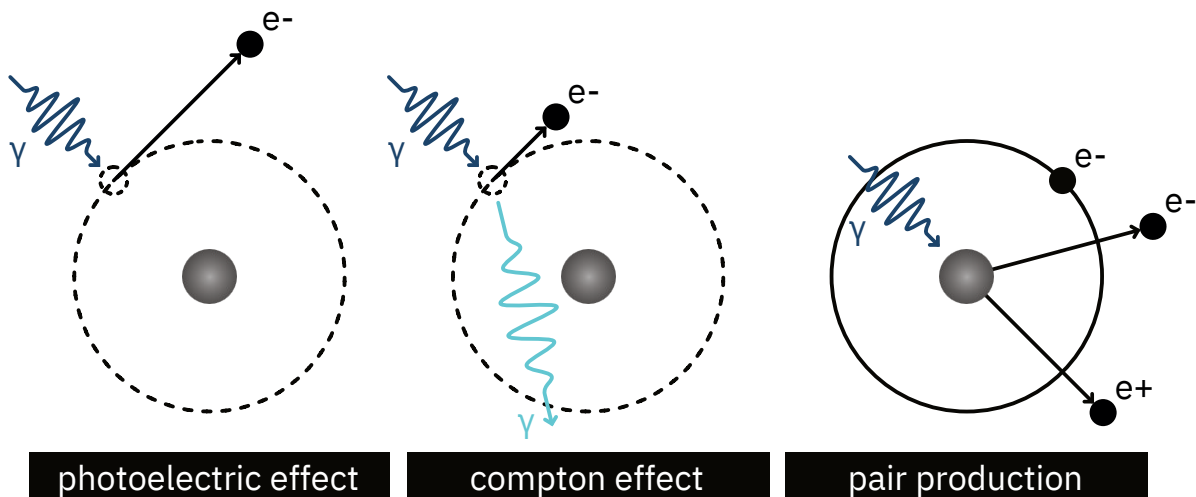


Figure 2.2: Illustration of the type of interactions between photons and matter. This figure is adopted from [36] without any changes.

Charged Particles

There are three kind of interactions that can happen as a results of matter being struck by a charged particle. Charged particles include particles such as pions (π^\pm), protons (p^\pm) and kaons (K^\pm), but also the leptons with a charge like the muon (μ^\pm), tau (τ^\pm) and electron (e^\pm). These particles and leptons can contain an electric charge of positive or negative value. For the case of the electron with a positive charge, it would be a positron. The interactions of these particles are listed below and the matching illustrations can be seen in Figure 2.3. All of the three interactions shown are a Coulombic interactions, or some form of Rutherford scattering.

- Bremsstrahlung: When a particle without much mass (e.g. an electron) passes past the nucleus of an atom, the electric field of the nucleus can deflect the charged particle. The particle then loses some of its energy which is emitted as a photon.
- Ionization: When a charged particle travels through an electron cloud with an energy higher than the binding energy of the electron, the electron will be ejected from the cloud.

- **Excitation:** When a charged particle travels through an electron cloud with an energy lower than the binding energy of the electron, the electron will be absorb this energy and move into a higher energy state (state excitation). After some time, the electron will fall back to its original state and emit a photon in the process.

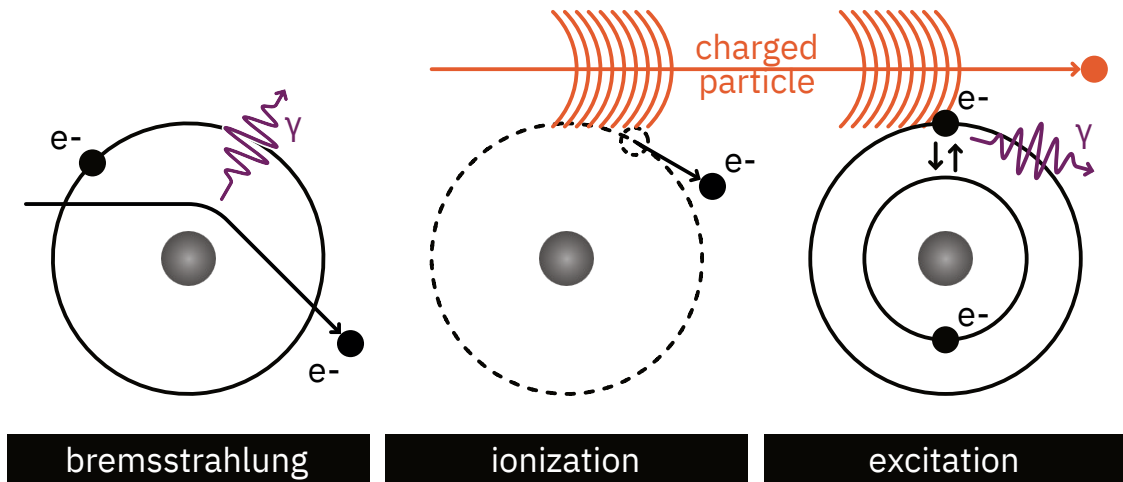


Figure 2.3: Illustration of the type of interactions between charged particles and matter. This figure is adopted from [36] without any changes.

Neutrons

There are three kind of interactions that can happen as a results of matter being struck by a neutron. These interactions are listed below and the matching illustrations can be seen in Figure 2.2. Since neutrons do not contain any electrical charge, the interactions are only nuclear interactions.

- **Absorption:** When a neutron (mostly thermal neutrons that have an energy higher than 24 MeV) hits the nucleus, the energy of the nucleus is increased and is left in an excited state. This energy is later released by the release of a photon.
- **Fission:** A neutron that is absorbed by a very heavy nucleus, the nucleus can split into smaller nuclei also referred to as fission fragments. These is also energy released in the form of photon emission.
- **Inelastic scattering:** A neutron is absorbed by the nucleus. Subsequently, the nucleus emits a neutron of lower energy than the striking neutron and the nucleus stays in an excited state while being scattered. Later, the energy is released by photon emission.
- **Elastic scattering:** A neutron that strikes the nucleus transfers part of its energy to the nucleus. Both the neutron and the nucleus are scattered.

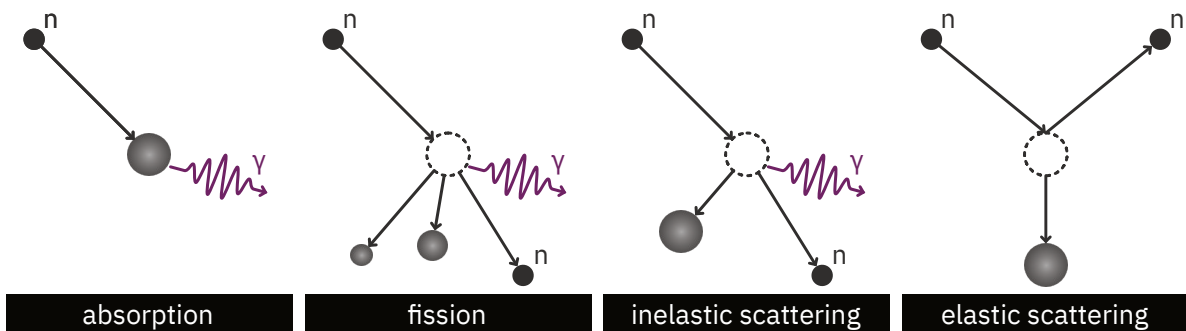


Figure 2.4: Illustration of the type of interactions between neutrons and matter. This figure is adopted from [36] without any changes.

Energy Loss

When a particle hits matter, there can be ionization. Direct ionization is when the ionization is caused by the primary particle that hits the matter. This interaction of the primary particle can create more particles, namely secondary particles. If these secondary particles further ionize the matter, it is called indirect ionization. The particle that strikes the matter will experience a loss of energy. This energy loss can be divided into two groups, Ionizing Energy Loss (IEL) or Non-Ionizing Energy Loss (NIEL). IEL is energy lost due to ionizing interactions, like the photoelectric effect or ionization. NIEL is energy lost due to non-ionizing interactions, like pair production, bremsstrahlung, excitation, etc. With each interaction, the energy of the hitting particle is reduced until being without energy. Linear Energy Transfer (LET) is used to quantify the amount of energy lost for each distance travelled, giving it the unit eV/cm (usually MeV will be used). It can be seen in Equation 2.1, where E is the amount of energy and x the distance.

$$\text{LET} = \frac{\partial E}{\partial x} \quad (2.1)$$

2.1.3. The Space Radiation Environment

The radiation environment in space is an incredibly complex mixture of various particles with different energies, originating from sources within and outside of the Milky Way [48]. In orbits close to Earth, like a LEO, the geomagnetic field of the Earth deflects a portion of the GCRs and almost all radiation due to Solar Particle Events (SPEs), except when they are very intense ones. The Earth itself, or any other planet with a magnetic field, also has radiation belts. There are trapped electrons and protons in the magnetic field and have low to medium energy with intense particle count rates. In deep space or interplanetary travel, the GCR exposure is more severe than in LEO. However, the further away from the Sun also means less solar activity. Some of the radiation varies in energy levels. Relatively low energy (lower than 10 eV) is non-ionizing and higher energies can be ionizing, also depending on the charge of the incident particle. Ionization occurs when an atom or a molecule loses an electron after the passage of a particle, resulting in the atom or molecule being positively charged. The ionization process is dependent on the energy of the particle and the particle type, as well as the characteristics of the material that is subject to the radiation [44]. Some examples of radiation are alpha particles (an atom nucleus moving at high speed), beta particles (high speed electron or positron), gamma rays, x-rays and GCR (heavy ion particles) from space. Non-ionizing radiation examples include radio frequencies, micro-waves, infrared, visible light and Ultra-Violet (UV) light. Each type of radiation can cause damage to both living and non-living objects [27]. The effects of this damage are discussed later in this section. An overview of the main sources of radiation in the space environment with particles and energies can be seen in Table 2.1.

Table 2.1: Main sources of the natural space radiation environment. Taken from source [29].

Radiation source	Particle type	Energy range
Inner radiation belt	Electrons	eV to 10 MeV
	Protons	keV to 500 MeV
Outer radiation belt	Electrons	keV to 10 MeV
	Protons	keV to 500 MeV
	Ions	keV to 500 MeV
Solar flares	Protons	keV to 500 MeV
	Ions	1 to few 10 MeV/n
Galactic cosmic rays	Protons	Max flux at about 300 MeV/n
	Ions	Max flux at about 300 MeV/n

The space radiation environment contains a various amount of sources each emitting their own types of radiation as already mentioned before. This sub-section will elaborate more on the main types of radiation in space, which are trapped radiation, Solar Energetic Particles (SEPs) and GCRs.

Radiation Belts

The trapped radiation are electrons, hadrons and ions trapped in the magnetic field of a celestial body. For the Earth, this trapped radiation is located in the van Allen belts. The time averaged radiation belt omnidirectional fluxes for protons with an energy larger than 10 MeV and electrons with an energy

larger than 0.5 MeV can be seen in Figure 2.5. As seen in this figure, the van Allen belts consist out of two main belts. The inner belt contains a combination of protons and electrons while the outer belt is similar with additionally holding some ions. The inner belt starts relatively close to the Earth surface (approximately 1.1 times the Earth's radius (R_E) from the center of the Earth) and ends at around $4 R_E$. The outer belt location starts at approximately $4 R_E$ and ends at $6 R_E$. The inner van Allen belt is also the cause of the South Atlantic Anomaly (SAA). This is an area over the southern part of Brazil where higher radiation is observed because it is closer to Earth. It is closer to the surface of the Earth in that area since there is a displacement of the magnetic dipole axes from the Earth's center [53].

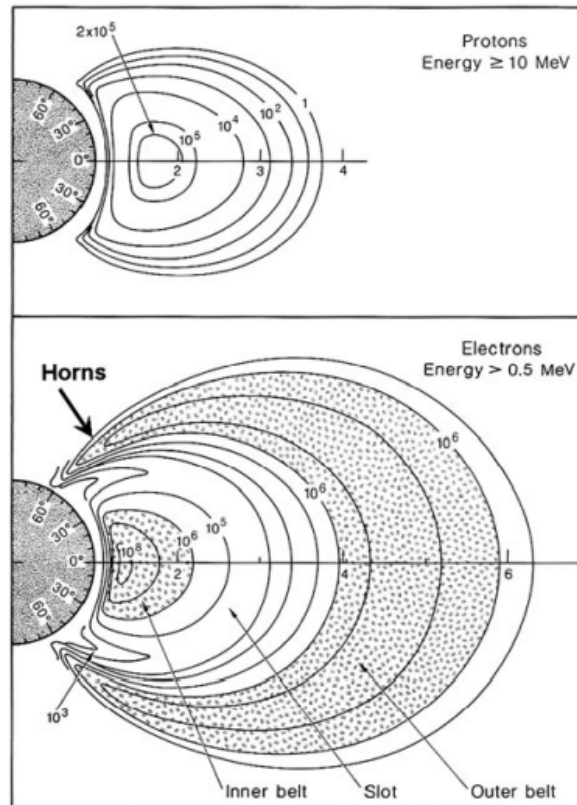


Figure 2.5: Time averages radiation belt omnidirectional fluxes for protons (>10 MeV, top) and electrons (>0.5 MeV, bottom). This figure is adopted from [42] without any changes.

Solar Radiation

The Sun emits, besides electromagnetic radiation in the form of light, also a continuous stream of particle radiation consisting out of mostly electrons and protons. This particle radiation is the so called 'solar wind' and can also be referred to as SEPs. The energies of these particles are relatively low compared to the radiation belts, for a proton between 100 eV and 3.5 keV. The intensities of the particles can vary between two orders of magnitude, between 10^{10} and 10^{12} particles $\text{cm}^{-2} \text{s}^{-1} \text{sr}^{-1}$. The velocities of these particles can range from 300 km to 800 km s^{-1} [53]. Additional to the continuous particle radiation, the Sun can also emit higher energy particles during SPEs. In these SPEs, large currents and moving magnetic fields in the solar corona, called Coronal Mass Ejections (CMEs) accelerate the solar matter. Coronal particles with energies up to multiple GeV escape into interplanetary space and will spiral around the interplanetary magnetic field lines. Major SPEs are observed on Earth as random events with a low frequency, typically once per month. Events with significant fluxes of protons with higher energies can be observed as Ground-Level Events (GLEs) by Neutron Monitors (NMs). Figure 2.6 shows the number of GLEs observed in former solar cycles. Earth is currently in the 25th solar cycle (starting 2019) [53]. As seen in the figure, energies measured are typically larger than 10 MeV and can be larger than 30 MeV. The flux during a minimum period is around $2 \cdot 10^6$ protons cm^{-2} and during a maximum can be up to 10^{10} protons cm^{-2} . The time profile of a SPE usually starts of with an exponential increase in flux. The peak of this increase can take minutes to hours and the emitted energy

of the protons lies between 15 and 500 MeV with an intensity of maximum 10^4 particles $\text{cm}^{-2} \text{s}^{-1} \text{sr}^{-1}$ [21]. As seen in Figure 2.6, SPEs have a higher occurrence during solar maxima but could also occur in solar minima (see year 1964 for example). No clear pattern of SPE occurrences has been established yet.

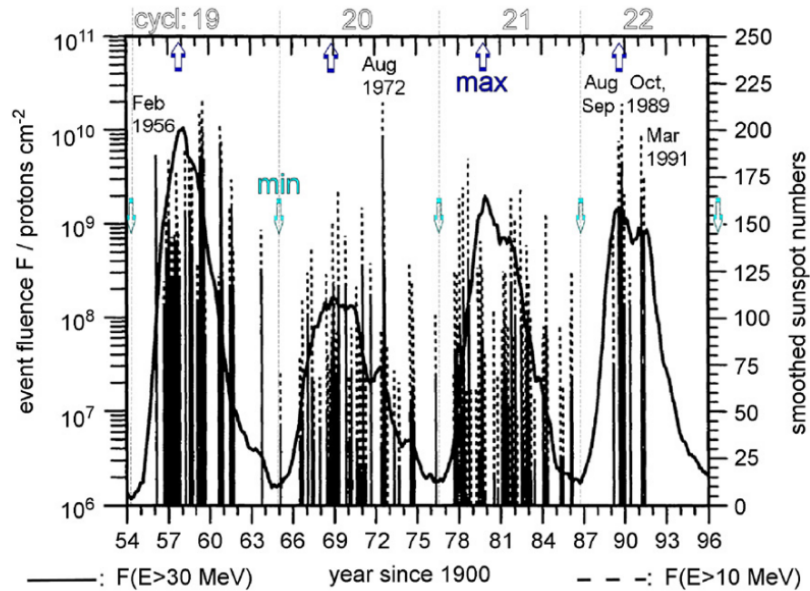


Figure 2.6: GLEs measured on Earth by NMs during the former solar cycles. This figure is adopted from [52].

Cosmic Radiation

GCRs are a type of radiation that originates from outside of the Solar System and arrives on Earth from all directions, isotropically. There is no information about the direction of the sources of the radiation, since the particles are scrambled by irregular interstellar magnetic fields on their way towards the Earth. The energies of these particles is very high (up to 10^{20} eV or 0.1 ZeV), which implicates that they most probable originate from supernova explosions, neutron stars, pulsars and other sources with high energetic phenomena. Most particles are up to several GeV. The detected particles consist of 83.3% protons (hydrogen nuclei), 13.72% alpha particles, 2% electrons and 0.98% heavier nuclei [53]. Some ions with significant energy that are heavier than helium nuclei have been named HZE particles, where the "Z" and "E" stand for charge and high energy respectively [28]. GCR fluxes are not constant and can vary between two extremes which correspond in time with the maximum and minimum solar activity. Solar activity and GCR fluxes have an inverse correlation, as is observed in Figure 2.7. This figure shows the count of secondary particles from the Earth's atmosphere, after interacting with GCRs. This correlation is caused by the magnetic field of the Sun, which is coupled to solar wind and Sun spots. During a Sun spot maxima, the magnetic field is stronger, deflecting more GCRs in the Solar System. This is only the case for particles with energies up to 1 GeV per nuclei [21]. Next to GCR, there is also an anomalous component observed called Anomalous Cosmic Rays (ACRs). ACRs consist out of neutral particles coming from the interstellar gas which become single ionized by solar radiation after entering the heliosphere, an area where the main particle flux originates from solar wind. The particles are accelerated due to collisions in this region and are therefore able to penetrate deeper into the magnetic field than fully ionized GCRs. Their energies are around 20 MeV per nuclei, which means that small shielding would already stop the particle having an effect [28].

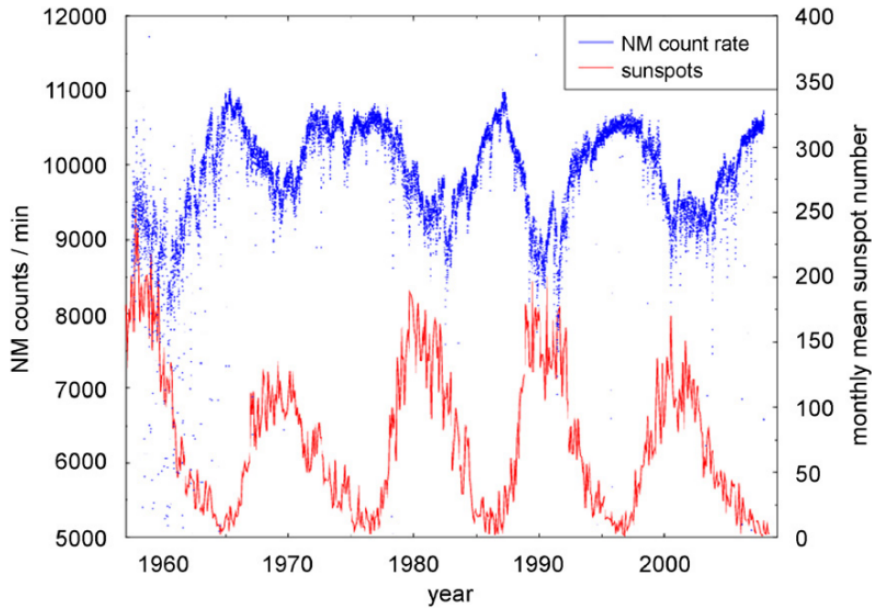


Figure 2.7: GCR variation with the Solar cycle measured by NMs showing an inverse relationship. The figure has been adopted without change from [53].

2.1.4. Radiation Effects on Micro-Electronics

The radiation mentioned in the previous sub-sections can have a various amount of effects on micro-electronics. There are three different effects that can be caused by radiation: TID, DD and SEEs. The latter one, SEEs, can be divided into non-destructive and destructive events. An overview of the radiation effects can be seen in Table 2.2, where the important parameter is shown together with the particle type that causes the effect and the units in which the effect is measured. The trapped radiation mostly causes TID effects. The protons and ions in the trapped radiation could possibly also cause DD and SEEs, although the DD will be limited in space. For Solar radiation, the protons can cause any of the three effects. The ions will mostly cause SEEs. For Cosmic radiation, which are mostly ions or charged particles, SEEs will be caused. In space systems, SEEs are also the most common cause of an anomaly. Radiation effects or the major cause of space system anomalies, covering 45%. Of this percentage, the anomalies are for 86% caused by SEEs (giving a total percentage of 38.7%) [29].

Table 2.2: Radiation effects overview with the parameters, relevant particles and typical units. This table was taken from source [61] with some minor adjustments.

Radiation effect	Parameter(s)	Particles	Units
TID	Ionizing dose in material	Electrons, Hadrons	Grays, rad
DD	Displacement damage equivalent dose, Equivalent fluence of 10 MeV protons/1 MeV electrons	Electrons, Hadrons, Neutrons, Ions	MeV/g, cm ⁻²
SEE (direct ionization)	Events per unit fluence from LET spectra and cross section vs LET	Ions (Z>1)	cm ² vs MeV cm ² / mg
SEE (nuclear reactions)	Events per unit fluence from energy spectra and cross section vs particle energy	Hadrons, Neutrons, Ions	cm ² vs MeV
Payload specific	Energy loss spectra, charge deposition spectra, charging	Electrons, Hadrons, Neutrons, Ions, Induced radioactivity	counts s ⁻¹ MeV ⁻¹

Total Ionizing Dose

TID is caused by ionizing radiation that travels through the semiconductor material in micro-electronics.

The interactions of electrons, protons and ions present in the space environment can ionize the atoms of the semiconductor and generate electron-hole pairs. If the energies of the electrons and holes created are higher than the minimum energy to generate such a pair, the secondary electrons can in turn generate additional electron-hole pairs. This leads to the case that a single high-energy incident particle can create up to a thousand pairs. When a MOSFET is exposed to this high-energy ionizing radiation, the electron-hole pairs will be created in the oxide layer. The created carriers move in the presence of an electric field and can induce the buildup of charge at the device interface, which can lead over time to device degradation [55]. A schematic of how the electron-hole pairs are generated and how the transport of those work in the silicon-oxide semiconductor, can be seen in Figure 2.8. On the right side of the image, the interface with the pure silicon can be seen. Because of the charges at the interface, an interface trap is created where the holes are stuck.

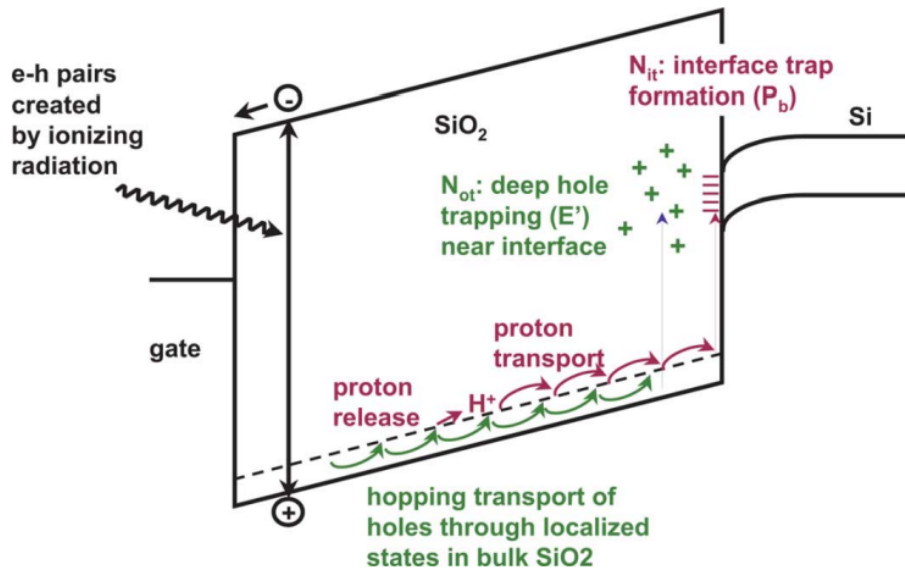


Figure 2.8: Band diagram of a MOSFET with a positive gate bias. Illustrated are the main processes for radiation-induced charge generation. The figure was taken from [55].

TID effects also lead to some physical effects in certain technologies. An overview of these physical effects can be seen in Table 2.3. This table does not cover all the possible effects, just the relevant effects for this research.

Table 2.3: Relevant technologies that are susceptible to TID effects. This table was taken over from the designated ECSS document [61].

Technology category	Sub-category	Effect
MOS	NMOS	Threshold voltage shift
	PMOS	Decrease in drive current
	CMOS	Decrease in switching speed
	CMOS/SOS/SOI	Increased leakage current
Analogue micro-electronics	General	Changes in offset voltage and offset current
		Changes in bias current
		Gain degradation
Digital micro-electronics	General	Enhanced transistor leakage Logic failures
CCDs		Increased dark currents Effects on MOS transistor elements Some effects on CTE
APS		Changes to MOS based circuitry of imager

Displacement Damage

DD is another term that describes effects related to the accumulation of physical damage to a crystal structure. Some of the electrical properties degrade as the effect increases. Unlike TID, which is mainly surface accumulation of trapped charge and interface states, DD is a volumetric effect in that the entire silicon volume is accumulating damage (the semiconductors crystal structure). This ultimately changes the electric and optical properties of the bulk and can limit the semiconductor reliability and functionality. However, MOSFET devices are much less sensitive to DD dose and can tolerate higher doses until performance is compromised. This is because the active region of the MOSFET is the channel formed between source and drain, which is very thin so the volume is also small [7]. An illustration of DD can be seen in Figure 2.9. The figure shows the general displacement of an atom in the lattice due to a striking particle, as well as a stable defect when the silicon material has been doped.

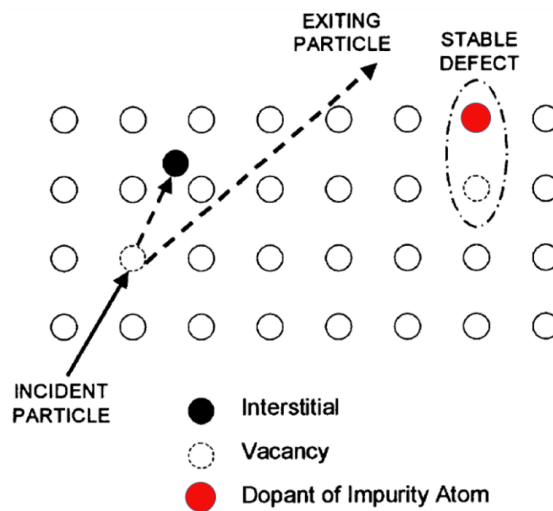


Figure 2.9: Illustration of displacement damage. The figure was taken from [41].

The authors in [63] suggest that a particle with a NIEL effect can result in phonon production. This phonon can subsequently cause the displacement of lattice atoms, altering the performance of the matter. DD can occur through interaction with an incident particle by one of the following processes:

- (i) Coulombic interaction (or Rutherford scattering);

- (ii) Nuclear elastic scattering;
- (iii) Nuclear inelastic scattering.

Nearly all effects of DD on the electrical and optical properties can be understood by using energy levels and the band-gap. Radiation induced levels will result in the following effects: recombination lifetime and diffusion length shortened, decrease of generation lifetime, increase in carrier trapping, majority carrier concentration changes, increased thermal generation of electron-hole pairs (when there is a high electric field) and finally, tunneling at junctions is enabled. Additionally, the defects can also reduce the carrier mobility. Figure 2.10 shows the radiation induced energy levels in a silicon band-gap. This gives rise to the following processes:

- (a) Enhanced thermal generation;
- (b) Enhanced recombination;
- (c) Enhanced temporary trapping;
- (d) Reduced carrier concentration.

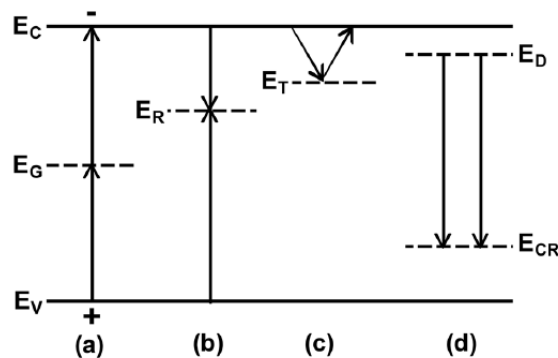


Figure 2.10: Illustration of four effects of displacement damage due to energy levels introduced in the band-gap: a) increased thermal generation of carriers; b) increased carrier recombination; c) increased temporary trapping; d) reduction in majority-carrier concentration. This figure was taken from [63].

This primary physical effect by (a) is an increase in dark current for any device containing a depletion region. The second process (b) causes a reduced power output in for example solar cells and decreased gain in bipolar transistors. Process (c) affects the charge collection efficiency in particle detectors based on silicon and the charge transfer efficiency in Charge Coupled Devices (CCDs). The fourth process (d) can affect the operation of the device. The authors in [62] confirm these effects.

The NIEL, as mentioned before in this subsection, is a very common parameter to scale degradation by DD. It has been demonstrated that many radiation effects that contribute to defect formation in the material scale linearly with the NIEL [35]. The authors in [45] reported an analytical approach to use NIEL for heavy ion dosage. They showed that NIEL for heavy ions at low energies can be completely accounted for by using screened Coulomb potential. This model applied to any incident particle on any target material where the Coulomb interaction is primarily responsible, as explained using the band-gaps.

Single Event Effects

SEEs is an overarching name for a collection of phenomena where electronics can be permanently damaged or temporarily disrupted by single particles. The particles that can induce these effects are mainly hadrons, neutrons and (heavy) ions. In the case of ions, the effect occurs by ionization of the sensitive regions in the semiconductor. For hadrons and neutrons, the nuclear interactions within (or very near to) the semiconductor can generate a localized charge generation. They are two main groups of SEEs, namely destructive and non-destructive. They can again be divided in more categories based what is happening during the effect. The physical process that happens in the semiconductor when a particle

passes through that can lead to a SEE can be seen in Figure 2.11. It shows the three main processes in the semiconductor. First (a) the passage of the particle/ion, generating charge or electron-hole pairs. Secondly (b), the drift of the charges creating a current in the semiconductor. Lastly (c) the diffusion of the charges which slowly reduces the current.

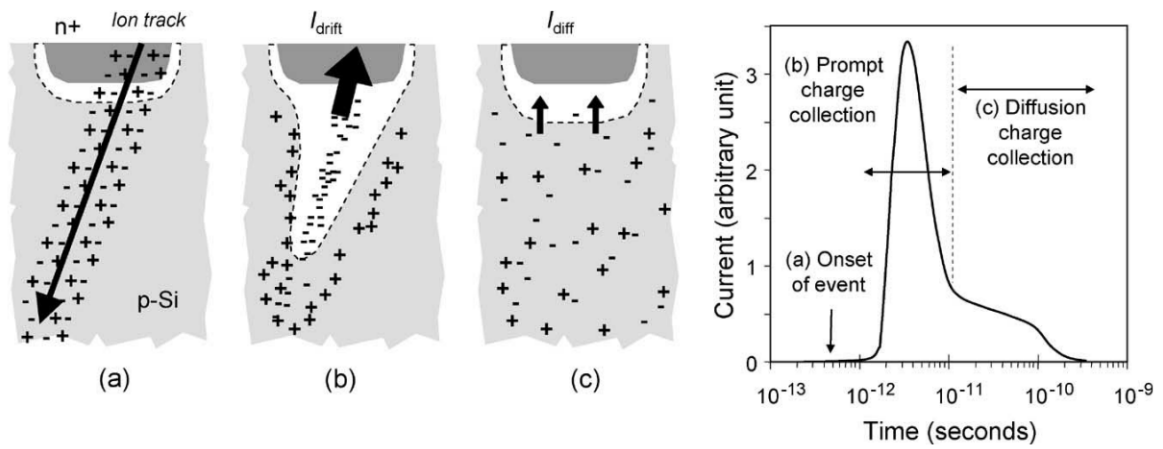


Figure 2.11: Charge generation and collection phases in a reverse-biased junction and the resultant current pulse caused by the passage of a high-energy ion. This figure was taken from [8].

Destructive events are the events where a high current is induced, which can lead to hardware issues. Non-destructive events are events where data gets corrupted or the device is placed in a different operational state. These are mostly software issues. An overview of the single event types, definition and destructiveness is seen in Table 2.4. It is important to note that there also is a difference between digital and analogue Single Event Transients (SETs), called DSETs and ASETs respectively.

Table 2.4: Different type of SEEs with definition and destructiveness level, classified by soft or hard SEE. From source [44].

SEE type	Definition	Desctructive?
Single Event Upset (SEU)	SEUs may occur in a digital circuit when a particle strike causes data to change states in a storage element such a flipflop, latch or memory bit.	No, it can be recovered by a soft reboot.
Single Event Functional Interrupt (SEFI)	SEFIs are interrupts cause by a single particle strike which lead to a temporary non-functionality (or interruption of normal operation) of the affected device. SEFIs occur in a register that controls configuration in, for example, processors, FPGAs or SDRAMs.	No, it can be recovered by a hard or soft reboot.
Single Event Transient (SET)	SETs are voltage glitches in electronics by a single particle. This can occur on global non-latched elements such as combinational logic, clock lines or control lines. The voltage transient can propagate any significant distance depending on the pulse width and the transistor capacitance	No, however technology scaling causes an increased sensitivity to transients.
Single Event Latch-up (SEL)	SEL is an abnormal high current state in a device cause by the passage of a single energetic particle through sensitive regions resulting in the loss of device functionality.	Yes. If power is not removed quickly, catastrophic failure may occur due to excessive heating or bond wire failure.
Single Event Gate Rupture (SEGR)	SEGRs are events in which a single energetic particle's strike results in a breakdown and subsequent conducting path through the gate oxide of a MOSFET.	Yes. A SEGR is manifested by an increase in gate leakage current and can result in either the degradation or the complete failure of the device.
Single Event Burnout (SEB)	SEBs occur when a single energetic particle's strike induces a localized high current state in a device.	Yes. If not rapidly quenched, the resultant high current causes the device to go into thermal runaway resulting in destructive failure.

As mentioned, SEEs can cause bit flips. This is crucial to remember, since this can lead to significant system errors. To combat this issue, Fault Detection Isolation and Recovery (FDIR) systems can be put in place. A bit change from a 0 to 1 or vice versa could have a significant impact on system, especially for digital sensors. Another important factor in countering SEE effects on software is predicting the rate of SEEs. The authors in [19] proposed an algorithm that can predict SEE error rates. This method utilizes the Markov Chain Monte Carlo (MCMC) algorithm. In terms of mitigation, the best technique for the physical damage of SEEs is shielding or using radiation hardened components. Another method of measuring SEEs is by using a SRAM sensor. In the next chapter, there is explained how SEEs can be measured using this technique and how this can be used to measure the HEH fluence.

2.2. High Energy Hadron Fluence Measurement using SRAM

An important part of monitoring the space environment is measuring the HEH fluence. In first approximation, the SEE rate can be assumed as proportional to the HEH fluence, which is defined as the integral hadron flux above 20 MeV [59]. High energy particles or heavy ions can induce SEEs on microelectronics. This means that it is also essential to measure, not only the TID, but also these particles that can induce SEEs for the prevention and recognition of these SEEs. One of the methods for detection is using a SRAM. Using the mechanism of SEEs in this SRAM, the highly ionizing radiation can be detected. They are sensitive to SEUs and SELs, and can thus detect the highly ionizing radiation that causes it. They can then also alarm in case of excess radiation conditions, such as heavy solar flares [5]. The cross-section of such a device is given by [59]:

$$\sigma = \frac{SEU_{tot}}{N_{bits} \cdot \phi}, \quad (2.2)$$

where SEU_{tot} is the total amount of SEUs recorded throughout the irradiation time, ϕ the particle (HEH) fluence and N_{bits} the number of bits in the SRAM memory. Two values here are essential for measuring the HEH fluence: the SRAM cross-section, whose value can depend on the SRAM operating voltage and the energy of the particles crossing the memory with the correct evaluations of the SEUs in the memory [58]. The 8 Mbit 90 nm Cypress SRAM was chosen as detector on the Space RadMon-NG for the HEH fluence. This SRAM has been characterized in a variety of papers, including [24], [57] and [58].

2.2.1. Cypress 90 nm SRAM Sensor

Source [24] performed a first qualification on this SRAM by testing two lots of memories over a wide range of energies ranging from thermal neutrons to 480 MeV protons in order to calibrate the sensor for CERN applications in the LHC. This was done at the Proton Irradiation Facility (PIF) in the Paul Scherrer Institute (PSI), which can provide an energy range of 30 MeV to 230 MeV. Other testing facilities used were the TRIUMF Laboratory, with an energy range of 230 MeV to 480 MeV and at the PTB facility for neutrons. Despite being a COTS device, it showed to be a good candidate to be used as HEH monitor. It did not show any latch-up below a fluence of $6.5 \cdot 10^{12}$ pp/cm² and TID effects can be neglected up to 30 krad (Si). It was also concluded that the thermal neutron contribution to the total number of SEUs can be neglected, which is a significant advantage compared to previous devices. The cross-section of this SRAM was found to be in the order of 10^{-13} cm²/bit. During the qualification, an issue presented itself in the form of SEU burst events with a large number of error bits. This was the first qualification where such an error was observed. These events, defined as bursts, are potentially harmful and may corrupt the measurement of SEUs leading to a measuring performance loss. After research, the burst observation was found in previous works [64] and is described as a SEE that induces several bits in a chip to fail at the same time. The error bits are located physically at very close distance, resulting from a micro-latch-up event across the semiconductor die [65].

2.2.2. Multiple Cell Upset Bursts and Detection

As mentioned, a problem arose during the first qualification of the SRAM sensor. This issue is a "burst" of bit flips that is caused initially by the irradiation of the device. This phenomenon was seen before in [64]. It was analysed by the authors of [24] and found that the control circuitry for the reading and writing operations plays a large role on the presence of these series of upsets. It is also significantly decreased if the Chip Select (CS) signal is disabled in the set-up. Investigations lead also to the conclusion that the activation of this CS signal increases the amount of bursts. Two of these burst are visualized in Figure 2.12, where the amount of upset rapidly increases in a short amount of readings.

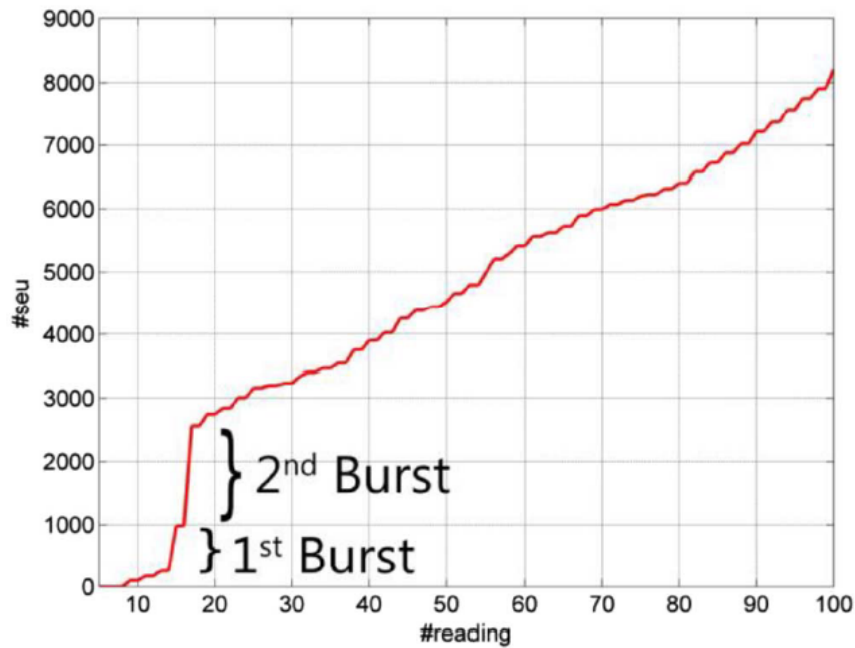


Figure 2.12: Burst events seen at a low flux of $6.82 \cdot 10^6$ pp cm^{-2} . Figure was taken from [24].

Since the amount of errors burst depend partly on the CS signal, they can be reduced by limiting the number of accesses to the memory. They can unfortunately not be fully eliminated. The same researchers also proposed that one can recognize these series of upsets and that they can subsequently be mitigated. The recognition of the burst is performed by dumping part of the memory or the entire memory during the irradiation and analyzing the data. This data is referring to the physical internal structure of the SRAM. By making a bit-map, there is evidence that these bursts can be recognized as they belong to the same memory block. An algorithm has then been developed to check if multiple SEUs of a single reading have this burst signature and subsequently account them as one event only. It has been applied which successfully reduces the amount of SEUs by a factor of five. As of writing the publication, the verification still needed completion by means of a radiation test [24]. A visualization of such a mitigation is seen in Figure 2.13. It shows that by a proper compensation, the correct amount of hadrons (by SEUs) can still be detected.

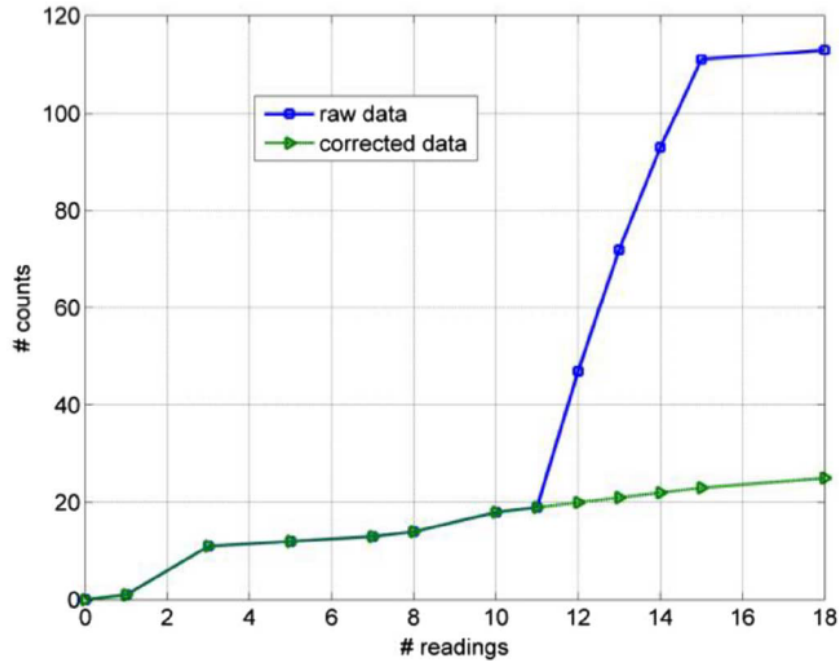


Figure 2.13: Raw readings vs data corrected with the algorithm for bursts mitigation. Figure was taken from [24].

A second characterization was done by the authors of [57] at the PIF in the PSI. The initial algorithm for detection proposed by [24] was found not practical for the CERN RadMon application. The number of devices to scan in the LHC is too large and would be computationally too expensive. Another method for detection is by implementation on a Field Programmable Gate Array (FPGA), which is a first approach toward real-time detection and correction of these bursts. The results of this characterization and the burst detection algorithm used during the tests is elaborated in the next sub-section.

2.2.3. On-line Burst Detection Algorithm

The algorithm proposed by the authors of [57] make use of a scrambled addressing scheme that is applied by the manufacturer. The Cypress SRAM is characterized by this scrambled addressing scheme. After decoding, it is possible to get information on the cells physical location. The detection algorithm accesses the memory using this scheme, which allows for reading the address locations row by row and block by block. Previous experiments have showed that a burst has always involved error bits located in neighbouring rows along the full width of a memory block which is 64 bits. An example of a burst event observation can be seen in Figure 2.14.



Figure 2.14: Example of a burst observation. Black pixels represent a high number of SEUs in nearby cells with neighbouring rows of the same block. White lines represent the boundaries between memory blocks. Figure was taken from [57].

Using these types of observations, a detection window of size 64 bits by 10 rows has been made. This window acts as a moving first-in-first-out buffer. It moves with one row each time across each memory block of the SRAM. All the cells are read at each step, where the output is the total number of SEUs located in that current window. It is then compared to a used set threshold value (Th_{SEU}). When this value is exceeded, a burst event is detected and the number of SEUs counted within that window (SEU_{burst}) is returned with the row and block position. In order to prevent the detection algorithm from detecting the same burst event twice, it is disabled for 16 rows (window of 10 rows + margin) after the detection has taken place. The algorithm has been tested with an optimal threshold value of $Th_{SEU} = 40$. Equation 2.2 can then be rewritten to take burst events into account as follows [57]:

$$\sigma_{corr} = \frac{SEU_{tot} - SEU_{burst}}{N \cdot \phi}, \quad (2.3)$$

where it is now essential to count the total burst upsets to determine the particle fluence. Testing can be done in static or in dynamic mode. Static means that the Device Under Test (DUT) is initialized with a known pattern and then irradiated. Dynamic mode means that the DUT is continuously accessed with a certain period during the irradiation. The tests using this algorithm were run in dynamic mode and the address of each array containing error bits was returned. This allowed for plotting a map of the SEU physical location within the SRAM at the end of each irradiation. Results from the proton tests showed several burst events and a high number of error bits arising when there are readings with small periods (T_{read}). This suggests that low T_{read} values can increase the probability of bursts. Analysis of the error bits showed another effect, as seen in Figure 2.15. In addition to SEU bursts raising in nearby rows, there were also several error bits found on the same column array following the direction of address reading. A fast reading period together with a linear addressing scheme did not yield a high number of SEUs, however the analysis of the error bit locations showed evidence of burst events with no bit column arrays upsets. This means that the physical reading, which is necessary for the detection algorithm, is also responsible for generation of these column bits upsets. This adds complexity of the SEU_{burst} detection needed to compute the corrected cross section σ_{corr} .

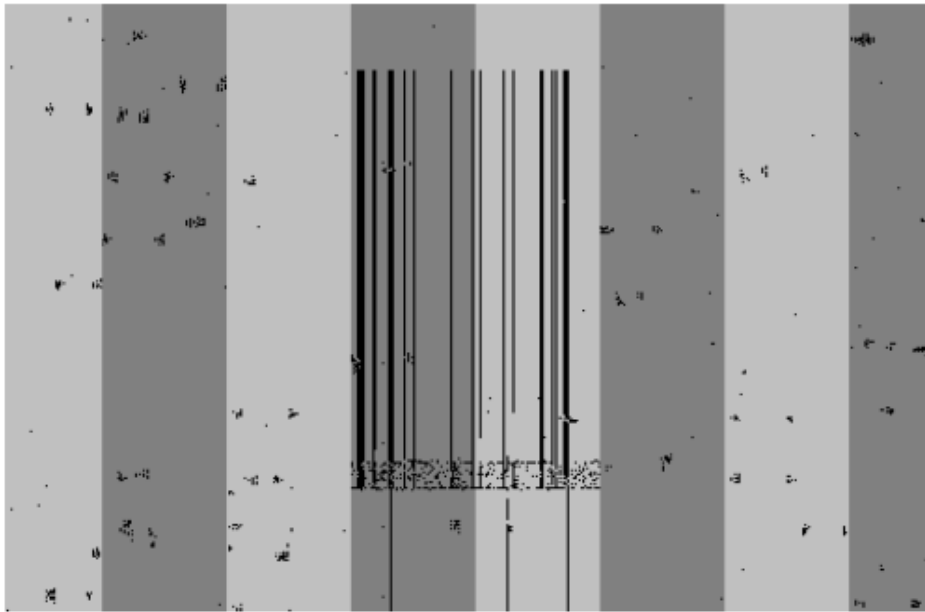


Figure 2.15: Example of an SEU burst event involving several bit upsets on neighbouring rows and error bits located on the same column array. Memory Blocks are highlighted with different shades of grey. Figure was taken from [57].

The detection algorithm output was analyzed during irradiation sessions in dynamic mode with memory rewriting enabled. The returned SEU physical locations were evaluated with the implemented software algorithm and results were compared with the FPGA output. In all cases, the algorithm was able to detect SEU bursts in nearby rows and classifying them as bursts. A direct comparison of σ_{corr}

determined using SEU_{burst} returned by the FPGA algorithm, together with the cross-section reference, was not possible. This was due to the effect of the bit column upsets and several modification of the firmware were required. Since the observed bit column errors were highly affecting the count of cell upsets occurring in a SRAM block, a statistical approach to detect and correct these bursts might prove more effective. Results showed that the amount of upsets within the blocks affected by bit column errors, as well as the value of SEU_{burst} , were much higher than the expected average number of SEUs per SRAM block. In this case, a possible solution to detect and correct SEU bursts would be to evaluating SEUs occurring only within SRAM blocks with a number of events below a threshold value close to the average SEU counts occurring in each block. The number of SEUs within blocks affected by a large number of upsets could then be replaced by the average count of SEUs per block.

2.2.4. Alternating On-line Burst Detection Algorithm

A third characterization on the SRAM was done by [58] at the CHARM facility at CERN. They had first modified and optimized the algorithm from subsection 2.2.3 for better performance. To create the algorithm, a distinction between different sorts of SEU bursts were created. These give rise to SEU burst type *A*, which are smaller SEU burst clusters and SEU burst type *B* which are the SEU bursts located in adjacent rows with the full width of a memory block. They can be seen in Figure 2.16. They proposed that the type *B* SEU bursts, the number of bits involved and the distribution is connected to the structure of the SRAM and the nature of their latchup. The cells in the SRAM are electronically connected in rectangular blocks defined by the well taps of the internal architecture, meaning created currents generated by a micro-latch-up are confined within that rectangular area.



Figure 2.16: Examples of a small cluster of bit upsets (a) and a burst event characterized by several single bit upsets following a rectangular geometrical shape (b). Figure was taken from [58].

Tests of the SRAM and the algorithm at CHARM showed that the desired performance was not yet reached. The bursts were not recognized when below the threshold value (Th_{SEU}). The algorithm was also disabled right after detection of a burst for 16 rows, meaning in some cases where the column pattern were not taken into account, hence ultimately resulting in the wrong corrected cross section. A statistical approach was suggested but has yet to be investigated for its feasibility.

Instead, another method was used that utilized alternating block addressing. It used linear addressing as this did not yield any bit column errors, while showing many type *B* SEU bursts. In the new configuration, the same block was accessed twice at different rows before moving to another block. Once the addresses of the second block were read, the previous block was accessed again. This is repeated for all blocks until a full cycle of the memory was obtained. As mentioned before, it was assumed that the straight lines of bit upsets were formed due to a constant electrical stress of SRAM cells in the same block. When a location of memory is addressed, the rest of the SRAM is kept in data retention and held at a lower voltage than the operating one. Using linear addressing, blocks are constantly switched, therefore memory cells are alternatively active and held at lower voltage for longer periods. This reduces the effective duration of micro-latch-ups and explaining why column SEU bursts were not occurring when using a linear scheme.

Assuming the set of SRAM blocks B_n where $n = 0..63$, the memory was divided into a left part $n = 0..31$ and a right part $n = 32..63$. Starting from the first block, the SRAM is accessed in an alternating manner giving two detection windows. These modification give an increase of 5% of the FPGA area, which is acceptable. In addition, the disabling of the detection window after detection is turned off which allows for full scanning of the memory. The different DUTs were irradiated for more than two weeks and in all

runs with alternating block addressing no bit column errors were detected. Figure 2.17 shows the SEU map of the SRAM die during one of these irradiation sessions. As seen in the figure, three type *B* SEU bursts were detected and the detection window stopped twice for each burst. Results from the software version of the algorithm are perfectly corresponding with the output of the firmware detection, hence this technique is selected for usage in the Space RadMon-NG.

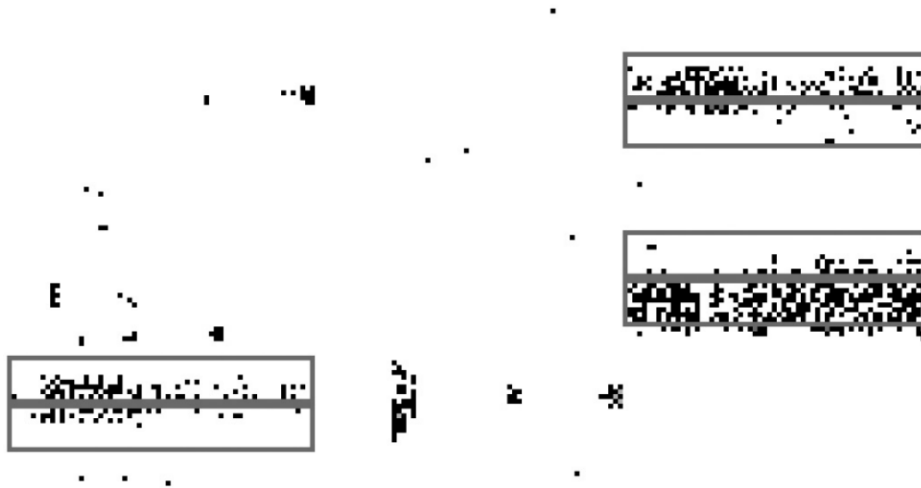


Figure 2.17: SEU map of the SRAM die during irradiation with the alternate block detection algorithm. The rectangles correspond to the detection window at the location where a burst was recognized. Figure was taken from [58].

2.3. Radiation Dose Monitoring with Floating Gates

The FGDOS is relatively new and has been used in space only in a few cases. The sensor was developed by Sealicon and the earliest publication came in 2012. Around 2014, they started testing at CERN and published several joined papers on the sensor. CERN is currently using RADFETs as radiation monitoring devices in their particle accelerators and are doing research to see how to further improve them [12]. In particular the 2 main applications of the FGDOS are in the CERN radiation monitoring systems called the Internet of Things (IoT) RadMon (or BatMon) and in the Space RadMon-NG payload which is flying on-board of the CELESTA mission (launched in 2022) and is planned to be used in more future missions. First of all, this section will present the basic working principles of the sensor. When this is clarified, the layout of the sensor will be analyzed in terms of its hardware components and the different pins. Next to the layout, the different possible operational modes will be discussed as well and the influence of certain variables on the sensitivity on the sensor. Finally, the sensor will be compared to the state-of-the-art RADFET.

2.3.1. Working principles

According to the authors of [50], a FG transistor is one of the building blocks of a non-volatile memory cell (able to store information after power is removed). This transistor is basically the same as a MOS transistor with a conductive layer 'floating' in between the channel and the gate. A schematic can be seen in Figure 2.18, with the sub-circuit included. The FG acts as a potential well, meaning if charge is forced into the well it cannot move from there without applying an external force. The FG stores this charge and the presence of this charge in the FG can alter the threshold voltage of the MOS transistor.

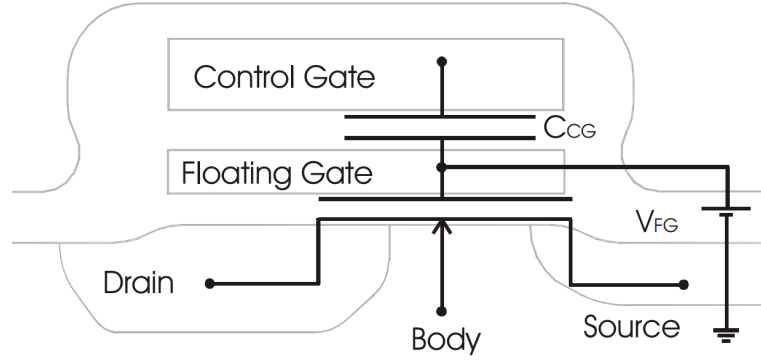


Figure 2.18: Cross section of a FG transistor and basic schematic of the sub-circuit. The figure has been adopted without change from [50].

There are several ways of inducing charge to the FG in the transistor. The capacitance associated with the FG can be charged by an avalanche breakdown or by tunneling from an auxiliary electrode. By having this charge, it can then act as memory cell without need for any power to retain it. Another possible use case is to monitor radiation, which rests on the mechanism of electron-hole creation in semiconductors. Electron-hole creation in the oxide will lead to all TID effects, as mentioned in the first section of this chapter. The buildup of charge that is induced by the generated carriers can quickly lead to device degradation. The mechanisms that cause this degradation can be seen in Figure 2.8. Note that this is for a MOSFET, so the location where the gate is indicated (left of figure) would be the FG in a FG transistor. Figure 2.8 is a MOS band diagram of a p-substrate capacitor with a positive gate bias. Immediately after the electron-hole pairs are generated, the electrons will drift within pico-seconds to the gate side and the hole drift towards the silicon interface. Not all electrons and holes will drift away to the gate and interface, some of them will recombine instead. The fraction of electron-hole pairs that escape the recombination process is called the electron-hole yield or the charge yield. The holes that escaped the recombination process will transport through the oxide towards the interface by hopping through localized states in this oxide. As these holes approach the silicon interface, some fraction of the holes will be trapped. This forms a positive oxide trap charge [55].

A quantitative model can be created as well for describing the FGDOS mechanism, however some assumptions must be made. This model rests on [16]. First, the charge created by radiation in the oxide can be described as:

$$Q_{gen} = \frac{e E_{dep}}{W_{e-h}}, \quad (2.4)$$

where e is the elementary charge, E_{dep} the deposited energy by the ionizing particle and W_{e-h} the energy needed to create one electron-hole pair. The deposited energy can be considered as follows to highlight the dependence of voltage variation and the dose.

$$E_{dep} = m D = \rho_{ox} A t_{ox} D. \quad (2.5)$$

In this equation, m is the mass, D is the dose, ρ_{ox} the oxide density, A the area and t_{ox} the oxide thickness. Assuming that all electrons that survive the initial recombination reach the plates and that no positive charge is trapped in the oxide and silicon interface, the collected charge will be proportional to the generated charge with the recombination rate R :

$$Q_{col} = Q_{gen} (1 - R(\mathcal{E})), \quad (2.6)$$

where \mathcal{E} indicates the electric field which affects the charge yield by reducing the probability of recombination. When the charge has been collected on the metal plate, the voltage variation on the capacitor can be determined as a function of the dose. This is done using the capacitor relationship:

$$\Delta V = \frac{Q_{col}}{C}, \quad (2.7)$$

where C is the capacitance of the capacitor:

$$C = \frac{\epsilon A}{t_{ox}}, \quad (2.8)$$

in which ϵ is the permittivity of the dielectric given by the product of the relative permittivity (ϵ_r) and the permittivity of free space (ϵ_0). Combining all equations yield the final equation for the voltage variation:

$$\Delta V = \frac{e (1 - R(\mathcal{E})) \rho_{ox} t_{ox}^2}{\epsilon W_{e-h}} D. \quad (2.9)$$

As the equation indicates, the voltage variation is a function of the dose. However, the function is not completely correct as the charge yield depends on the electric field, which is then again a function of the voltage variation. The fraction of carriers surviving the recombination against the electric field for different particles is shown in Figure 2.19. If the electric field in the insulator can be determined as the ratio of the voltage over the capacitor and the oxide thickness, it results in the following expression:

$$\mathcal{E} = \frac{V_{cap}}{t_{ox}} = \frac{V_{init} - \Delta V}{t_{ox}}. \quad (2.10)$$

To make the relation completely correct, it would be necessary to know the expression of the charge yield.

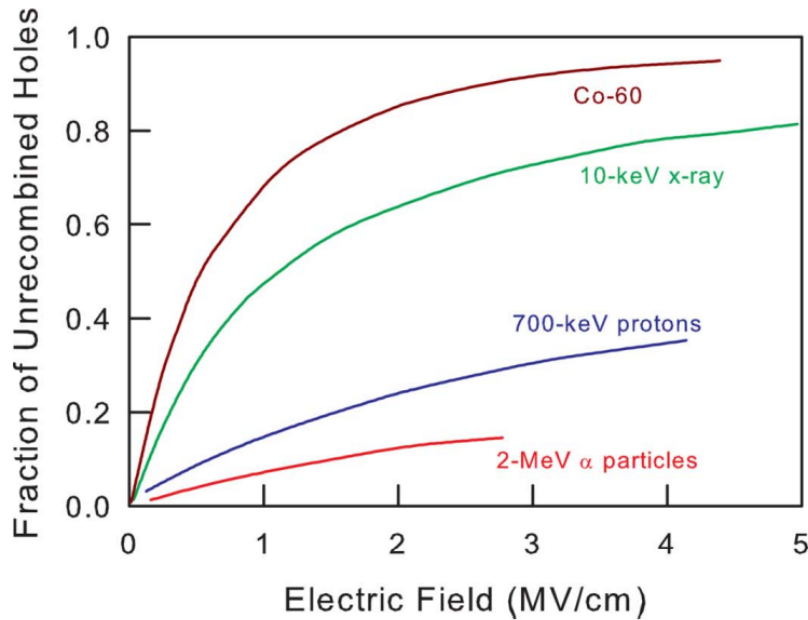


Figure 2.19: The fraction of holes that escape initial recombination (charge yield) for alpha particles, protons, x-rays and a Cobalt-60 source. The figure was taken from [55].

Holes generated in the oxide transport much slower through the lattice than electrons. In the presence of an electric field, holes can transport to either the gate (negative gate bias) or the oxide-silicon interface (positive gate bias). There is a distortion of the local potential field of the lattice as holes move through it due to their charge. This local distortion creates an increased trap depth at certain sites which tend to confine holes to their immediate vicinity's. In other words, the hole tends to trap itself at these certain sites. As a hole moves through the lattice, the distortion moves with it. When holes come close to the interface there are a large sum of oxygen vacancies because of the diffusion of oxygen in the oxide and the lattice mismatch at the interface. These vacancies will act as trapping centers. As the holes approach the interface, some percentage of them will be trapped. The number of holes trapped is dependent on the capture cross-section at the interface, which is again dependent on the electric field and is also very dependent on the device fabrication. This can range from only a few percent of the

holes being trapped in hardened oxides to as much as 50% to 100% for softer oxides [55]. When the transistor is irradiated by injection of carriers (ionizing particle) and electron-hole pairs are created in the oxide, one of these types of carriers (electron or hole depending on the polarity of the FG charge), is attracted toward the FG and will gradually discharge it. This means that the FG charge is the primary indicator of the ionizing dose by radiation. The FG can therefore be used a type of dosimeter while being able to operate at a zero-bias, since the electric field required to drift the generated carriers to the FG is produced by the initially stored charge in the FG. However, to read the absorbed dose a small bias voltage must be applied [32].

According to the authors of [32], the changes in charge of the FG can be monitored by measuring the drain current of the transistor. Another method would be to measure the FG potential and compare it with a conventional transistor of identical size. In the latter case, both transistors need to be biased at the same drain source potential and forced to drive the same current, resulting in a similar gate potential. The second solution is initially the preferred one for space application, since the drain current is strongly temperature dependent. It is however the final goal to only use FGDOS devices, meaning the temperature read-out sensitivity needs to be characterized. Other reasons why FG dosimeters are suitable for space is their reduced size, the straightforwardness to manufacture and low voltage supply requirements [2]. A major advantage of the sensor is its response to radiation. The response can be linearized by setting a threshold and target current. The raw characteristic response of the sensor and the constrained (linearized) characteristic can be seen in Figure 2.20.

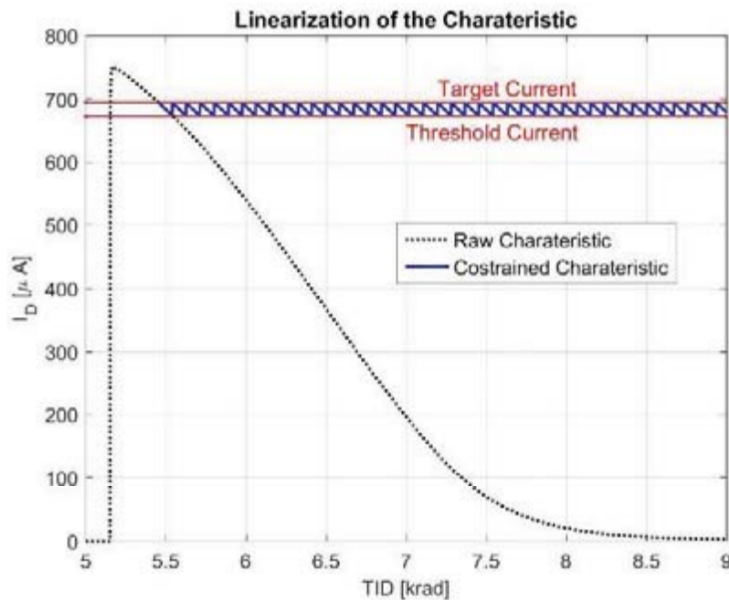


Figure 2.20: Linearization of the sensor response. The black curve in the figure represents the characteristic (raw) response and the blue curve shows the response obtained by limiting the current by means of the charge injection. This figure was found in [14].

A zoomed in version of this linearization can be seen in Figure 2.21, where the drain current is staying inside the linear range. This figure shows that there is an initial charge of the FG, then radiation causes the FG to discharge and when it reaches a pre-set threshold it charges again until the set target. This will result in a saw tooth like signal for the charge. When no radiation is applied, the charge remains constant as seen on the right part (after 2) of the figure.

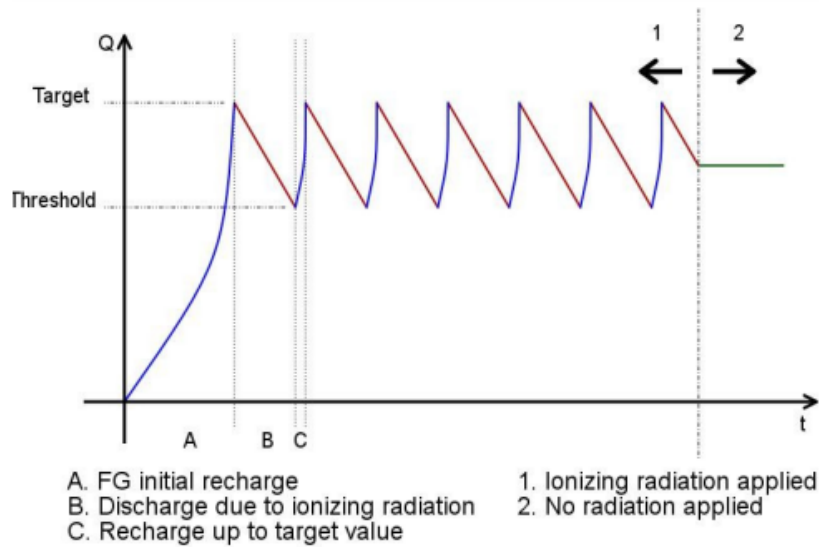


Figure 2.21: The working principle of FGDOS from Sealicon, found in source [56].

After reading the drain current of the FGDOS, the current is converted to frequency using an I - f converter seen in Figure 2.22. The drain current input can be seen on the left top of the diagram and the output frequency can be seen on the right of the diagram. The purpose of this conversion is to switch from an analog drain current to a digital compatible frequency, as the chip operates digitally and communicates using Serial Peripheral Interface (SPI). The frequency is then given as an integer and can be read using three different registers in the chip.

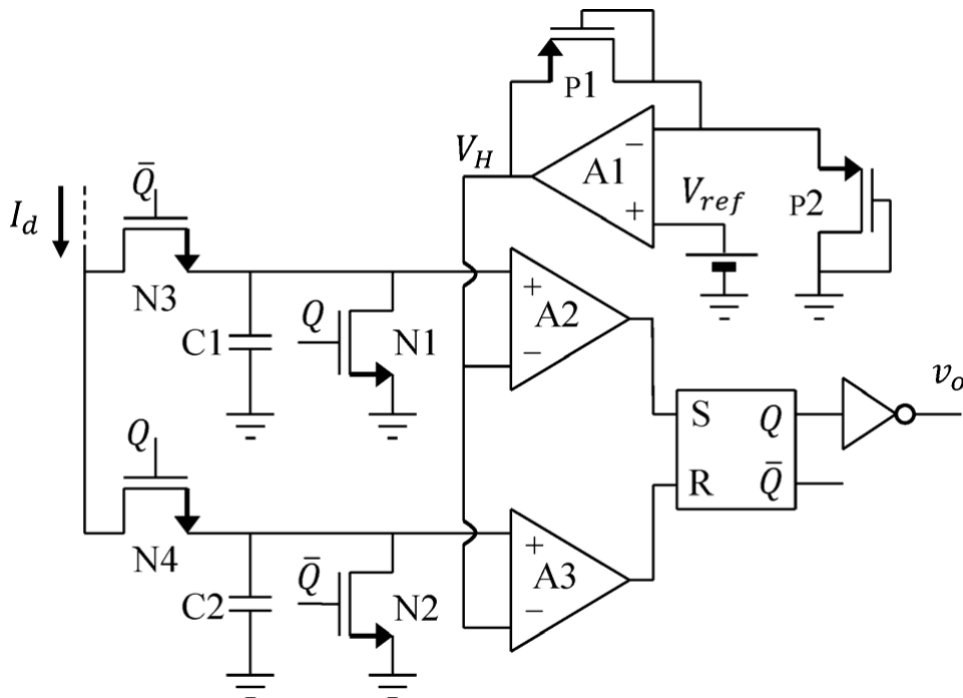


Figure 2.22: Electronic diagram of the I - f converter used to turn the drain current into a frequency signal [32].

2.3.2. Layout

The FGDOS chips by Sealicon have multiple variations. The dosimeters currently on the market are the FGD-02F and the FGD-03F sensor. There is also a FGD-04D sensor and an updated version of the 03F

which are currently in development, but for this study the current FGD-03F sensor will be considered. This sensor specifications can be seen in Table 2.5.

Table 2.5: FGD-03F specification by Sealicon from source [56].

Dose Range (Passive mode)	TID (Active mode)	TID (Passive mode)	Resolution	Supply Voltage	Radiation	Features	Interface
0 to 3 Gy	500 Gy	500 Gy	20 mrad	5 V	Gamma, X-ray, Protons	Re-usable, Serial nr, +18 V charge pump, Standby mode	SPI Slave

The sensor comes with several features, which have been extracted from the data sheet. It has a 200 μGy (20 mrad) resolution and can measure up to a total dose (TID) of 500 Gy. It comes with a QFN32 sensor that has two independent sensors for added redundancy. The sensitivity of the sensors can be set to around 5 kHz/Gy or to around 60 kHz/Gy. These are the low sensitivity (LS) and high sensitivity (HS) mode respectively. The sensor has a passive detection mode that had zero power consumption, integrated temperature monitor and needs a 5 V supply voltage. The package of the QFN32 chip is 5.0 \times 5.0 \times 0.9 mm. A schematic of the FGDOS chip can be seen in Figure 2.23, note that this schematic only shows one sensor while there are actually two sensors.

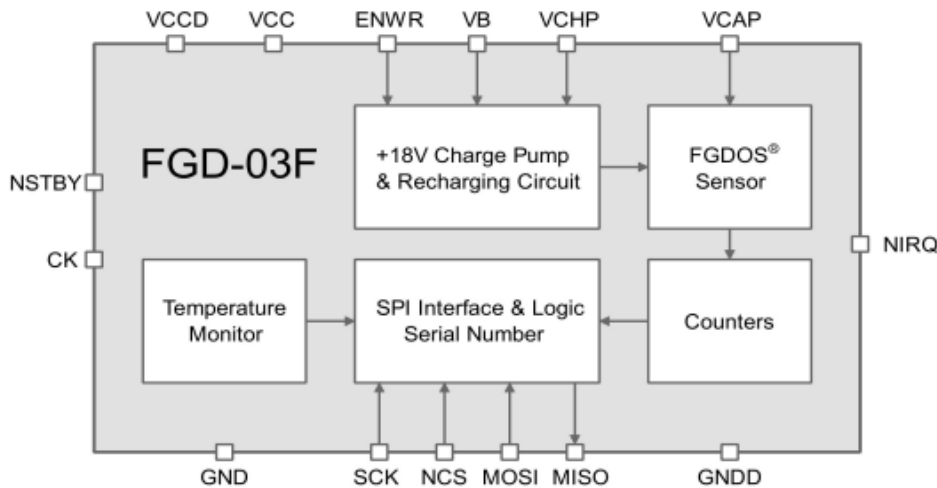


Figure 2.23: Schematic of the FGDOS chip developed at Sealicon.

In the schematic there are 15 pins for one sensor, meaning the actual package contains 30 pins. The chip also includes a reference oscillator to counter for any temperature related effects. The charge pump and the recharging circuit are there to recharge the sensor when it has been irradiated. The internal counters are used to count pulses generated by the sensor's frequency signal output. The chip has a SPI and can store data in the registers. This communication protocol is used so that the chip can be connected to other electronics, like micro controllers. The GND, GNDD, VCC and VCCD pins in the schematic are used for the analogue and digital power supply and the ground. The SCK, NCS, MOSI and MISO pins are used for the SPI connection (see bottom of schematic). The CK pin is used for the input of an external clock. This is then used as a reference by the internal counter. The NSTBY pin is used if the sensor needs to be put in standby mode. The standby mode reduces the power consumption significantly and no measurements will be performed. The NIRQ pin generates an interrupt signal when new measurement data is available to the sensor's registers. The VB and VCHP pins are shorted together so that the internal charge pump provides the necessary voltage to recharge the FG. An alternative to the shorting is to use an external voltage supply [26]. In the Application-Specific Integrated Circuit (ASIC) of the FGDOS, the drain current of the FG is converted to a square wave signal whose frequency is proportional to the current. The signal conditioning allows shaping for both the digital and analogue parts of the circuit. The analogue signal is generated by the buffer which produces a 0 V to 5 V square

wave that can be driven on loads such as coaxial cables or Printed Circuit Boards (PCBs). Accessing the registers is done by means of SPI and a Micro Controller Unit (MCU). The sensor can also be set to different operational modes using the Finite State Machine (FSM), of which an overview can be seen in Figure 2.24. These modes will be explained in more depth in the next sub-section [16].

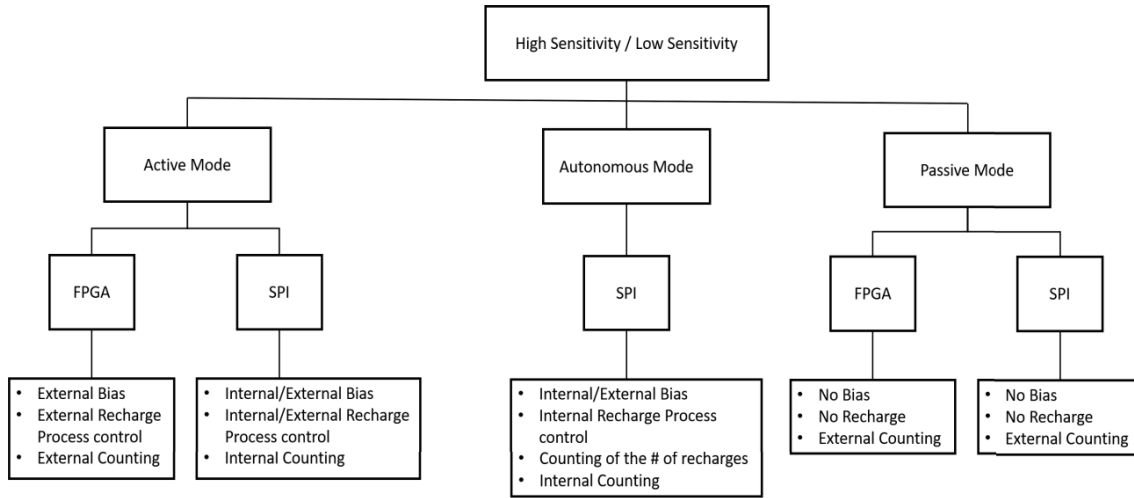


Figure 2.24: Different operational modes on the FG DOS. The figure was taken from [16].

2.3.3. Operational Modes

The FG DOS device has three main modes of operation: Active mode, Passive mode and Autonomous mode. These modes have been implemented with the purpose of providing a flexible monitoring system. The modes were investigated in [13], on which this subsection rests. Configuring the sensors is all done through the SPI. A short overview of the different modes can be seen in Figure 2.24 with the different characteristics in Table 2.6.

Table 2.6: Characteristics of the FG DOS device in different modes.

Mode	Characteristics
Active	Constantly checking the frequency of the sensor, automatic recharge when threshold is reached
Passive	Checking frequency of sensor every set time, manual recharge when frequency is below threshold
Autonomous	Checking frequency of sensor every set time, automatic recharge when frequency reaches threshold

For Active and Passive mode, the dose can be determined using:

$$D = \frac{f_{sens}(t_2) - f_{sens}(t_1)}{S}, \quad (2.11)$$

where f_{sens} is the sensor frequency at a specific time and S the sensor sensitivity. When determining the dose in autonomous mode, there is one additional factor in the equation:

$$D = \frac{N_{rech} \cdot \Delta f_{sens}}{S} + \frac{f_{sens}(t_2) - f_{sens}(t_1)}{S}, \quad (2.12)$$

where N_{rech} is the number of recharges and Δf_{sens} the difference in frequency between the target and threshold of the sensor. This first part of the equation takes care of the recharges happened while the

sensor was not read by a master.

Active mode is the setting where the sensor uses an external circuit for the readout and the recharge. This can be done by, for example, using a FPGA and an external power supply. The frequency variation is read throughout the irradiation. This mode needs to be used for on-line monitoring and for recording.

The use of the sensor in passive mode gives the ability to read the dose without needing to bias or wire the sensor in any way. The output frequency is converted to the dose in two separate ways, resulting in different dose ranges and resolutions. The frequency is evaluated before and after the irradiation. The variation of the frequency obtained can be converted to dose by using the sensitivity of the sensor as calibration factor or by exploiting the characterization as calibration curve. A downside to using this mode is that the dose range will be limited to the single discharge of the FG capacitor.

Using the sensor in autonomous mode overcomes this downside. It allows the extension of the dose range up to the lifetime of the sensor. The measurement in this mode can be performed by occasionally accessing the registers through the digital interface, which allows the communication with a MCU meant for reading the data and configuring the sensor. This is thanks to the integration of the recharging circuit on the FGDOS and the improvement of the communication controller. The sensor in autonomous mode is configured to control the recharge process. The absorbed dose can be determined by reading the number of recharges and the output frequency at the reading time. A recording of the output data is then not necessary and only the sensor needs to be supplied.

The sensor also has the ability to switch between sensitivity modes. There is a high sensitivity (HS) mode and a low sensitivity (LS) mode. These sensitivities are obtained by using two separate reading transistors whose dimensions determine different voltage to current gains. The performances of the different modes in the sensor (active not included) with different sensitivity settings can be seen in Table 2.7. As can be concluded from the table, the dose range is much larger for the autonomous mode. The error in this mode will probably also be smaller for small dose rates.

Table 2.7: Summary of the characteristics of the different operation modes. For autonomous mode, the error depends on the dose rate. Found in source [13].

Mode	Method	Sensitivity	Dose range [Gy]	Error
Passive	Calibration curve	High	0.51	2.6 mGy
		Low	2.72	90 mGy
	Linear approx.	High	1.18	0.5 mGy
		Low	12.25	3.1 mGy
Autonomous	Equation	High	~300	$5.4 \cdot 10^{-3} \times \text{DR} \%$
		Low	~300	$6.6 \cdot 10^{-3} \times \text{DR} \%$

2.3.4. Sensitivity

When using the drain current as output, there is a strong temperature dependency. The full dosimeter device will then consist out of the FG sensor, the signal conditioning electronics and a current to frequency converter. This means the dosimeter output will be a square wave signal, where the frequency will vary with the radiation dose absorbed. The dosimeter integration only requires a very small silicon area. Together with the low power consumption of the dosimeter, it is well suited for being embedded in Integrated Circuits (ICs). Having a frequency output makes it possible to measure sensitivity in terms of Hz/rad instead of V/rad as in conventional dosimeters. The lowest detectable dose should be in the range of other FG dosimeters, meaning if there is a correction for temperature changes it should be possible to resolve doses as low as 1 rad (10 mGy) [32]. Using the voltage variation from Equation 2.7, the radiation generated current can be related to the FG potential:

$$I_r = -C \Delta V_{FG}. \quad (2.13)$$

Expanding this equation by using the expanded relation for the voltage variation gives:

$$I_r = -C \frac{e(1-R(\varepsilon))\rho_{ox}t_{ox}^2}{\mathcal{E}W_{e-h}} D. \quad (2.14)$$

Using experimental data collected on the FG sensor, it was determined that the operation range of the sensor can be empirically approximated by:

$$f = f_0 \left(1 + \frac{\mathcal{E}}{\mathcal{E}_r}\right), \quad (2.15)$$

where f_0 and \mathcal{E}_r are two constants dependent on the ionizing particle. The voltage of the FG can then be solved as:

$$V_{FG} = V_r \left[\left(1 + \frac{V_{init}}{V_r}\right) \exp\left(-\frac{D}{D_r}\right) - 1 \right], \quad (2.16)$$

where V_r is the product of \mathcal{E}_r times the distance and D_r a constant given by:

$$D_r = \frac{W_{e-h}C\mathcal{E}_r}{eA\rho_{ox}f_0}. \quad (2.17)$$

Equation 2.16 indicates that the sensor sensitivity decreases exponentially as the total dose grows. This exponential decrease is however not what was seen in [69]. The study showed a linear decrease divided in a first regions with faster degradation and a second region which degraded slower with respect to the first region, also close to linearly. The switch of regions is around 80 Gy according to the study. The sensitivity degradation curves are seen in Figure 2.25.

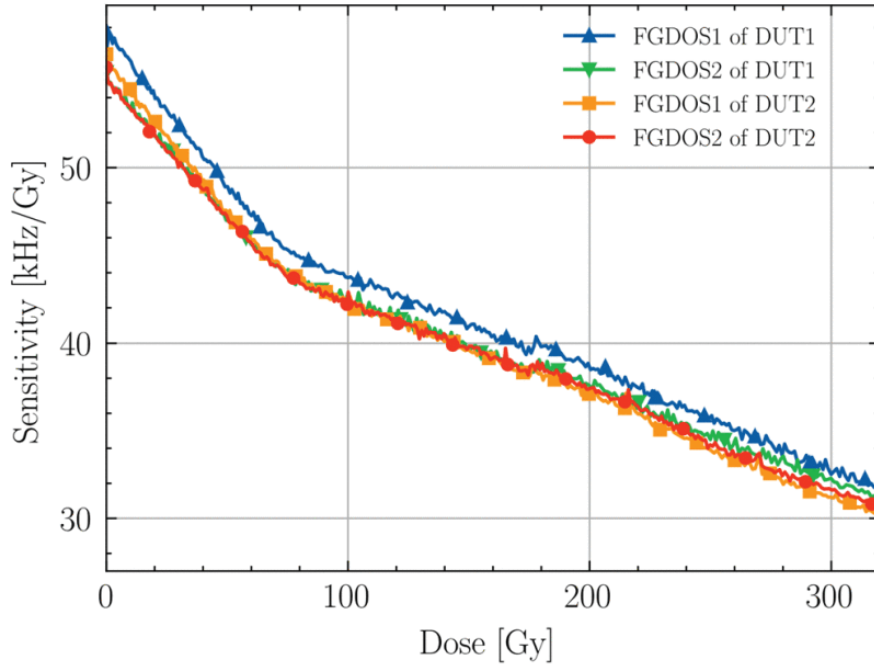


Figure 2.25: Sensitivity degradation of the FGDOS sensor. Taken from source [69].

The maximum sensitivity of the FGDOS sensor at $D = 0$ can be defined as:

$$S_{D=0} = \left. \frac{dV_{FG}}{dD} \right|_{D=0} = -\frac{V_r + V_o}{D_r}. \quad (2.18)$$

The lowest limit of detection is then determined by the equivalent voltage noise over the FG capacitor v_n and the maximum sensitivity [32]:

$$\Delta D_{\min} = \frac{v_n}{S}. \quad (2.19)$$

So far, it has been established that the sensitivity of the FGDOS is dependent on two main mechanisms. One is the total accumulated dose and the one is temperature variation. An important requirement with testing was that the additional circuit should not be sensitive to both the dose and the temperature. The total dose influence on sensitivity was investigated in [14] by comparing two separate test runs. In the first run (run 1), the charge injection was activated every 6 krad in the first 20 krad and every 12 krad for the rest of the irradiation. During the second run (run 2), the charge injection interval was changed several times throughout the irradiation from 300 rad to 2.4 krad. More specifically, it was kept constant to 300 rad for the first 30 krad and afterwards to 600 rad for the following 60 krad. The results of the dose on the sensitivity can be seen in Figure 2.26, which includes both runs. As seen, the sensitivity degradation is globally more significant in run 2. However, during the first 20 krad the degradation of both runs is very similar where the sensitivity decreases very quickly. In run 1 and run 2, the degradation is 22.8% and 19.3% respectively. After the first 20 krad, the sensitivity of run 2 keeps degrading until the charge injection interval becomes higher than 1.2 krad. The sensitivity then partially recovers during the 1.8 krad and a 2.4 krad interval. Run 1, compared to run 2, degrades very little after the dose of 20 krad. This degradation is almost negligible. This means that the recharge rate has a very strong influence on the sensitivity degradation. For injection intervals shorter than 1.8 krad, the sensitivity can be decrease. From an operational point of view, the recharge rate depends only on the rate of the dose and the linear range amplitude meaning that both factors have an indirect influence on the sensitive degradation of the radiation monitoring device. The same paper also showed a potential sensitivity variation due to charge annealing in the oxide layer of the transistor [14].

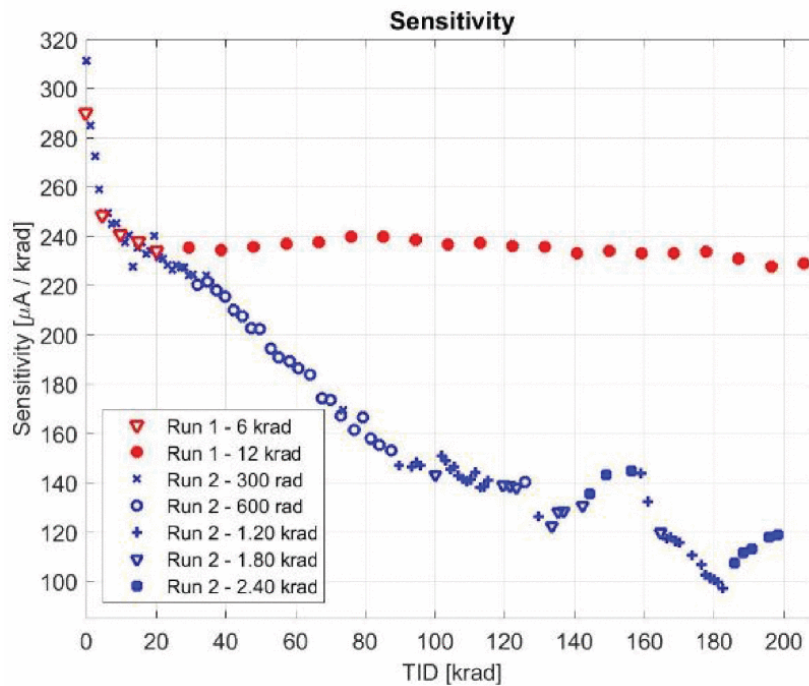


Figure 2.26: Sensitivity degradation over the total dose. The red and blue symbols represent the first and the second run, respectively. Each recharge interval is represented by a specific symbol, as reported in the legend. Figure was taken from [14].

As mentioned, the output signal of the FGDOS is also influenced by temperature fluctuations. This is why the authors of [11] did a complete qualification on the sensor. During the qualification, they integrated an identical (twin) MOSFET to the one reading the FG capacitor on the chip with a $I-f$ converter. This output was taken as reference since the MOSFET is immune to TID and will react similarly to the temperature fluctuations as the FG. The tests were done by using an oven to heat the transistors slowly. The results of the sensitivity influence can be seen in Figure 2.27 (frequency against temperature) and in Figure 2.28 (temperature sensitivity against temperature).

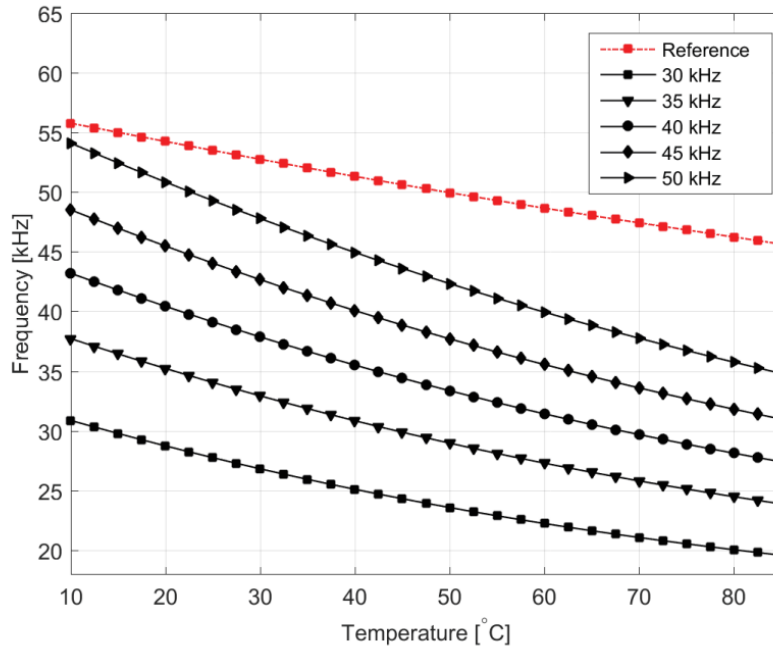


Figure 2.27: Frequency as a function of temperature. The highest curve shows the frequency variation of the twin MOSFET, which is the reference frequency. The lower curves show the frequency variation of the FG transistors for different amounts of charge stored in the FG. Figure was taken from [16].

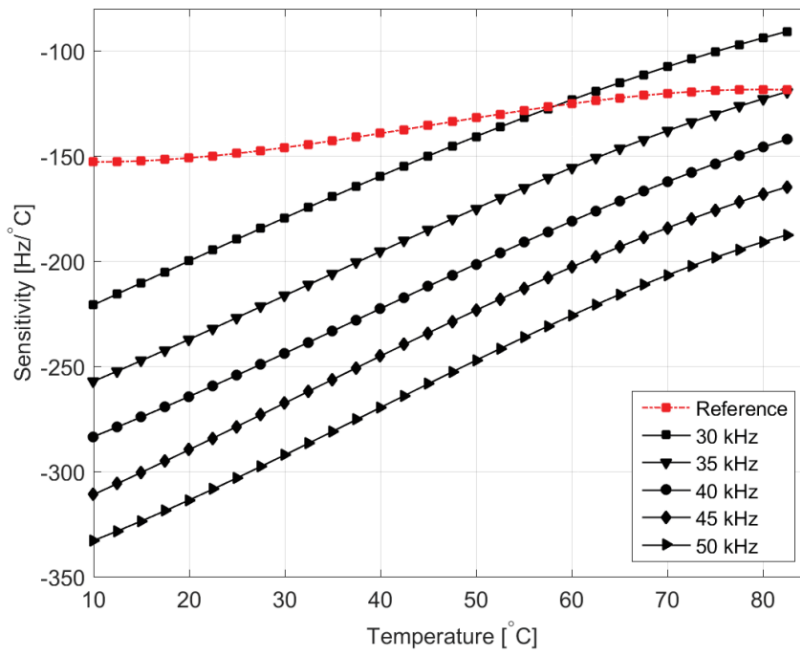


Figure 2.28: S_t as a function of temperature. Increasing the temperature, the output signals become less sensitive to the variations in temperature. The same effect can be observed by increasing the charge stored in the FG. Figure was taken from [16].

In the figures, it can be seen that the output variation given by the temperature variations depends on the charge stored in the FG. In Figure 2.27, the sensitivity in temperature is much more constant in the MOSFET than the FGs, resulting in $-135 \text{ Hz}/^\circ\text{C}$. The sensitivity in the FG transistor changes not only

depending on the charge stored but also on the working point of the current to frequency converter. By charge injection in the FG to increase the frequency from 30 kHz to 50 kHz yields a sensitivity drop from $-315 \text{ Hz}/^\circ\text{C}$ to $-200 \text{ Hz}/^\circ\text{C}$ at 20°C . It can also be observed in Figure 2.28 that the temperature sensitivity changes over the temperature range of the tests [11]. It is possible to compensate for the temperature using the temperature sensitive part of the ASIC. This has been demonstrated in paper [12]. In this paper, the compensation was done by means of a look-up table for small doses.

2.3.5. Comparison with RADFET

At CERN, the FGDOS was compared to a 0 V and a +5 V biased RADFET sensor for radiation measurements at the CERN High-energy Accelerator Mixed-field (CHARM) facility [12]. As seen in Figure 2.29, the higher resolution of the FGDOS sensor is clearly visible comparing it to RADFET sensors. This is also in good indication why investigation the change from RADFETs to FGDOS sensors is worth it. The specifications on dose and resolution of the RADFET sensor with the FGDOS can be seen in Table 2.8. As seen in this table, the dose range is larger for the RADFET but the resolution for the FGDOS is much, much smaller. If the radiation field needs to be characterized in a short run, the RADFET might not be sensitive enough. Other advantages of the FGDOS with respect to the RADFET is the re-usability and the usage in mixed radiation fields. In addition, the FGDOS is highly linear and sensitive, where the RADFET needs a calibration curve for measurement. An advantage of the RADFET is that it is already widely used in practise.

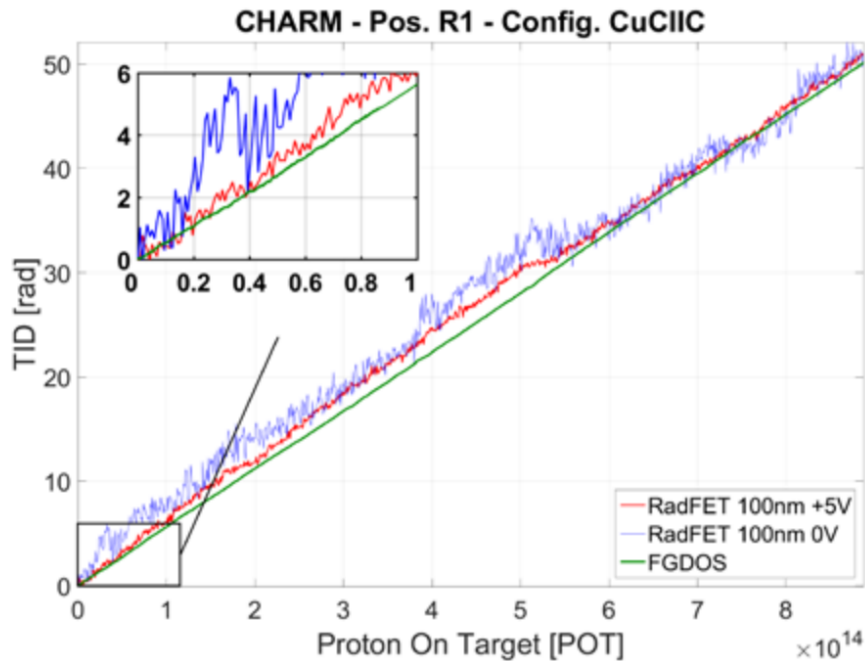


Figure 2.29: TID measured by RADFETs (biased to 0 V and +5 V) and FGDOS. The radiation type used is a mixed field generated by the interaction between the 24 GeV proton beam and a copper target, labeled as Cu. Figure was taken from [12].

Table 2.8: Comparison of RADFET and FGDOS sensors in terms of main specifications. From source: [15].

Sensor	Bias	Resolution [mGy]	Dose range [kGy]
RADFET	0 V	212	4.3
	5 V	57	2.3
FGDOS	-	2	0.8

3

Space RadMon-NG Payload

This chapter will address the first research sub-question of the thesis by elaborating on the hardware and firmware of the payload, as well as the system engineering approach to derive the requirements of the system. The first part will provide information regarding the missions the payload will fly with stakeholders involved, the requirements and preliminary risk analysis of the payload. After this introduction of the payload, the payload design will be studied in more detail. The payload originated from the compact radiation monitoring device called the RadMon, that is being used in the LHC tunnels at CERN. It is being used at various CERN irradiation facilities since 2013, with the current version of the device being the RadMon V6. The monitoring device consists out of three boards, with each their own function. It contains a main board, a power board and finally a sensor board. The modularity was chosen to be able to easily replace components damaged by radiation [59]. From this system the initial 1U CubeSat and payload by CERN were developed, called CELESTA. The mission was designed to study the effects of cosmic radiation on micro-electronics, mainly by measuring SELs. The satellite carries the first version of the Space RadMon as payload, a miniature version of the RadMon V6 mentioned before. The Space RadMon had a few iterations (V1, V2, Mx) and finally came to the Space RadMon-NG version. This version has different SRAMs, a different dosimeter and some more hardware changes compared to the former versions which should improve the performance of the radiation monitor. The system design will be further elaborated later in this chapter.

3.1. System Engineering

The CELESTA mission with the Space RadMon payload sets a precedent on how CERN technologies can have an application beyond particle physics experiments. It has very sensitive components that are characterized and calibrated by CERN. The Space RadMon is a light-weight and low-power instrument, which will fulfill the following needs in future dependable space systems:

In order to assure dependability of future space systems, there is a need to develop a system-level testing methodology in relevant environmental conditions and to perform radiation monitoring on-board of spacecraft.

In accordance with these need statements, a final formulation for the mission statements was created:

CERN's mission is to develop an embeddable radiation monitor based on the CERN RadMon device compatible with CubeSats and to validate the radiation qualification test method on system-level for LEO missions in the CHARM facility.

The Space RadMon-NG development aims to further fulfill this mission statement. The Space RadMon-NG payload is planned to fly on two CubeSat missions, one by ISISPACE in Delft (Netherlands) and one by GOMspace in Aalborg (Denmark). The involved stakeholders in these two missions can be seen in Table 3.1. The table shows the stakeholder, the stakeholder type and the description of the stakeholder activities.

Table 3.1: Identification of key stakeholders and key requirements for the ISISPACE and GOMspace missions.

Stakeholder	Type	Description
CERN	Active	Develops the payload for the missions
R2E	Active	Distributes part of CERN's funding to the Space RadMon project, defined some requirements
Research Institutes	Active	Use the information retrieved by the payload, define some system requirements
Industry Companies	Active	Use the information retrieved by the payload, define some system requirements
TU Delft	Passive	Sent a student to work on the payload research and development
ISISPACE	Passive	Launches the payload on one of their CubeSats
GOMspace	Passive	Launches the payload on one of their CubeSats
KU Leuven	Passive	Supplies the custom SRAMs for on the payload
ESA	Passive	Provides funding for the space missions to ISISpace and GOMspace
EU	Passive	Provides funding for research and development activities at CERN
Suppliers	Passive	Supplies the remaining necessary components for the payload

No official requirements were found in the documentation of the payload. In discussions with the CERN thesis supervisor, the requirements seen in Table 3.2 were said to be important and relevant for the testing and system qualification that is to be performed during the thesis research. The requirements are to be used as guideline, while also taking into account the research questions that need to be answered.

Table 3.2: Requirements for the Space RadMon-NG payload that will be used for testing. The priority has been divided into essential (E) and conditional (C). The verification has been divided into test (T), analysis (A) and inspect (I).

ID	Requirements	Priority	Verification
SRM-HEH	The payload shall measure HEH fluence using a COTS SRAM	E	-
SRM-HEH-1	The payload shall be able to detect SEUs	E	T
SRM-HEH-2	The payload shall have on-board burst detection for the Cypress SRAM	E	T
SRM-HEH-3	The payload shall be able to measure the HEH fluence within 2.5% accuracy	C	T/A
SRM-FGD	The payload shall measure TID using the FGDOS	E	-
SRM-FGD-1	The FGDOS shall have higher resolution than the RADFET	E	T/A
SRM-FGD-2	The FGDOS measurements shall be temperature compensated	E	T
SRM-FGD-3	The payload shall be able to monitor the TID within 2.5% accuracy	C	T/A
SRM-ENV	The payload shall be able to withstand the space environment	E	-
SRM-ENV-1	The payload shall be able to withstand a TID of at least 500 Gy	E	T/I/A
SRM-ENV-2	The payload shall be able to withstand possible SEEs	E	T/I
SRM-OPR	The payload shall not have any operation problems	E	-
SRM-OPR-1	The payload shall have communication redundancy to the outside world	E	T/A
SRM-OPR-2	The payload firmware shall perform what it is intended to do	E	T/A

Some of the potential risks can be seen in Table 3.3 where a preliminary risk register is depicted. It also contains the likelihood of the risk and the impact of the consequence.

Table 3.3: Risk register for the Space RadMon-NG payload. Likelihood and consequence have been divided into high (H), moderate (M) and low (L).

Number	Risk Description	Likelihood	Consequence
1	Communication to OBDH failure	L	H
2	Flash*Freeze failure	L	M
3	Single sensor failure	M	L
4	Multiple sensor failures	L	M/H
5	FPGA failure	L	H
6	MCU failure	L	M/H
7	Voltage regulator failure	L	H
8	Oscillator failure	L	M
9	Mechanical failure	L	M/H
10	Launch and Deployment failure	L	H
11	Satellite OBDH or CDHS failure	L	H

3.2. Hardware Architecture

The Space RadMon-NG system will be able to measure TID using the FGDOS chip on the board, it will be able to measure the HEH fluence using the Cypress SRAM and other SRAMs on the board by determination of the SEUs. This section will describe the architecture of the Space RadMon-NG, the interfacing of the controllers consisting out of a Micro Controller Unit (MCU) and a Field Programmable Gate Array (FPGA), the configurations used and the communication interfacing used to the outside world. The flow diagram for the Space RadMon-NG can be seen in Figure 3.1. It consists out of two boards, a main board for the FPGA, MCU, power and interfaces, and a mezzanine board with the COTS SRAMs, the ASICs, the FGDOS and the temperature sensor. This chapter will provide a documentation for the sensor module, its architecture and internal structure, as this has not been created yet.

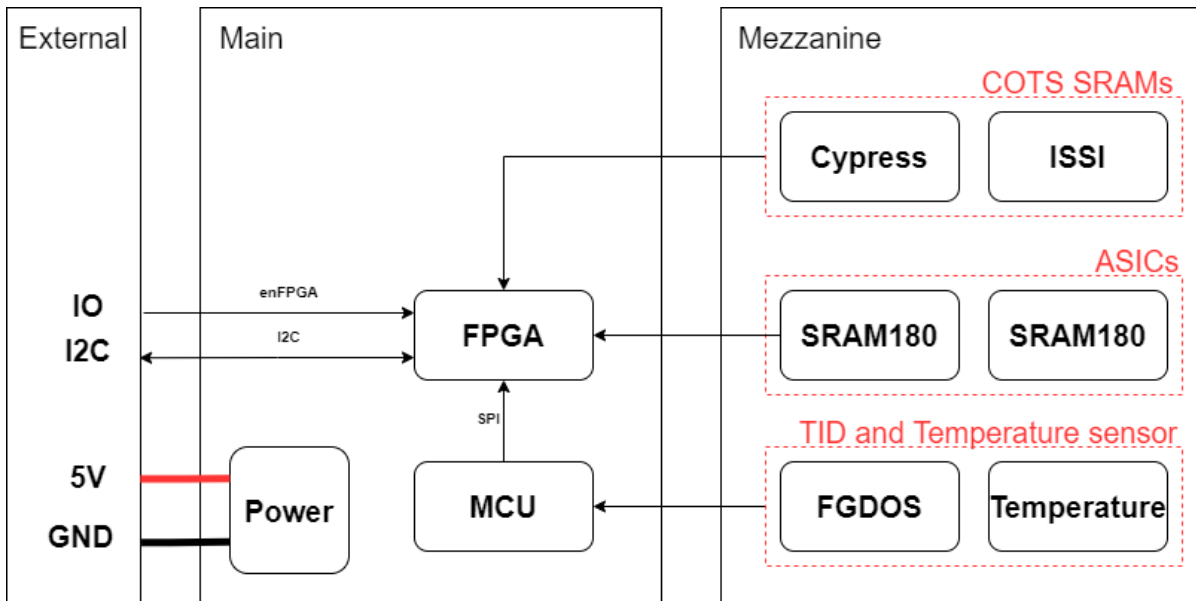


Figure 3.1: Flow chart for the Space RadMon-NG boards (physically) based on the interface control document of the Space RadMon-NG [68].

The whole payload has dimensions of 92.0 mm × 96.0 mm × 16.56 mm, giving it a volume of around 0.2 U in CubeSat units. The total weight of the payload is 57.5 g and has a lifetime of 500 Gy [68].

3.3. MCU Firmware Architecture

The MCU firmware architecture is fairly straight forward, as the MCU is mainly used to interface to the FGDOS using Serial Peripheral Interface (SPI), read the voltages from temperature sensor and regulators, and communicate with the FPGA through SPI. Formerly, the payload contained an Analog Digital Converter (ADC) instead of a MCU. The reason for this exchange is the radiation tolerance of the MCU and the lower power consumption. Now the RADFET has been replaced by the FGDOS chip, an ADC would have not been sufficient anymore to get the readings from the sensor. The temperature sensor and voltage regulators still require an ADC, for which the internal one of the MCU is used. A flow diagram of the architecture can be seen in Figure 3.2. Please note that in this figure only the temperature sensor is denoted, but the voltage regulators have an identical flow.

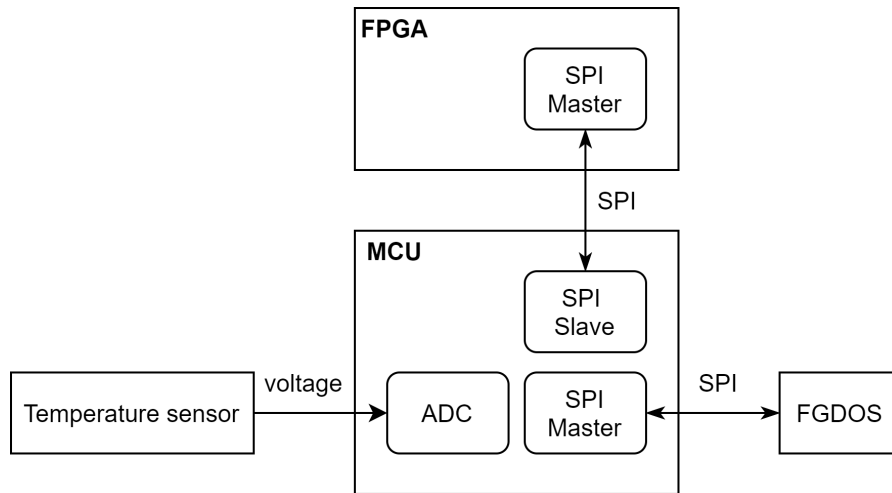


Figure 3.2: Flow diagram to depict the MCU and internal ADC implementation for the Space RadMon-NG.

The FGDOS is in passive mode, meaning the MCU will decide when a recharge is necessary. The MCU reads the sensor frequency after a certain time interval and when the frequency is lower than the threshold, it is recharged to its target frequency. Using the registers of the FGDOS and the SPI connection, the device can be configured. Then, using the same SPI connection, the measurements can be retrieved from the FGDOS registers. The temperature measurement is a voltage which is linear to temperature, meaning by a simple transformation the temperature can be measured. The voltage regulators give the voltage directly to the MCU. Together, the readings of all the sensors are collected in the MCU and retrieved by the SPI connection from the FPGA. After, the process starts again.

3.4. FPGA Design Architecture

The architecture designed for the Space RadMon-NG consist out of various blocks, linked to a component or function of the system. Each of the blocks represent a controller that is handled by a Finite State Machine (FSM), which will be explained in more detail below. Communication from the FPGA with the outside world is done using the I2C protocol as is mentioned before. All blocks in the system take care of the internal operation of the system and can be described as follows:

- Main controller: a module that takes care of the start of the SPI communication and the reading of the SRAM sensors.
- MCU controller: a controller that manages the data retrieval from the FGDOS sensor, the temperature sensor and voltage sensors on the board and sends it to the SPI block.
- SRAM controller: responsible for the data retrieval of the Cypress SRAM sensor and the ISSI SRAM.
- SRAM180 controller: responsible for the data retrieval of the two custom ASIC SRAM sensors.
- Flash-Freeze management IP: this part of the system will manage the power consumption and will also allow the system to enter low power mode.
- SPI: implementation of the SPI for the communication between the MCU and the FPGA and forwards most of it to the I2C module.
- I2C: implementation of the I2C protocol for communication of the FPGA to the outside world.

The FSMs of these internal blocks and their method of operation are explained in the next sub-sections. The Flash-Freeze component is explained in section 3.5 on the power usage and the communication protocols are explained in the end of this section and in section 3.5. The most important FSMs are the ones for the main controller, the MCU controller, the SRAM180 (ASICs) controller and the SRAM (COTS) controller. The communication interfaces (SPI and I2C) have their own state machines but these will be treated separately in another section. Note that the diagrams depicted of the FSMs are

for each positive edge of the clock. The arrows in the diagrams contain conditions which are checked each clock cycle. When this condition is reached, the arrow is followed to the next (sub-)state. If the condition is not reached before the next rising edge of the clock, the FSM stays in that current state and continues its operation. The diagrams that will be given show the current flow of the system. This will give a good overview of the Space RadMon-NG lower-level operations and can be used as basis for improvement propositions or general documentation.

3.4.1. Main Controller

The main controller has a FSM implemented containing two states which are elaborated below and can be seen in terms of a diagram in Figure 3.3. Every rising edge of the clock (by means of an always block in Verilog), the start signal is checked. This regards the `sram65_180_o` signal which will put the system in NOMINAL mode, the `test_srams_single` signal which will put the FSM in the TEST_SRAMS (TEST) state and finally the `rst_single` signal which will put the system in the RST_SRAMS (RST) state. Additionally, there is the IDLE_LOW_POWER (IDLE) state which is the state where the main controller will wait in until it receives activation by one of the signals.

IDLE: The lower power mode of the system. All counters are set to 0, the `reset_MCU_o` signal is set to 0 and the `rst_flag` signal is set to 0. The system waits in this state until one of the start signals is changed and checks this every rising edge of the clock.

NOMINAL: The nominal mode of the system for the mission. As soon as this state starts, the `sram65_180_counter` starts increasing by 1 at every rising edge of the clock. When it is equal to `SRAM65_180_PERIOD`, the `reset_MCU_o` signal is set high. When this condition is not reached, the `reset_MCU_signal` is set low. The controller also has two important input wires. These are the `SPI_finished_i` and the `rd_wr_end_i` signals. If either one of these is set high, the `cnt` counter increases by 1 that particular rising edge of the clock. When `cnt` reaches the value of 2, the `self_clear_o` signal is set high and the state changes to IDLE_LOW_POWER. The `cnt` value is also reset to 0. If this does not happen another condition can change the state. When the `sram65_180_counter` is equal to `SRAM65_180_MCU_RST`, the `sram65_180_counter` is reset to 0. The `self_clear_o` signal is set high, the `cnt` value is reset to 0 and the FSM also changes to the IDLE_LOW_POWER state.

TEST: The mode to test the SRAMs of the system. When this state is activated, a counter called `sram65_180_test_cnt` starts increasing at every rising edge of the clock. This state also makes use of an input wire, which is called `test_end_i`. When this signal is set high, the `self_clear_o` signal is set high and the FSM changes to the IDLE_LOW_POWER state. Another condition is when the value of `sram65_180_test_cnt` is equivalent to `TEST_SRAM_PERIOD` value. The `self_clear` signal is then set high, the `sram65_180_test_cnt` value is reset to 0 and the state changes back to IDLE_LOW_POWER.

RST: The mode to reset the system SRAMs. When this state is activated, a counter called `sram65_180_rst_cnt` starts increasing at every rising edge of the clock. This state also makes use of an input wire, which is called `rd_wr_end_i`. When this signal is set high the `rst_flag` is set high, the `sram65_180_rst_cnt` value is reset to 0 and the `self_clear_o` signal is set high. The FSM then changes to the IDLE_LOW_POWER state. Another condition is when the value of `sram65_180_rst_cnt` is equivalent to `TEST_SRAM_MCU_RST` value. The `sram65_180_rst_cnt` signal is then reset to 0, the `self_clear` signal is then set high, the `rst_flag` is set low and the state changes back to IDLE_LOW_POWER.

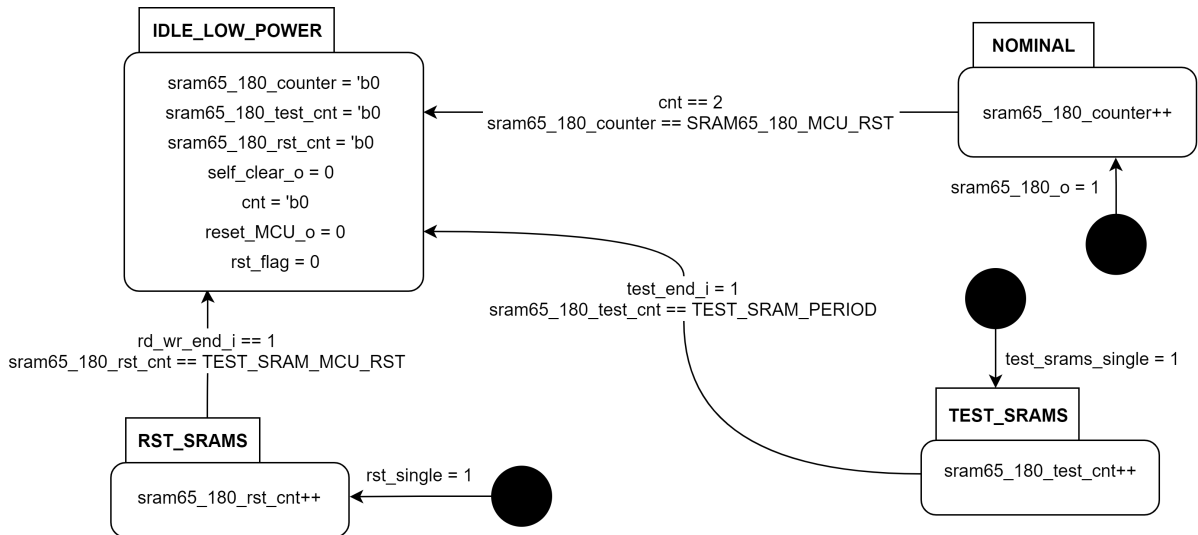


Figure 3.3: Block diagram to depict the FSM of the main controller.

3.4.2. MCU Controller

The MCU controller is the controller that takes care of the data acquisition from the sensors that are connected, which are the FGDOS, the temperature sensor and the voltage sensors. The MCU acts like an ADC to convert the analogue values from the sensors the digital ones that can be used by the FPGA. The MCU has own dedicated firmware to receive data from the sensors. The MCU controller is used to retrieve the data that is stored on the MCU. The controller contains 6 states which are elaborated below and can also be seen in Figure 3.4. Every rising edge of the clock, the reset_i signal is checked and when it is high, the FMS will go into IDLE state.

- IDLE:** This is the initial state of the FSM. In this state, the rst_MCU_o signal is set high, the SPI_finished_o is set low and all the counters used in this controller are set to 0. This state utilized one input wire named sram_65_180_i and one register names set_adc_meas. When either one of these is set to high, the FSM changes to the S5 state and the rst_MCU_0 signal is set high.
- S5:** This state initiates a delay of around 500 ms to capture a stable voltage. The state starts a counter (set_delay_cnt) for a delay when it is initiated. When this counter reaches the equivalence of the set_delay_period parameter, the FSM changes to the S0 state. The set_delay_cnt is reset to zero and the MCU_wake signal is set high. The MCU_state_o signal (output wire) is set to a 0111 bit configuration.
- S0:** This state starts a counter when reached called the set_pulse_width_cnt and sets the MCU_state_o equal to a 1100 bit configuration. When the counter reaches the value of set_pulse_width, the FSM changed to the S1 state. The set_pulse_width_cnt is reset to 0 and the MCU_wake is set to low.
- S1:** This state starts another counter called set_wake_ass_cnt and sets the MCU_state_o equal to a 0010 bit configuration. When the counter reaches the value equal to set_wake_ass_time, the FSM changes to the S6 state, the rst_MCU_o is set low and the counter is reset to 0. This state also has another condition. When the MCU_ctrl_reg is set high, the FSM changes to the S2 state and the counter is also reset.
- S2:** The S2 state starts, again, another counter called the set_rst_period_cnt and sets the MCU_state_o equal to a 0011 bit configuration. When the counter reaches the value of set_rst_period, the FSM changes to the S6 state, the rst_MCU_o is set low and the counter is reset. Another condition is that if the MCU_ctrl_reg is set low, the read_data_o signal is set high, the FSM changes to the S3 state and the counter is reset.
- S3:** This state has another new counter called the SPI_wait_time_cnt. It also sets the MCU_state_o equal to a 0100 bit configuration and the read_data_o signal to high. The state has multiple

conditions. When the counter is equal or larger than `SPI_wait_time`, the CRCs of the SPI and MCU are equal and the SPI CRC is not 0, the FSM changes to the S4 state, the `SPI_finished_o` signal is set high and the counter is reset. For the same condition, but the SPI CRC is equal to zero, the `rst_MCU_o` signal is set low, the FSM changes to the S6 state and the counter is reset. The same happens when the SPI CRC is not equal to the MCU CRC. At last, if the counter is lower than the `SPI_wait_time` value, the counter is increased.

S6: This state contains another counter, named the `set_rst_delay_cnt`. The `rst_MCU_o` signal is set high and the `MCU_state_o` signal is set to a 1000 bit configuration. If the counter reaches the value of `set_rst_delay_period`, the FSM changes to the S0 state, the `MCU_wake` signal is set high and the counter is reset.

S4: This state is just a pass through state, probably used for synchronisation. The `MCU_state_o` signal is set to the 0101 bit configuration, the `read_data_o` signal is set low, the `SPI_finished_o` signal is set low and the FSM changes back to the IDLE state.

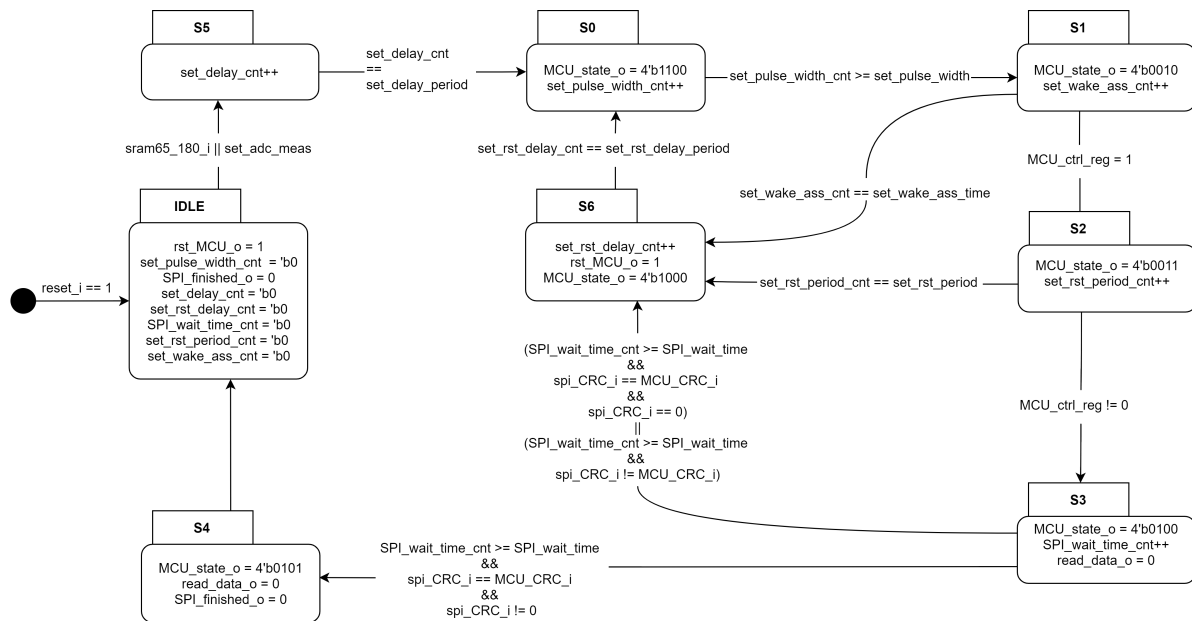


Figure 3.4: Block diagram to depict the FSM of the MCU controller.

3.4.3. SRAM Controller

The SRAM controller has a FSM implemented containing two main states with each various sub-states. These are elaborated below and can be seen in terms of a diagram in Figure 3.5. This controller performs the write, read and test operations of the Cypress and ISSI SRAMs in series. It was implemented using combinational logic for the ISSI SRAM to minimize operation time and the scrambling has been implemented for the burst detection of the Cypress SRAM. The FSM starts when the `reset_i` signal or the `ctrl_reset_fsm` signal are set high. It sets all the counters to 0. The `sram_io_wen_o` signal, the `sram_io_oen_o` signal, the `ctrl_init_flag` signal, the `csn` signal, the `sram_cs_o` signal and the `is_start` signal are all set to high. The first state enabled by the FSM is the MEM_INIT-S0 state. Quite some conditions are implemented as the controller controls two different SRAM devices. The writing will start with the Cypress SRAM as the `is_ISSI` signal is initially set low.

1. MEM_INIT: This state starts writing the memory of the SRAM.

S0: The initial state of the FSM. The state starts with a condition. If the `is_ISSI` signal is set low, the `csn` is set low as well. If this is not the case, the `sram_cs_o` signal is set low. The state sets the `data_en` signal to high which enables the writing of the `sram_data_o` into the memory and the `sram_io_wen_o` signal is set low. The `sram_data_o` uses a ternary operator. The signal is set to `16'hcafe` when the `ctrl_selftest` is high and else sets it equal to all 0's. A

counter called waitstate is initiated and when this reaches the value WRITE_WS, the counter is reset and the FSM changes to the MEM_INIT-S1 state.

- S1: This state set the writing enables signal called sram_io_wen_o to high and the FSM changes to the MEM_INIT-S2 state.
 - S2: This state contains one condition. If the ctrl_init_flag signal is low, the data_en signal is also set low and the FSM changes to the MEM_CHECK_RESULTS-S3 state. This means that the initial writing of the memory has already been finished. If this is_ISSI signal is low, the state starts the initial writing of the memory. It has a start address and loops through the different memory blocks (indicated by addr_block). It does the writing per half memory block, meaning first the 'left' part will be written (0...31) and subsequently the 'right' part will be written (32...63). Using the addr_row_col signal, it loops through each row and column in the partial memory block. When finished (14th memory row), the writing window is changes and the addr_row_col signal is reset to 0. Each positive edge of the clock, the FSM state changes to MEM_INIT-S3, meaning that the loops only continues when it gets back to this MEM_INIT-S2 state.
 - S3: This state stops the writing of the memory. The data_en signal is set low and the FSM changes to the MEM_INIT-S0 state. If the is_ISSI signal is set to low, the sram_addr is set to the current addresses of the memory block and row/column of the previous sub-state. If the is_ISSI signal is high, the sram_addr is increased by 1. There is also checked if the end memory address is reached. For both the Cypress and the ISSI SRAMs, the addresses are reset to the start address. For the Cypress SRAM (low is_ISSI signal), the FSM changes to the MEM_INIT-S4 state instead and the is_ISSI signal is set high (together with the is_start signal). This means that the writing of the Cypress SRAM has finished and it is now the ISSI SRAM turn. When the ISSI end address is reached, the FSM changes to the MEM_CHECK_RESULTS-IDLE state. The sram_cs_o, rs_wr_end_o and is_start signals are set high, while the is_ISSI is set low.
 - S4: This state is simply a delay state and starts a counter named cnt_delay. The csn signal is also set high. When the counter reaches the value equal to delay, the FSM changes to the MEM_INIT-S0 state while setting the sram_cs_o signal low and resetting the counter.
 - S5: This state is simply a wait state that is not used. It enables the counter called waitstate and when the value is equal to 10, the FSM changes to the MEM_INIT-S3 state and resets the counter.
2. MEM_CHECK_RESULTS: This state will read the number of MBUs and SEUs when requested. It will also set the ctrl_init_flag signal low to indicate that the initial writing has ended.
- IDLE: This state sets the counters to 0, the sram_data_o to 16'hfff, the csn to high and the reset_burst_detection_o, flag_right and rd_wr_end_o signals to low. If the test_srams_i signal is set high, the sram_addr changes to the TEST_ADDRESS, the sram_cs_o signal is set low and the FSM changes to the MEM_TEST-IDLE state. When the memory_errors_check_i signal is high and the memory_errors_check signal is low, the results of the SEEs are analyzed. The sram_addr is set to START_ADDR, the sram_io_oen_o signal is set high and the FSM changes to the MEM_CHECK_RESULTS-S0 state. When the is_ISSI signal is low, the csn is set to low. Otherwise, the sram_cs_o signal is set to low instead.
- S0: This state is a wait state. It initiates a counter called waitstate and sets all the SEU triggers and SEU counters to 0. It sets the reset_burst_detection_o signal and the sram_io_oen_o signal to low. When the is_ISSI signal is low, the csn is set to low. Otherwise, the sram_cs_o signal is set to low instead. If the waitstate counter is equal to READ_WS, the FSM changes to MEM_CHECK_RESULTS-S1. The counter is reset and the data from the memory using the sram_io_data_io signal is passed to the sram_data_i signal.
 - S1: This state detects the SEUs. It starts by setting the sram_io_oen_o signal high and initiating the bit_index counter. For the case of the Cypress SRAM (is_ISSI signal low), the counting works as follows. First the low and high SEUs are counted, and subsequently the general SEUs. For bit_index lower than 8, the wseu_counter_low is increased when the

sram_data_i[bit_index] does not correspond to test_data[bit_index]. When bit_index is 8 or higher, the wseu_counter_high is increased for the same scenario. When the same data does not correspond, the wseu_counter is increased for any bit_index. When the bit_index hits 15, the sram_addr_burst_o is changed to the updated sram_addr. The FSM is also changed to the MEM_CHECK_RESULTS-S2 state. During this condition, there is also checked for the occurrence of bursts in the SRAM. First the right burst detector is triggered (with the flag_right signal being high) using the seu_trigger_right_o signal. Then the left burst detector is triggered using the seu_trigger_left_o signal. The wseu high and low counters are then passed to their corresponding output wires. The 15th bit is also taken into account by one final check of the correspondence of sram_data_i[bit_index] and test_data[bit_index]. For the ISSI SRAM, the implementation is somewhat easier. The algorithm loops through the 16 bits (which should all be 0). When the sram_data_i[i] is equal to 1, the wseu counter is increased. When i hits 16, the FSM changes to the MEM_CHECK_RESULTS-S2 state.

- S2: This state resets the bits where the SEUs occurred. It starts by resetting the i counter and the seu trigger signal (left and right). If the wseu_counter from the previous state is larger than 1, the mbu_counter is increased by 1. If the wseu_counter is not equal to 0, the seu_counter is increased by the value wseu_counter. The FSM changes in this case to the MEM_INIT-S0 state to rewrite the current address. When the is_start signal is high, it is directly set to low. If the current address block is smaller than 32, the flag_right signal is set high and the block address is given the value of addr_pivot_block + 6'd32. If the address block is 32 or larger the flag_right signal is set low and the address of the row/column is increased by 1. When the end of the block is reached, the pivot block address is increased by 1, the row/column address is reset and the block address is decreased by half a block. If the end is not found, the block address is decreased by half a block. The FSM will change in any case to the MEM_CHECK_RESULTS-S3 state.
- S3: This state starts by setting the data_en signal low. If the is_ISSI signal is low (Cypress SRAM), the sram_addr is updated by assigning the current address block and row/column. If it is for the ISSI memory, the sram_addr is increased by 1. If the memory scan has not ended yet, the FSM changes to the MEM_CHECK_RESULTS-S0 state. If the end address of the Cypress SRAM is reached, all the burst detection signals are reset and the addresses are set to 0. The is_ISSI signal is set high, the flag_right signal is set low and the FSM changes to the MEM_CHECK_RESULTS-S4 state. If the end address of the ISSI SRAM is reached, the counters and addresses are reset, while the SEUs are being saved. The rd_wr_end_o signal, csn signal and the sram_cs_o signal are set high, while the is_ISSI and the set_data signals are set low. The FSM changes to the MEM_CHECK_RESULTS-IDLE state.
- S4: This state is a delay state. It initiates a counter called cnt_delay, set the csn signal to high and sets the sram_addr to the starting address. If the cnt_delay is equal to 0, the error counters and the mbu counter are saved in extra ctrl registers. If it is not equal to 0, the seu_counter and the mbu_counter are reset to 0. When the cnt_delay value equals the set value of delay, the counter is reset and the reset_burst_detection_o signal is set high. The FSM then changes to the MEM_CHECK_RESULTS-S0 state.
3. MEM_TEST: This state will test the SRAMs for their functionality.
- IDLE: This state is simply a pass through state which delays the system one clock cycle. The FSM changes to the MEM_TEST-S0 state.
- S0: This state resets the ISSI_MBU_i and the ctrl_mbu_counter counters to 0. The sram_data_o is set equal to 16'hcafem the sram_io_wen_o is set low and the data_en is set high. There is a counter named waitstate initiated and when this counter reaches the value equal to WRITE_WS, the counter is reset and the FSM changes to the MEM_TEST-S1 state.
- S1: This state is again simply a pass through state. It delays the system one clock cycle and sets the sram_io_wen_o signal to high. The FSM changes to the MEM_TEST-S2 state.
- S2: This state sets the data_en signal low and the FSM changes to the MEM_TEST-S3 state.
- S3: This state sets the sram_io_oen_o signal low and initiates the waitstate counter. When this

counter reaches the value of READ_WS, the sram_data_i is set equal to the data from the memory (sram_io_data_io), the counter is reset and the FSM changes to the MEM_TEST-S4 state.

S4: This state sets the sram_io_oen_o signal high and the data_en signal low. If the is_ISSI signal is low, the ctrl_err_counter signal is filled with the sram_data_i. The state then changes to MEM_TEST-S5 and the is_ISSI signal is set high. If the is_ISSI signal was already high, the ISSI_SEU_i registers are filled with the sram_data_i information. The state then changes to the MEM_CHECK_RESULTS-IDLE state. The sram_addr is reset to 0, the is_ISSI signal is set low and the sram_sc_o signal is set high.

S5: This state is a delay state. It starts a counter named cnt_delay and sets the csn signal to high. When cnt_delay reaches the value equal to delay, the FSM changes to the MEM_TEST-S0 state and the counter is reset.

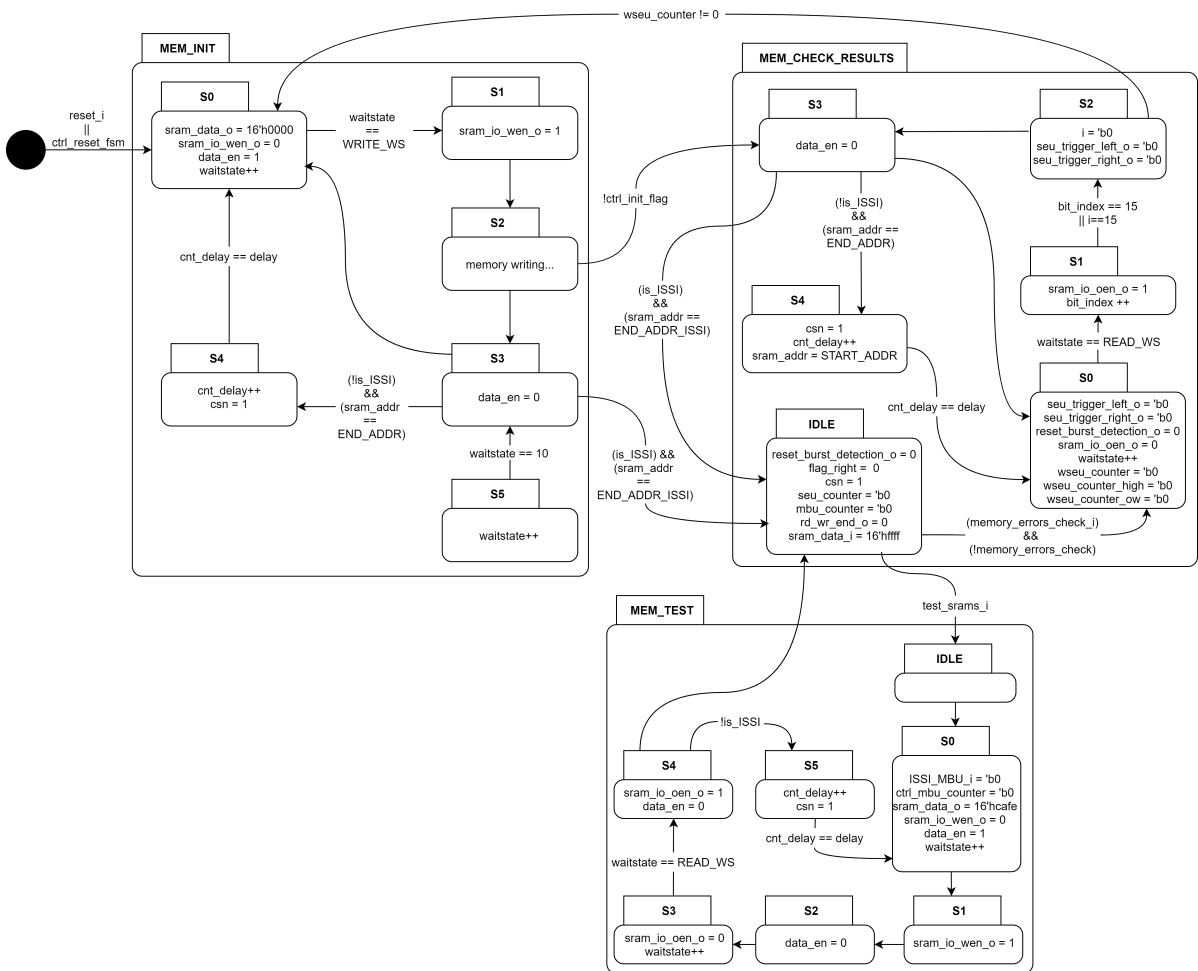


Figure 3.5: Block diagram to depict the FSM of the SRAM controller.

3.4.4. SRAM180 Controller

The SRAM180 controller has a FSM implemented containing four main states with each sub-states. These are elaborated below and can be seen in terms of a diagram in Figure 3.6. The initial state of the FSM is the MEM_WR-S0 state, which is enabled when the reset_ext signal is turned high. When initiated, all signals, triggers and counters are reset to zeroes.

1. MEM_IDLE: The IDLE state of the memory controller. In this state, the address are set to 0 and the rst_vctrl is set low. Both the test_end_o and the disable_ext_req are also set low. There are two input wires called sram65_180_i and test_srams. When the sram65_180_i signal is high, the

counters for the SEUs are reset. The `disable_ext_req` is set high, as well as the `nm180_GPIO0_int` and the `nm180_GPIO1_int` registers. The `nm180_GPIO2_int` register is set to high impedance. The FSM will then change to the `MEM_RD-S0` state. If the `test_srams` signal is set high, the `disable_ext_req` signal is also set high. The `nm180_GPIO0_int` and the `nm180_GPIO2_int` registers are both set to a high impedance. The `nm180_GPIO1_int` register is set to high. The FSM changes to the `MEM_TEST-S0` state.

2. `MEM_RD`: The state for reading the memory.

S0: This is a delay state to stabilize the voltage. The state starts a counter named `cnt_delay` and when it reaches the value of `delay_time`, the FSM changes to the `MEM_RD-S1` state and resets the counter.

S1: This state sets the `trig_start_180nm` and the `rw_180nm` signals high, the `idle_180nm` signal to 0 and the `datain_180nm` signal to `16'hcafe` or to 0, depending on `set_data_i`. When that signal is high, it will be the first one and when low the latter one. The FSM changes to the `MEM_RD-S2` state.

S2: This state sets the `trig_start_180nm` signal low. There is a wire called `trig_rdy_180nm` and when high, the address of the 180 nm SRAM is increased by 1 and the FSM changes to the `MEM_RD-S3` state.

S3: This state checks if the end address has been reached. The state loops through each bit of the `dataout_180nm` signal to check for SEUs (for both SRAMs) and when encountered, it will increase the `count1` and the `count2` variable for SRAM180 1 and 2 respectively. Then it adds the counters to the `sram180_errors` variables for both SRAMs. If the end address of the SRAM180s has not been reached, the counters are reset and the FSM changes to the `MEM_RD-S1` state. If the end address has been reached, the counters and the address are reset. The `disable_ext_req` signal is set high and `datain_180nm` is again set to `16'hcafe` or 0 depending on the same condition as before. The FSM then changes to the `MEM_WR-S0` state.

3. `MEM_WR`: This state is the initial state of the FSM and also the state for writing the memory.

S0: This state sets the `disable_ext_req` signal is set high and `datain_180nm` is again set to `16'hcafe` or 0 depending on the same condition as before. It also sets the `nm180_GPIO0_int` and the `nm180_GPIO2_int` registers to a high impedance. The `nm180_GPIO1_int` register is set high. A counter called `cnt_delay` is initiated and when it reaches the value of `delay_time`, the counter is reset and the FSM changes to the `MEM_WR-S1` state.

S1: This state sets the `trig_start_180nm` signal high and the `rw_180nm` to low. The `idle_180nm` signal is set to 0 and the FSM changes to the `MEM_WR-S2` state.

S2: This state sets the `trig_start_180nm` signal low. When the `trig_rdy_180nm` signal is high, the address of the SRAM is increased by 1 and the FSM changes to the `MEM_WR-S3` state.

S3: This state checks if the end address has been reached. If not, the FSM simply changes back to the `MEM_WR-S1` state. If the end address has been reached, the counter is reset, the address is reset and the `disable_ext_req` signal is set to low. The FSM then changes back to the `MEM_IDLE-S0` state.

4. `MEM_TEST`: State to test the SRAM180 devices for reading and writing.

S0: This state initiates a counter for a delay to let the voltage stabilize. The counter is called `cnt_delay` and when it reaches `delay_time` the FSM will change to the `MEM_TEST-S1` state. The counter is reset, the `trig_start_180nm` signal is set high, the `rw_180nm` signal is set low and the `idle_180nm` signal is set to 0's. The address if the SRAM is changes to the test starting address and the `datain_180nm` signal is set equal to the test data.

S1: This state is a wait state that finished for the writing of the SRAMs. It sets the `trig_start_180nm` signal to low and when the `trig_rdy_180nm` signal is high, the FSM changes to the `MEM_TEST-S2` state.

S2: This state sets the `disable_ext_req` signal to high. The `nm180_GPIO0_int` signal and the `nm180_GPIO1_int` signal are also both set high, while the `nm180_GPIO2_int` signal is set to a high impedance. A delay is then initiated using the `cnt_delay` counter and when this reaches the value of `delay_time`, the FSM changes to the `MEM_TEST-S3` state. The `trig_start_180nm` is then set high, the `rw_180nm` is set high, the `idle_180nm` signal is set to 0's and the counter is also reset.

S3: This state sets the `trig_start_180nm` signal to low. When the `trig_rdy_180nm` wire is set high, the FSM changes back to the `MEM_IDLE` state (also activating sub-state S0). The `test_end_o` output wire is set high, the `sram180_errors` signals (for both SRAMs) are set equal to the `dataout_180nm` signals and the `disable_ext_req` signal is set low.

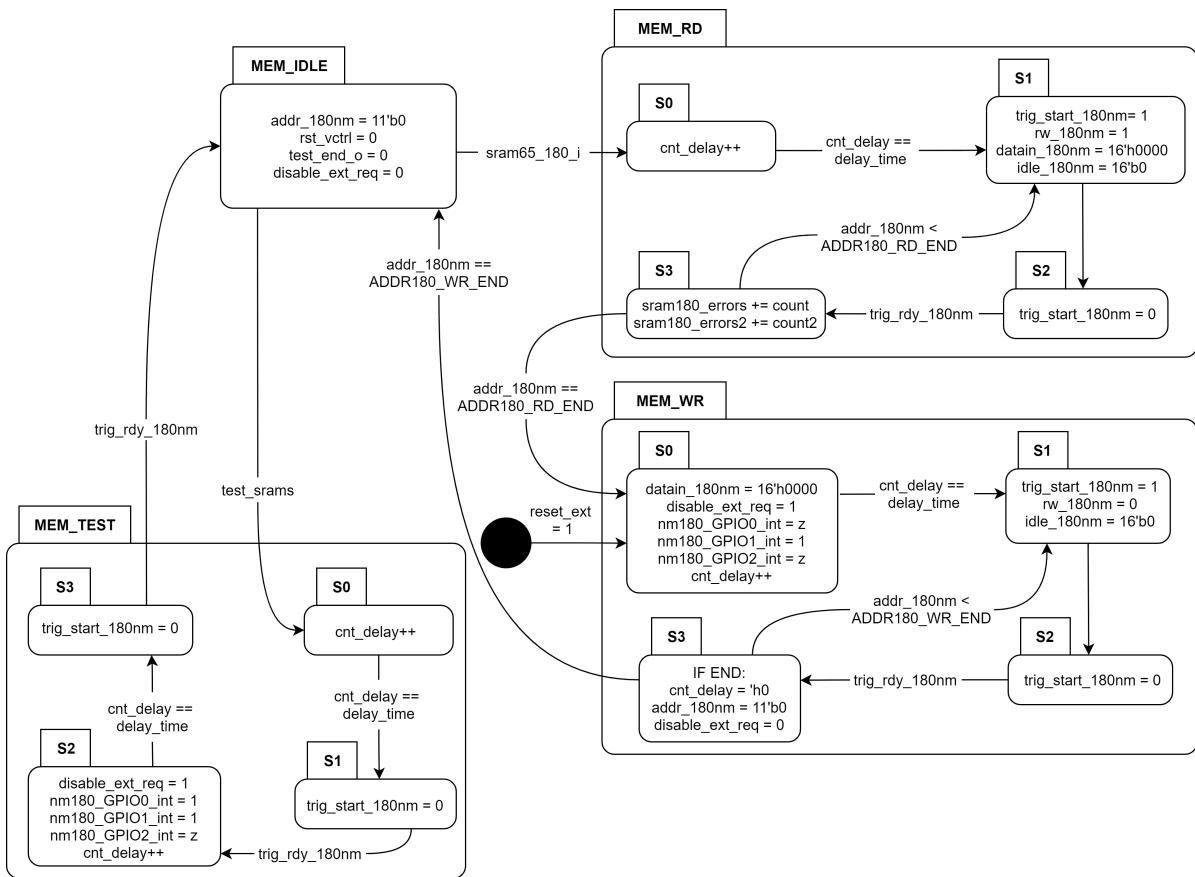


Figure 3.6: Block diagram to depict the FSM of the SRAM180 controller.

3.4.5. SPI Communication

The SPI modules consists out of one main module called `top_spi`, with two sub-modules called `SPI` and `memory_spi`. The `memory_spi` initiates the memory that the SPI needs while in operation and to store the received SPI data. The `SPI` sub-module handles the control of the SPI using a state machine implementation which is elaborated further below. The `top_spi` module binds the SPI controller and the memory of the SPI together so that it works properly. An overview of the signals for the SPI implementation can be seen in Figure 3.7.

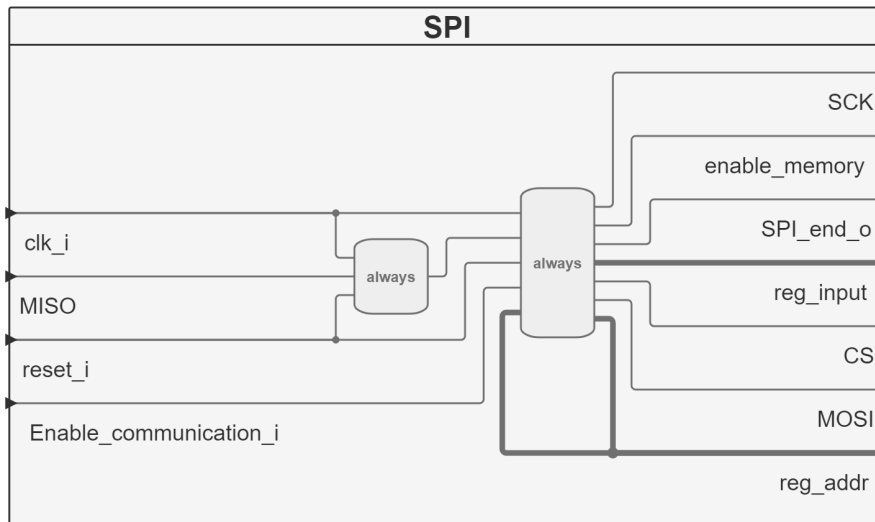


Figure 3.7: Block diagram of the various signals in the SPI implementation. Figure was made using the block diagram view in Sigasi.

The FSM that is implemented for the SPI to work contains six states. Each of these states can be seen in the FSM diagram in Figure 3.8 and are also explained below. The controller is initiated when the `reset_i` signal is set high. Then, the counter is set to 0, the Master-Out Slave-In (MOSI) and Serial Clock (SCK) are set low, the `number_bytes_acquired` and `number_of_bits` are set to 0, the `byte_received` signal is reset, the `enable_memory` is set low, the `reg_input` and `reg_addr` are both reset and the CS signal is set high. The FSM then initially changes to the IDLE_STATE. Again, if nothing changes or if some condition is not yet met, the FSM stays in the same state for the next rising edge of the clock.

- IS: IDLE_STATE state. This is the initial state of the FSM. The CS is set to high and the `SPI_end_o` signal is set low. Every rising edge of the clock, the `Enable_communication_i` is checked. When this signal is high, the state changes to START and the CS signal is set low.
- SRT: START state. This state is a pass-through state. The `reg_addr` is set to zeros and the SCK signal is set high. The FSM then changes to the HIGH_WINDOW state.
- HW: HIGH_WINDOW state. This state uses a counter that will be increased each rising edge of the clock. When the counter reaches the equivalent value of `'b10`, the `byte_received` signal is set to `MISO_sync_two` and the `number_of_bits` signal is increased by `4'd1`. If the counter is equivalent to the value of `HALF_CLK_PERIOD`, the counter is reset to 0, the SCK is set low and the FSM changes to the INITIAL_LOW_WINDOW state.
- ILW: INITIAL_LOW_WINDOW state. The counter is now increased by 1. If the number of bits is equal to 8 (`4'd8`), the input of the register (`reg_input`) is set equal to the byte that is received (called `byte_received`). The `enable_memory` signal is set to high, the `number_bytes_acquired` is increased and the state machine changes to the STOP_BIT state. If the number of bits received is not equal to 8, the state is changed to RESTANT_LOW_WINDOW.
- RLW: RESTANT_LOW_WINDOW state. This state also increases the counter by one at every rising edge of the clock. When the counter reaches the value of `HALF_CLK_PARAMETER`, the counter is reset and the SCK is set high. The FSM then changes to the HIGH_WINDOW state.
- SB: STOP_BIT state. This state again increases the counter at every rising edge of the clock. If the number of bits is equal to 8, `enable_memory` is set low (disabled), `reg_addr` is increased for the next saving and both the `byte_received` and the `number_of_bits` signals are reset. If the `number_of_bytes_acquired` signal is equal to `NUMBER_OF_BYTES_REQUIRED`, the counter and the `number_of_bytes_acquired` signal are reset. The state machine then changes back to the IDLE_STATE and the `SPI_end_o` signal is set high. If that is not the case and the counter reaches the value of `STOP_PERIOD`, the counter is reset and the SCK is set to high. The FSM will then change to the HIGH_WINDOW state.

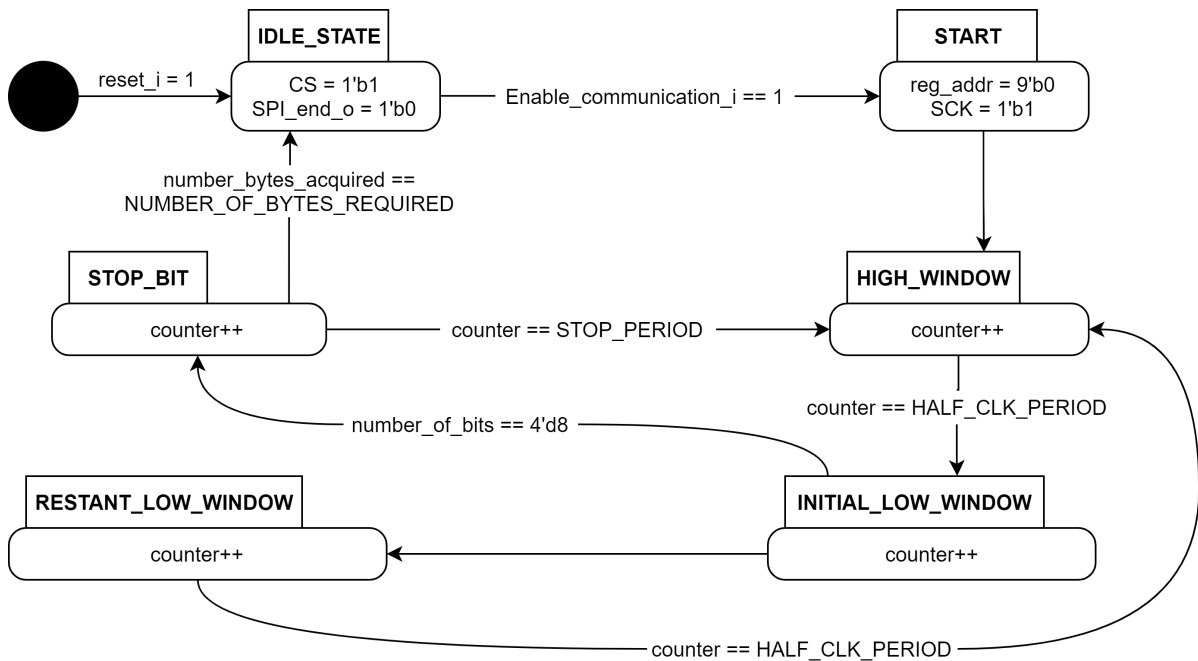


Figure 3.8: Block diagram to depict the FSM of the SPI protocol implemented.

To check if the communication between the MCU and FPGA is working properly, a Cyclic Redundancy Check (CRC) is used. It is an error detecting code to check data integrity. This is calculated twice, one time in the MCU and subsequently sent with the data and the second time in the FPGA where it is checked with the one determined in the MCU. The signals of the CRCs in the FPGA are handled in the MCU controller and can be seen in subsection 3.4.2.

3.5. Payload Operation

This section will explain the operation of the payload. It will briefly touch upon the power consumption, the I2C implementation and the steps on how to interface with the payload.

3.5.1. Power Consumption

The power usage of the system is partly managed by the Flash-Freeze on the board. This module has two modes of working:

Flash_Freeze_N = 1: The CLK_GATED is equal to the input CLK.

Flash_Freeze_N = 0: The CLK_GATED is set to low and instantaneously shuts off the dynamic power consumption. All the information saved in the SRAM and registers are retained because the power to the system is not fully cut off.

The total power consumption in normal mode (Flash_Freeze_N = 1) is equal to 73.5 mW and the power consumption in Flash-Freeze mode (Flash_Freeze_N = 0) is equal to only 45 mW, giving a significant reduction of power usage [68]. The current consumption on normal operation conditions can be seen in Figure 3.9. Taking the 5 V input voltage, the power can be determined. The first peak is explained due to the cold power-up and initial reset. The second peak is the testing. The third and fourth peak are the sequential reset and measurement. Then, the overall current drops due to the Flash-Freeze mode. The peaks afterwards are temporarily exiting the Flash-Freeze mode and performing a measurement.

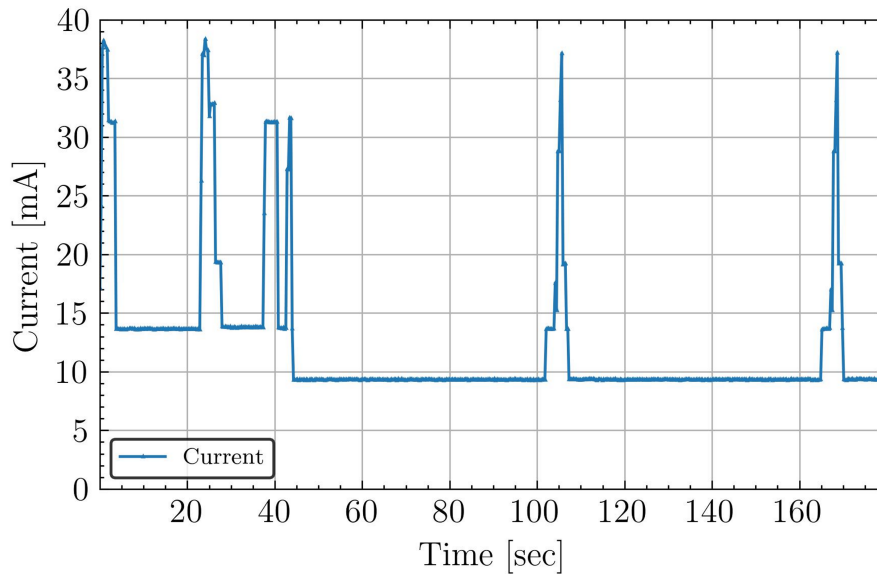


Figure 3.9: Current consumption of the Space RadMon-NG in normal operation conditions. The start-up procedure is seen in the beginning ending with a measurement, then a 1 minute freeze and measurement on loop.

3.5.2. I2C Communication

The Inter-Integrated Circuit (I2C) communication module is also implemented using a top module to bind every thing together called `i2c_top`. This top module has a sub-module called `i2cSlaveTop`, which uses a module called `i2cSlave`. The `i2cSlave` then uses a serial interface and a register interface in its implementation. The I2C implementation (`i2cSlaveTop`) was taken from Steven Fielding on OpenCores.org (2008). The `i2c_top` module implements this with the rest of the FPGA. It is also the only module that needs modification for it to work. It basically creates the wires for the implementation and assigns all registers. It also determined the CRC for the I2C communication, which can then be checked on the receiving end. This I2C CRC will also be used during the testing campaigns with the Space RadMon-NG.

The registers are of great importance for the initialisation using the I2C protocol. The first registers called `reg0 (0x00)` is the control register. This register can be used for reading and writing. It has the length of 1 byte and the possible configurations can be seen in Table 3.4. The register is self cleared after a command is executed (including the `Vctrl` which is set back to 00). The various possibilities from the outside using the I2C can also be depicted using a FSM, which is seen in Figure 3.10. In this figure, there is a separate signal as well called `enFGPA` as GPIO, which was also showed in Figure 3.1. This signal is used to trigger the sleep mode on the FPGA.

Table 3.4: Various bit configurations for the control register (0x00).

Bit configuration	Name	Purpose
0000 0000	-	Standard configuration of control register
0000 0001	START	Start a new measurement
0000 0011	RST	Will reset the system
0000 0101	TEST	Will start the write/read/verify (test) operation for each SRAM
0000 0001	Vctrl	Sets the SRAM voltage when idle to 0.40 V
0000 1001	Vctrl	Sets the SRAM voltage when idle to 0.60 V
0001 0001	Vctrl	Sets the SRAM voltage when idle to 1.79 V
0001 1001	Vctrl	Sets the SRAM voltage when idle to 2.20 V

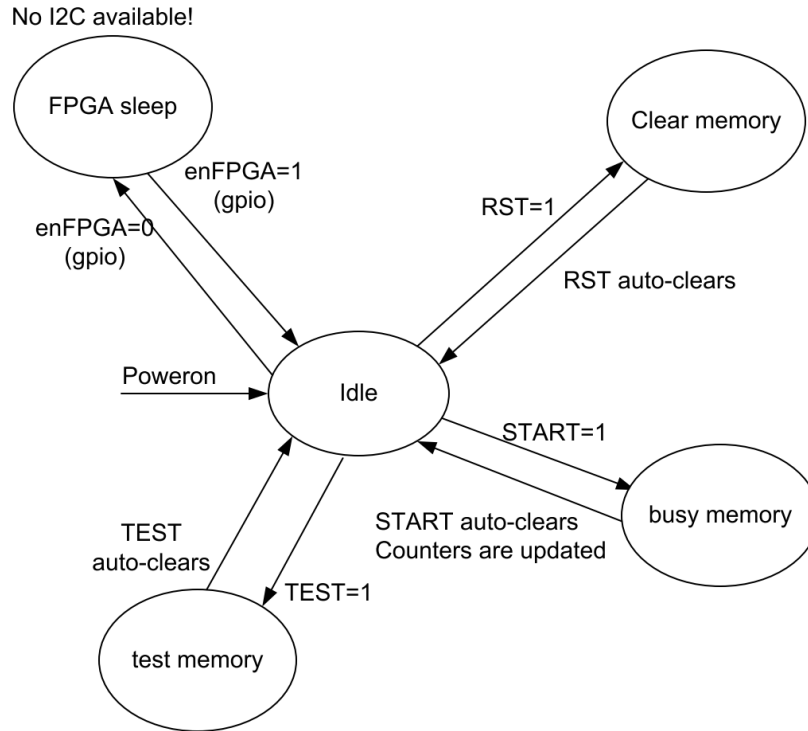


Figure 3.10: Diagram for the FSM seen from the outside of the system. Taken from the interface control document of the Space RadMon-NG.

3.5.3. Interfacing with the Space RadMon-NG

To interface and read the data from the Space RadMon-NG sensor module, a couple of things are required. This is a power supply to supply 5.0 V, an Arduino with the read-out program, a computer with CoolTerm and finally the payload itself. By connecting the Arduino to the I2C port on the Space RadMon-NG motherboard (J9 connector), an initial connection is established. The I2C port has 6 pins in total, 4 coming from the Arduino and the remaining 2 coming from the power supply (positive and ground), which should be set to 5.0 V. The Arduino is then loaded with the read-out program, which can be seen in Appendix A. By starting CoolTerm on the computer and connecting to the Arduino COM port, the data measured by the Space RadMon-NG can be seen and possibly logged. The schematic of the interfacing setup can be seen in Figure 3.11. It is important to mention this, since the same type interfacing will be used with the testing of the Space RadMon-NG with some extra steps in between the connections. This will be elaborated further in the appropriate chapters.

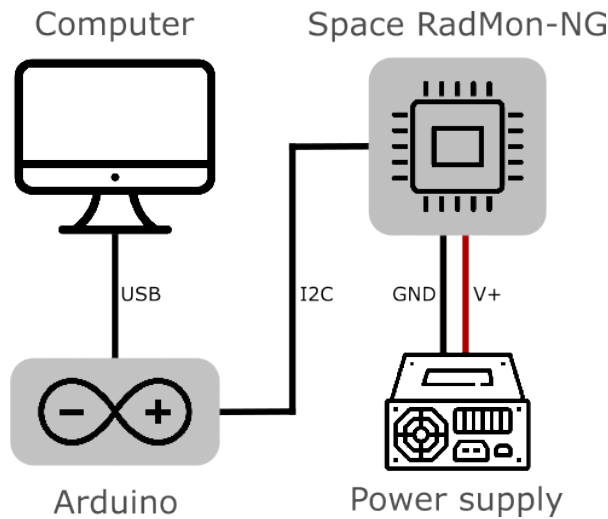


Figure 3.11: Diagram of the interfacing setup with the Space RadMon-NG.

The pin layout of the J9 connector on the motherboard is important for the interfacing. The connector has 6 pins, to which the power and I2C are connected. Pin 1 is used for a 5 V supply voltage and the pin 2 is for ground. The I2C uses pin 4 for the Serial Data (SDA) and pin 5 for the Serial Clock (SCL). Pin 3 of the connector is used for the Flash Freeze mode and pin 6 is unused. The cabling for the I2C from the Arduino to the Space RadMon-NG J9 connector and the power supply can be seen in Figure 3.12. The pins of the Arduino can be selected by own preference, but must be accordingly configured in the Arduino code.

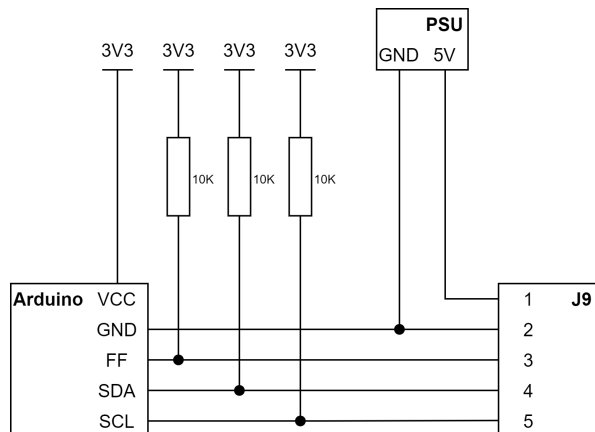


Figure 3.12: Cables schematic for the interfacing with the Space RadMon-NG using the power supply and Arduino.

3.6. State-of-the-Art Comparison

Now the ins and outs of the Space RadMon-NG payload are fully worked out, it can be compared to the current state-of-the-art used in general radiation monitoring and radiation monitoring specifically for space. In this section, first the current state-of-the-art will be described and afterwards there will be a comparison of this state-of-the-art with the Space RadMon-NG payload.

3.6.1. Current State-of-the-Art

In this sub-section, radiation monitoring devices that have been recently tested in space or have been used for a long time are studied. Most radiation detectors are based on the principle of electron-hole creation in semiconductor material such a silicon or germanium. The advantage of this type of sensor is their small size, responsiveness and resolution. They are however quite sensitive to radiation damage on a longer term. Currently, there are two main small monitoring devices used. These are based on the

Timepix sensor and on the RADFET. These are explained in detail below respectively.

SATRAM

The SATRAM is type of radiation monitor with a hybrid active pixel detector, developed within the Medipix collaboration at CERN. The SATRAM has been launched onboard the Proba-V satellite in a 820 km altitude LEO. the Timepix chip is equipped with a 300 μm silicon sensor with a signal threshold of 8 keV per pixel to low energy X-rays and all charges particle types including minimum ionizing particles. A unique characteristic of the Timepix is the capability of particle tracking, including directional sensitivity for energetic charged particles. The single quantum sensitivity (zero-dark current noise level) combined with per-pixel spectrometry and micro-scale pattern recognition analysis of single particle tracks enables the composition (particle type) and spectral characterization (energy loss) of the mixed radiation fields. The detector operates in wide dynamic range in terms of absorbed dose starting from single particle doses in the pGy level, particle count rate up to 10^{6-10} / cm^2/s and particle energy loss (threshold at 150 eV/ μm) [33].

The authors in [34] have developed a highly sensitive technique to measure the energy loss and linear energy transfer (LET) spectra of energetic charged particles in high resolution and over a large collection of particle event types. Their measurements were performed with a single semiconductor pixel detector. Both the deposited energy along the particle trajectory (energy loss) and the path length of the particle track across the semiconductor sensor were precisely measured for each particle. This allowed for the determination of the particle LET in silicon in high accuracy and over a wide-range of energies, particle types and directions. This technique applies to energetic ($E > 10$ MeV/u) charged particles generating tracks greater than the pixel size and incident at non-perpendicular direction ($>20^\circ$) to the sensor plane. The technique applies also to electrons of energy above few MeV as well as highly energetic and Minimum-Ionizing-Particles (MIPs).

The particles identification in the sensor is based on the semiconductor pixel detector. The SATRAM sensor consists out of 256 by 256 pixels of pitch size 55 μm which are operated in a Time-over-Threshold (ToT) mode, meaning that the increased voltage time above the threshold created by particle impact is measured. The energy deposited by ionizing particles in each pixel is registered in the square matrix of pixels and read out in frames of preset acquisition time. The ionizing particles passing through the Timepix sensor leave tracks in this pixel matrix and these tracks are sets of energy depositions in neighbouring pixels (also referred to as clusters). A big downside of using this sensor is that it cannot detect and identify particles with energy lower than 20 MeV due to the shielding of the sensor. The authors in [54] proposed a new method for particle detection based on neural networks trained with GEANT4 data. This method can be used since in most cases the tracks of protons and electrons in the Timepix are, depending on the incident angle and the energy, quite different. Convolutional Neural Networks (CNNs) can detect these features specific to the object.

Based on the Timepix and its outstanding performance records, IEAP together with a spin-off company called Advacam received a contract from ESA. They needed to design, develop and test four prototypes of the miniaturized radiation monitor (MIRAM) planned for Geostationary Orbit (GEO) Telecom satellite missions. The objective of these devices based on the Timepix sensor is to monitor cosmic radiation dose to satellites. This version of the Timepix sensor has reduced power consumption, lower complexity and lower cost compared to previous solutions [31].

RADFET

Another method of measuring radiation is using MOSFETs, or specifically radiation sensitive MOSFETs. RADFETs already have a proven record of successful exploitation in space missions. The RADFETs are composed of materials sensitive to radiation. The working principle is again the ionization created in the semiconductor, resulting in electron-hole pairs.

MOSFET dosimeters consist of two electrodes (source and drain) which are embedded within a silicon substrate (N-doped). N-doped material is negatively charged, meaning there are free electrons in the material. Between the source and drain there is a silicon oxide layer with a metal gate electrode on top. When a current is applied to the source and drain electrodes, the current will not pass

through the silicon substrate beneath the gate and oxide layer until the threshold voltage is reached (an adequate amount of voltage). This threshold voltage is changed in the material when it is subject to radiation. When ionization occurs within the oxide layer while a positive voltage is applied to the gate, the electron-hole pairs are liberated. Electrons will migrate into the metal electrode and are carried away by the positive voltage bias while the holes drift in the silicon oxide and silicon substrate. This increase in hole density within the substrate leads to an increase in the threshold voltage necessary to be able to have a current between the source and drain electrodes. The voltage difference can be correlated to dose with a high accuracy. There are however some limitations to the RADFET. Dose response for particles other than photons and electrons is dependent upon incident LET and energy, so accurate measurement of equivalent dose in a mixed radiation field is not currently possible with a RADFET alone [17]. The sensors also are only able to determine the dose without the dose rate.

The authors of [3] have proposed a new unique design concept that supports the simultaneous operation of a single RADFET as absorbed dose and dose rate monitor. This leads ultimately to a cost reduction in the implementation of a radiation monitoring sensor, since the need for other types of radiation sensors can be minimized or fully eliminated. The processing of such a RADFET response there is a read-out system proposed composed of an Analog Signal Conditioner (ASC) and a self-adaptive Multi-Processing System-on-Chip (MPSoC). Using this set-up, the soft error rate of the MPSoC can be monitored in real time with embedded sensors which allows for autonomous switching between three operating modes. These modes are high-performance, de-stress and fault-tolerant mode. The selected mode depends on the application requirements and the radiation conditions.

3.6.2. Payload Differences

By comparing the Space RadMon-NG to the state-of-the-art, some important differences can be noticed. As the Space RadMon-NG contains multiple sensors for different purposes in radiation monitoring, more than one comparison needs to be made.

The first sensor that can be compared is the HEH fluence sensor. On the Space RadMon-NG, a general SRAM by Cypress is used that has been calibrated at PIF in PSI. By using a COTS SRAM, it is very cheap and accurate to measure the HEH fluence in space. The closest state-of-the-art comparison would be the Timepix, as this is also very accurate and only sensitive to higher energy particles above 20 MeV. An advantage of the Timepix is the directional sensitivity and ability to track particles. A downside compared to the COTS SRAM is the price of the device and it requires a very high bias voltage to operate and detect particles.

The second sensor that can be compared is the dosimeter. On the Space RadMon-NG, the FGDOS sensor is used while the RADFET is current state-of-the-art. The RADFET is rather expensive and does not have the best resolution, but it is easy to install and use. It can also be replaced very easily when the sensor has degraded too much. The FGDOS has a much better resolution than the RADFET and is cheaper. It is however slightly more difficult to use as it is a digital interfacing chip and replacing it is less straight forward once it is installed. Another major advantage of the FGDOS compared to the RADFET is that it can operate without a bias voltage, while the RADFET always requires a 5 V bias to detect radiation.

Overall, the Space RadMon-NG is a very important step forward in radiation monitoring by using cheaper COTS components and sensors with enhanced resolution compared to current state-of-the-art. There are also hardware and software improvements compared to the previous Space RadMon payload version, which contained a RADFET and SEL sensors. The results of the FGDOS and HEH fluence sensor will be more useful in terms of comparing data to models and adding to the body of science. On top of this, the Space RadMon-NG payload also contains custom SRAMs developed by KU Leuven that can alter their sensitivity by altering their bias voltage, something that had not been used before in radiation monitoring.

4

System-Level Testing

This chapter addresses the second research sub-question by means of discussing the needed system-level tests, to allow the payload to be qualified and to identify possible optimizations to be proposed and implemented in the future. The system-level tests performed at the CHARM facility at CERN will also be discussed. One of the main goals of these tests was to check if the burst detection algorithm works and if there are any other underlying issues that still need to be solved in the system or can be optimized, as mentioned before. First the CHARM facility will be introduced, then the test set-ups will be explained together with the dry-runs. Afterwards, the actual radiation tests are explained in more detail, the communication of the payload is tested and a conclusion to the tests is given.

4.1. Radiation Tests CHARM

The radiation test at CHARM required some preparation and a specific set-up. These preparations and set-up will be explained in the next sub-sections. The main reasons behind the system-level testing and the to be achieved goals are given below, linking the testing goals to the requirements set at the beginning of chapter 3:

- The Burst detection firmware verification will address the requirements SRM-HEH-1 and SRM-HEH-2.
- The sensor benchmarking will address the requirements SRM-FGD-1, SRM-FGD-3 and SRM-HEH-3.
- The Payload operation and communication test will address the requirements SRM-ENV-1 and SRM-ENV-2, as well as the operation requirements starting with SRM-OPR.

These goals of the radiation testing campaigns in CHARM, that will be elaborated in the following sub-sections, will be re-evaluated after each testing campaign.

4.1.1. The CHARM Mixed-Field Facility

First of all, it might be advantageous to explain what the facility exactly is that will be tested in. The CERN High Energy Accelerator Mixed-field (CHARM) facility was build for testing electronic systems in a variety of representative radiation environments. There can be thought about atmospheric, particle accelerator and space applications [43]. The CHARM facility is located in the Proton Synchrotron (PS) East Area Hall, of which a 3D rendered image can be seen in Figure 4.1. The East Area can also be seen in Figure 1.2 at the bottom right side in pink.

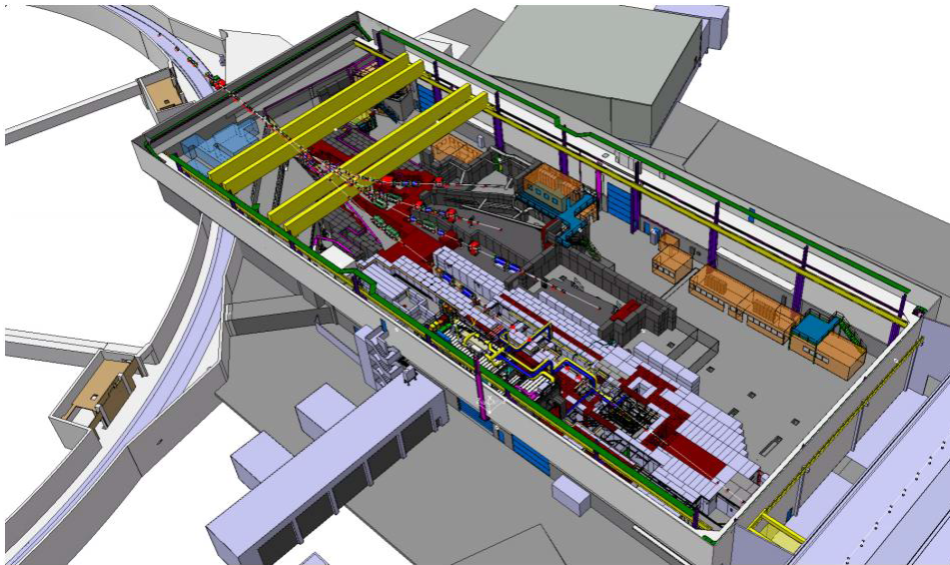


Figure 4.1: 3D render of the PS East Area Hall at CERN. From source [66].

The PS supplies the East Area Hall with a 24 GeV proton beam. Using various beam-lines, the beam is directed to various physics experiments in the building. The T8 beam-line is the line that supplies the proton beam to the CHARM facility, together with the IRRAD facility. The IRRAD facility is another experimental facility upstream of CHARM, meaning that the beam intensity can vary after passing through IRRAD. When the proton beam enters the CHARM facility, it strikes one of the three possible targets in the facility: aluminium with holes, solid aluminium and solid copper. The beam hitting one of these targets creates a mixed-field radiation area or around 70 m³. The layout of the CHARM facility where the proton beam enters and strikes the target is seen in Figure 4.2. The beam coming from the PS is structured in "pulses" and is not a constant beam without interruptions. These pulses are referred to as spills. The spills from PS are of 350 ms in length, separated by 1.2 seconds and ordered in so called 'super-cycle' of around 30 spills. The spills of the super-cycle are distributed between the different extraction lines of the accelerator. On average, the CHARM facility receives around three spills per minutes with an average of 3.1·10⁸ protons per spill. [30]

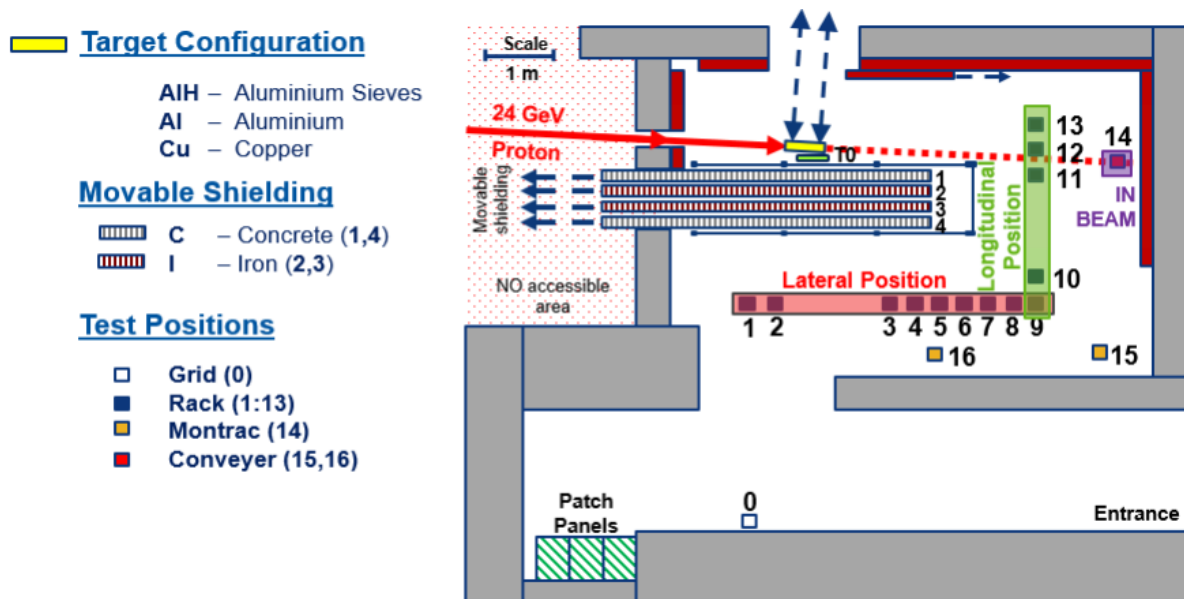
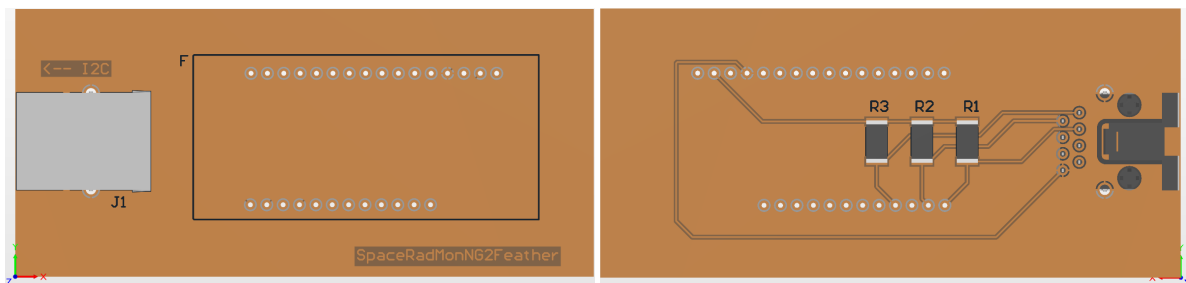


Figure 4.2: Layout of the CHARM mixed-field radiation facility at CERN. From source [30].

The layout of CHARM contains four movable shielding structures (two concrete, two iron) to adjust the intensity of the radiation at certain positions. The experimental positions in the CHARM facility are split up in a grid position (G0), the lateral rack positions (R1 to R9) and the longitudinal rack positions (R9 to R13). The radiation environment in the CHARM facility is composed of a wide variety of particles (protons, electrons, neutrons, kaons, pions, muons, positrons, photons) of which the energies can range from meV up to GeV.

4.1.2. Preparation, Set-up and Installation

Before the radiation runs can be performed, the test set-up needs some preparation. This mainly regards the power and the cabling for the I2C, with a separate signal for the Flash-Freeze mode of the FPGA, as described in subsection 3.5.2 and subsection 3.5.3. For this purpose, a PCB has been designed to act a Arduino Feather M0 shield. This PCB in combination with an Arduino Feather M0 can act as I2C master and convert the signal to serial data, such that the data can be logged using a laptop. The PCB design can be seen in Figure 4.3. For the PCB, an Ethernet connector is used as this is compatible with the control panel and patch panel in the CHARM facility. On the bottom view of the PCB, the pull-up resistors needed for the I2C communication can be seen. These 10 k Ω resistors are used for the Flash-Freeze, the SDA and the SCL signals.



(a) Top view of the Arduino Feather M0 I2C shield PCB.

(b) Bottom view of the Arduino Feather M0 I2C shield PCB.

Figure 4.3: Design of the the Arduino Feather M0 I2C shield PCB.

In addition to the PCB made for the interfacing with the payload, also custom cables with the appropriate connectors were manufactured. Two cables were made, one for in the CHARM facility and the other for in the control room. The cables can be seen respectively in Figure 4.4. The figure on the right also shows the finished version of the I2C over Ethernet to serial data conversion PCB.



(a) Cable made for from the payload to the patch panel.

(b) Cable and Arduino for in the control room of CHARM.

Figure 4.4: Harness manufactured for the communication of the Space RadMon-NG payload during testing in CHARM.

The payload will be placed on the G0 position in the CHARM facility (see Figure 4.2 for reference). From this position, the cable shown in Figure 4.4a will go from the payload to two ports in the patch panel on the bottom left of the figure. One of the ports is for the data communication using the Ethernet cable. The other port is a Bayonet Neill–Concelman (BNC) port used to power the payload from a power supply in the control room. In the control room, the payload connection is established using the cable seen in Figure 4.4b, which will go from a laptop to the corresponding Ethernet port. In addition, the power supply is connected to the corresponding BNC port to supply the necessary 5 V and current needed. An illustration of the set-up can be seen in Figure 4.5. An important thing to note in this set-up is that there is around of 20 m in cables in between the patch panel and the control panel (dotted lines).

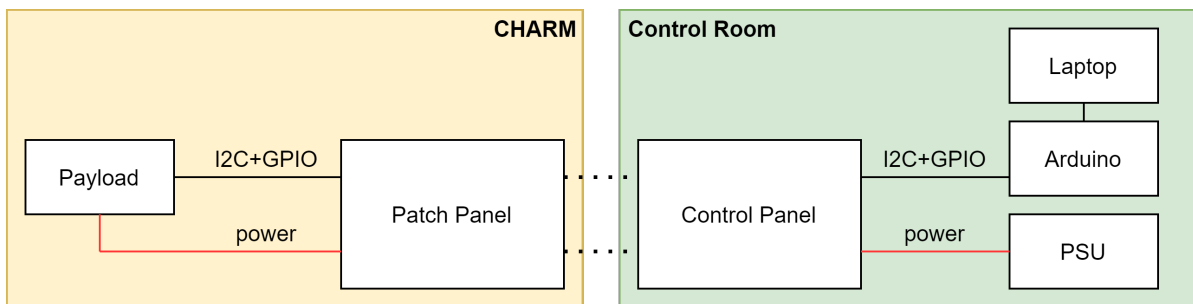
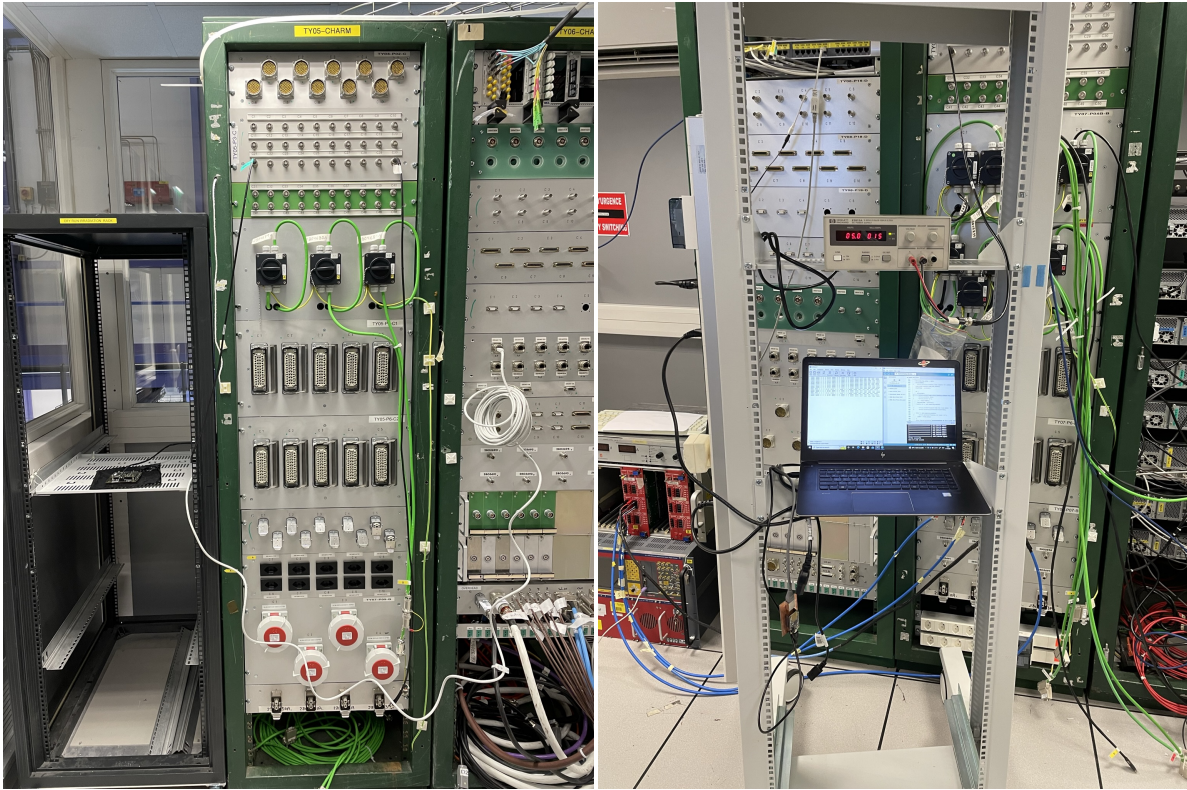


Figure 4.5: Illustration of the set-up that will be used for the testing at CHARM.

4.1.3. Dry Run CHARM

The test set-up was tested in the preparation room of CHARM. This area is a designated place to test the experimental set-ups before irradiating them. It has an identical patch panel and control panel set-up compared to the irradiation room and the control room. The installation on the patch panel side (irradiation room equivalent) can be seen in Figure 4.6a. The payload can be seen on the rack on the left. From the payload, the Ethernet and coax cable go to the patch panel. Then, in Figure 4.6b, the control panel side (control room equivalent) can be seen. The coax cable for the power is connected to the Power Supply Unit (PSU) at the top of the rack. Then, the Ethernet cable is connected to the Arduino hanging below the laptop, which is then connected to the laptop in the middle of the rack. The set-up was tested and was working without any problems.



(a) Set-up dry run at the patch panel in the preparation room.

(b) Set-up dry run at the control panel in the preparation room.

Figure 4.6: Dry run test set-up in the preparation room at CHARM.

4.1.4. Radiation Runs CHARM

In total, there were three radiation campaigns performed at CHARM during the period of the thesis. Irradiation at CHARM is for approximately one week continuously, with a stop on Wednesdays for access to the facility. An overview of the different campaigns can be seen in Table 4.1. This table shows which campaigns were on what dates, together with the TID during the run and the TID accumulated up until that point by the system.

Table 4.1: Overview of the radiation campaigns performed with the payload during the testing period. **One of the voltage regulator was changed.*

Campaign number	Timestamps	TID during run [Gy]	TID accumulated [Gy]
1	27-07-2022 to 03-08-2022	24.04	24.04
	03-08-2022 to 10-08-2022	31.03	55.07
	10-07-2022 to 17-08-2022	41.87	96.94
	17-08-2022 to 24-08-2022	45.87	142.82
	24-08-2022 to 31-08-2022	25.13	167.95
	31-08-2022 to 07-09-2022	39.11	207.06
	07-09-2022 to 14-09-2022	24.80	231.86
2	07-10-2022 to 14-10-2022	15.54	247.40
3	09-11-2022 to 16-11-2022	24.47	272.87*
	16-11-2022 to 23-11-2022	21.66	294.52

After the three campaigns, the payload received in total 294.52 Gy. It has to be noted that this is a worst-case amount. During some of the runs, the device that measures the radiation (the RadMon) was not placed near the payload or a RADFET had failed. In these cases, the worst-case scaling factor was used to determine the TID from the Protons-On-Target (POT) measured, which is a measure of how many protons arrive in the CHARM facility by the beam from PS. The results from each campaign with elaborations are showed in the following sections.

4.2. CHARM Campaign 1

This section will elaborate on the first CHARM campaign completed. The test started at 27-07-2022 and the payload was removed from CHARM on 14-07-2022. First some remarks will be given on the test that was done and afterwards the test results are discussed.

4.2.1. Test Remarks

One of the first things to remark during this test is that an older cable was used with standard jumpers. This cable did not always work properly as it was not robust enough. This was also the reason why the cable mentioned in the previous section was developed. At some points during the test, the logging failed but the payload continued to work (timestamp 2022-07-30 09:00:00). After timestamp 2022-08-04 00:00:00, there was only little logging and after timestamp 2022-08-09 00:00:00 there is no logging at all. After the timestamp 2022-08-10 00:00:00, there was a connection failure between the payload and the control room. This was identified because the CRCs did not match between the one given by the payload and the one calculated in the control room. This connection failure was after the test identified to be something related to the cable, since the payload still worked properly when testing the system directly in the facility without the patch panel and control panel in between. In the end, only data was retrieved from 27-07-2022 to 10-08-2022 (a period of around 2 weeks). The payload was in the facility during this test until 14-07-2022, as it could not be removed sooner.

4.2.2. Burst Algorithm and Fluence Results

One of the first to analyze during this campaign is if the burst detection algorithm functions well and how accurate the HEH fluence measurements are, as stated in requirements of SRM-HEH. The hypothesis is that when the HEH measurements based on the corrected amount of SEUs in the SRAM of the payload are compatible with the HEH fluence measurements from the RadMon, the algorithm works well. The results from the Cypress SRAM SEUs with and without compensation can be seen in Figure 4.7. The flat regions in the figure are points where the logging or connection failed. In between the red lines in the figure, there was no incoming beam in CHARM due to the access period between runs.

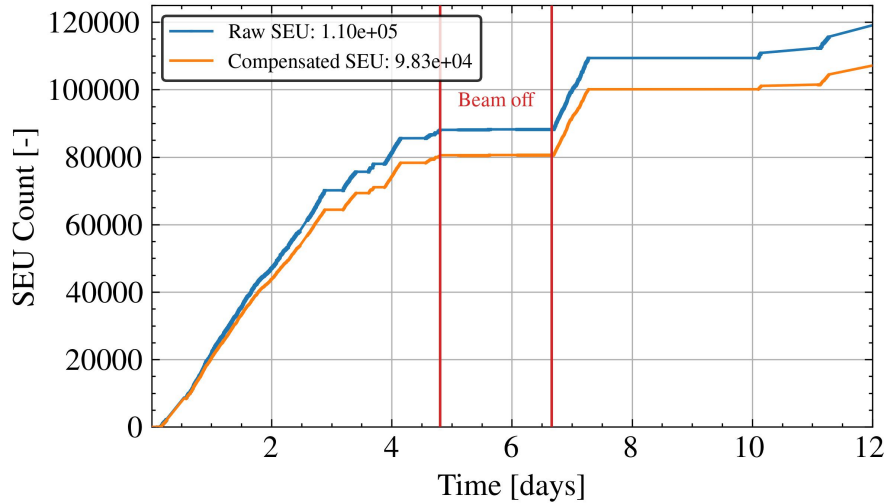


Figure 4.7: Cypress compensated SEU count and raw SEU count over time.

In the figure can be seen that there is indeed a compensation happening when comparing the raw SEU count and the compensated SEU count. In both cases, the counts are quite linear. Since there are some time ranges with missing data, there will be looked at approximately day 0.6 to day 2.25. In this time range, there was a continuous stream of data and the results can be compared accurately. This time range is seen in Figure 4.8. The data has been set to start from 0 on the y-axis and the x-axis for a clearer comparison.

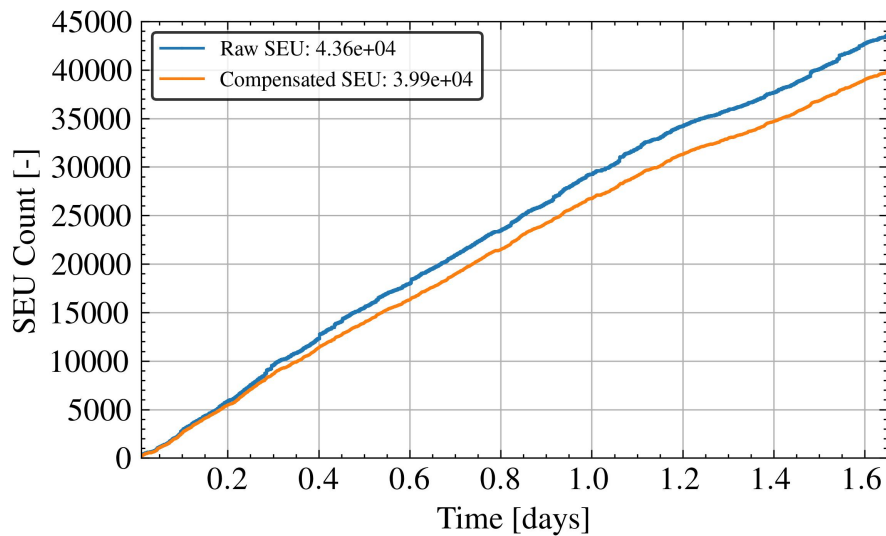


Figure 4.8: Cypress compensated SEU count and raw SEU count over time from day 0.60 until day 2.25.

First of all, this figure shows that SEUs can be detected. This already means that requirement SRM-HEH-1 has been tested and verified. The difference between the compensated count and the count that still has the bursts included can be seen more clearly. Starting from 0, the final raw SEU count ends at around 43600 counts, while the final compensated count ends at around 39900 counts. Based on these counts, the Relative Percentage Difference (RPD) can be determined at the final value, giving:

$$\text{RPD} = 100 \frac{2(43600 - 39900)}{43600 + 39900} = 8.86\%. \quad (4.1)$$

An example of a burst being corrected can be seen in Figure 4.9. If looked closely, just after minute 426 there are two bursts in series. Both of the bursts are reduced to a correct amount of SEUs. Quantitatively,

the result of the burst correction can be seen in Table 4.2. The amount of SEUs corrected for the first burst is 123 upsets and the amount for the second burst is 35 upsets. This successful detection of bursts means that the requirement SRM-HEH-2 is satisfied thus far. It is however only really fulfilled if the corrected amount of SEUs is compatible with other measurements.

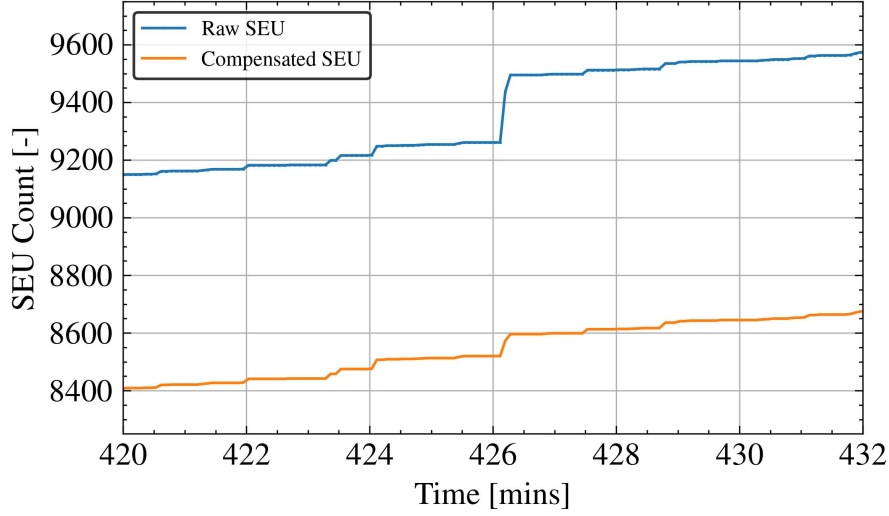


Figure 4.9: Cypress compensated SEU count and raw SEU count over time zoomed in on a compensated burst.

Table 4.2: On-board correction of the bursts happening in the Cypress SRAM in the Space RadMon-NG.

Time [mins]	Raw SEUs [-]	Compensated SEUs [-]	Amount corrected [-]
425.950	9261	8520	0
426.033	9261	8520	0
426.117	9261	8520	0
426.200	9437	8573	123
426.283	9495	8596	35
426.367	9495	8596	0
426.450	9495	8596	0
426.533	9495	8596	0

Now, having the corrected SEU count, it can be compared to the HEH fluence in the CHARM facility. As reference the data from the RadMon placed in the facility was used. The fluences are determined by the following equation, similar to the one shown in Equation 2.3:

$$\phi_{HEH} = \frac{SEU_{tot}}{\sigma_{HEH} N_{bit}} \quad (4.2)$$

Using this equation implies that all counted SEUs are caused by HEHs, which is not the case in CHARM. Since CHARM also has thermal neutrons in the mixed radiation field, these will also cause upsets in the SRAMs. The cross-sections of the memories used during the testing can be seen in Table 4.3.

Table 4.3: Various cross-section of the Cypress SRAM used on the mezzanine board on the Space RadMon-NG.

SRAM	σ_{HEH} [cm ²]	σ_{ThN} [cm ²]
Cypress 1125	$1.87 \cdot 10^{-13} \pm 4.00 \cdot 10^{-14}$	$3.84 \cdot 10^{-16} \pm 7.50 \cdot 10^{-17}$
Cypress 1531 (PSI 2019)	$1.56 \cdot 10^{-13} \pm 2.64 \cdot 10^{-14}$	$9.82 \cdot 10^{-16} \pm 1.11 \cdot 10^{-16}$
Cypress 1531 (PSI 2022)	$2.19 \cdot 10^{-13} \pm 2.19 \cdot 10^{-14}$	-
Cypress 1531 (CHARM)	$3.44 \cdot 10^{-13}$	-

Usually, with two memories that each have a different HEH and thermal neutron cross-sections, a system of equations can be set-up and solved for each respective fluence. This is seen in Equation 4.3, where there are two equations and two unknowns. This can then be solved for each respective fluence.

$$\begin{cases} \text{SEU}_{tot}^1 = \sigma_{HEH}^1 \phi_{HEH} + \sigma_{ThN}^1 \phi_{ThN} \\ \text{SEU}_{tot}^2 = \sigma_{HEH}^2 \phi_{HEH} + \sigma_{ThN}^2 \phi_{ThN} \end{cases} \quad (4.3)$$

However, this will not be necessary as the thermal neutron cross-sections of the Cypress memories used are very small compared to the HEH cross-section. This means that they can be neglected. Figure 4.10 shows the different fluences determined from the amount of SEUs counted. A cross-section of $1.56 \cdot 10^{-13} \text{ cm}^2$ was used for the Cypress SRAM, as this is also the one used in the RadMon device that was used in the first radiation campaign. This RadMon device contained the same memory as the Space RadMon-NG.

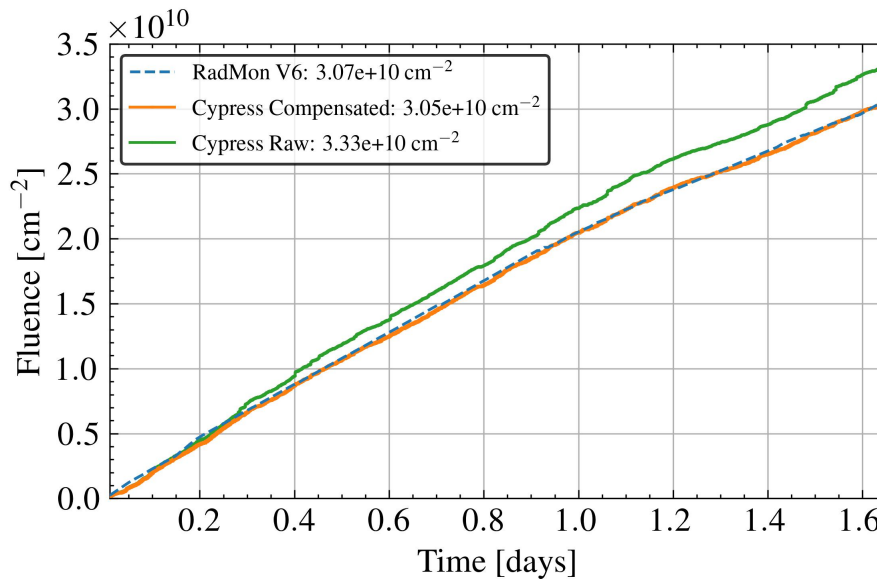


Figure 4.10: Particle fluence determined from the SEUs measured by the SRAMs over time from day 0.60 until day 2.25 compared to the RadMon V6 measurements.

In the figure can be seen that the corrected SEUs from the Cypress memory correspond very nicely to the fluence from the RadMon V6. The RPD of the compensated SEUs with the RadMon V6 is only 0.65%, while the RPD of the raw SEUs with the RadMon V6 is 8.1% with the $1.56 \cdot 10^{-13} \text{ cm}^2$ cross-section used for both the RadMon and Space RadMon-NG SRAM. This result also means that the requirement SRM-HEH-3 is satisfied thus far, being below an accuracy of 2.5%. Since the results are very compatible, requirement SRM-HEH-2 is also fulfilled.

4.2.3. FGDOS and TID Results

The second data to analyze during this campaign are the TID measurement results from the FGDOS. The FGDOS measurements of the Space RadMon-NG can be compared to the TID measured by the RADFET of the RadMon V6 as reference. The total dose can be seen in Figure 4.11, with sensitivity degradation taken into account. This test and analysis is conducted to verify the SRM-FGD-1 and SRM-FGD-3 requirements.

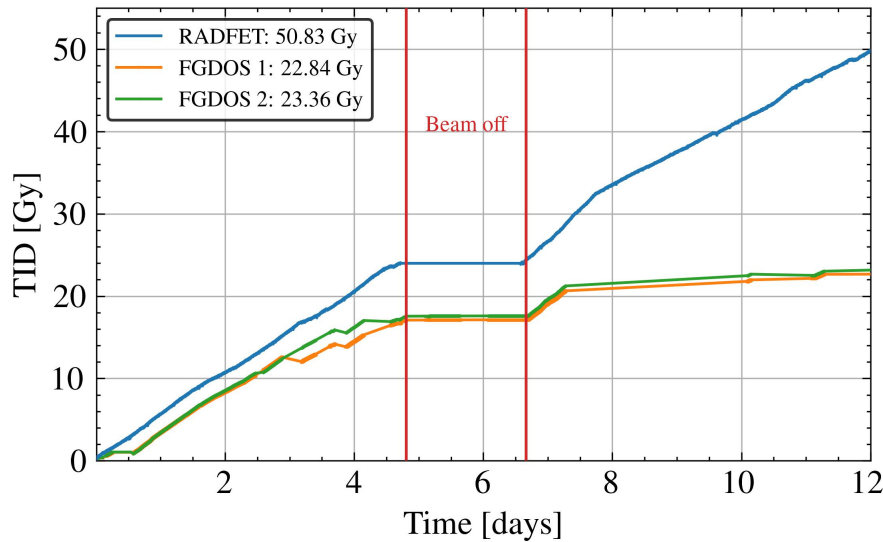


Figure 4.11: FGDOS TID over time with sensitivity degradation included compared to RADFETs.

One of the first things to notice in this figure is that the TID measured by the FGDOS sensors on the Space RadMon-NG is much lower than the TID measured by the RADFETs. This is caused by the communication interruptions and terminations encountered during this first campaign. One of the main issues is that the recharges of the FGDOS were not accumulated during the so called 'blind time', meaning the TID data during such a period was completely lost. This led to one of the firmware improvements of the Space RadMon-NG, namely saving the amount of recharges in the flash memory of the MCU on the main board of the payload. This firmware update is to be tested and validated in the next campaigns (campaign number 2 and 3). The amount of recharges can also be seen in Figure 4.12, where the flat region between day 7 and day 11 can be clearly noticed. This is one of the large regions where the recharges were missed and the TID could not be reconstructed.

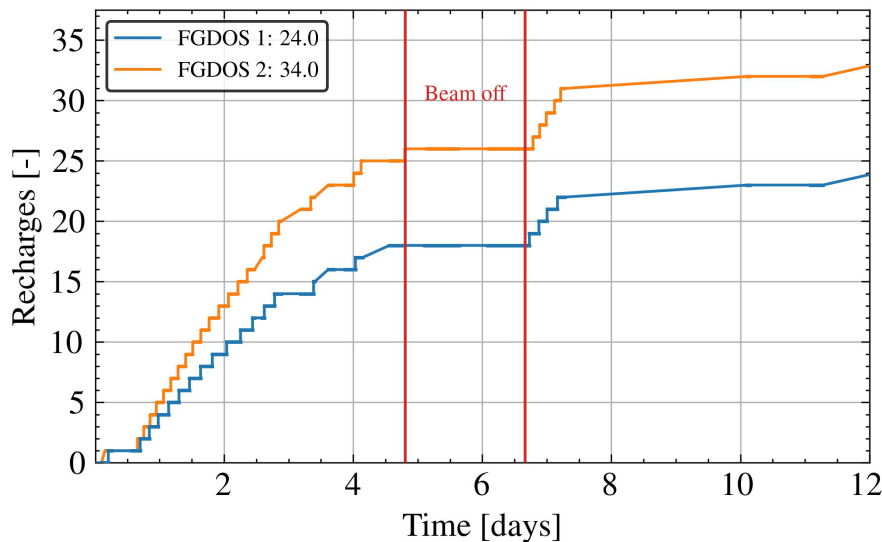


Figure 4.12: FGDOS recharge counts over time during campaign 1.

When focusing on the continuous data received between day 0.6 and day 2.25, the data can still be compared to the RADFET to benchmark the FGDOS, as for requirement SRM-FGD-3. This can be seen in Figure 4.13. In this figure can be seen that the FGDOS sensors are very compatible to the RADFET in the RadMon, with a final RPD of 1.08% and 2.35% for FGDOS 1 and FGDOS 2 respectively. This

verifies the SRM-FGD-3 requirement for this shorter data stream.

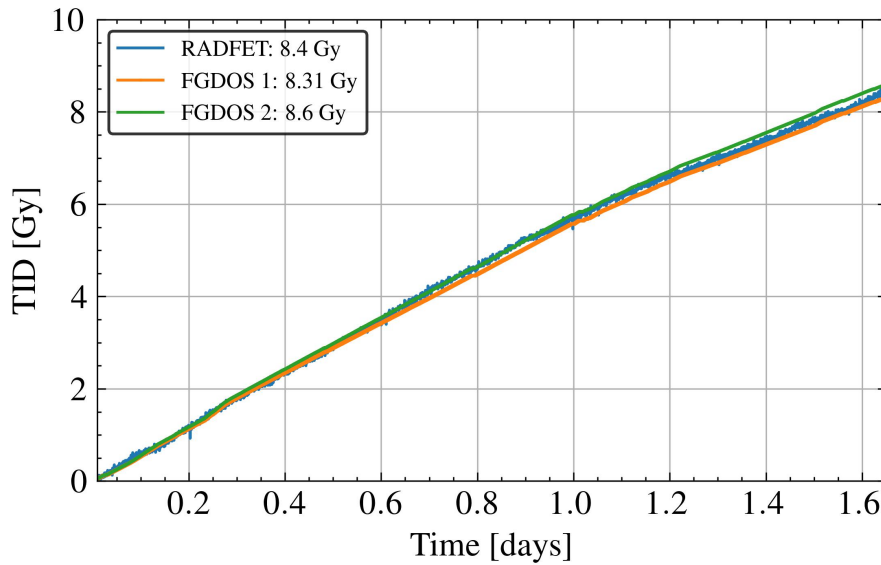


Figure 4.13: FGDOS TID over time with sensitivity degradation included from day 0.60 until day 2.25 compared to RADFETs.

Zooming in on the first few hours of the data, the reason why the RADFET has been replaced by the FGDOS becomes very clear. As seen in Figure 4.14, it can be seen that the resolution is much better for the FGDOS sensor compared to the resolution of the RADFET. According to the data sheets, the resolution of the RADFET is around 200 mGy while the FGDOS can reach a resolution of 2 mGy, a factor of 100 better. This will drastically improve the measurements and determining dose rates while in orbit will be much more precise. This data also verifies the the SRM-FGD-1 requirement.

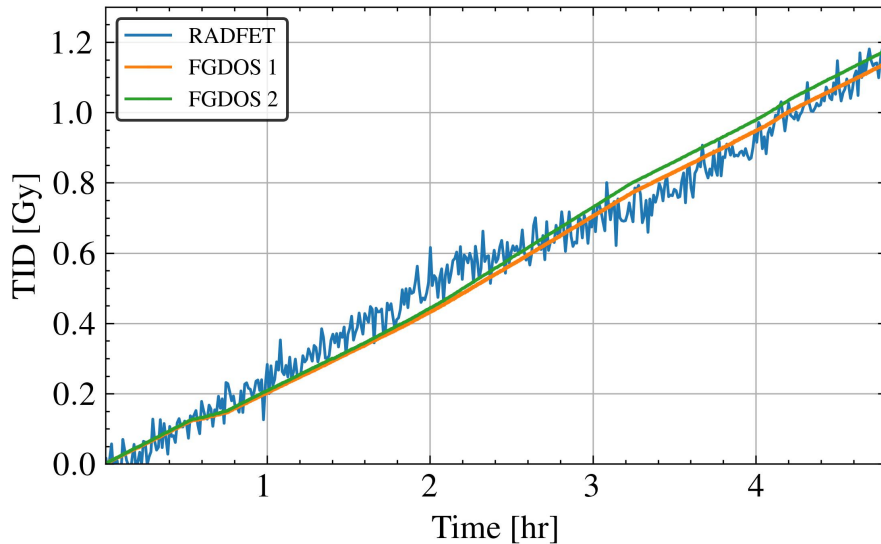


Figure 4.14: FGDOS TID over time with sensitivity degradation included from day 0.60 until day 0.8 (around 5 hours from day 0.6) compared to RADFETs.

Finally the FGDOS will be benchmarked again in the second and third campaign to check the results where there is reconstruction with the recharges saved in the MCU flash memory as part of the MCU firmware update. The performance and accuracy will also be checked over a longer run.

4.2.4. Other Payload Results

A small overview of the other payload results can be seen in the following figures. These will also be checked to verify the SRM-OPR-2 requirement. The other payload data includes the temperature data in Figure 4.15, the voltages in Figure 4.16 and the adjustable voltage in Figure 4.17.

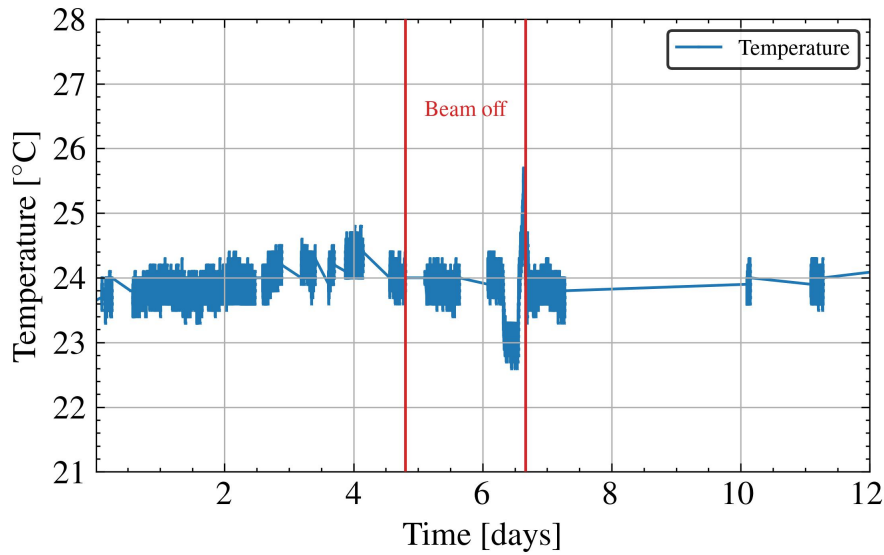


Figure 4.15: Temperature on the mezzanine board of the payload over time.

In Figure 4.15 can be seen that the temperature gives a steady output, however the resolution is not great. It can also be seen that the temperature goes up just before the beam goes on, which is to be expected because of the access and the people around the payload. Overall, the temperature sensors works very well.

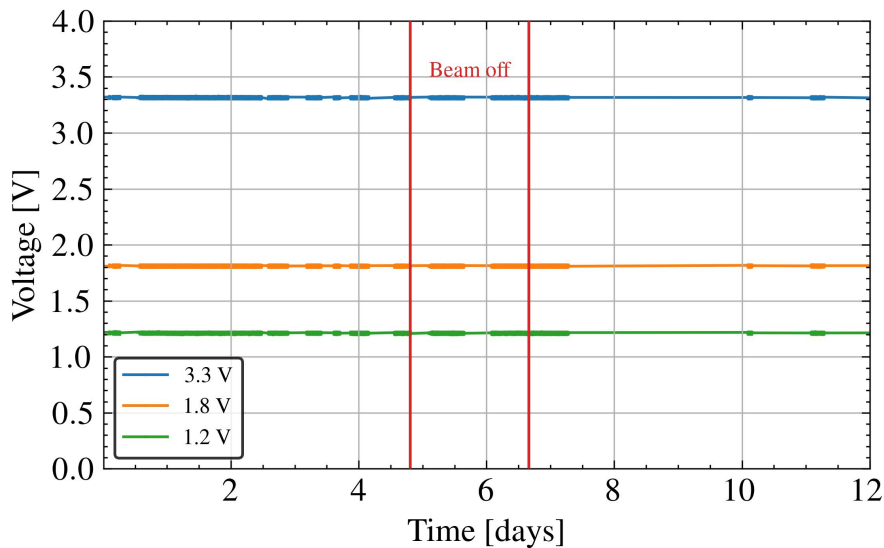


Figure 4.16: The various voltages from the voltage regulator in the payload over time.

In Figure 4.16, the different voltages of the payload can be seen. The voltages are very steady and show the correct values. They also do not change when going from without radiation to being irradiated. The regulators also work very well thus far.

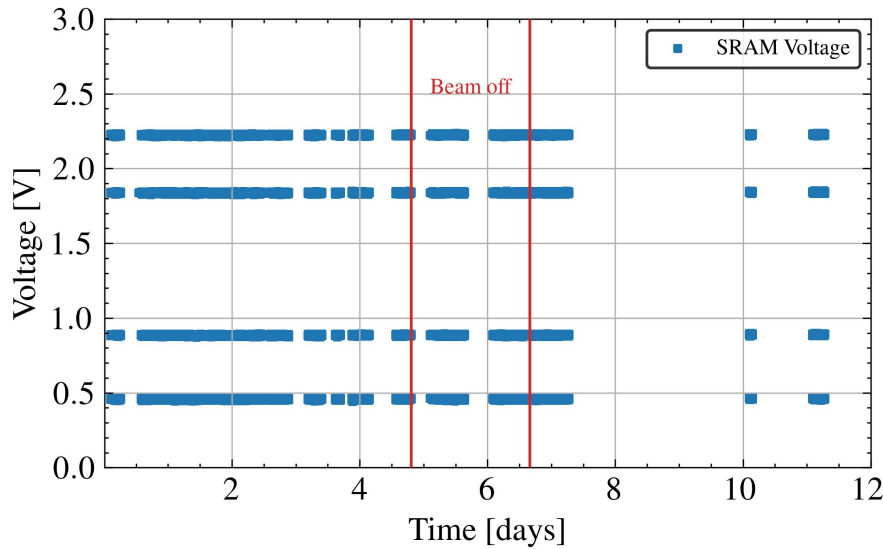


Figure 4.17: The SRAM voltage of the payload over time.

In Figure 4.17, the voltage adjustment of the custom SRAMs can be seen. This is used to vary the sensitivity of the SRAMs for the amount of SEUs happening, basically varying the cross-section of the device. During the test, there was alternated between the possible four voltages and each of them worked well. Overall, the general firmware of the payload is working great. As the communication issues are not yet resolved, the SRM-OPR-1 requirement is yet to be verified. The SRM-OPR-2 requirement is partially verified, since there needs to be concluded that the communication issues are not firmware related first.

4.3. CHARM Campaign 2

As results of the first testing campaign, the goals for the second campaign changed slightly. Only the burst detection firmware requirements have been fully verified so far. The list of test goals can now be summarized as follows:

- Sensor benchmarking: Requirements SRM-FGD-1, SRM-FGD-3 are to be verified with TID reconstruction, requirement SRM-HEH-3 is to be verified over a run longer than in campaign 1.
- Payload operation and communication: Requirements SRM-ENV-1 and SRM-ENV-2, as well as the operation requirements SRM-OPR-1 and SRM-OPR-2 are to be fully verified.

These are the topics that will be checked in this radiation testing campaign. This campaign however only lasted for one week due to an unfortunate failure in the voltage regulator for the FPGA. The voltage can be seen in Figure 4.18.

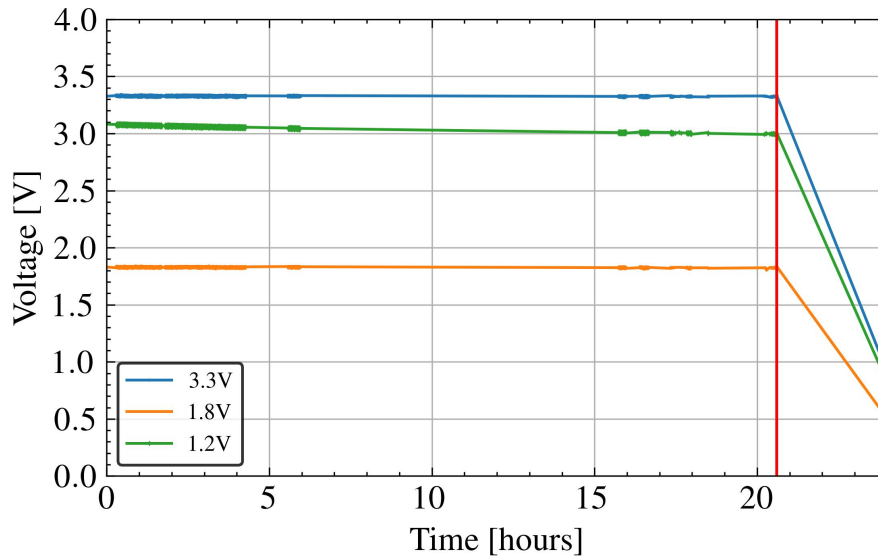


Figure 4.18: The voltages in the payload over time.

This figure shows that the FPGA voltage, which should be 1.2 V, is equal to 3.1 V (green line). During the test campaign, the data retrieval was very irregular due to the communication with the FPGA and after a little over 20 hours the communication was permanently terminated. During the first 20 hours of data retrieval, the payload required a lot of resets and power cycles due to the FPGA getting a voltage that is too high. The regulator failure was already a known issue in the CHARM facility from other systems tested at around 150 Gy. The payload took more than this amount of radiation, meaning the failure was to be expected. Unfortunately, there are no alternatives found yet for the regulator that are tested in CHARM, have the same package and also the same pin configuration. Analyzing the FGDOS data to check the firmware update, it can be seen that the recharges are correctly saved in the flash of the MCU. This can be concluded from the recharges seen in Figure 4.19.

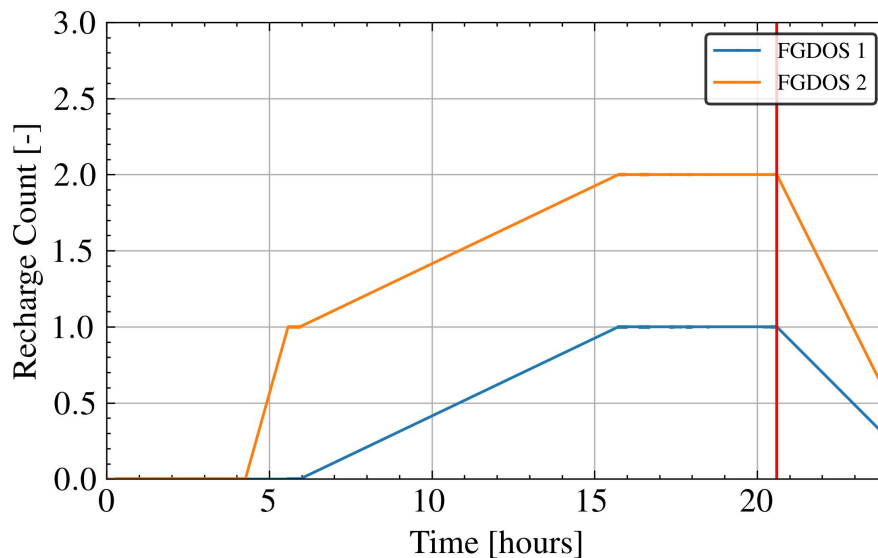
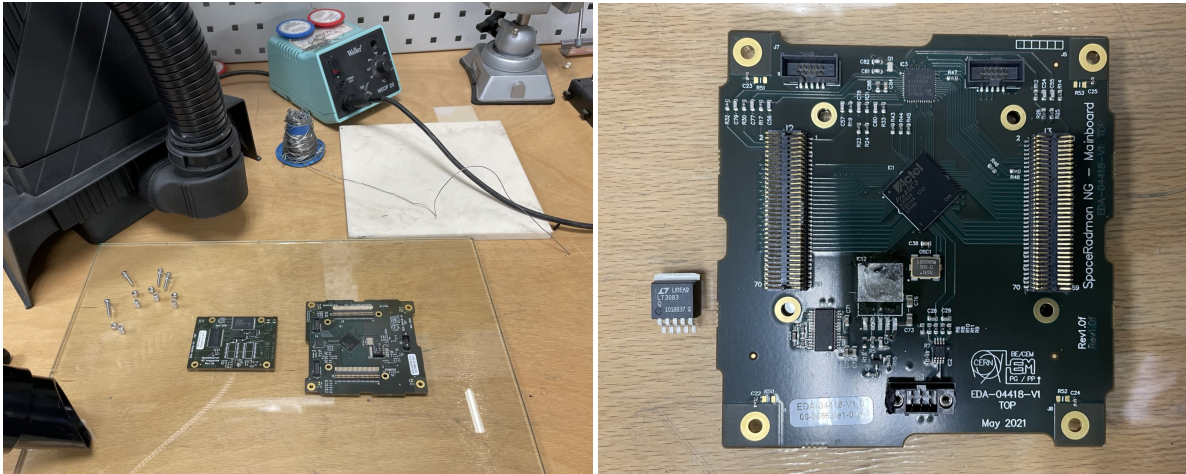


Figure 4.19: The FGDOS recharges of the payload over time.

This figure shows that the recharges read in the FPGA registers are not reset, even though the payload is reset or power cycled in between readings. This was the case before but is improved now due to the firmware update. There are only three recharges in total for the two FGDOS sensors, meaning the data

might not be too reliable. In any case, it is a step in the right direction and needs to be checked again in another radiation campaign. To be able to do a next radiation campaign, the broken regulator had to be replaced. The reparations of this regulator can be seen in Figure 4.20. The reparations were done in the buffer zone radiation lab of the CHARM facility, a special room where there can be worked on systems that have been irradiated and are possibly still radioactive.



(a) Reparations of the Space RadMon-NG payload in the buffer zone of CHARM. This picture shows the dismantled payload with the broken regulator on the main board. (b) Close up of the reparations of the Space RadMon-NG payload in the buffer zone of CHARM. This picture shows the main board of the payload with the broken regulator taken off and the new regulator on the left.

Figure 4.20: Reparations of the Space RadMon-NG payload in the buffer zone of CHARM.

Initially, after the reparations, the payload still did not work. However, after re-flashing the FPGA with the test firmware, the payload worked again as it should with the correct internal voltages. This means it was ready for another radiation campaign for further system-level testing. During this second campaign, no requirements have been verified. Due to this regulator failure, the requirements that fall under SRM-ENV and SRM-OPR need to be investigated critically.

4.4. CHARM Campaign 3

As results of the failure in the second test campaign, the goals for the final radiation test campaign did not change compared to before. The list of test goals can again be summarized as follows:

- Sensor benchmarking: Requirements SRM-FGD-1, SRM-FGD-3 are to be verified with TID reconstruction, requirement SRM-HEH-3 is to be verified over a run longer than in campaign 1.
- Payload operation and communication: Requirements SRM-ENV-1 and SRM-ENV-2, as well as the operation requirements starting with SRM-OPR are to be fully verified.

During this last campaign, there was an almost continuous stream of payload data, as the communication problems were partly resolved. The communication was improved by reducing the I2C frequency, indicating the problems might be caused by the long distance. There was one small interruption somewhere between day 1 and day 2 because the laptop logging the data did an automatic Windows update. This issue for the SRAM sensor has been solved by extrapolating the SEUs, as they are fairly linear. For the FGDOS, this was solved using the reconstruction using the new firmware update, as will be explained in a few paragraphs. There were still some minor communication problems which are analyzed in the section after this one. There will be started with looking at the SRAM results. The SEU counts of the Cypress 1531 SRAM, for both the raw and compensated count, can be seen in Figure 4.21.

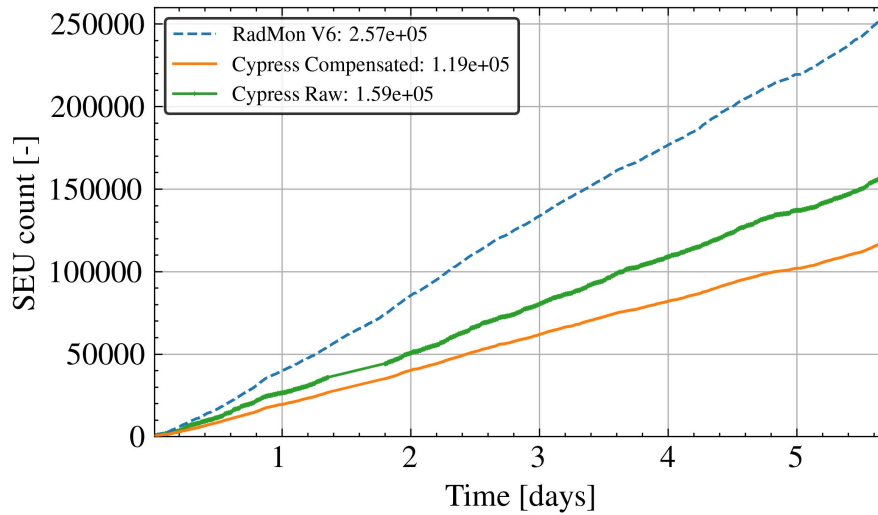


Figure 4.21: The SEUs measured by the payload over time.

As seen in the figure, there is still a good compensation going for the Cypress 1531 SRAM as seen by the green and orange line, even after around the 273 Gy the payload took before this test. This re-verifies the SRM-HEH-1 and the SRM-HEH-2 requirements. The counts between the RadMon SRAM and the Space RadMon-NG SRAM are very different, because this time the RadMon had a Cypress memory from a different batch, namely the Cypress 1125 which has a HEH cross-section of $1.87 \cdot 10^{-13} \text{ cm}^2$ as seen in Table 4.3. Using the correct cross-section, the fluence can still be compared. For the comparison, all three different cross-sections in Table 4.3 for the Cypress 1531 SRAM were taken and compared to the Cypress 1125 SRAM in the RadMon. The fluence comparison can be seen in Figure 4.22.

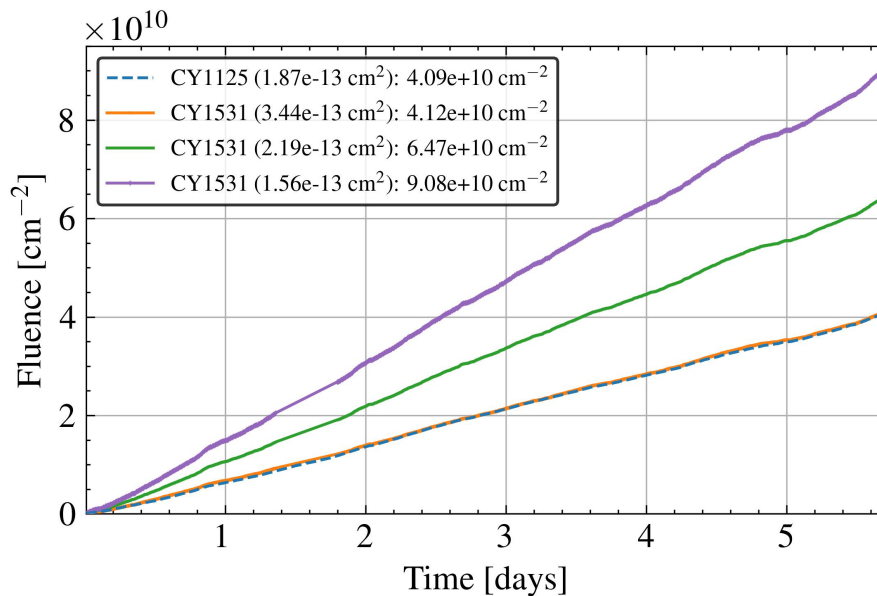


Figure 4.22: The HEH fluence measured for different cross-sections by the payload over time.

This figure shows there is quite some divergence between the different cross-sections. It can be seen that, the cross-section matching the best to the RadMon, is the one cross-calibrated at CHARM. Looking at the RPD over time in Figure 4.23, it can be seen that the RPD of the cross-calibrated cross-section in CHARM is close to 0% in difference. The PSI calibrated cross-sections are around 45% and 75% different relative to the RadMon, for the 2022 and the 2019 PSI cross-sections respectively. The difference

between the cross-section implies that there should be some type of verification for which cross-section use for the final payload data analysis, but for CHARM usage the highest cross-section is the most suitable. No matter which cross-section is chosen in the end, the space environment can still be compared to different positions in CHARM, if the same memory batch and cross-section are used for both analyses. This result also re-verifies the SRM-HEH-3 requirement of an accuracy better than 2.5% over a longer run.

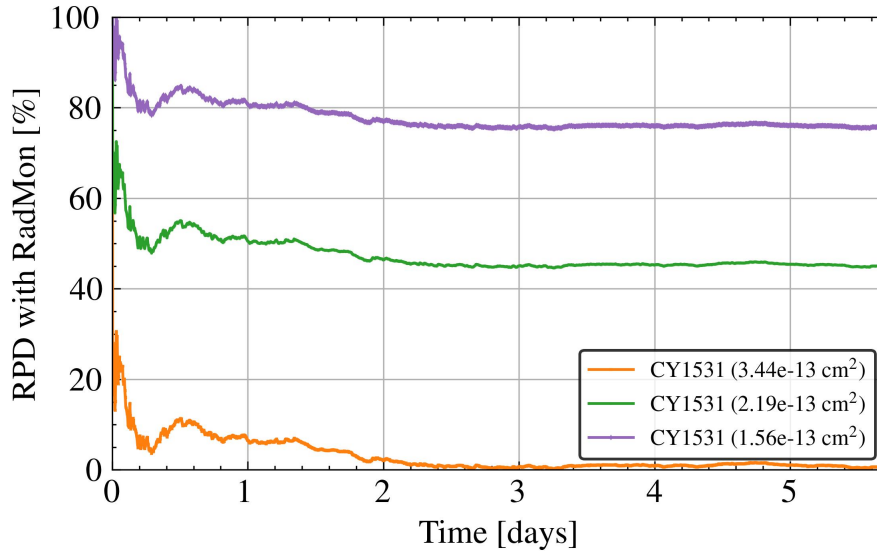


Figure 4.23: The RPD of the HEH fluence measured by the payload over time compared to the fluence measured by the RadMon V6.

One of the things left checking is the general TID data from the FGDOS, the recharges and the reconstruction. The TID measured by the FGDOS can be seen in Figure 4.24. The figure shows five lines in total. The blue-dotted line is the reference line coming from the RADFET on the RadMon. The other four lines are from the FGDOS sensor, with the difference being the sensitivity degradation compensation method. The purple and cyan lines have been compensated using the traditional compensation method, using the sensitivity degradation curve to compensate for the damages in the FGDOS due to radiation. The second compensation method is by characterizing the sensor using the first Gy the RADFET took. The sensitivity during this first Gy is taken as the initial sensitivity of the sensor, after which it is placed on that position of the sensitivity degradation curve. The data that was lost when the laptop was not logging during the Windows update, has been reconstructed using the recharges saved by the firmware update. This update worked extremely well, as the results are very compatible with the RADFET.

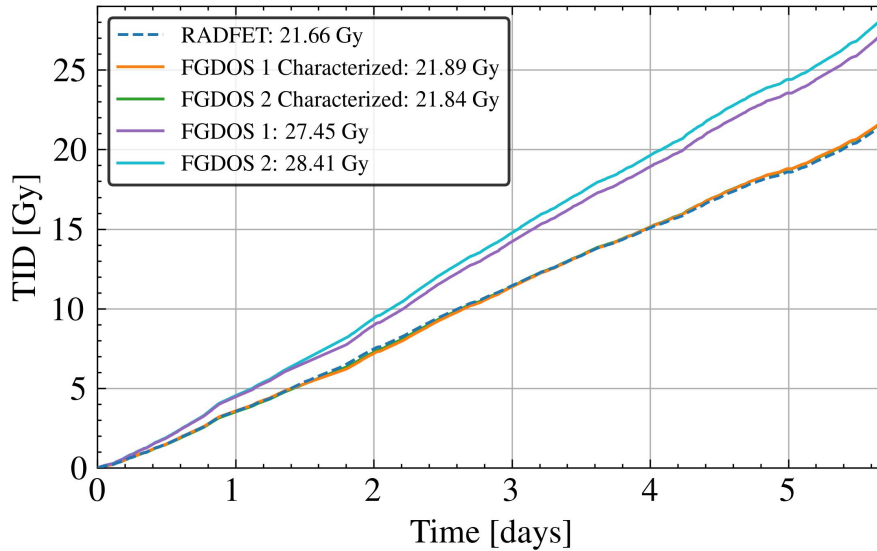


Figure 4.24: The TID measured by the payload over time.

The result of the compensation method is that, after 273 Gy and annealing effects, the traditional method is over-compensating the sensitivity of the FGDOS sensor. In contrast to the traditional compensation method, the characterized method shows a very good correspondence to the reference, for both FGDOS sensors in the chip. The RPD of the different methods can be seen in Figure 4.25.

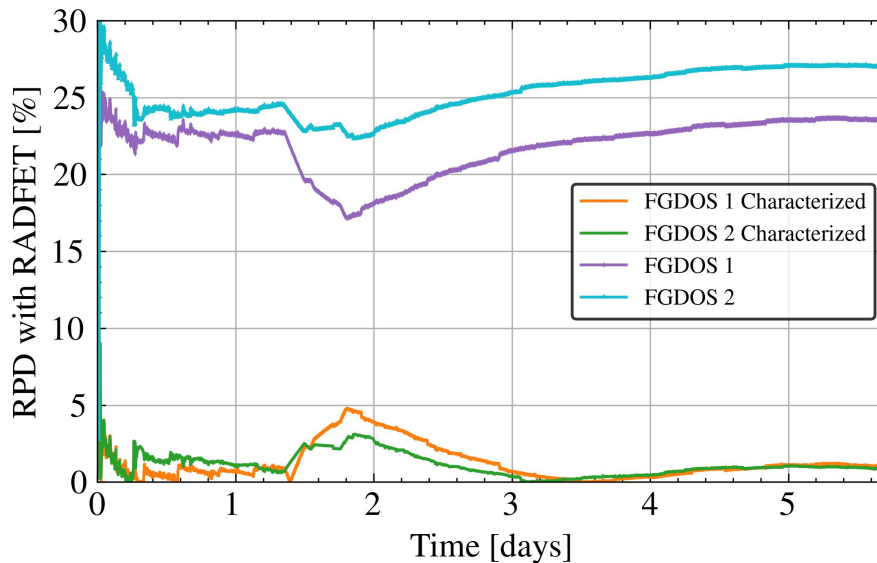


Figure 4.25: The RPD of the TID measured by the payload over time compared to the RadMon V6 RADFET.

As seen in this figure, there is quite a large difference in RPD between the two methods. The traditional methods shows a 23% to 27% RPD compared to the RADFET, with a difference of around 5% between the two FGDOS sensors in the chip. The characterized compensation method only shows a 1% RPD with the FGDOS sensors showing almost no difference. This latter method is well within the benchmark set in the SRM-FGD-3 requirement. When neglecting the factors of the TID received before the test and annealing in between runs, this would mean that characterizing the FGDOS is much more accurate. However, the difference are hypothesized to be smaller when irradiating the sensors from 0 Gy without stopping (similar to the space environment). For a space mission however, it will still be recommended to shortly characterize the FGDOS sensor on the flight model of the payload using a short ^{60}Co irradiation.

tion. This is recommended because also the initial sensitivities of the FGDOS can vary without having ever received radiation.

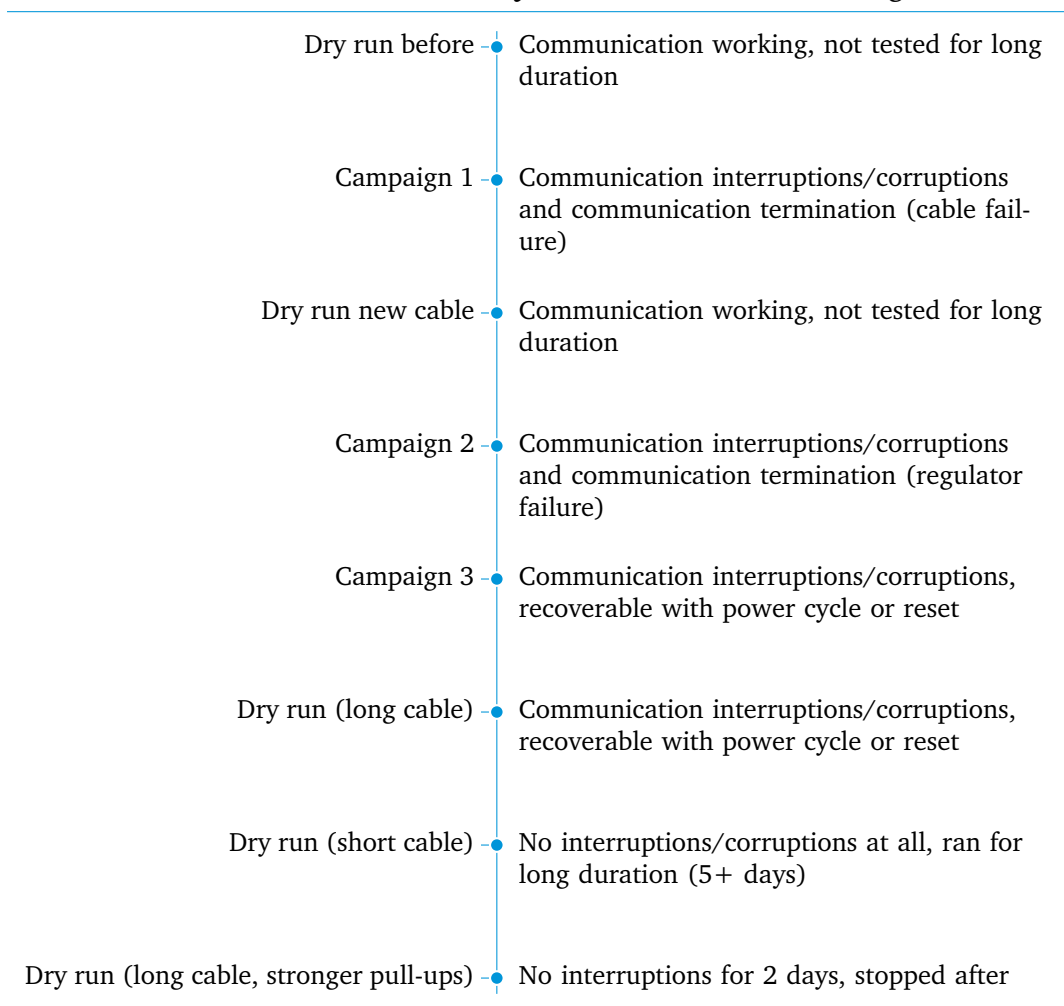
4.5. Payload Communication

As results of the three radiation test campaign, the goals for the system-level testing are now mainly completed. As the radiation testing has now come to an end, the 500 Gy requirement can never be reached again. This means the SRM-ENV-1 requirement needs to be further verified by means of analysis. During a previous test at the PIF in the PSI, the payload survived more than 500 Gy by a proton beam, meaning the requirement can still be verified with a caution. The payload also survived SEUs and did not show any SELs that were known of. This means that the SRM-ENV-2 is also partially verified with a caution. The one goal that remains is the payload communication and operation, that will be tested in this section. An updated list of the goals is seen below.

- Payload operation and communication: Requirements SRM-OPR-1 and SRM-OPR-2 are to be fully verified.

The communication of the payload has been tested using several dry runs in the CHARM facility with different configurations. One of the first things adjusted to check the communication was altering the master I2C settings in terms of frequency, as mentioned before. Using a lower frequency resulted already in an improved redundancy in communication over the long cable length in the facility. Another setting that improved the communication over the longer length was the reading interval, which was changed from 30 seconds the 5 minutes for the last test. The total testing timeline can be seen below:

TIMELINE 1: *Payload communication testing timeline.*



At the beginning of the testing, the cabling was tested in the preparation room in CHARM. During

these dry runs, the communication worked well without any problems, although the dry run was not conducted for a long time. During the first radiation campaign, there were some communication issues mainly related to the cable itself, as an older cable was used. There were some interruptions and corruption of the data, as seen in the text box below. The corrupted data is recognized by the incorrect CRC ("Wrong CRC") after the timestamp of the data.

```

2022-11-18 14:17:37 434 15552 15552 4597 0 3567 28.60 77864 49108 18 53404
33972 20 5941 75880 3306 1817 1867 1213 15477026

2022-11-18 14:22:40 434 36016 36016 4617 0 3635 28.70 77248 49108 18 52796
33972 20 5961 75868 3317 1815 2254 1211 15780046

2022-11-18 14:27:43 Wrong CRC - 434 56480 56480 4682 0 3730 29.00 76516
49108 18 52088 33972 20 12287 16777215 105598 105598 105598 105598 16083066

2022-11-18 14:32:46 434 11408 11408 4803 0 3796 29.00 76088 49108 18 51572
33972 20 6147 75860 3319 1814 916 1218 16386086

2022-11-18 14:37:49 434 31872 31872 4888 0 3845 29.00 75492 49108 18 50964
33972 20 6232 75812 3309 1811 1869 1214 16689105

```

To fix the issue, a new cable was developed and another dry run was done in the preparation room. The dry run worked again and also was not conducted for a long duration. During the second radiation campaign, there were some communication interruptions and corruptions again, now hypothesized to be related to the regulator failure. At the end of the second campaign, the communication was also completely terminated because of this failure. The third campaign, with the regulator now replaced, still had some interruptions and corruptions in the communication but much less than before and also could be re-established every time the communication was failing by doing a power cycle or a reset of the payload. To make sure these issues were not related to the radiation, the payload was tested in the same configuration without radiation. During this dry run, the exact same problems arose meaning it was not related to being irradiated. The payload was then moved to the buffer zone, to test the same communication using a shorter cable to check if the cable length was the cause of the issues. From this test was concluded that the length was indeed the problem, as there were no communication problems at all using the shorter cable. The test ran for more than 5 days, meaning it was very redundant with the shorter cable. This also excluded the possibility of the problems being related to the firmware. At the end, there was one more test using the longer cable with lower resistance (stronger) I2C pull-ups on the master side of the communication. This test gave promising results, with communication for 2 days straight without any problems. Unfortunately, the test set-up had to be removed from the facility after the 2 days because of the winter stop at CERN.

In conclusion for the communication and operation part of the payload, is that it is very redundant. The communication issue that arose during tested were not related to the payload, the firmware or the radiation damage at all. They were caused by the length of the I2C cabling in the facility. For future tests, it is proposed to use a so called 'I2C-Buffer', being developed at CERN in parallel to this project. If this device is not yet ready for use when the next test is conducted, an alternative would be to use the stronger I2C pull-up configuration of the cabling. This means that the SRM-OPR-1 and SRM-OPR-2 requirements can now be marked as fully verified.

4.6. Conclusions and Implications

The testing in CHARM was very important for gaining understanding on how the payload operated in a radiation environment, how redundant the payload is and how good the firmware and sensors of the payload are. After all the radiation campaigns and dry runs in the CHARM facility, most requirements were verified. An updated overview of the requirements can be seen in Table 4.4

Table 4.4: Requirements for the Space RadMon-NG payload that will be used for testing. The priority has been divided into essential (E) and conditional (C). The verification has been divided into Yes (Y), No (N). The asterisk means that it was not verified as a result of the test, but rather by analysis of previous tests and available data.

ID	Requirements	Priority	Verified?
SRM-HEH	The payload shall measure HEH fluence using a COTS SRAM	E	-
SRM-HEH-1	The payload shall be able to detect SEUs	E	Y
SRM-HEH-2	The payload shall have on-board burst detection for the Cypress SRAM	E	Y
SRM-HEH-3	The payload shall be able to measure the HEH fluence within 2.5% accuracy	C	Y
SRM-FGD	The payload shall measure TID using the FGDOS	E	-
SRM-FGD-1	The FGDOS shall have higher resolution than the RADFET	E	Y
SRM-FGD-2	The FGDOS measurements shall be temperature compensated	E	N
SRM-FGD-3	The payload shall be able to monitor the TID within 2.5% accuracy	C	N
SRM-ENV	The payload shall be able to withstand the space environment	E	-
SRM-ENV-1	The payload shall be able to withstand a TID of at least 500 Gy	E	Y*
SRM-ENV-2	The payload shall be able to withstand possible SEEs	E	Y*
SRM-OPR	The payload shall not have any operation problems	E	-
SRM-OPR-1	The payload shall have communication redundancy to the outside world	E	Y
SRM-OPR-2	The payload firmware shall perform what it is intended to do	E	Y

The firmware of the payload worked very well in during the tests and the sensors have the capability of being very accurate. The communication of the payload in the environment it will be operating in is also working well. There are two important remarks that can be taking from the testing results. One of the first is the characterization of the FGDOS sensitivity. The FGDOS gives a far better result when it is characterized compared to when it is not. The characterization should be done for the flight model by temporarily irradiating the device to gain the sensitivity. In the future, it might also be possible to self-characterize the FGDOS by relating the sensitivity of the sensor to the current consumption or the amount of time it takes the recharge the floating gate in the sensor. This topic still requires further investigation. The second remark for the test is related to the cross-section of the Cypress 1531 SRAM. It is not clear yet which cross-section is the best to use during the mission and it would be best to do a re-calibration or verification on what the cross-section actually is of the SRAM. If this is not possible, the sensor can still be used to compare the space environment in LEO to different CHARM positions, as long as the same SRAM with the same cross-section is used.

In the future, it would be interesting to do more tests in the CHARM facility. This should be done in the different positions available, so the environment in the positions can be compared to the environment encountered in space. This can in the end give an improved testing capability without over-estimation of the radiation environment, meaning that more COTS components could be accepted to be used in space. The study [20] suggested that the R5 position in CHARM has many similarities to LEO based on models. Using the actual data coming from the payload, the similarity of this position can be confirmed or an even better one could be found. When conducting these tests, it is important to use the 'I2C-Buffer' or the strong pull-up configuration for the cabling to the payload in the CHARM facility.

5

Floating Gate Dosimeter

The most important aspect allowing to make significant advances in space radiation monitoring, is the use of a sensor with a better resolution compared to previous ones. Previous missions have quite often used RADFET sensors, which have a resolution in the order of 10^{-1} Gy. The new payload developed by CERN will use the FGDOS, which as we have seen in the previous chapters has promising performances. As a matter of fact this sensor has a much better resolution which is in the order of 10^{-3} Gy, resulting in a significant increase in the accuracy of the measurements. This improved resolution was already verified in chapter 4. The FGDOS sensors on the payload are of great importance for the mission. A problem with the FGDOS sensors however, is that these sensors show some difference in behaviour after being exposed to radiation and temperature variations, as shown in subsection 2.3.4. There is some sensitivity degradation in the sensor due to receiving radiation, which needs to be compensated for. There is also an influence on the sensitivity because of temperature changes, since the read-out of the sensor is based on a current. This also needs to be compensated for to get proper measurements. For this purpose, a characterization test of the FGDOS sensors will be done where a custom experimental set-up is irradiated by a ^{60}Co source and experiences temperature variations simultaneously, similar to a space environment. One of the purposes of this test is to verify the SRM-FGD-2 and SRM-FGD-3 requirements. The other purpose is getting a deeper understanding on how the sensor will act while subjected to a space environment. The next section will explain the test in more detail and afterwards the results and implications will be discussed.

5.1. Temperature Characterization Test

This section will describe the test methodology, the set-up that will be used for the test and the test results. Throughout the chapter, the test results will also be discussed. The test plan was created after a careful literature study to select the temperature ranges applicable for space applications, which is explained in the next sub-section.

5.1.1. Background

As mentioned, for the development of the temperature characterization test, it is required to dive into some literature first to gain understanding for what and why the device is being tested, as well as to study what has been tested before. The basic principle of the FGDOS is the discharging of the FG which happens due to electron-hole pairs. The current induced from this discharging can be measured to relate it to a TID. One of the problems is however that a current is temperature dependent, meaning that compensation is required at certain temperatures. In addition, the FGDOS chip makes a conversion from current to frequency to facilitate an analogue to digital conversion of the dose value [46]. This frequency-current relation can be given by:

$$f_{osc} = \frac{I_d}{2 C \Delta V}, \quad (5.1)$$

meaning that the frequency is proportional to the current. The sensitivity of the output frequency due to temperature can then be given by:

$$S_T = \frac{\Delta f_{osc}}{\Delta T}, \quad (5.2)$$

where T is the temperature. According to the data sheet of the FGD-03F QFN chip by Sealicon, the operating ambient temperature range should range from $-40\text{ }^\circ\text{C}$ to $85\text{ }^\circ\text{C}$ [56]. The temperature dependence of current is induced by the resistivity of the material the current flows through that changes when the temperature is varying. The resistivity of a material with temperature dependence is given by:

$$\rho_T = \rho_0 (1 + \alpha (T - T_0)), \quad (5.3)$$

where ρ_T the resistivity at temperature T , ρ_0 is the resistivity at equilibrium temperature, T_0 the reference temperature and α is the temperature coefficient of resistivity. The resistance due to the resistivity of a material can be determined by:

$$R = \frac{\rho_T L}{A}, \quad (5.4)$$

where R is the resistance, L is the length and A is the area of the cross-section. Using Ohm's law, the current can then be expressed using the temperature as follows:

$$I = \frac{V A}{L \rho_0 (1 + \alpha (T - T_0))}. \quad (5.5)$$

Additionally to the temperature dependence of the drain current, there is another FGDOS principle that is temperature dependent. This is the creation of electron-hole pairs. According to [6], average energy consumed by the creation of electron-hole pairs varies significantly with temperature. As example, at a temperature of 343 K it only takes around 88% of the energy it does to create an electron-hole pair compared to at a temperature of 261 K . This is taken on average for $\text{Al}_{0.8}\text{Ga}_{0.2}\text{As}$. It means that a higher temperature would yield a higher dose measured due to the thermal excitation of the atoms in the semiconductor materials compared to a lower temperature with the same amount of particles and energies. To put this quantitatively, the equation for the voltage variation related to dose can be used:

$$\Delta V = \frac{q(1 - R(\epsilon)) \rho_{ox} t_{ox}^2 D}{\epsilon W_{e-h}}. \quad (5.6)$$

The W_{e-h} parameter represents the energy needed to create an electron-hole pair. When this energy needed goes down for higher temperatures and the voltage variation stays the same, the results is measuring a higher dose than is actually received. This means it will be important to test with both temperature variations and radiation simultaneously, to characterize the sensitivity of the FGDOS chip with both mechanisms, so that there can be compensated for both afterwards.

The state-of-the-art FG temperature tests have already been described in subsection 2.3.4. According to the Figure 2.27 and Figure 2.28 in that section, it shows that the frequency has an inverse relation with temperature and thus also with the drain current. The sensitivity of the FGDOS chip increases negatively with decreasing temperatures, meaning it gets more sensitive. This phenomena requires some form of compensation and since the response can vary per batch, a new characterisation is needed. The authors of [22] researched the temperature dependency of the FGDOS chip in the low sensitivity and the high sensitivity configurations. They found that the sensor shows a higher error for lower temperatures and the high sensitivity configuration shows the biggest error generally. This study was however only done on a temperature range from $20\text{ }^\circ\text{C}$ up until $40\text{ }^\circ\text{C}$. The largest temperature range found was in [14] and it ranged from $10\text{ }^\circ\text{C}$ to $85\text{ }^\circ\text{C}$.

The temperature variations that can be encountered in a space environment vary a lot. For this test, mainly the temperature variations for general electronics on-board satellites in LEO will be considered. According to [51], general electronics in spacecraft can experience an operating temperature range of $-10\text{ }^\circ\text{C}$ to $45\text{ }^\circ\text{C}$. The temperature these electronics need to be able to survive range from $-30\text{ }^\circ\text{C}$ to $60\text{ }^\circ\text{C}$. A typical temperature profile of the electronics on-board a LEO satellite will usually range from around $8\text{ }^\circ\text{C}$ up to around $30\text{ }^\circ\text{C}$ [60] [40]. The temperature on-board the CELESTA mission, a mission currently in operation by CERN, was also analyzed using the payload data. This mission in a higher

orbit than LEO, with the satellite having an altitude of around 5850 km above the Earth surface. The minimum temperature reached on-board CELESTA was determined to be 7.0800 °C and the maximum temperature was 17.471 °C. In a mission by NASA in GEO, the temperature range experiences was from -20 °C to 60 °C [1]. An overview of all the temperature ranges can be seen in Table 5.1.

Table 5.1: Various temperature ranges that can be encountered in space.

Source	Lowest temperature	Highest temperature
Literature survival	-30 °C	60 °C
GOES NOP (GEO, NASA)	-20 °C	60 °C
Literature operation	-10 °C	45 °C
CELESTA (MEO)	7.0800 °C	17.471 °C
General LEO	~8 °C	~30 °C
Measured LEO	~8 °C	~30 °C

Based on the state-of-the-art and what is necessary for the payload, the following items are proposed for the test:

- The FGDOS chip under irradiation of a ^{60}Co source.
- The FGDOS settings will be similar to the Space RadMon-NG FGDOS settings in term of target, threshold and sensitivity.
- A test in the temperature range of -10 °C to 45 °C.
- A sinusoidal temperature profile created using a Peltier module which is current-controlled by a PSU.

The next sub-section will show the set-up that will be used to achieve this desired test and how the results will be measured.

5.1.2. Set-up

The test set-up will consist out of a sensor board, thermal regulator, a PSU, an Arduino feather M0, a laptop and cabling. The FGDOS on the sensor board is set to active mode. Active mode was chosen instead of passive mode, because the sensor requires less configuration. It is also more redundant when there are communication issues, since the sensor will still be recharged and stay in the linear region. The extra consumed power for the test is not a problem, as it is connected to a PSU. Next to the formal set-up, an identical control board will be used together with another control device in passive mode as verification. The thermal regulator is made from a Peltier module, thermal pads and a fan with heat sink. The Peltier module is then connected to the PSU, which gives a variable output over time controlled by a Python script on the laptop. This is possible because the PSU has an Ethernet connection and can be accessed and controlled through the laptop using this connection. A schematic of the test set-up is seen in Figure 5.1.

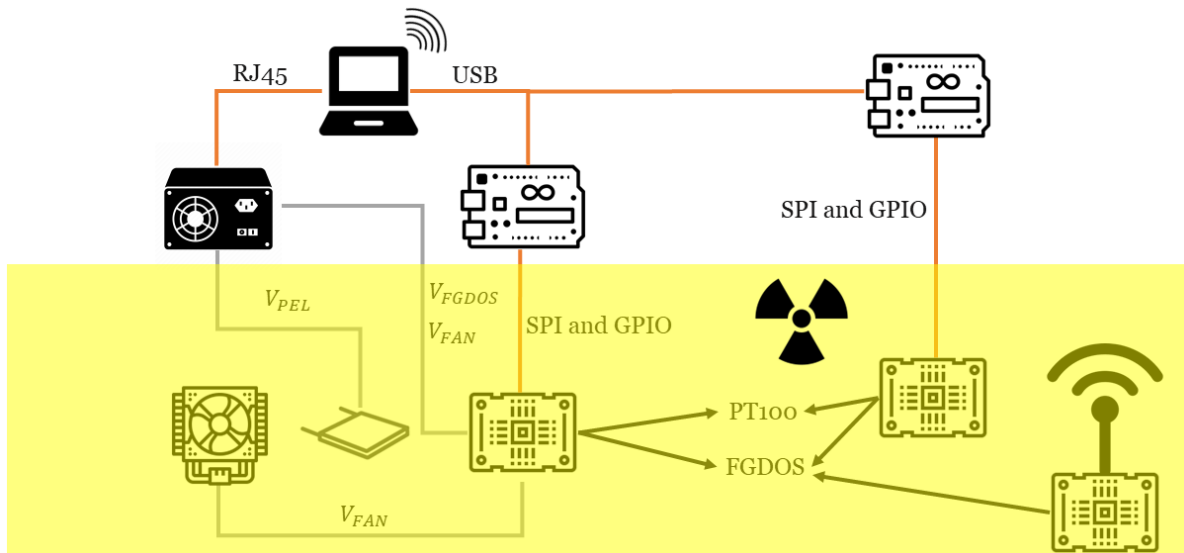
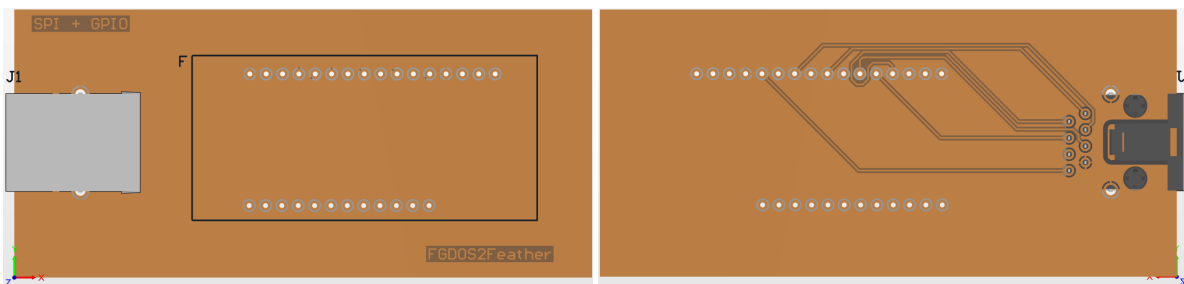


Figure 5.1: Schematic of the test set-up that will be used for the FGDOS sensitivity test.

The sensor board consist out of one FGDOS chip, a temperature sensor which is a thermistor (PT100), an oscillator for the FGDOS and connectors for power and communication. The sensor board has an SPI connection with the Arduino M0 as master, which will be outside of the radiation zone. As mentioned, the Peltier module will be attached to the back of the sensor board using a thermal pad and there will be a heat sink on the other side of the Peltier module. A reversed voltage will be used to be able to heat and cool using the Peltier module using only one side. All the sensor information is then read out by the Arduino and logged on a laptop using CoolTerm. This data can then be analyzed after the test.

The PCBs for the testing have been designed in Altium. One PCB was created for the interfacing of the Arduino with the sensor board through SPI (FGDOS chips) and an analogue signal (PT100 voltage). The PCB consists out of a shield where the Arduino can be placed and an Ethernet connector. There are six signals going to the connector, which are the SCK signal, the MOSI signal, the MISO signal, two CS signals and the temperature voltage signal. There is one additional cable and pin used for ground. The Arduino on this PCB can be connected to a laptop by using the common micro-USB cable. The PCB view the Arduino shield can be seen in Figure 5.2.



(a) Top view of the Arduino Feather M0 SPI shield PCB.

(b) Bottom view of the Arduino Feather M0 SPI shield PCB.

Figure 5.2: Design of the the Arduino Feather M0 SPI shield PCB.

The sensor board runs on a 5 V supply voltage and can be seen in Figure 5.3. The board also contains various pull-up resistors for some of the signals, a number of voltage decoupling capacitors for the voltage inputs, an oscillator for the desired clock speed and connectors. One of these connectors is a voltage connector for the fan on the back of the board. On the backside of this PCB, the Peltier module will be placed. The Peltier module will be attached using thermal pads, which will fit over a bigger region than the FGDOS chip and the temperature sensor take up. Since these are all Surface Mount

Device (SMD) components, it is hypothesized that they will reach a very similar temperature. Internally in the FGDOS chip is also a temperature sensor, which will be used to check the value given by the thermistor and to average the temperature measurements. This board schematic is the second working version of the test board, designed for the second testing campaign which unfortunately did not happen due to time constraints. During the first campaign, the first version of the test board was used, with the only difference being the placement of the PT100.

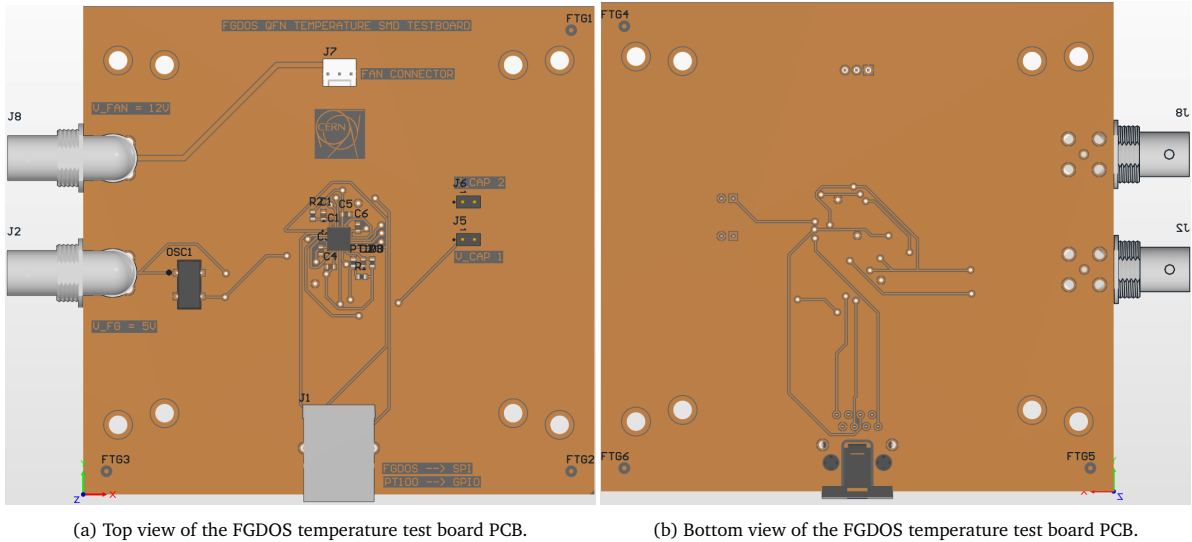


Figure 5.3: Design of the FGDOS temperature test board PCB version 2.

The PSU will be connected to both the Peltier module and the FGDOS test board. As mentioned, the FGDOS test board requires a 5 V supply voltage. Additionally, there is a connector for 12 V on the board which will be sent to another connector for the fan. For the temperature regulator to work, the current-temperature relation of the Peltier module needs to be calibrated. The result of this calibration can be seen in Figure 5.4, where the temperature is plotted against the current. Note that a negative current means a polarity switch of the voltage. The calibration was performed by applying a certain current and measuring the temperature. This was repeated for multiple currents and afterwards checked for repeatability. The data was then interpolated and subsequently filtered, to create a smooth look-up table where the appropriate current can be found based on a temperature reference, which will in this case be a sinus wave.

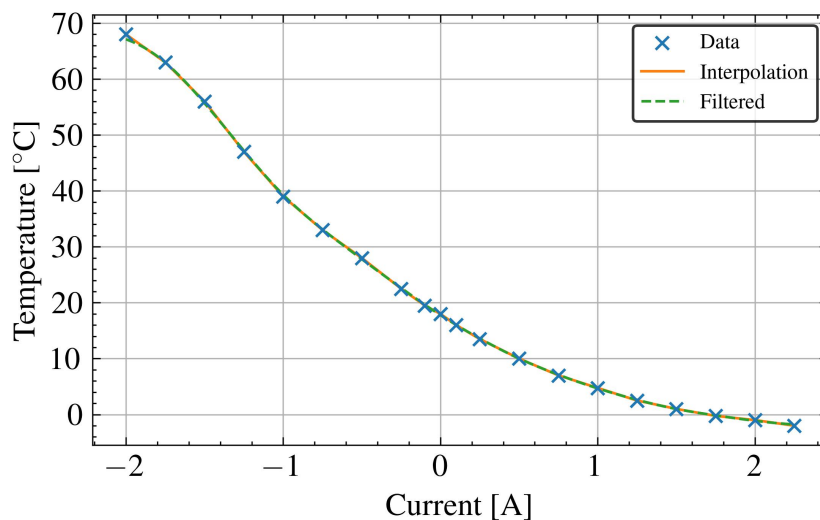


Figure 5.4: Calibration curve of the thermal regulator to be used during the FGDOS temperature compensation experiments.

The final goal of the test is to analyze the influence of temperature variations on the temperature coefficient of the sensor, check if there is an influence on the sensitivity degradation of the sensor and study the best method for temperature compensation to a varying temperature profile. The system engineering goal is to verify the SRM-FGD-2 and SRM-FGD-3 requirements.

5.1.3. Dry Run Testing and Characterization

The test set-up was tested without radiation in the section laboratory available at CERN. Figure 5.5 shows the dry run set-up with the board in the middle, one of the control devices next to it, the cabling, the Arduino M0 and the laptop. This dry run set-up was used to perform the Peltier calibration and afterwards to check the sinusoidal temperature profile. The initial temperature profile used was:

$$T = 27.5 \sin\left(\frac{2\pi}{6000}t - \frac{\pi}{11}\right) + \frac{45 - 10}{2} \quad (5.7)$$

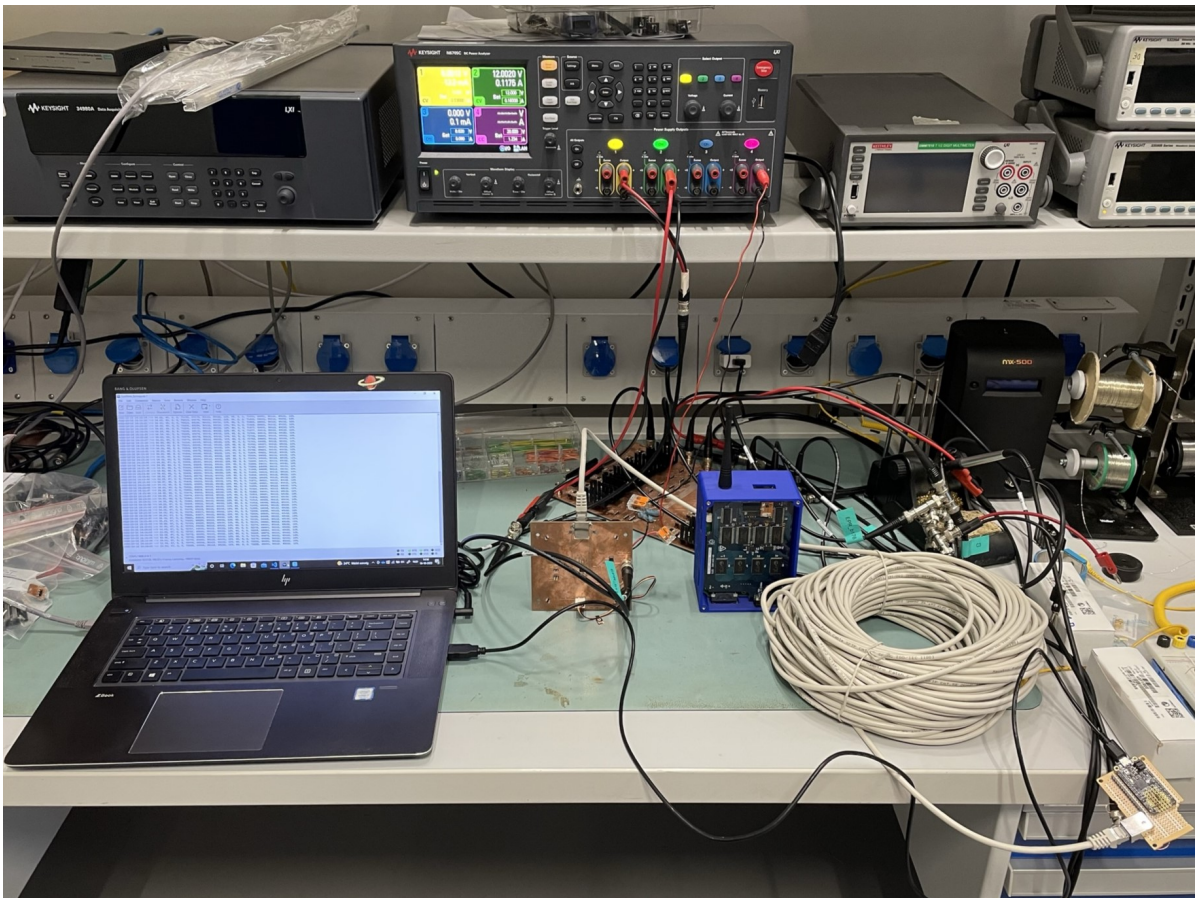


Figure 5.5: The set-up of the FGDS testing used for the dry runs in the CERN BE-CEM-EPR laboratory.

During the dry testing of the set-up, the temperature profile resulted in one major problem: condensation on the board. This condensation can be seen in Figure 5.6. This condensation happened every time the board was heating up from its minimum temperature in the temperature profile. For the time being, it was decided to still try the same temperature profile under irradiation, but if the condensation results in failures the temperature profile can be adjusted.

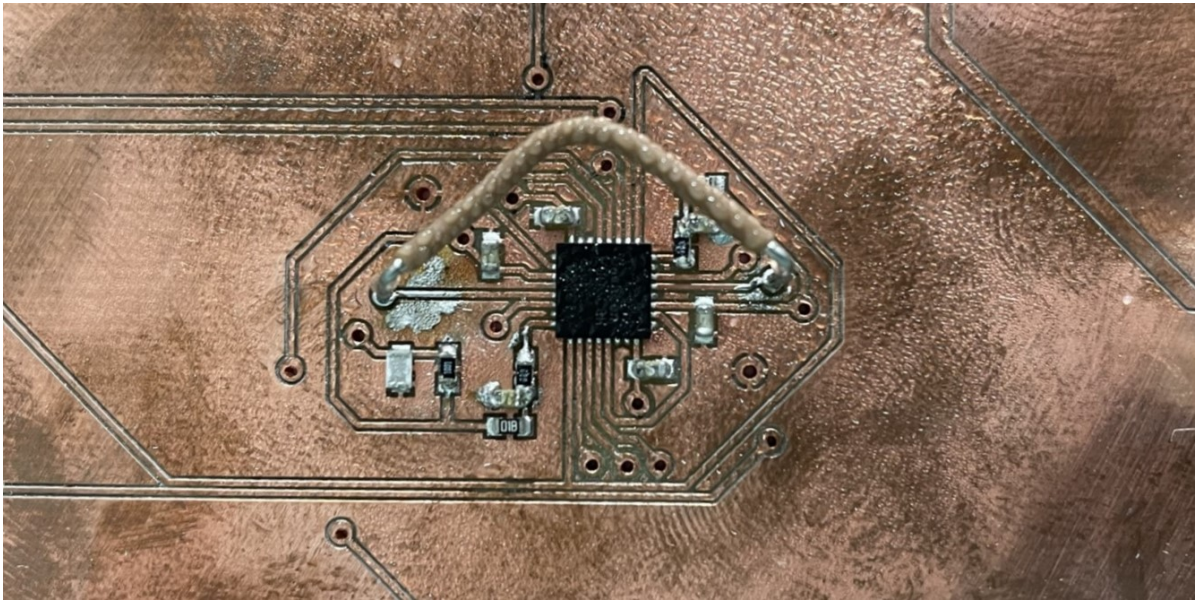


Figure 5.6: The condensation on the FGDOS test PCB during the heating up from below 0°C.

The dry tests were also useful to characterize the sensors. This was done by cooling and heating up the devices slowly (not using the temperature profile but manually) and measuring the sensor frequency, reference frequency and temperature. The results of the characterization in the dry run can be seen in Figure 5.7 and Figure 5.8. Figure 5.7 shows the sensor frequency against the reference frequency. This characterization can be used for temperature compensation based on the reference frequency. It is compensated by setting a base reference frequency and determining the difference at another temperature. From the difference in reference frequency, the required compensation in the sensor frequency can be determined using a linear fit through the characterized data.

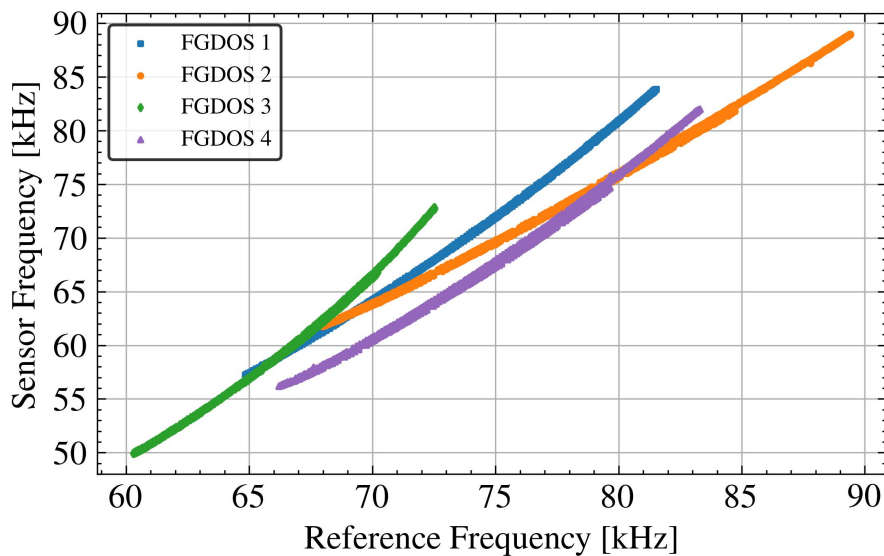


Figure 5.7: Sensor frequency against the reference frequency from the twin NMOS during the dry run.

Figure 5.8 shows the sensor frequency against temperature. This characterization can be used to compensate for temperature variations in the actual test with the temperature coefficient. This compensation is done by setting a base temperature and determining the sensor frequency difference with the actual temperature. The difference is then determined based on a linear fit through this characterized data.

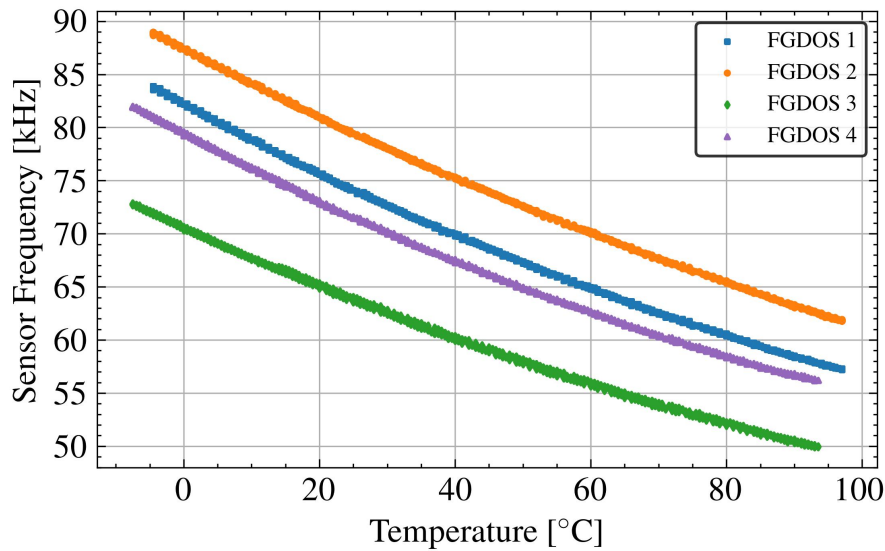


Figure 5.8: Sensor frequency against the temperature during the dry run.

One other phenomenon that was observed during the dry run was a thermally induced recharge, as shown in Figure 5.9. When the sensor frequency is close to the threshold and the temperature rises, the sensor frequency will go down further. It can eventually reach the threshold and recharge the sensor, while there is no radiation. When the temperature drops again to its nominal value, the sensor frequency goes back up to above the target.

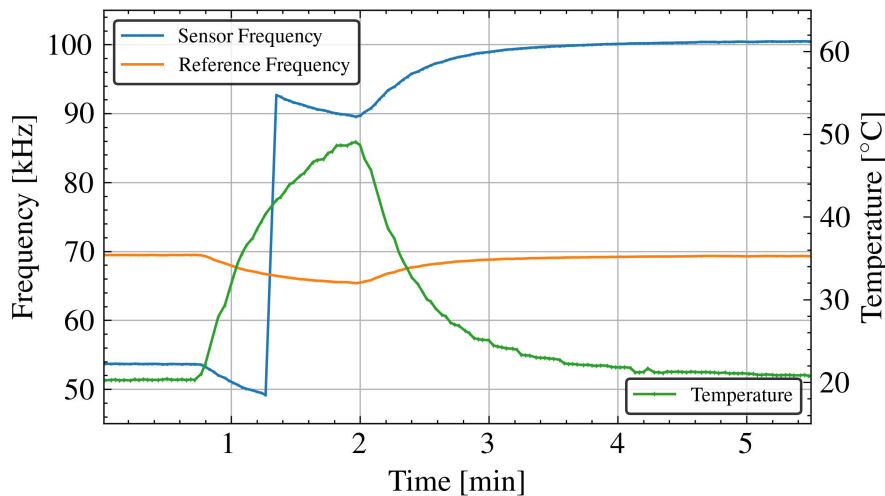


Figure 5.9: Sensor frequency, reference frequency and temperature over time during the dry run with an induced recharge.

This has some implications for usage of the sensor, with the most important one being a possibility of going outside the linear region of the sensor. A solution to this problem could be to use the sensor in passive mode and have on-board temperature compensation. The actual frequency can then be checked before a recharge is initiated.

5.1.4. Cobalt-60 Thermal Radiation Testing

The radiation testing was done using a ^{60}Co source in the designated test facility at CERN. The test set-up of the test board and control boards can be seen in Figure 5.10, where the identical control board in active mode is on the left-hand side, the control board in passive mode is at the center and the test board in active mode undergoing the temperature variations is on the right-hand side.

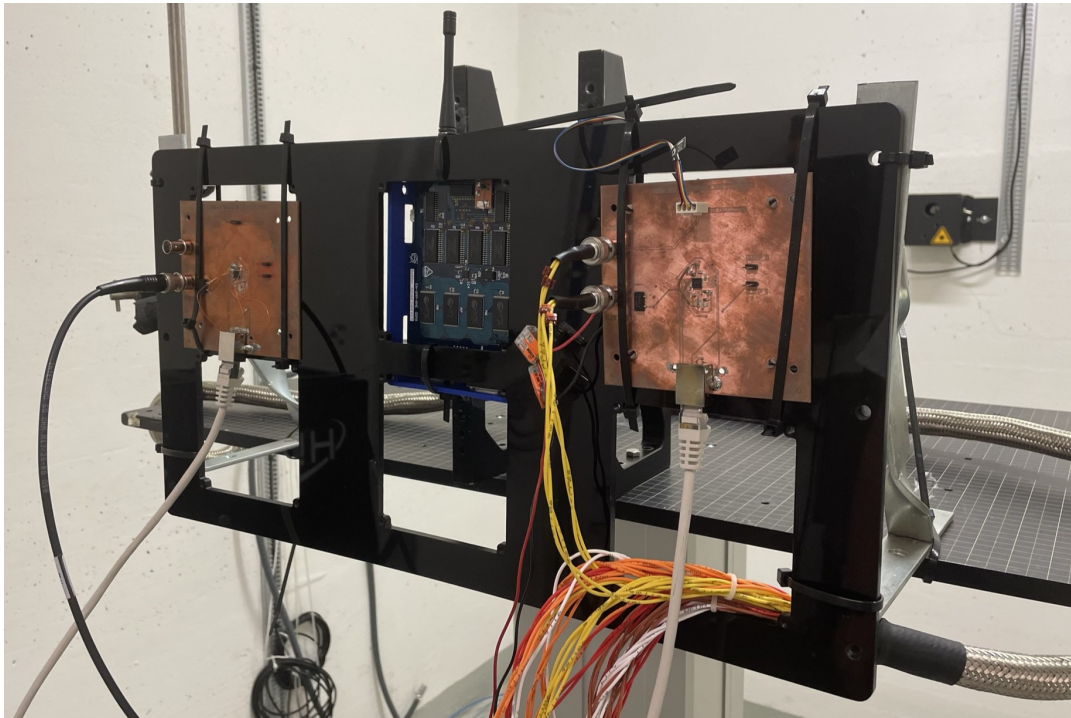
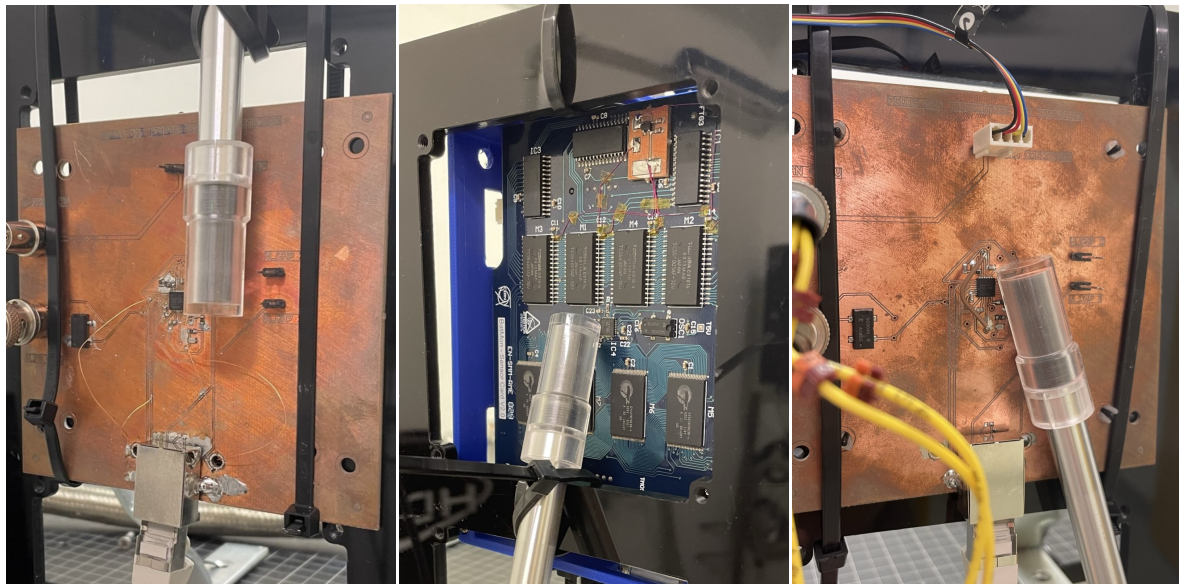


Figure 5.10: The set-up of the FGDOS testing used for the dry runs.

Each of the sensors on the boards have been carefully calibrated using an ionization chamber. The calibration for each sensor can be seen in Figure 5.11. The dose rates determined are: 1.543 mGy/s for the active control board, 1.527 mGy/s for the passive control board and 1.538 mGy/s for the active test board. These dose rates were chosen since it will result in a significant dosage in the time frame available, while not over saturating the sensor measurements in the sense that the temperature variations are barely visible.



(a) Ionization chamber calibration for the active control board, resulting in dose rate of 1.543 mGy/s. (b) Ionization chamber calibration for the passive control board, resulting in dose rate of 1.527 mGy/s. (c) Ionization chamber calibration for the active test board, resulting in dose rate of 1.538 mGy/s.

Figure 5.11: Calibrations using the ionization chamber of the dose rate on the active control board (left), passive control board (center) and active test board (right).

During the radiation campaign, multiple runs have been performed. The timeline of these runs can be seen in Figure 5.12. When the set-up was installed, there was first of all a problem with the SPI connection and the cable length. This was able to be resolved by lowering the SPI clock frequency. In the first run, two issues were encountered. The first one being that the target and threshold were not correctly configured, meaning the sensor was sometimes operating outside of the linear region. The second issue was the condensation, which was also seen during the dry testing. The condensation resulted in some corrupted data when heating up and could not be used. In the second run, one of the two FGDOS sensors was always stuck in a recharge. It is hypothesized that a shortage because of the condensation is the cause of this problem. The temperature profile was shifted up slightly in this run, but there was still condensation on the board. In the third run, a temperature profile was used without cooling. The focus was shifted towards the temperature variations instead of the actual minimum and maximum temperature. The new temperature profile used is given by:

$$T = 20 \sin\left(\frac{2\pi}{6000}t - \frac{\pi}{12}\right) + \frac{65 + 25}{2}. \quad (5.8)$$

During this run there were no problems encountered at all. The fourth and final run was identical to the third run, but ran for a much longer time to get more data. Up until the start of this fourth run, a total amount of 82.5 Gy was received by the boards. This is also the run where the analysis will focus on. There was an attempt for a fifth run, but unfortunately the FGDOS chips both failed when a power cycle was performed, possibly because of the radiation it had received and the annealing that took place in the long time between the two tests.

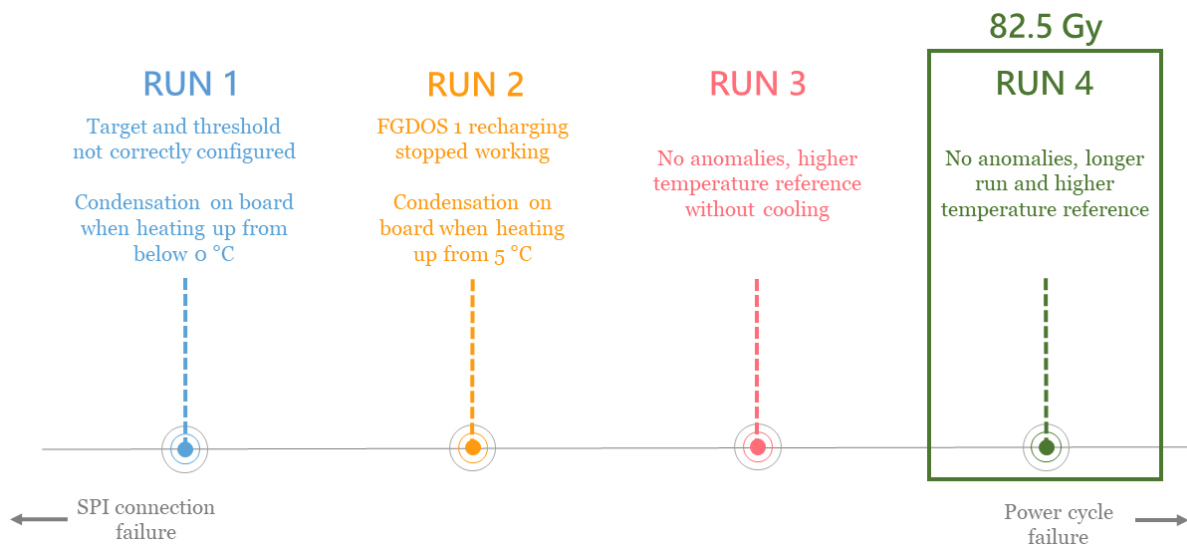


Figure 5.12: The ^{60}Co testing timeline of the FGDOS. At the start of the final run, the board received a total amount of 82.5 Gy.

The temperature profiles of the active test board and active control board are shown in Figure 5.13, where it can be seen that the active test board was following the reference temperature profile very nicely, while the active control board stayed about constant in temperature. There is a slight change, but the test had a duration of 23 hours and 20 minutes, meaning this temperature shift can be explained by the environmental temperature shift. The test done consisted of a total of 14 periods, or so called artificial 'orbits'. The total TID received was around 130 Gy, the maximum temperature reached was 67 °C and the minimum temperature reached was 24 °C.

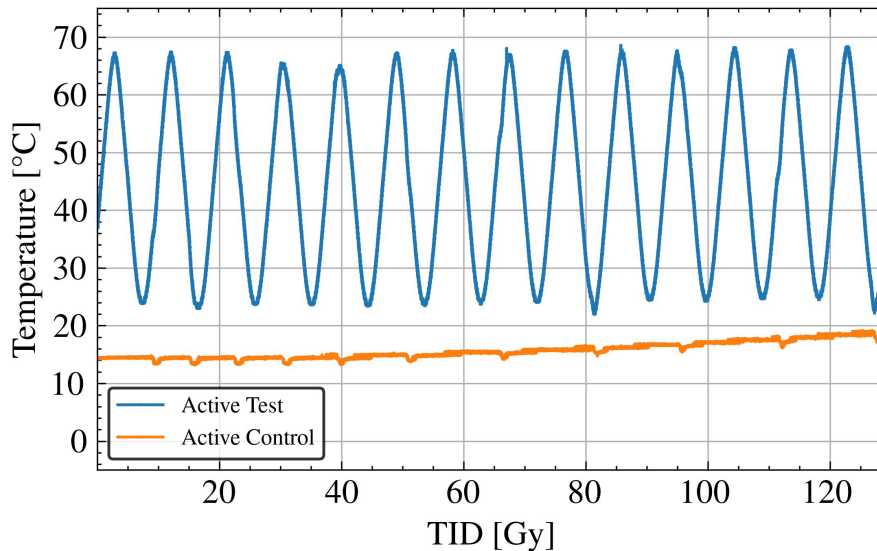


Figure 5.13: Sensor frequency, reference frequency and temperature over time during the dry run with an induced recharge.

5.2. Results

This section will discuss the results of the test with the FGDOS in the ^{60}Co facility. As mentioned before, there will be focused on three main topics: evolution of the the temperature coefficient, sensitivity degradation and temperature compensation. Additionally, the SRM-FGD-2 and SRM-FGD-3 requirements will be kept in mind during the analysis. The results will be discussed in separate subsections.

5.2.1. Temperate Coefficient Evolution

The first topic studied during this test was the evolution of the temperature coefficient. The temperature coefficient can be defined as a change in a physical quantity divided by a change in temperature, in this case given by the following equation:

$$S_T = \frac{\Delta f}{\Delta T}. \quad (5.9)$$

This equation takes the sensor frequency as the physical quantity and divides it by the difference in temperature. Applying the equation to the test data and plotting the results, gives the plot that can be seen in Figure 5.14.

The figure shows the temperature coefficient plotted over the temperature. The data shows very symmetrical behaviour for both increasing and decreasing temperatures, meaning that the temperature itself does not affect the temperature coefficient of the FGDOS. At the minimum and maximum temperatures, the temperature coefficient goes up exponentially. This is caused by the temperature profile used where the change in temperature is much smaller near the minimum and maximum temperatures. In the middle region from 35 °C to 55 °C, the temperature coefficient stays relatively constant around $\pm 3 \text{ kHz}/^\circ\text{C}$.

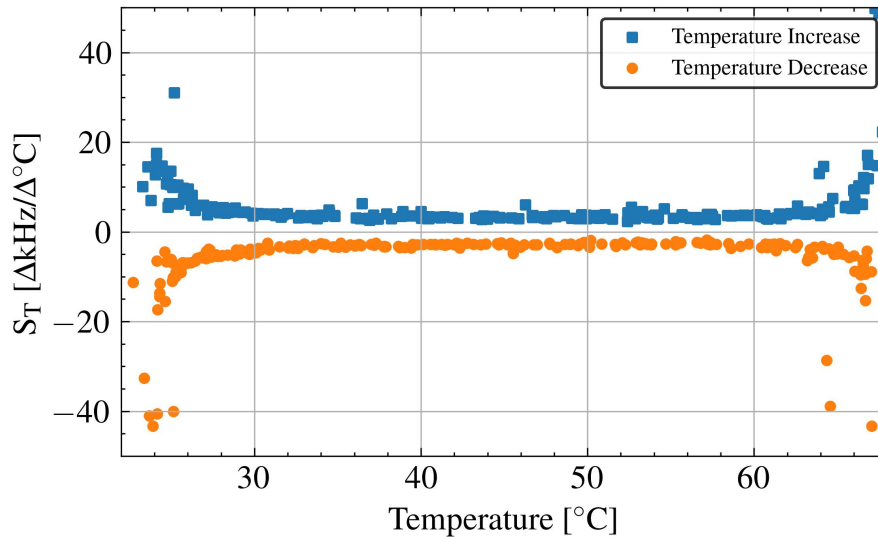


Figure 5.14: Temperature sensitivity of the sensor over the temperature, split up in increasing and decreasing temperatures while being irradiated.

To check the evolution of the temperature coefficient over the TID, the data needs to be filtered slightly. The filtering of the data is done by looking at the 40 °C to the 50 °C region, which is then plotted over dose. This can be seen in Figure 5.15. The data shows the temperature coefficient evolution over dose, with the 2- σ confidence intervals and a linear fit. From this data can be concluded that there is no change in the temperature coefficient over TID in the FGDS. The temperature increase data is straight and the temperature decrease data changes slightly. This can however also be caused by the sensitivity degradation or the lack of more data. The repeatability of this data could be verified in a next study, as due to time constraints it was not possible to conduct the test twice.

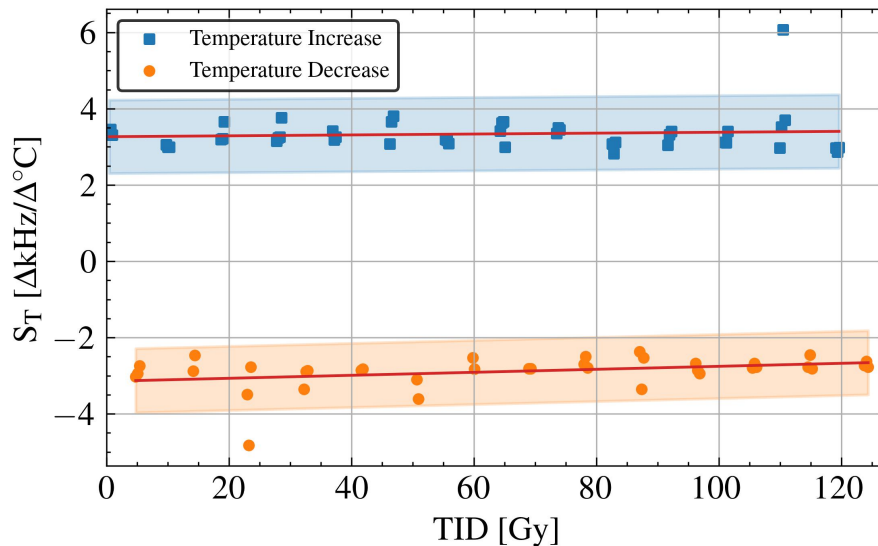


Figure 5.15: The temperature coefficient evolution over the TID received of the flat region between 40°C and 50°C, both for increasing and decreasing temperatures.

5.2.2. Sensitivity Degradation

The second important topic studied is the sensitivity degradation. One of the reasons why this is topic is important is that the compensation for the sensitivity degradation must be applied very carefully. The individual sensors can vary in initial sensitivity and need to be compensated for this accordingly.

It was hypothesized that when the FGDOS is subjected to a constantly varying temperature profile, the sensitivity degradation might be enhanced compared to the usual operation environments with relatively steady temperatures. To test this hypothesis, the sensitivity was determined for the FGDOS sensors based on the ionization chambers in the calibration. The sensitivity is given by the change sensor frequency divided by the change in dose as follows:

$$S_D = \frac{\Delta f}{\Delta D}. \quad (5.10)$$

Plotting the sensitivity of the TID received results in the data that can be seen in Figure 5.16. This figure shows the sensitivity of the three FGDOS sensors after the initial 82.5 Gy reached in previous tests. It is seen that active and passive control board have a very similar sensitivity. The sensitivity of the test board is 'artificially' altered, since the temperature changes alter the sensitivity. When the temperature rises, the FGDOS becomes more sensitive since the frequency goes down due to radiation and temperature. When the temperature decreases, the FGDOS becomes less sensitive because frequency goes up due to temperature but then down because of the radiation. In the end, this results in the wave-like signal which can be seen in the figure.

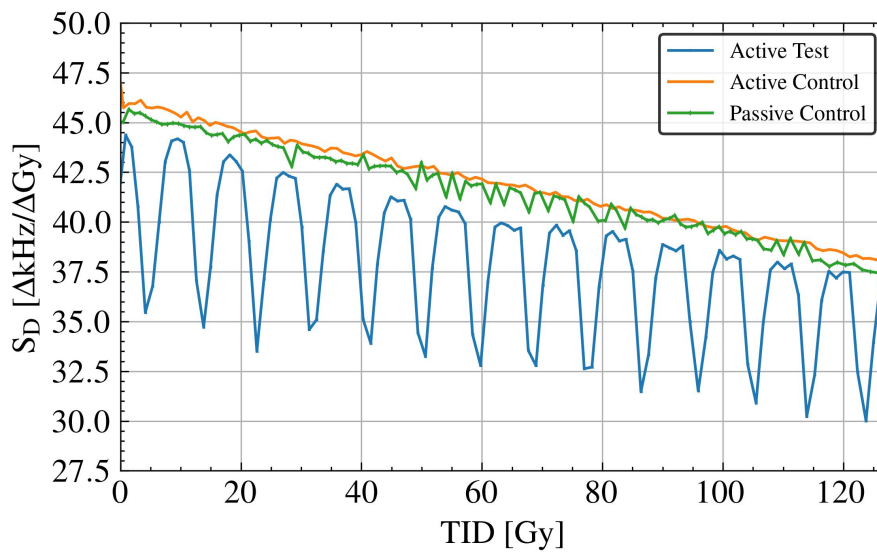


Figure 5.16: Sensitivity degradation of the sensor over the TID for the different boards. Note that the actual starting TID is 82.5 Gy and not 0 Gy.

The FGDOS sensors do have different sensitivities after the initial 82.5 Gy. An overview of these sensitivities can be seen in Table 5.2.

Table 5.2: Sensitivities of the FGDOS sensors at the start of the temperature characterization test.

Active Test	Active Control	Passive Control
42 kHz/Gy	47 kHz/Gy	45 kHz/Gy

The results of the comparison of the sensitivities obtained in this work and the ones obtained in [69] (see Figure 2.25) can be seen in Figure 5.17. These curves have also been plotted from 82.5 Gy onwards. This plot shows the same sensitivity degradation curves from the studies done with and without temperature variations. On top of that, it can be seen that the evolution of all the sensitivity curves over the TID are very similar, ignoring the oscillations of the test board and focusing on the trend of the curve.

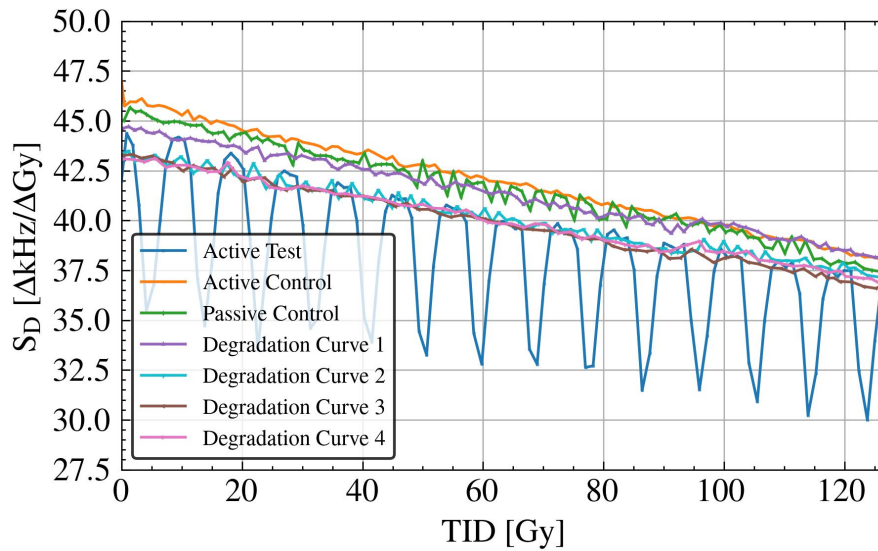


Figure 5.17: Sensitivity degradation of the sensor over the TID for the different boards with degradation results from former tests as verification. Note that the actual starting TID is 82.5 Gy and not 0 Gy.

Usually, when compensating for the sensitivity degradation, the third degradation curve is used. This one is taken as main reference and compared to the ones from the temperature test. The result in terms of RPD can be seen in Figure 5.18. The figure shows that the both control boards have a RPD of around 5% and stay constant around this value during the whole test. The test board shows variations as already discussed before, ranging from 0% to around 22% maximum. Throughout the whole test, the RPD of the test board does not seem to change due to dose and temperature variation received.

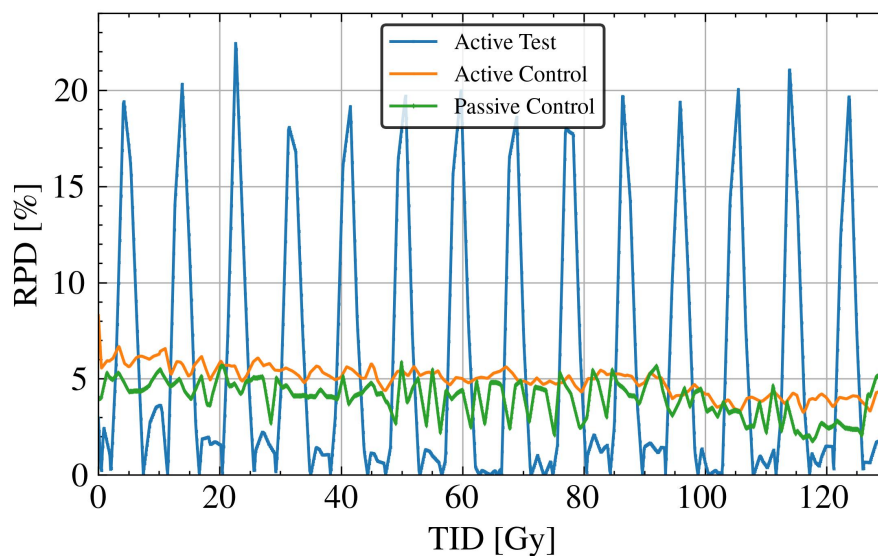


Figure 5.18: Relative percentage difference of the sensitivity degradation of the boards tested at ^{60}Co and one of the former degradation curves. Note that the actual starting TID is 82.5 Gy and not 0 Gy.

From these results for the sensitivity degradation, there can be concluded that they are very compatible with previous sensitivity degradation tests and that temperature variations do not have any influence on the sensitivity degradation.

5.2.3. Total Ionizing Dose Compensation

The last topic of the test is the study of the compensation method of the TID subjected to the continuously varying temperature. This also related to the SRM-FGD-2 requirement. There are two methods of compensation as already explained before, one is based on the twin MOSFET which is not susceptible to radiation giving a reference frequency and the other method is using the temperature coefficient. The characterization of the FGDOS sensors was done in the dry run and can now be used for the compensation. First of all, the reference frequency output can be checked to see if it is in accordance with what is expected. The reference frequency of all the DUTs can be seen Figure 5.19. As expected, the active test board shows a sinusoidal profile while the control boards stay rather constant over dose. The down shift of the control boards can be explained by the environmental temperature changing, as the test took 23 hours and 20 minutes in total. The reference frequency can vary between sensors as the twin MOSFET is neither charged or discharged.

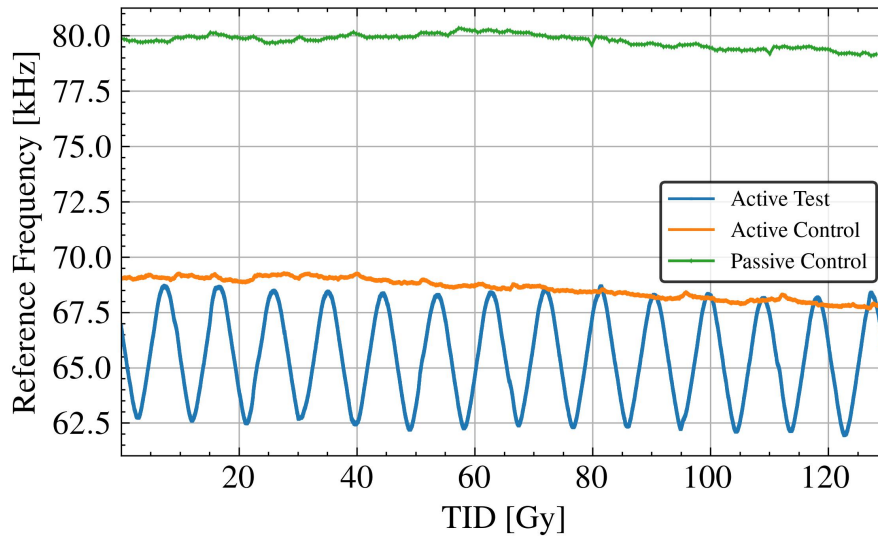


Figure 5.19: Reference frequency of the twin NMOS in the FGDOS that can be used to analyze the influence of the temperature variations without any TID influence. Note that the actual starting TID is 82.5 Gy and not 0 Gy.

From the test data, the dose was determined without any temperature compensation performed. There was sensitivity degradation used based on the initial sensitivity of each FGDOS sensor. This means that the degradation curve was taken and the FGDOS was placed on the curve where the sensitivity was at that point in time. The TID results of the test with only sensitivity degradation compensation can be seen in Figure 5.20 where they are compared to their respective ionization chamber. As seen in the figure, all lines are very close due to the dose rates used. The active test board has a final difference of around 4.34 Gy, the active control board a final difference of around 2.92 Gy and the passive control board a final difference of 2.26 Gy. The difference in final dose is around 67.6% bigger than the average of the control boards, meaning the temperature variations are certainly affecting the TID measurements.

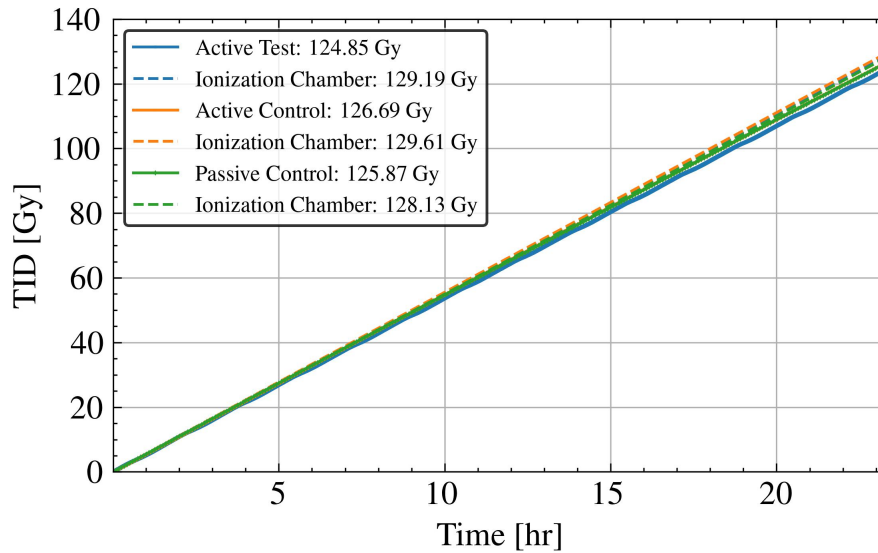


Figure 5.20: The TID measured by the different boards over time compared to the respective ionization chamber calibration. Note that the actual starting TID is 82.5 Gy and not 0 Gy.

To study the TID difference in more detail, the RPD of each sensor with each respective ionization chamber is plotted in Figure 5.21. Here the oscillations due to the temperature changes can clearly be seen for the test board. The dampening of the oscillations is there because the dose increases over time, meaning the difference in RPD also gets smaller. This figure also shows that the RPD of the test board is higher than both the control boards. The RPD of the test board is around 3.5% while the RPD of the control board are around 2%. An important thing to note is that these RPD values are just an indication. When the dose rate would have been much lower, the RPD oscillations would be a lot higher. The final temperature is also equal to the temperature that the test was started with, meaning the final RPD is also in the middle of the trend line.

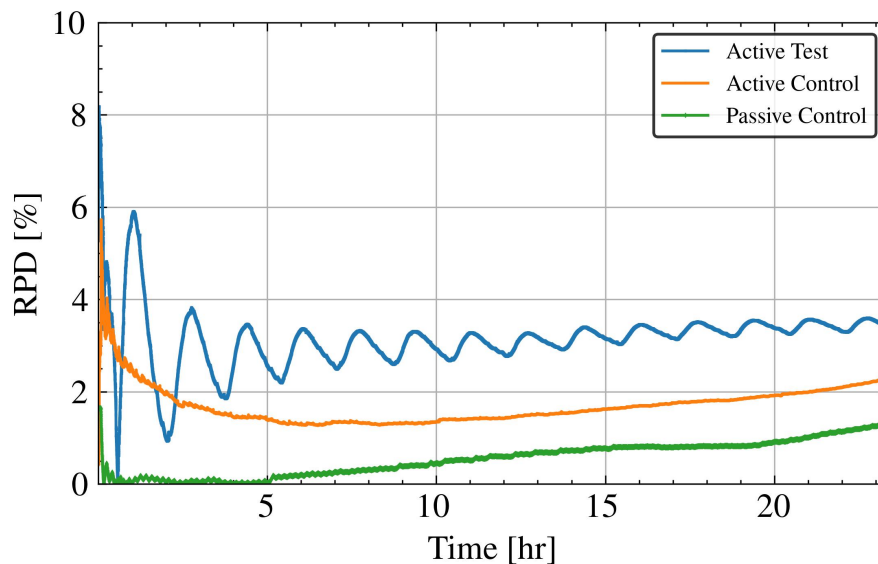


Figure 5.21: Relative percentage difference of the TID received of the boards tested at Co60 and each respective ionization chamber calibration. Note that the actual starting TID is 82.5 Gy and not 0 Gy.

The results of applying the different temperature compensation methods can be seen in Figure 5.22. In this figure, the blue line is the test board (same as before), the blue dotted line is the respective ionization chamber, the orange line is the compensated TID using the reference frequency method and

the green line is the compensated dose using the temperature coefficient method. One thing that already can be clearly seen is that the reference frequency compensation method is working exceptionally well for this kind of temperature profile. This compensation method is extremely close to the ionization chamber, even closer than the control boards are. This also shows that the SRM-FGD-2 requirement is now verified.

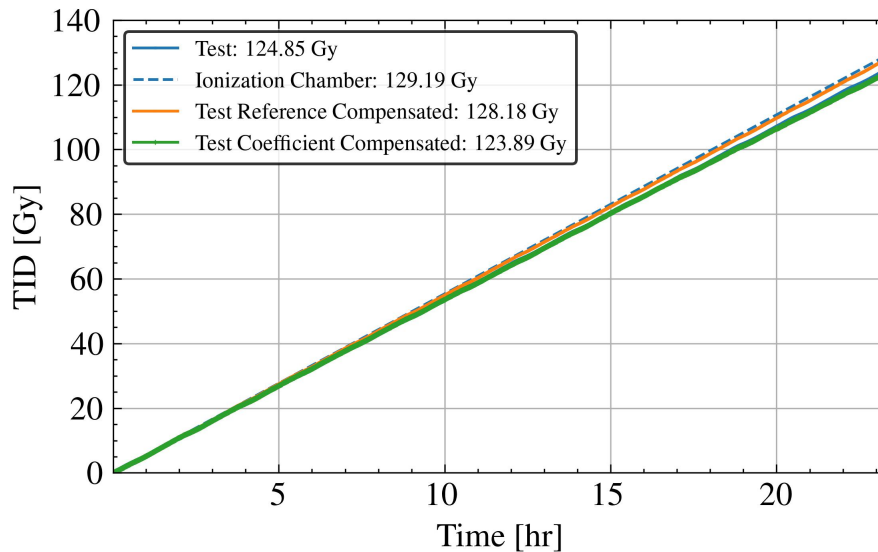


Figure 5.22: The TID measured by the test board over time compared to the test ionization chamber calibration with the different compensation methods. Note that the actual starting TID is 82.5 Gy and not 0 Gy.

The compensation techniques are highlighted in Figure 5.23, where again the RPD is plotted over time. In this figure, the reference frequency compensation method has been split up into a characterized one and a non-characterized one. With characterized reference compensation, it means that the data from the dry run was used. From this data, the relation between the sensor frequency change and reference change has been determined for this specific sensor. In the non-characterized method, the sensor and reference frequency from different FGDOS devices have been taken which were characterized in previous tests (from a study by M. Brucoli [16] in particular). The results clearly show that the reference compensation method is working extremely well. On top of this, a characterized sensor can be compensated even better, although the improvement in this study is smaller than 1%. Both the reference compensated TID techniques show a RPD of less than 1%, which is extremely good. This performance is also very much in accordance with requirement SRM-FGD-3. The oscillations are however not fully eliminated and are damped slightly. A study with a lower dose rate could be performed to see the dampening effect better. The coefficient compensation technique is not working as well, since it does not seem to take the general underestimation of the dose into account. The waves are also not as damped as the reference compensation method.

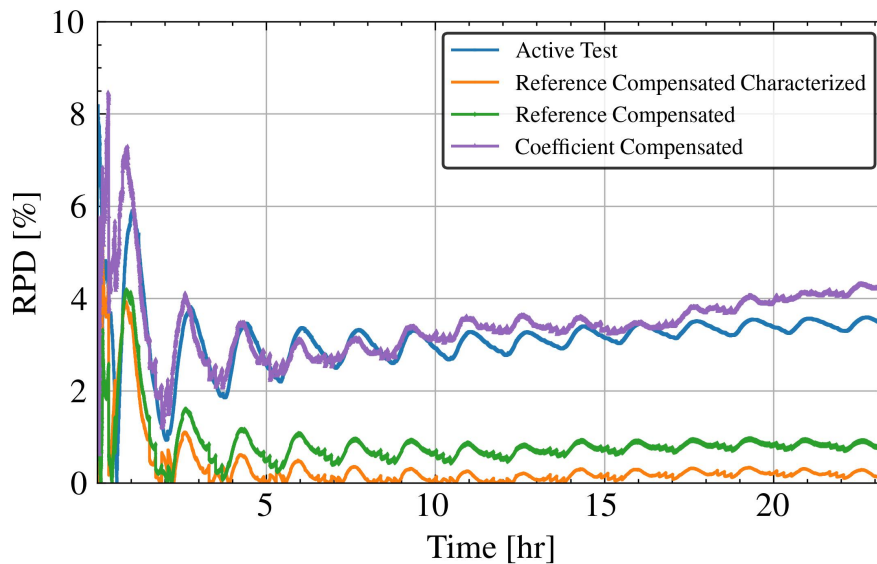


Figure 5.23: Relative percentage difference of the TID received of the test board with different types of temperature compensation methods and the ionization chamber. Note that the actual starting TID is 82.5 Gy and not 0 Gy.

In terms of criticality, it is important to note that all the data retrieved during this test was done during a single test and repeatability could still be checked. Due to time constraints, this could be done in a future study on the topic. It would certainly be interesting to conduct a similar test with lower dose rate and to check how much the general underestimation of the TID would be with different dose rates. Further more, the results could also be verified by means of a second experiment.

5.3. Conclusions and Implications

The FGDOS temperature testing at the ^{60}Co facility resulted in some fundamental understanding on how the sensor will operate when subjected to a space-like environment. The test set-up worked very well after some minor obstacles were overcome and an identical set-up can also be used in the future for similar experiments. The most challenging parts of the test were the cabling and the condensation happening on the board. The test resulted in critical understanding on the following three topics:

- Temperature coefficient evolution over TID
- Sensitivity degradation in an environment with constantly varying temperatures
- TID compensation for influences induced by temperature variations

Additionally, requirements SRM-FGD-2 and SRM-FGD-3 have now also been verified. From the analysis of the results, the following statements can be made about the topics. The temperature coefficient stays constant in an environment with constantly varying temperature and simultaneous irradiation. The sensitivity degradation is not affected by the space-like temperature profile while simultaneously being irradiated. The characterized reference frequency compensation method gives the most accurate TID results in a space-like environment, where the non-characterized reference frequency compensation method shows almost identical results in terms of performance, which can save time in not needing to characterize the sensor.

Fortunately, these results are very positive in terms of what implications they have on the Space RadMon-NG payload. The temperature coefficient that stays constant over TID does not require any additional compensation. This is similar for the sensitivity degradation, that might have been different with a constantly varying temperature. This also does not require any additional compensation as the sensitivity degradation evolution of the FGDOS was identical in both cases with and without varying temperature. As last, the best method of compensation was found. This is the characterized reference frequency method. However, as characterization takes quite some time and the non-characterized reference frequency method achieves almost the same results, this might be the preferred method. In

the future to verify these results, it might be favourable to conduct a very similar test with lower dose rates, or do a FGDOS simulation based on the information gained during this test.

6

CELESTA Mission

The CELESTA mission is the first space mission by CERN, in collaboration with the University of Montpellier Space Centre (CSUM). The CELESTA satellite is based on the ROBUSTA-1U platform and carries the first version of the Space RadMon payload, the Space RadMon V1. This chapter will provide an analysis of the payload data retrieved during the CELESTA mission and map the data on the orbit. Then, using the knowledge of the analysis and the algorithms made, the analysis for the new payload can be set up and predictions can be made using simulations in OMERE. This should give a very streamlined analysis when the new payload data will come in during one of the missions where the Space RadMon-NG will fly. The analysis of actual radiation data in space is crucial for improving testing techniques, as some models can already be quite outdated and some could also lead to a massive overestimation, meaning some components might not be considered even though they would have been perfectly suitable for the mission.

6.1. Space RadMon V1 Payload

First, the Space RadMon V1 payload analysis will be elaborated by giving the orbit information of the CELESTA mission, an OMERE simulation of the environment where the mission takes place and the orbit mapping of the payload data received.

6.1.1. Orbit Information and Environment

The orbit information can be extracted from two sources, the first one being the mission design and the second one being the Two-Line Element (TLE). The mission design is the desired mission orbit, while the TLE orbit information gives the actual observed orbit in a so-called 'snapshot' of the satellite. The TLEs of the CELESTA mission can be extracted from space-track.org, giving all the TLEs at the times that the satellite was observed. The list of CELESTA TLEs can be seen in Appendix B. The general orbit information can be summarized in Table 6.1. The symbols in this table stand for semi-major axis (a), eccentricity (e), inclination (i), argument of periapsis (ω) and the right ascension of the ascending node (Ω). The mission was launched on 13-07-2022 and officially started on 20-07-2022. This information can be used to model the radiation environment encountered in orbit using OMERE.

Table 6.1: General orbit parameters of the CELESTA mission.

a [km]	e [-]	i [deg]	ω [deg]	Ω [deg]
12212.190613	0.001556	70.1541	226.5	73.35

In OMERE, the orbit environment of CELESTA was modelled. As CELESTA is a SEL experiment in the middle of the inner Van Allen belt, the most interesting part of the environment will be the protons above 20 MeV (HEH). The AP8 solar maximum standard model was used to create a map of the proton flux, as this is the standard model in OMERE. The mission duration was set to two months, which is

the time the mission lasted for. The visualization of the predicted fluxes along the CELESTA orbit as obtained with OMERE can be seen in Figure 6.1. In this figure, it can be seen that the region around the poles has the lowest flux and the middle region the highest flux, which is expected in the inner Van Allen belt. The South Atlantic Anomaly (SAA) also cannot be seen, since the orbit is too high for this characteristic. The maximum flux around the equator is about $3.5 \times 10^4 \text{ cm}^{-2} \text{ s}^{-1}$, while the minimum around the poles is about $1.0 \text{ cm}^{-2} \text{ s}^{-1}$ (minimum value with lack of data). The wave of the flux map also shows how the Van Allen belt is tilted around the Earth. When the SELs are mapped on the ground track of the satellite, it is hypothesized that something similar will be found, with higher SEL rate around the equator and lower SEL rates around the poles. The rapid switch from green to blue around a latitude of 45° , is caused by the threshold of 20 MeV protons used. This means that around the polar regions, or higher/lower than $\pm 45^\circ$, it is mostly lower energy protons as far as can be modelled.

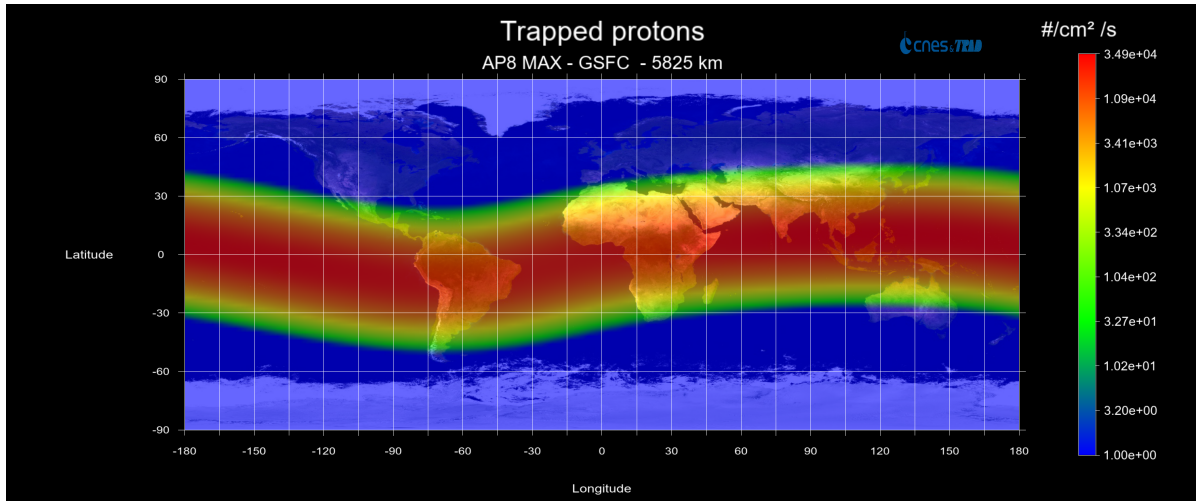


Figure 6.1: CELESTA HEH flux OMERE simulation from radiation belt particles as reference for the results.

6.1.2. Orbit Mapping and Payload Results

Using the data itself retrieved from CSUM and retrieving the TLEs from space-track.org, the data can be mapped on the orbit to get a figure that looks like the OMERE simulation in Figure 6.1. For this purpose, an algorithm was created to map the data on the orbit of CELESTA. The flow diagram of this algorithm can be seen in Figure 6.2.

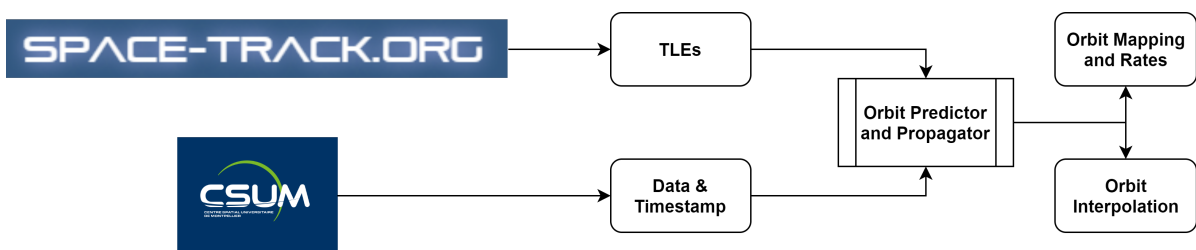
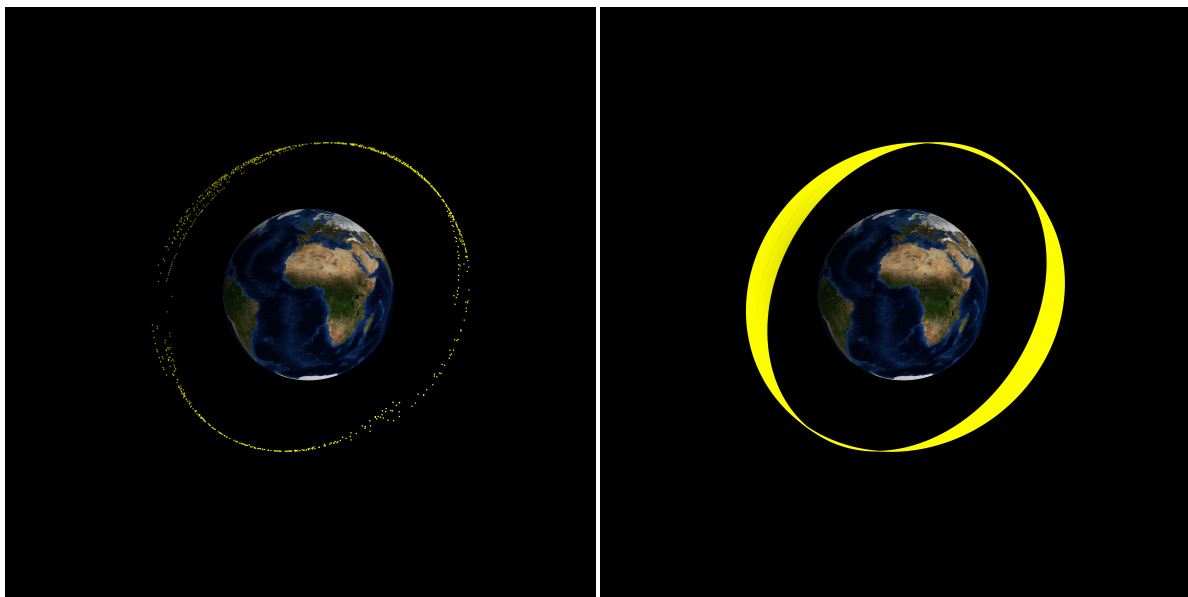


Figure 6.2: Global schematic of the algorithm used for the trajectory determination of CELESTA and data mapping.

This algorithm combines the TLEs with the data and timestamps available. To map the data on the ground track and determine the trajectory of the satellite, there is looped through the timestamps in the data. Based on the timestamp, the TLE closest to the timestamp is chosen as reference orbit. This timestamp and TLE are then put in the orbit propagator (both Skyfield and an orbit predictor by Satellogic were used in the algorithm) to get the results. The full algorithm is on Github and access can be requested. The results consist out of three-dimensional (interpolated) orbit trajectory information, the rates determined from the time and values between two data points and ground track mapping. The 3D trajectory in Earth Centered Inertial (ECI) frame (rotating Earth) can be seen in Figure 6.3,

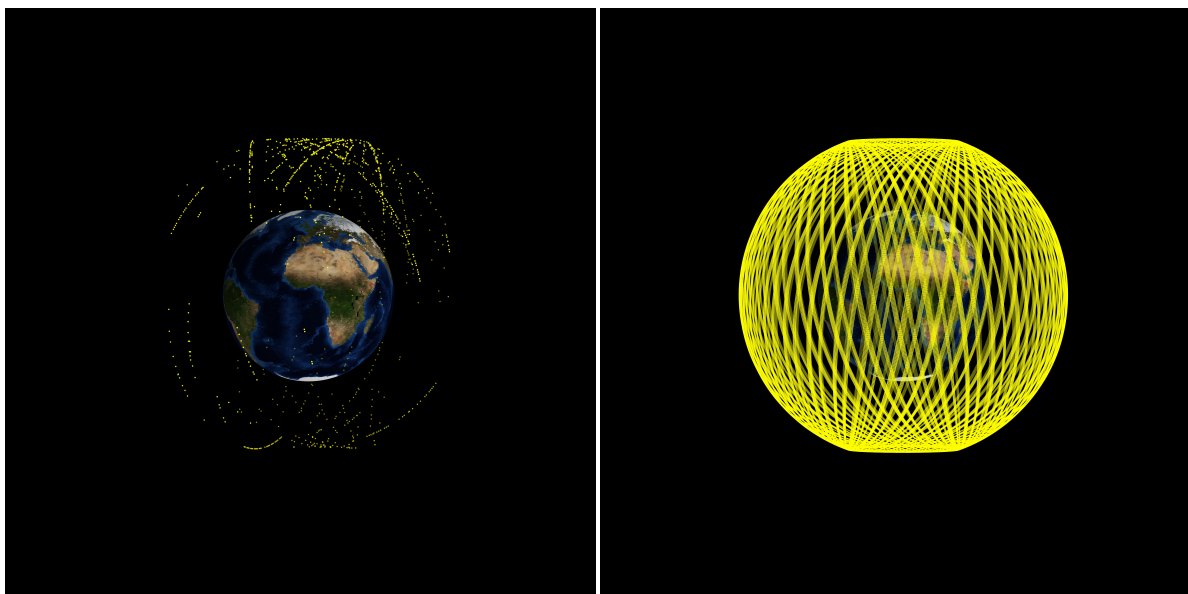
where on the left the location of the satellite is seen where data was transmitted and on the right the full interpolated trajectory can be seen. This data has also been converted to Earth Centered Earth Fixed (ECEF) frame (stationary Earth), which can be seen in Figure 6.4. This latter conversion gives any easier conversion to latitude and longitude coordinates for ground track mapping.



(a) Position in 3D ECI frame of the CELESTA satellite when data was transmitted.

(b) Interpolated position in 3D ECI frame of the CELESTA satellite during the mission.

Figure 6.3: CELESTA trajectory data using the described algorithm in 3D ECI frame.



(a) Position in 3D ECEF frame of the CELESTA satellite when data was transmitted.

(b) Interpolated position in 3D ECEF frame of the CELESTA satellite during the mission.

Figure 6.4: CELESTA trajectory data using the described algorithm in 3D ECEF frame.

As mentioned, the left figure show the location of the satellite in 3D were data was transmitted. If looked closely, it can be seen that most communication is towards the polar regions, in particular above Europe. Around the equator, less communication was established resulting in a lower payload data resolution as the time interval during the mission was sometimes more than one orbit. Possible reasons

for this can be communication interference with other satellites in a lower orbit, ground-station beacon placement or the transmitter type on the ROBUSTA-1U platform. For now, there needs to be worked with the data and locations available. The data from the ECEF trajectory can be converted to latitude and longitude as mentioned to create a ground track. The full ground track of the CELESTA satellite with data transmission locations given by points can be seen in Figure 6.5.

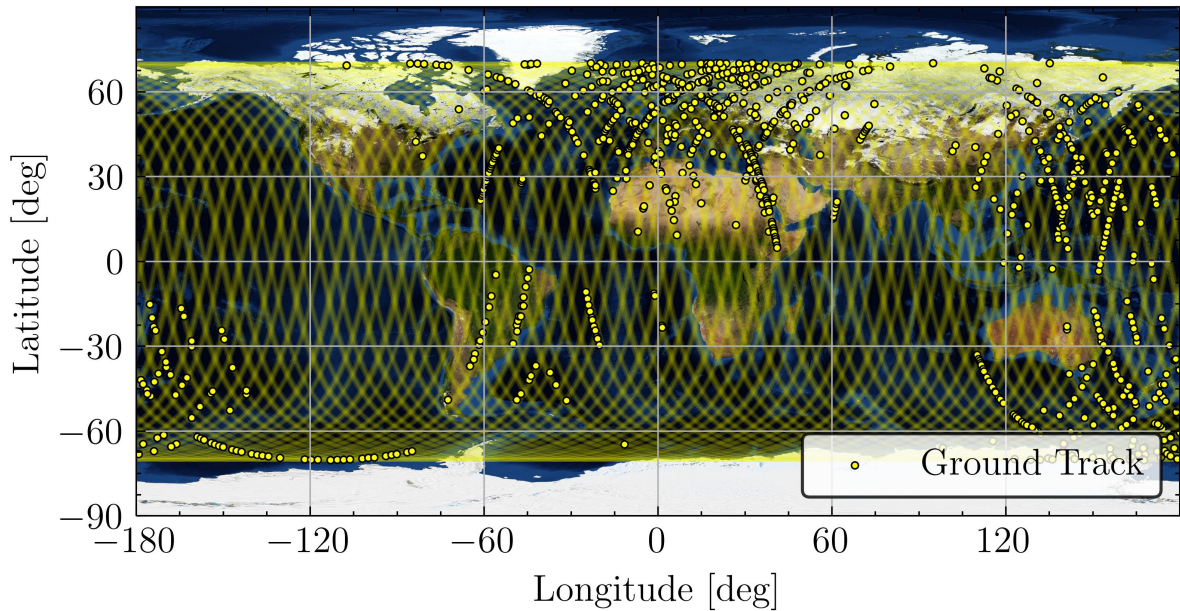


Figure 6.5: CELESTA full ground track with data transmission position depicted as dots.

In this kind of figure, the ground track data points can be used to map information retrieved in the orbit. In this case, it will be the SEL data from the satellite. The satellite contained two separate SEL sensors, of which the results can be seen in Figure 6.6. One of the SEL sensor measured a total of 87 SELs and the other sensor measured a total of 67 SELs. The divergence between the two sensor may have to do with the sensitivities of each sensor respectively or the placement in the satellite. This was measured over a period from the 20th of July in 2022 to the 12th of September 2022, giving a total of just a bit less than two months duration. Both SEL data have a linear trend, which is also what was expected for the mission.

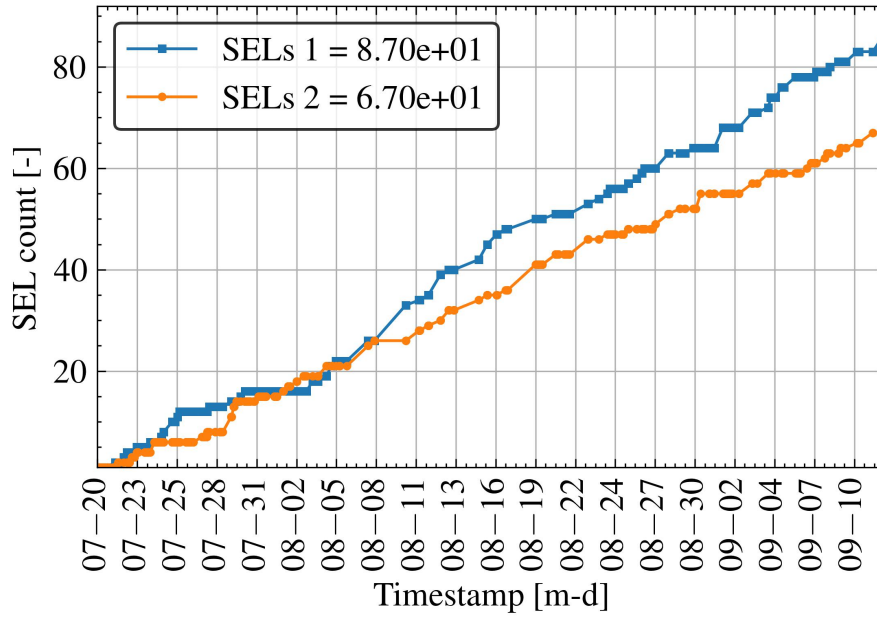


Figure 6.6: CELESTA SEL data of the two sensors during the mission in 2022.

Combining these measurements and plotting them on the ground track gives the result that can be seen in Figure 6.7. It can be noted that the resolution is too low to draw any clear conclusions. However, comparing the data to the OMERE simulation in Figure 6.1, there can be seen some slight similarities. For example, the highest SEL rate data point is near the equator similar to the proton flux modelled. The lighter coloured dots are more towards the polar regions, which also corresponds to the simulation. Although there a conclusive analysis cannot be performed, the proposed method of analyzing and comparing scientific data retrieved in orbit looks promising.

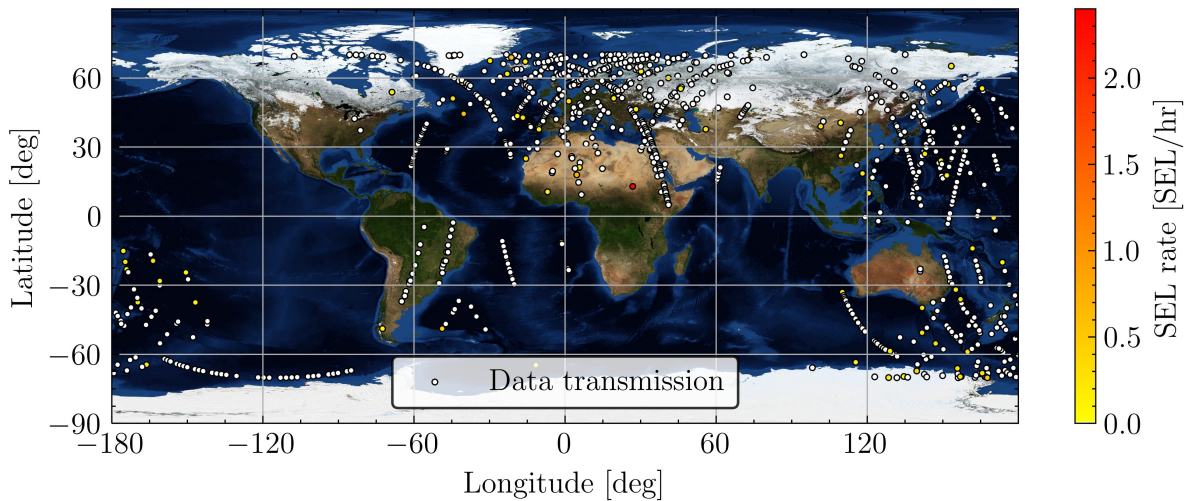


Figure 6.7: CELESTA ground track with SEL rate data embedded.

6.2. Space RadMon-NG Payload Analysis Preparation

The analysis from the last section can now be used to anticipate the analysis required for the Space RadMon-NG data coming in, now it has been fully qualified and verified for space operation. For this mission the GOMX-5 mission will be used. This is one of the two missions where the payload is scheduled to fly. This specific mission also contains the updated burst detection firmware, while the ISISPACE mission contains the older version of the firmware. For the analysis preparation, there will

be focused on the mission HEH flux (based on the trapped protons), the dose curve and a prediction of the amount of SEEs to be measured in the SRAM sensor. The algorithm made for CELESTA does not require any modifications, only the input of the TLEs will be different and the data supplier (GOMspace instead of CSUM). An absolute worst case of 1 mm thickness will be assumed for the shielding, as no information could be found about it for this specific mission.

6.2.1. Mission Dose

First of all, the mission dose can be measured on the payload using the FGDOS sensor. To determine the total dose, the mission dose curve can be used. This curve is seen in Figure 6.8. When a worst case of 1 mm shielding is used for a 5-year mission, the modelling results in an expected total dose of 30000 rad or 300 Gy.

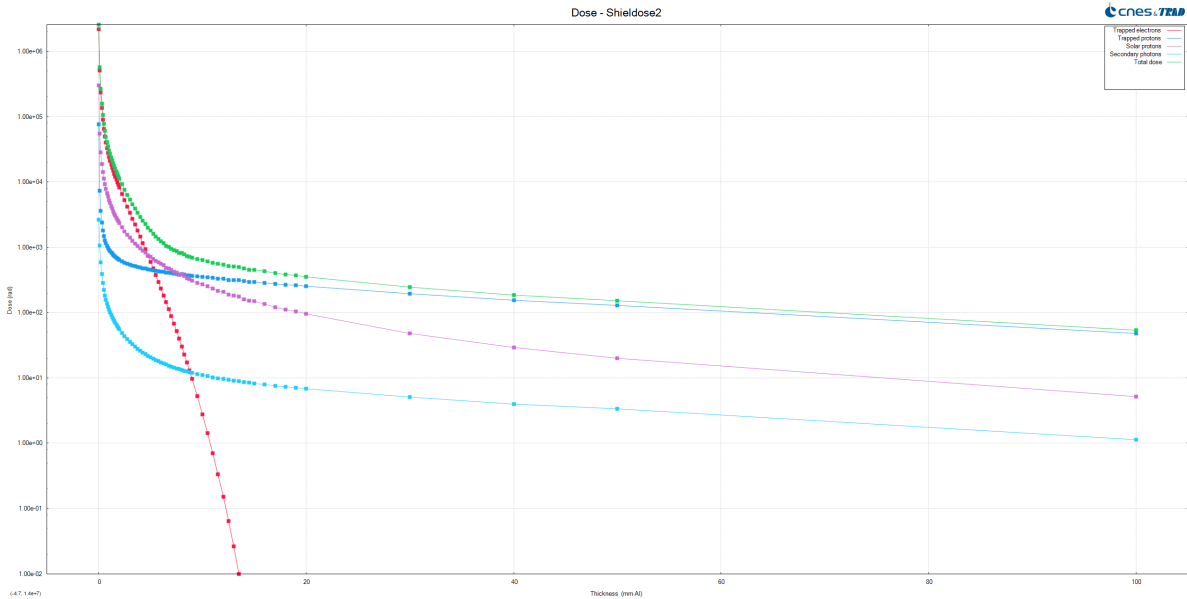


Figure 6.8: Dose curve over shielding for the GOMX mission in OMERE.

This dose can also be mapped on the orbit using OMERE in rates, as seen in Figure 6.9. These on-orbit dose rates are again for a worst case scenario of 1 mm shielding. The highest dose rate is observed in the SAA or near the polar regions, which has a maximum rate of $4.92 \cdot 10^{-3}$ rad/s (17.712 rad/hr). The lowest orbit dose rates are expected to be near the equator (excluding the SAA). The lowest dose rates are expected to be around $7.66 \cdot 10^{-14}$ rad/s ($2.7576 \cdot 10^{-10}$ rad/hr), which is practically zero. The background radiation rate on Earth is higher than this low dose rate region on the map.

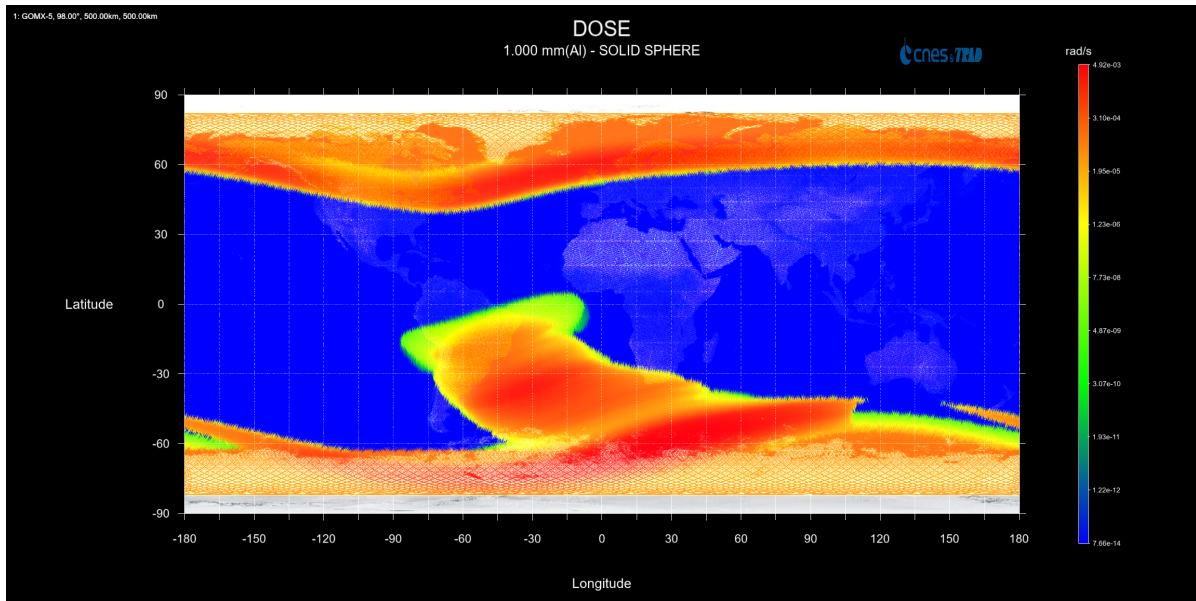


Figure 6.9: Dose map for 1 mm shielding for the GOMX mission in OMERE.

6.2.2. Mission Flux and SEE Prediction

Instead of SEL sensors like in the CELESTA mission, the Space RadMon-NG payload contains SEU sensors. These SEUs will also be caused by HEH, which is why analyzing the flux is one important part. Ultimately, the SEU measurement will also be converted to the HEH fluence using the determined cross-sections of the SRAMs. The HEH flux, trapped protons with an energy higher than 20 MeV, for the GOMX-5 mission orbit height can be seen in Figure 6.10. This flux map shows a maximum flux of $2.88 \cdot 10^3 \text{ cm}^{-2} \text{ s}^{-1}$ in the location of the SAA, which will also be the cause of the larger flux. The minimum flux is $1.0 \text{ cm}^{-2} \text{ s}^{-1}$ on the rest of the map because not enough data is available yet of higher energy particles.

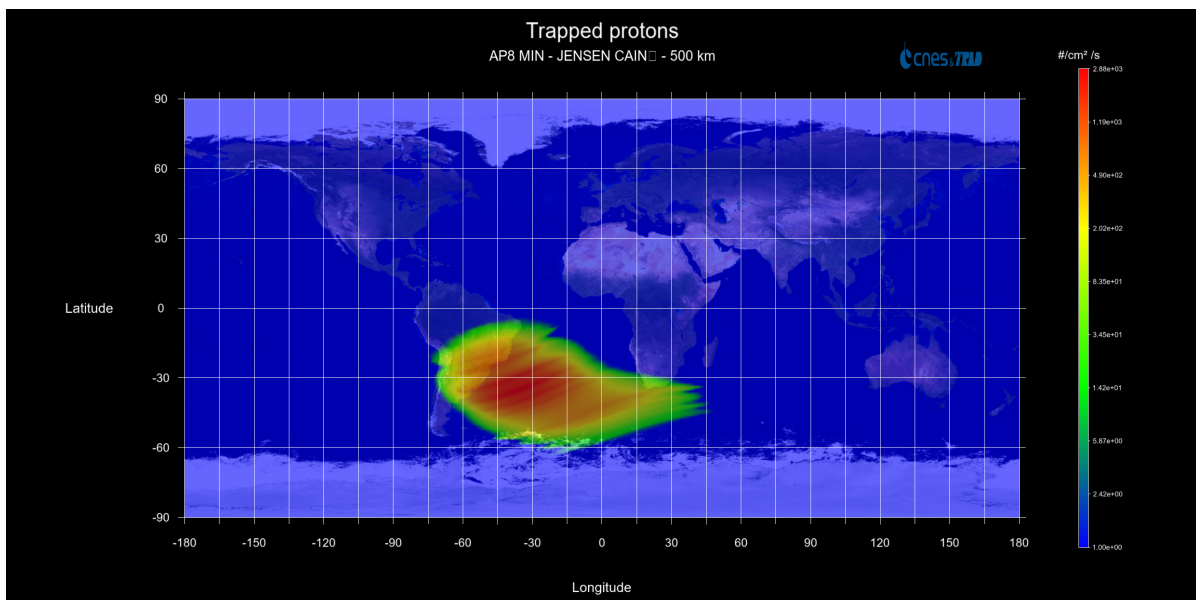


Figure 6.10: HEH flux for the GOMX mission in OMERE.

To make a prediction of the amount of SEEs in the SRAM sensor because of these higher energy particles, a Weibull fit through the cross section data can be used. This Weibull fit is seen in Figure 6.11. The

settings used to determine the SEE rate is a threshold LET of 10 MeV for protons and a 0.1 MeV for ions. The lowest LET for protons where SEEs were observed is around 16 MeV. This was tested by CERN at the PIF in the PSI in Zürich. To assume a worst case and take into account all the effects, 10 MeV is used instead of the 20 MeV of HEH particles. The device size is $8 \times 1024 \times 1024 = 8388608$ bits with a $0.5 \mu\text{m}$ cell depth. The shielding used is again a worst case assumption of 1 mm. The results of the SEEs and their causes (type of radiation source) can be seen in Table 6.2. A total SEE rate of 5.44 SEEs per device, per day is expected. The biggest contributors are the trapped protons and the solar protons.

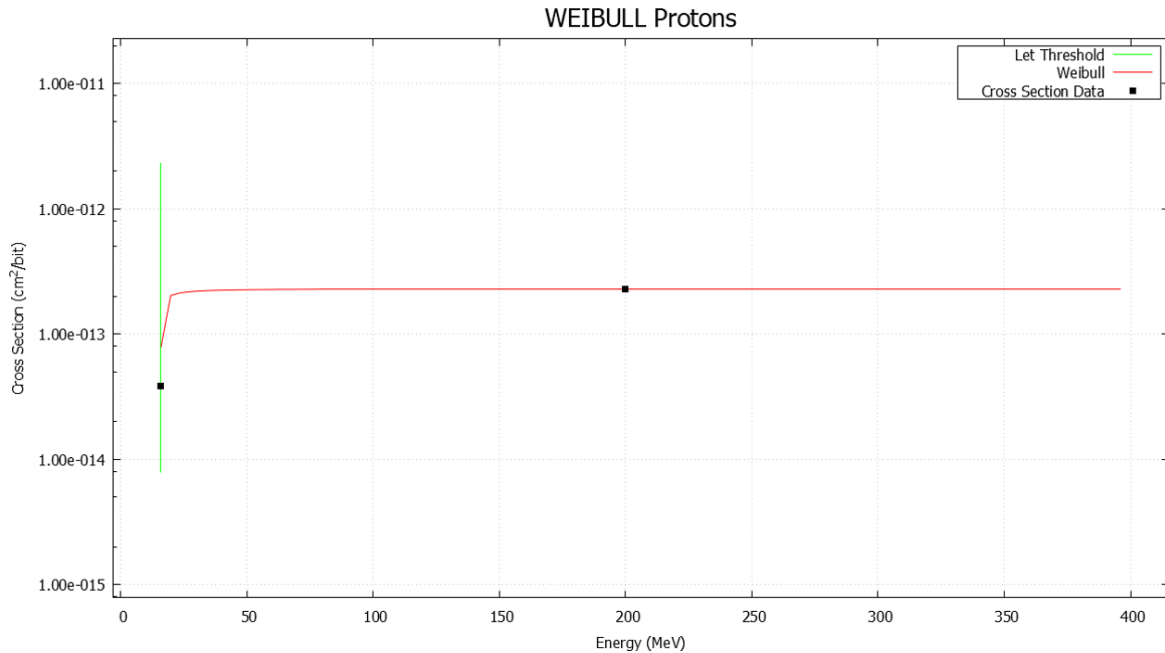


Figure 6.11: Weibull fitting for Cypress SRAM cross section in OMERE.

Table 6.2: Prediction of the amount of SEEs in the SRAM of the payload for the GOMX-5 mission.

Source	[/bit/day]	[/device/day]
GCR Protons	2.52E-08	2.11E-01
Trapped Protons	3.58E-07	3.00E+00
Solar Protons	2.65E-07	2.22E+00
GCR Ions	1.76E-15	1.48E-08
Total	6.49E-07	5.44E+00

Mapping these SEEs on the orbit trajectory can ultimately lead to a better understanding of the shape of the radiation environment. For this to work, the resolution should be high enough for differences and if only 5.44 per day are expected, it might be too low to accurately map the effects. It might be very informative to create a HEH flux map for the Earth orbit around the Sun, meaning that information about the HEH flux in the near Earth environment is available for different months or seasons.

6.3. Conclusions

Several conclusions can be made from the analysis of the CELESTA mission and the set-up for the new payload. The first conclusion that can be made from the CELESTA analysis is that the resolution of the payload data was too low to make any conclusions actually based on the data and mapping. The SEL rate over the whole mission timeline was linear, which is also what was expected. Although the resolution was low, there was a small correlation observed between the SEL rate mapped on the orbit and the OMERE simulation of the high energy protons in the radiation belt. It was also shown that the

method of mapping the rates on orbit is very feasible and can also be used for the analysis of the new payload.

A preliminary analysis for the GOMX-5 mission, the mission that will carry the Space RadMon-NG payload with the burst detection firmware, was also conducted. For this analysis, a worst case shielding of 1 mm was assumed. This scenario for a 5-year mission resulted in a total mission dose of 300 Gy or 30000 rad. In terms of dose rates, the highest rates are expected in the polar regions and the SAA. The dose rates in these locations can reach up to 17.7 rad/hr. The lowest dose rates encountered near the equator are negligible compared to the general background radiation received on Earth. The highest mission flux for high energy protons is expected to be in the location of the SAA, where the flux can reach up to $2.88 \cdot 10^3 \text{ cm}^{-2} \text{ s}^{-1}$. The lower flux regions do not contain much data in the model. Using information of the SRAM SEU sensor and a Weibull fit through the cross section, the SEE rate can be predicted. This resulted in a total amount of 5.44 SEEs per device per day, with the biggest contributors being trapped protons and solar protons. The same mapping algorithm can be used for the GOMX-5 mission, where only the TLEs need to be changes and the data input. This will then be GOMspace instead of CSUM.

7

Conclusion

Radiation monitoring in the LHC is of great importance for safety, reliability and to get a better understanding of the physics in the experiments at CERN. For this reason, the RadMon was developed, a compact radiation monitoring device. Since similar essential themes are also very relevant in space, the Space RadMon-NG payload was developed. This resulted in a compact, low power version of the RadMon system that can be used for space applications. The payload has been developed as reliability improvements for CubeSats, but also with science goals to study the complex radiation environment in orbit. The goal of this thesis study was to system-level test the payload, research and characterize the sensors on the mezzanine board and prepare the mission analysis. To achieve these goals, a literature review was conducted and the payload itself was studied to get a fundamental understanding of the topics encountered during the thesis. In the end, these topics and goals can be combined to answer the research question proposed in the introduction of this thesis.

This final chapter will summarise the conclusions for the system-level testing performed, for the FGDS temperature characterization experiment conducted and the CELESTA mission analysis. Afterwards, the research question and sub-questions proposed in the introduction of the thesis will be answered. This is subsequently followed by recommendations for future work.

7.1. System-Level Testing

The main goals of the system-level testing were the burst detection firmware verification of the payload, the sensor benchmarking on the mezzanine board of the payload and the payload operation and communication between a master and the FPGA (as slave) in general. Also the requirements set in chapter 3 related to this system-level testing were all verified (except for SRM-FGD-2 and SRM-FGD-3). As overall additional purpose, the system-level testing was also used to validate CHARM as system-level test facility for space systems and to compare future payload results retrieved in orbit with various positions in CHARM. This way, certain orbits can be linked to certain positions in CHARM for optimized system-level testing for space systems. For the experiment in CHARM with the payload, a custom cable with custom PCB was designed for the interfacing over the control and patch panel. The dry run with the set-up was successful. Afterwards, the test set-up and payload have been placed in the G0 position in the CHARM facility.

In total, three radiation campaigns were performed at the CHARM facility. During the first campaign of seven weeks, a total of around 232 Gy was received by the payload. In this campaign, some communication issues between the master and slave arose in terms of unstable communication and termination of the communication. Fortunately, some useful results could still be retrieved. The burst detection algorithm has been analyzed and is working according to expectations. Over a period close to 2 days, the relative error of the uncompensated SEUs with respect to the RadMon as reference was observed to be 8.1%. When the algorithm was used for compensation of the bursts, this error reduced to 0.65%, which is well within the acceptable range. Hence can be concluded that the burst algorithm was effective

and is working. The TID and FGDOS have also been benchmarked against the the RADFET, the current standard, with results being very compatible. The differences in TID of the two FGDOS sensors with the RADFET were only 1.08% and 2.35%, also well within the acceptable range. When the results were zoomed in, it was also confirmed that the FGDOS resolution is much better than the RADFET resolution. Since due to communication issues some of the TID data missing and could not be reconstructed, a MCU firmware update was done. The payload operation seemed to work well, as the voltages gave the correct outputs and the adjustable voltages also worked well for the custom SRAMs.

The second campaign had the main purpose of verifying the new MCU firmware update and to check the payload communication problems. The test lasted for 1 week where the payload took another 15.5 Gy (total of around 247 Gy up until now). However, due to a failure of the voltage regulator, the test was not successful. The FPGA voltage was around 3.1 V and should have been 1.2 V. The board was taken out of CHARM to the buffer-zone, where the voltage regulator was replaced. The payload worked again in the dry run with the new regulator. Due to the failure, there were still some communication issues and after around 20 hours in the test, the communication was fully terminated. There was fortunately a recharge that was saved in the memory, already demonstrating that the MCU firmware update was working.

In the third campaign, the payload was tested for two weeks and took around 46 Gy (around 295 Gy in total). The voltages were working well with the new regulator and communication was also working better due to some changes in the master-slave configuration software. The test resulted in continuous data of close to six days. The SRAM was now being compared to another RadMon with a different SRAM. The results were very compatible if the $3.44\text{e-}13\text{ cm}^2$ cross-section was used on the payload. This is the cross-section that was a result from a cross-calibration in CHARM between the two SRAMs in another test. The result with this cross-section was a relative error of close to 0%, while two other cross-sections resulted in a 45% and a 75% error. A re-calibration of the payload SRAM is advised to decide which cross-section to use in the final analysis. The FGDOS results were also very compatible again to the RADFET. When the FGDOS were characterized in terms of sensitivity, the relative error was around 1% for both FGDOS sensors. When the sensor was not characterized for sensitivity, but the dose up until that point was taken as sensitivity reference, the relative error for the two FGDOS sensors were around 23% and 27%. This highlights the need for sensitivity characterization in critical applications such as a space mission.

The communication issues did not completely vanish throughout the radiation campaigns. After the campaigns, some dry runs were performed without radiation, with shorter cables and with stronger I2C pull-up configurations. From these tests can be concluded that the communication issues arose because of the long cabling in combination with using I2C. The problems only came to light after a certain time of continuous testing, which is why it was not found during the initial dry runs. A solution to the problem will be to use an I2C buffer or to use a stronger pull-up configuration on the master side, meaning the use of lower resistance pull-ups for communication in the CHARM facility.

7.2. Floating Gate Dosimeter

The FGDOS temperature characterization test had three main goals. These goals were to study evolution of the temperature coefficient, study the sensitivity degradation when subjected to radiation with temperature variations simultaneously and the study the temperature compensation of the TID. The test was also used to fully verify the SRM-FGD-2 and SRM-FGD-3 requirements. The set-up of the experiment was slightly complex, as a system needed to be made that can control the temperature without being in the radiation room. All the components used for the set-up also should be able to survive the radiation. This resulted in a set-up consisting out of two PCBs, one for testing and one as control. The board contained a FGDOS and a thermistor. The temperature was controlled by a current-calibrated Peltier module with a fan mounted on the back. The temperature profile chosen was based on a sinusoidal function to simulate the temperature variations encountered for an orbit around the Earth. The data was retrieved by an Arduino on a custom shield connected by a 20 m Ethernet cable. The experiment was performed under radiation of a ^{60}Co source.

After successful calibration of the thermal regulator, dry runs and dry run characterization, the system was ready for the experiment. When the set-up was installed, some hiccups were encountered. This had to do with communication over the long cables, sensor settings and condensation. The solution in the end was to shift the temperature profile up before the final test. Up until this point, the set-up received 82.5 Gy. During the actual test, the minimum temperature reached was around 24 °C and the maximum temperature reached was around 67 °C. A total of around 130 Gy was received and the test took 23 hours and 20 minutes. This resulted in a total of 14 'periods'.

One of the first results from the temperature experiment was the evolution of the temperature coefficient. Based on this part of the study, there can be thus far concluded that the temperature coefficient of the sensor does not change because of radiation. The second part of the study focused on the sensitivity degradation. There was hypothesized that there could be an enhanced degradation due to the temperature changes and radiation. After an analysis of the results, it can be concluded that the temperature variations do not enhance sensitivity degradation in the FGDOS, as the degradation curves are extremely similar to the ones resulting from a stable temperature experiment. The relative error also stays constant around 5%, which is caused by the initial sensitivity differences of the sensors. The final result is aimed at the TID compensation for temperature effects. From the study can be concluded that the method of using a twin MOSFET that is not affected by radiation but shows a similar temperature response is the most accurate method of compensation. The method of using the temperature coefficient did not perform according to expectations and increased the relative error even more due to temperature effects. The reference frequency method performed well, reducing the relative error from around 3.5% for uncompensated to around 0.2% for characterized compensation and to around 0.7% for not characterized compensation. This results also verified both the SRM-FGD-2 and SRM-FGD-3 requirements. The small difference between the two reference compensations means that without temperature characterization of the specific sensor that requires compensation, it works almost as good. This will save a lot of time and effort in preparing the sensors for their applications. The experiment was only conducted once and could still be checked for repeatability.

7.3. CELESTA Mission

The CELESTA mission plays an important role in analyzing the performance of the first version of the Space RadMon and preparing the analysis of the Space RadMon-NG results. The first step in analyzing the CELESTA mission results was to establish which orbit it was in and what the environment in this orbit is according to current available models. The height of the CELESTA orbit was around 5825 km above the Earth surface with an inclination of around 70.15°. The orbit was almost perfectly circular, with an eccentricity of 0.001556. By modelling the environment of this orbit in OMERE, focusing on the higher energy protons (>20MeV) in the radiation belt, there can be concluded that the highest flux can be expected around the equator and the lower flux regions are towards the poles. The higher flux region can reach a maximum of $3.5 \cdot 10^4 \text{ cm}^{-2} \text{ s}^{-1}$ and for lower flux regions the minimum is $1.0 \text{ cm}^{-2} \text{ s}^{-1}$ due to lack of data in the models.

The data from the CELESTA mission can be mapped on the surface of the Earth by means of an algorithm that takes the TLE, data and timestamps. The algorithm checks which TLE is closest to the timestamp in question and does an orbit prediction using the Skyfield and Satellogic orbit predictor library. The output of the algorithm is then the three-dimensional position of the satellite when data was transmitted, meaning the data captured can be localized in the orbit. By determination of the rates, a similar radiation map can be created to the one in OMERE and compared. The SEL results from the CELESTA mission were what was expected, which is a linear trend. One of the SEL sensors measured a total of 87 events during the mission and the other sensor measured a total of 67 events during the mission. The difference between these two sensor can either be caused by varying sensor sensitivities or by placement in the satellite. Unfortunately, the data resolution of the CELESTA mission was too low to create a full radiation map. The data could still be mapped on the orbit but because of the low resolution, the rates determined might not be completely representative. There was seen a small correlation between the highest flux region in OMERE and the highest SEL rate from the CELESTA data, which were both near the equator above Africa.

By demonstrating that the orbit mapping algorithm worked, it can also be used in the future for the Space RadMon-NG data once it is in orbit and sending data. For this purpose, a preliminary analysis was conducted on the environment the Space RadMon-NG will encounter on the GOMX-5 mission. The mission is close to a circular orbit, with a 98° inclination at around 500 km altitude. Since the payload can measure TID and SEUs, there will be focused on the mission dose and higher energy particle flux. These were all determined based on a worst case assumption of only 1 mm shielding. The total mission dose modelled for a five year mission was 30000 rad or 300 Gy, less than the lifetime of the payload. By mapping the dose rates in OMERE, there can be concluded that the highest dose rates will be encountered around the polar regions and near the SAA. In these regions, the dose rates could go up to around 17.7 rad/hr according to the models. The high energy proton flux is only high near the SAA. In this region, the flux of high energy protons could go up to $2.88 \cdot 10^3 \text{ cm}^{-2} \text{ s}^{-1}$. In the other regions the minimum flux is $1.0 \text{ cm}^{-2} \text{ s}^{-1}$ because there is not enough data or information available. The SEE rate for the SEU sensor has also been predicted, which resulted in a total SEU rate for the Cypress SRAM of 5.44 SEEs per device per day. The biggest contributors to these events are trapped protons and solar protons.

7.4. Research Questions

Using the conclusions drawn for each of the intermediary topics and using the knowledge gained during the thesis study, the research question of the thesis proposed in the introduction with the sub-questions can be answered. There will be started with the sub-questions and afterwards the answers will be combined for the main research question.

- (i) What are the operational principles of the Space RadMon-NG payload and how does the system compare to current state-of-the-art?

The payload has been analyzed in detail in chapter 3. This chapter explained the requirements of the Space RadMon-NG that required testing, the hardware layout, the software and firmware configurations in the device, the power consumption and how to interface with the device. The payload was then compared to current state-of-the-art radiation monitoring based on the sensors on the board. The main competitor of the Cypress SRAM HEH fluence sensor is the Timepix, which both have its own advantages and disadvantages. The SRAM does not require a high bias voltage, is a lot cheaper, is accurate, but can only determine the HEH fluence or flux. The Timepix is more expensive, requires a high bias voltage, but can measure the direction of the incoming particles. The FGDOS on the board has a lot more advantages than the RADFET for a space mission. The resolution is better, can operate without a bias voltage and is cheaper. It is a bit harder to configure the sensor and to replace it, but for a space mission these problems are very minor.

- (ii) How does the payload perform when in a mixed-field radiation environment such as space and how can this performance be optimized?

The payload performs very well in a mixed-field radiation environment. It was tested in the CHARM facility at CERN and took in total close to 300 Gy. Both the HEH fluence SRAM sensor and the FGDOS showed an excellent performance. The FPGA and MCU on the main board of the payload are very robust. The voltage regulator on the payload did give some problem after around 175 Gy, resulting in given a voltage to the FPGA that was too high. It has been hypothesized that this is due to the DD in the regulator, which will not be a problem in space. There were also some communication issues, but it was confirmed that these were not related to the payload itself. There are some optimization techniques that can be used to get the sensors well withing the 2.5% benchmark set in the beginning of chapter 3. Additionally, the correct cross-section for the SRAM has to be chosen. Now, $3.44 \cdot 10^{-13} \text{ cm}^2$ was most suitable, but this should be verified using another calibration. The FGDOS performance will also be well below 2.5% if the initial sensitivity of that specific sensor is characterized.

- (iii) What are the characteristics of the FGDOS sensor when exposed to a space-like environment and how can the sensor be as accurate as possible?

When exposed to a space-like environment, consisting of radiation and temperature variations, the FGDOS chip showed interesting characteristics. One of the characteristics found was that there can be a thermally induced recharge of the FGDOS, without any radiation. A second characteristic found it that the temperature coefficient stays constant over time. The third characteristic found is that the sensitivity

degradation when subjected to temperature variation while being irradiation is the same as without these temperature variations. To make the sensor as accurate as possible, temperature characterization is not necessarily required. The TID measured must be compensated for temperature using the reference frequency method, which was found to be the most accurate method of compensation. It resulted in an accuracy of below 1% over a total dose of around 130 Gy, which is again well within the requirement set.

- (iv) How can the data of the CELESTA mission be used to anticipate probable problems and to prepare the analysis of the Space RadMon-NG payload data?

Based on the data of the CELESTA mission, some probable problems have been identified. The resolution of the payload data must be sufficient enough to be able to map the data on the orbit. Communication between the satellite and ground-stations was also a problem for the CELESTA mission, but this might be different with other more experienced operators such as ISISPACE and GOMspace. The orbit mapping algorithm was verified using the CELESTA mission data and can be used for the Space RadMon-NG data once it comes in. As reference, OMERE simulations have been performed to be able to compare the payload data to existing models.

The main research question stated in the introduction is as follows:

How can the Space RadMon-NG payload make significant advances in space radiation monitoring compared to the current state-of-the-art?

Significant advances in space radiation monitoring can be made by full utilization of the enhanced sensors on the Space RadMon-NG payload and its compatibility with CubeSats. The sensors can be fully utilized by detecting bursts correctly on the Cypress SRAM, using the correct cross-section, by performing adequate temperature compensation on the FGDOS and by characterizing the initial sensitivity of the FGDOS. Since the components are mostly COTS, they are relatively cheap while still giving a good performance. Once the data is collected in one of the missions, the actual data can be compared to the different positions in CHARM. This will lead to more accurate testing without any over-estimation and unnecessarily disregarding components that are actually suitable for the mission.

In the future, the real advances could be made by adding the Space RadMon-NG to small satellites or CubeSat constellations to collect a lot of data of the near Earth radiation environment. This should be possible due to the compatibility of the device with CubeSats and the usage of COTS components making it cheaper. A much more accurate model could then be created of the near Earth radiation environment, which will also lead to less over-estimation of the needed requirements for space systems.

7.5. Future Work and Recommendations

Based on the conclusions and the answers to the research questions, quite some interesting future work could be proposed and good recommendations can be given.

First of all, the firmware could use a review and optimization. The firmware as it currently stands does exactly what it needs to do and works very well. However, with the current firmware implementation, the FPGA is quite close to being fully filled. State machine optimization has not been performed yet and already some possible state improvements were spotted during the analysis. By optimizing the firmware, it opens up more space on the FPGA which gives a future opportunity to add other functionalities or even sensors to the payload. Another possible improvement to the payload is removing the mezzanine board and integrating the sensors on the main board. This will save some space and weight, however then the payload will lose some of its modularity.

Secondly, it would be very interesting to see the Space RadMon-NG payload being tested in other positions than G0 in the CHARM facility at CERN. Currently, only the G0 position was used for system-level testing. As was already mentioned in the thesis, a position like R5 could be very interesting since it has similarities with LEO orbit [20]. If there is a one week test in all positions in CHARM, the positions can be compared the data that will be retrieved in orbit. This will result in valuable information on what position is actually very similar in practice for future space system testing at CHARM. For this compari-

son, the cross-section of the Cypress SRAM needs to be carefully chosen. As long as the same cross-section is used in the CHARM tests analysis and the orbit data analysis, the data can be compared. It might also be advantageous to do a re-calibration of the Cypress SRAM at the PIF in the PSI or in the CHARM facility.

A final proposal for future work is related to the FGDOS. As the sensitivity of the sensor can vary quite a bit between individual sensors, it will be very interesting to find some way of self characterizing the sensor since a characterization of the sensor takes quite some time. Two self characterization proposals were thought of, but it has not been studied yet how realistic these ideas are. The first idea is to correlate the sensitivity to the current increase, as due to radiation the current consumption of the FGDOS increases while the sensitivity decreases. Maybe they are related and can be correlated. Another possible idea would be to measure the recharge time, as recharging will also take longer when the sensitivity is lower due to the temporary damage in the oxide layer. It is however not known how steady the recharging times are or if the standard deviation of these times are too large to find any correlation to the sensitivity. It would also be interesting to see some type of FGDOS simulator with temperature and dose rate input to see the reaction of the FGDOS and to verify/hypothesize future experiment. This can now be created using the results from the temperature characterization test.

Bibliography

- [1] Plante et al. *Environmental Conditions for Space Flight Hardware – A Survey (NASA)*. 2004.
- [2] Maite Alvarez et al. “Total ionizing dose characterization of a prototype floating gate mosfet dosimeter for space applications”. In: *IEEE Transactions on Nuclear Science* 60.6 (2013), pp. 4281–4288. ISSN: 00189499. DOI: 10.1109/TNS.2013.2288573.
- [3] Marko Andjelkovic et al. “A Design Concept for Radiation Hardened RADFET Readout System for Space Applications”. In: *Microprocessors and Microsystems* 90 (Apr. 2022). ISSN: 01419331. DOI: 10.1016/j.micpro.2022.104486.
- [4] Marko Andjelkovic et al. “Design of Radiation Hardened RADFET Readout System for Space Applications”. In: *2020 23rd Euromicro Conference on Digital System Design (DSD)*. 2020, pp. 484–488. DOI: 10.1109/DSD51259.2020.00082.
- [5] J. Barak et al. “Detecting heavy ions and protons in space: single-events monitor”. In: IEEE, 1995. DOI: 10.1109/eeis.1995.514195.
- [6] A. Barnett, John Lees, and D. Bassford. “Temperature dependence of the average electron-hole pair creation energy in Al_{0.8}Ga_{0.2}As”. In: *Applied Physics Letters* 102 (May 2013). DOI: 10.1063/1.4804989.
- [7] Robert Baumann and Kirby Kruckmeyer. *Radiation Handbook for Electronics: A compendium of radiation effects topics for space, industrial and terrestrial applications*. 2013. URL: www.ti.com/radbook.
- [8] Robert C. Baumann. “Radiation-induced soft errors in advanced semiconductor technologies”. In: *IEEE Transactions on Device and Materials Reliability* 5.3 (2005), pp. 305–315. ISSN: 15304388. DOI: 10.1109/TDMR.2005.853449.
- [9] D. Binder, E. C. Smith, and A. B. Holman. “Satellite Anomalies from Galactic Cosmic Rays”. In: *IEEE Transactions on Nuclear Science* 22.6 (1975), pp. 2675–2680. DOI: 10.1109/TNS.1975.4328188.
- [10] S. Bourdarie and M. Xapsos. “The Near-Earth Space Radiation Environment”. In: *IEEE Transactions on Nuclear Science* 55.4 (2008), pp. 1810–1832. DOI: 10.1109/TNS.2008.2001409.
- [11] M. Brucoli et al. “A complete qualification of floating gate dosimeter for CERN applications”. In: *Proceedings of the European Conference on Radiation and its Effects on Components and Systems, RADECS 2016-September (2017)*, pp. 1–4. DOI: 10.1109/RADECS.2016.8093162.
- [12] M. Brucoli et al. “Floating Gate Dosimeter Suitability for Accelerator-Like Environments”. In: *IEEE Transactions on Nuclear Science* 64.8 (2017), pp. 2054–2060. ISSN: 00189499. DOI: 10.1109/TNS.2017.2681651.
- [13] M. Brucoli et al. “Investigation on Passive and Autonomous Mode Operation of Floating Gate Dosimeters”. In: *IEEE Transactions on Nuclear Science* 66.7 (2019), pp. 1620–1627. ISSN: 15581578. DOI: 10.1109/TNS.2019.2895366.
- [14] M. Brucoli et al. “Investigation on the Sensitivity Degradation of Dosimeters based on Floating Gate Structure”. In: *2017 17th European Conference on Radiation and Its Effects on Components and Systems, RADECS 2017 (2017)*, pp. 1–4. DOI: 10.1109/RADECS.2017.8696191.
- [15] Matteo Brucoli. “A new Floating Gate Dosimeter for CERN applications”. In: *R2E Annual Meeting (2018)*.
- [16] Matteo Brucoli. “Total ionizing dose monitoring for mixed field environments”. In: *HAL open science thesis (2018)*.
- [17] Jarvis A. Caffrey and D. M. Hamby. “A review of instruments and methods for dosimetry in space”. In: *Advances in Space Research* 47.4 (2011), pp. 563–574. ISSN: 02731177. DOI: 10.1016/j.asr.2010.10.005. URL: <http://dx.doi.org/10.1016/j.asr.2010.10.005>.

- [18] J. Cesari et al. “Floating gate dosimeter measurements at 4M lunar flyby mission”. In: *IEEE Radiation Effects Data Workshop 2015-November* (2015). DOI: 10.1109/REDW.2015.7336710.
- [19] Anthony Coburger, Matt Halstead, and Clayton A. Smith. “The Bounding Problem: Single Event Effect Rate Prediction Using Markov Chain Monte Carlo”. In: vol. 2021-May. Institute of Electrical and Electronics Engineers Inc., 2021. ISBN: 9781728180175. DOI: 10.1109/RAMS48097.2021.9605724.
- [20] Andrea Coronetti. “Relevance and Guidelines of Radiation Effect Testing Beyond the Standards for Electronic Devices and Systems Used in Space and at Accelerators”. 2021.
- [21] T. P. Dachev et al. “An overview of RADOM results for earth and moon radiation environment on Chandrayaan-1 satellite”. In: *Advances in Space Research* 48.5 (2011), pp. 779–791. ISSN: 02731177. DOI: 10.1016/j.asr.2011.05.009. URL: <http://dx.doi.org/10.1016/j.asr.2011.05.009>.
- [22] S. Danzeca et al. “Characterization and Modeling of a Floating Gate Dosimeter with Gamma and Protons at Various Energies”. In: *IEEE Transactions on Nuclear Science* 61.6 (Dec. 2014), pp. 3451–3457. DOI: 10.1109/TNS.2014.2364274. URL: <https://hal.archives-ouvertes.fr/hal-01635662>.
- [23] S. Danzeca et al. “Characterization and modeling of a floating gate dosimeter with gamma and protons at various energies”. English. In: *IEEE Transactions on Nuclear Science* 61.6 (2014). Cited By :18, pp. 3451–3457. URL: www.scopus.com.
- [24] S. Danzeca et al. “Qualification and characterization of SRAM memories used as radiation sensors in the LHC”. In: *IEEE Transactions on Nuclear Science* 61 (6 Dec. 2014), pp. 3458–3465. ISSN: 00189499. DOI: 10.1109/TNS.2014.2365042.
- [25] Salvatore Danzeca, Rudy Ferraro, and Georgios Tsiligiannis. *Guidelines for the Radiation Hardness Assurance (CERN-RHA) for CERN accelerators equipment. (V1.0)*. 2019.
- [26] William De Meyere. “Characterisation of a Floating Gate Dosimeter for Space Applications”. (2022).
- [27] Brian Dunbar. *Why Space Radiation Matters | NASA*. 2019. URL: <https://www.nasa.gov/analogs/nsrl/why-space-radiation-matters> (visited on 04/25/2022).
- [28] Marco Durante and Francis A. Cucinotta. “Physical basis of radiation protection in space travel”. In: *Reviews of Modern Physics* 83.4 (2011). ISSN: 00346861. DOI: 10.1103/RevModPhys.83.1245.
- [29] R. Ecoffet. “Overview of in-orbit radiation induced spacecraft anomalies”. In: *IEEE Transactions on Nuclear Science* 60 (3 2013), pp. 1791–1815. ISSN: 00189499. DOI: 10.1109/TNS.2013.2262002.
- [30] Rudy Ferraro. “Development of Test Methods for the Qualification of Electronic Components and Systems Adapted to High-Energy Accelerator Radiation Environments”. 2019.
- [31] R. Filgas. “Space radiation monitoring with Timepix”. In: *Astronomische Nachrichten* 339.5 (2018), pp. 386–390. ISSN: 15213994. DOI: 10.1002/asna.201813511.
- [32] E. Garcia-Moreno et al. “Floating Gate CMOS Dosimeter With Frequency Output”. In: 59.2 (2012), pp. 373–378.
- [33] Carlos Granja et al. “The SATRAM Timepix spacecraft payload in open space on board the Proba-V satellite for wide range radiation monitoring in LEO orbit”. In: *Planetary and Space Science* 125 (June 2016), pp. 114–129. ISSN: 00320633. DOI: 10.1016/j.pss.2016.03.009.
- [34] Carlos Granja et al. “Wide-range tracking and LET-spectra of energetic light and heavy charged particles”. In: *Nuclear Instruments and Methods in Physics Research, Section A: Accelerators, Spectrometers, Detectors and Associated Equipment* 988 (Feb. 2021). ISSN: 01689002. DOI: 10.1016/j.nima.2020.164901.
- [35] Christophe Inguibert and Scott Messenger. “Equivalent Displacement Damage Dose for On-Orbit Space Applications”. In: 59.6 (2012), pp. 3117–3125.
- [36] Richard Jung. “Design of a Test System for the Irradiation of the Cologne Chip GateMate A1 FPGA”. 2022.

- [37] H. Koshiishi. "Space radiation environment in low earth orbit during influences from solar and geomagnetic events in December 2006". In: *Advances in Space Research* 53 (2 Jan. 2014), pp. 233–236. ISSN: 0273-1177. DOI: 10.1016/J.ASR.2013.11.014.
- [38] K. Kudela. "On energetic particles in space". In: *Acta Physica Slovaca* 5960 (Nov. 2009). DOI: 10.2478/v10155-010-0098-4.
- [39] Ewa Lopienska. *The CERN accelerator complex, layout in 2022*. Feb. 2022. URL: <https://cds.cern.ch/record/2800984>.
- [40] Marian Lukowicz et al. "Thermoelectric Generators on Satellites—An Approach for Waste Heat Recovery in Space". In: *Energies* 9 (July 2016), p. 541. DOI: 10.3390/en9070541.
- [41] After Marshall. *Defect clusters produced by single ions - NSREC short course*. 1999.
- [42] B. H. Mauk et al. "Science objectives and rationale for the radiation belt storm probes mission". In: *Space Science Reviews* 179.1-4 (2013), pp. 3–27. ISSN: 00386308. DOI: 10.1007/s11214-012-9908-y.
- [43] J. Mekki et al. "CHARM: A Mixed Field Facility at CERN for Radiation Tests in Ground, Atmospheric, Space and Accelerator Representative Environments". In: *IEEE Transactions on Nuclear Science* 63 (4 Aug. 2016), pp. 2106–2114. ISSN: 00189499. DOI: 10.1109/TNS.2016.2528289.
- [44] Alessandra Menicucci. "AE4S15 – Space radiation environment and effects on embedded systems". In: (2020).
- [45] Scott R. Messenger et al. "NIEL for Heavy Ions: An Analytical Approach". In: *IEEE Transactions on Nuclear Science* 50.6 I (2003), pp. 1919–1923. ISSN: 00189499. DOI: 10.1109/TNS.2003.820762.
- [46] E. Garcia Moreno et al. "Radiation Sensor Compatible With Standard CMOS Technology". In: *IEEE Transactions on Nuclear Science* 56.5 (Oct. 2009), pp. 2910–2915. DOI: 10.1109/TNS.2008.2011804.
- [47] Lucy Reading-Ikkanda Natalie Wolchover Samuel Velasco. *Quanta Magazine*. Accessed: 21-11-2022. 2020. URL: <https://www.quantamagazine.org/a-new-map-of-the-standard-model-of-particle-physics-20201022/>.
- [48] John W. Norbury et al. "Advances in space radiation physics and transport at NASA". In: *Life Sciences in Space Research* 22. April (2019), pp. 98–124. ISSN: 22145532. DOI: 10.1016/j.lssr.2019.07.003. URL: <https://doi.org/10.1016/j.lssr.2019.07.003>.
- [49] European Organization for Nuclear Research. *Space RadMon: A flexible low-cost instruction for radiation monitoring in space*. 2022. URL: <https://kt.cern/aerospace/spaceradmon>.
- [50] Paolo Pavan, Luca Larcher, and Andrea Marmiroli. "Floating gate devices: Operation and compact modeling". In: *2004 NSTI Nanotechnology Conference and Trade Show - NSTI Nanotech 2004* 2. January (2004), pp. 120–123. DOI: 10.1007/b105299.
- [51] Vincent L. Pisacane. *Fundamentals of Space Systems (Second Edition)*. 2005.
- [52] R.C. Reedy. *Constraints on solar particle events from comparisons of recent events and million-year averages*. 1996.
- [53] Guenther Reitz. "Characteristic of the radiation field in low earth orbit and in deep space". In: *Zeitschrift fur Medizinische Physik* 18.4 (2008), pp. 233–243. ISSN: 09393889. DOI: 10.1016/j.zemedi.2008.06.015.
- [54] M. Ruffenach et al. "A New Technique Based on Convolutional Neural Networks to Measure the Energy of Protons and Electrons with a Single Timepix Detector". In: *IEEE Transactions on Nuclear Science* 68 (8 Aug. 2021), pp. 1746–1753. ISSN: 15581578. DOI: 10.1109/TNS.2021.3071583.
- [55] James R. Schwank et al. "Radiation effects in MOS oxides". In: *IEEE Transactions on Nuclear Science* 55.4 (2008), pp. 1833–1853. ISSN: 00189499. DOI: 10.1109/TNS.2008.2001040.
- [56] Sealicon Microsystems. *Radiation products*. 2022. URL: <https://www.sealiconmicro.com/sealicon-products-5/radiation> (visited on 05/17/2022).
- [57] R. Secondo et al. "Analysis and detection of multiple cell upsets in SRAM memories used as particle detectors". In: *Proceedings of the European Conference on Radiation and its Effects on Components and Systems, RADECS 2015-Decem* (2015). DOI: 10.1109/RADECS.2015.7365582.

- [58] R. Secondo et al. “Embedded Detection and Correction of SEU Bursts in SRAM Memories Used as Radiation Detectors”. In: *IEEE Transactions on Nuclear Science* 63.4 (2016), pp. 2168–2175. DOI: 10.1109/TNS.2016.2521485.
- [59] Raffaello Secondo. “Upgrades of the RadMon V6 and its Integration on a Nanosatellite for the Analysis and the Comparative Study of the CHARM and Low Earth Orbit Environments”. 2017.
- [60] Ladislav Sieger, Ondrej Nentvich, and Martin Urban. “Satellite temperature measurement in LEO and improvement method of temperature sensors calibration based on the measured data”. In: *Astronomische Nachrichten* 340 (Oct. 2019). DOI: 10.1002/asna.201913671.
- [61] European Cooperation for Space Standardization (ECSS). *Space engineering Methods for the calculation of radiation received and its effects, and a policy for design margins, ECSS-E-ST-10-12C*. ESA-ESTEC, 2008.
- [62] J R Srour, C J Marshall, and P W Marshall. “Review of Displacement Damage Effects in Silicon Devices”. In: 50.3 (2003), pp. 653–670.
- [63] J. R. Srour and J. W. Palko. “Displacement Damage Effects in Irradiated Semiconductor Devices”. In: *IEEE TRANSACTIONS ON NUCLEAR SCIENCE* 60.3 (2013). ISSN: 00280836. DOI: 10.1038/272108b0.
- [64] N. Sukhaseum et al. *Single event upset cross section dose dependence on 90 nm SRAM*. 2012.
- [65] Jake Tausch et al. “Neutron Induced Micro SEL Events in COTS SRAM Devices”. In: *2007 IEEE Radiation Effects Data Workshop*. 2007, pp. 185–188. DOI: 10.1109/REDW.2007.4342562.
- [66] A. Thornton. “CHARM Facility Test Area Radiation Field Description”. In: *CERN Accelerator Note* (2016). DOI: CERN-ACC-NOTE-2016-12345.
- [67] R. Vainio et al. “Dynamics of the Earth’s Particle Radiation Environment”. In: *Space Sci Rev* 147 (Nov. 2009), pp. 187–231. DOI: 10.1007/s11214-009-9496-7.
- [68] Alessandro Zimmaro, Jasper Dijks, and Panagiotis Gkountoumis. *SpaceRadMon NG Interface Control Document Version 3.0*. 2022.
- [69] Alessandro Zimmaro et al. “Testing and Validation Methodology for a Radiation Monitoring System for Electronics in Particle Accelerators”. In: *IEEE Transactions on Nuclear Science* 69.7 (2022), pp. 1642–1650. DOI: 10.1109/TNS.2022.3158527.

A

Arduino Code

A.1. Interfacing with Space RadMon-NG

A.1.1. SRM_NG_FPGA_TEST_BURST.ino

```
1 #include <Wire.h>
2 #include "wiring_private.h" // pinPeripheral() function
3 TwoWire myWire(&sercom3, 20, 21);
4
5 unsigned long StartTime;
6 unsigned long CurrentTime;
7 unsigned long ElapsedTime;
8
9 unsigned long reg0StartTime;
10 unsigned long reg0EndTime;
11
12 // #define set_read_req_value 0x11
13 #define set_rst_value 0x02
14 // #define test_srams_reg_value 0x0C
15
16 void setup() {
17     int x;
18     int limit;
19     //////////////////////////////////////////////////////////////////// INITIAL 5 SECOND
20     DELAY ////////////////////////////////////////////////////////////////////
21     delay(5000);
22     //////////////////////////////////////////////////////////////////// POWER-ON (
23     initialization) ////////////////////////////////////////////////////////////////////
24     Serial.begin(115200);
25     myWire.begin();
26     myWire.setClock(200000);
27     //////////////////////////////////////////////////////////////////// ENABLE FPGA
28     ////////////////////////////////////////////////////////////////////
29     pinMode(6, OUTPUT);
30     digitalWrite(6, HIGH);
31     delay(2000);
32     //////////////////////////////////////////////////////////////////// RESET
33     ////////////////////////////////////////////////////////////////////
34     reset_I2C(set_rst_value);
35     delay(2000);
36     //////////////////////////////////////////////////////////////////// SELF-TEST
37     ////////////////////////////////////////////////////////////////////
38     // test_srams(test_srams_reg_value);
39     // delay(1000);
40     //////////////////////////////////////////////////////////////////// READ COMMAND
41     ////////////////////////////////////////////////////////////////////
```

```

41 // 400 mV - 0x01, 800 mV - 0x09, 1800 mV - 0x11, 2200 mV - 0x19
42 int set_read_req_value = 0x19;
43 send_read_req(set_read_req_value);
44 StartTime = millis();
45
46 do {
47     delay(500);
48     x = read_reg0();
49 } while (x == set_read_req_value);
50
51 if(x != set_read_req_value){
52     limit = read_I2C();
53 }
54 else {Serial.println("XXXXXXXXXXXXX NO SELF CLEAR XXXXXXXXXXXXXXXX");
55 }
56
57 //////////////////////////////////////////////////////////////////// Delay for staying on
58 ////////////////////////////////////////////////////////////////////
59 // delay(2000000);
60 }
61
62 // Constants
63 uint8_t i = 0;
64 int Time2write = 0;
65
66 void loop (void) {
67     int x;
68     int limit;
69     int set_read_req_value;
70     //////////////////////////////////////////////////////////////////// FREEZE (1 SECOND)
71     ////////////////////////////////////////////////////////////////////
72     pinMode(6, OUTPUT);
73     digitalWrite(6, LOW);
74     delay(1000);
75     //////////////////////////////////////////////////////////////////// UNFREEZE
76     ////////////////////////////////////////////////////////////////////
77     pinMode(6, OUTPUT);
78     digitalWrite(6, HIGH);
79     delay(5000);
80     //////////////////////////////////////////////////////////////////// RESET
81     ////////////////////////////////////////////////////////////////////
82     reset_I2C(set_rst_value);
83     delay(1000);
84     //////////////////////////////////////////////////////////////////// READ COMMAND
85     ////////////////////////////////////////////////////////////////////
86     // 400 mV - 0x01, 800 mV - 0x09, 1800 mV - 0x11, 2200 mV - 0x19
87     set_read_req_value = 0x01;
88     send_read_req(set_read_req_value);
89     StartTime = millis();
90
91     do {
92         delay(500);
93         x = read_reg0();
94     } while (x == set_read_req_value);
95
96     if(x != set_read_req_value){
97         limit = read_I2C();
98     }
99     else {Serial.println("XXXXXXXXXXXXX NO SELF CLEAR XXXXXXXXXXXXXXXX");
100 }
101 //////////////////////////////////////////////////////////////////// FREEZE (1 SECOND)
102 ////////////////////////////////////////////////////////////////////
103 // pinMode(6, OUTPUT);
104 // digitalWrite(6, LOW);
105 // delay(1000);

```

```

106 ////////////////////////////////////////////////////////////////////////////////////////////////////////////////// UNFREEZE
107 //////////////////////////////////////////////////////////////////////////////////////////////////////////////////
108 // pinMode(6, OUTPUT);
109 // digitalWrite(6, HIGH);
110 delay(5000);
111 ////////////////////////////////////////////////////////////////////////////////////////////////////////////////// RESET
112 //////////////////////////////////////////////////////////////////////////////////////////////////////////////////
113 // reset_I2C(set_rst_value);
114 // delay(1000);
115 ////////////////////////////////////////////////////////////////////////////////////////////////////////////////// READ COMMAND
116 //////////////////////////////////////////////////////////////////////////////////////////////////////////////////
117 // 400 mV - 0x01, 800 mV - 0x09, 1800 mV - 0x11, 2200 mV - 0x19
118 set_read_req_value = 0x09;
119 send_read_req(set_read_req_value);
120 StartTime = millis();
121
122 do {
123     delay(500);
124     x = read_reg0();
125 } while (x == set_read_req_value);
126
127 if(x != set_read_req_value){
128     limit = read_I2C();
129 }
130 else {Serial.println("XXXXXXXXXXXXX NO SELF CLEAR XXXXXXXXXXXXXXXX");
131 }
132 ////////////////////////////////////////////////////////////////////////////////////////////////////////////////// FREEZE (1 SECOND)
133 //////////////////////////////////////////////////////////////////////////////////////////////////////////////////
134 // pinMode(6, OUTPUT);
135 // digitalWrite(6, LOW);
136 // delay(1000);
137 ////////////////////////////////////////////////////////////////////////////////////////////////////////////////// UNFREEZE
138 //////////////////////////////////////////////////////////////////////////////////////////////////////////////////
139 // pinMode(6, OUTPUT);
140 // digitalWrite(6, HIGH);
141 delay(5000);
142 ////////////////////////////////////////////////////////////////////////////////////////////////////////////////// RESET
143 //////////////////////////////////////////////////////////////////////////////////////////////////////////////////
144 // reset_I2C(set_rst_value);
145 // delay(1000);
146 ////////////////////////////////////////////////////////////////////////////////////////////////////////////////// READ COMMAND
147 //////////////////////////////////////////////////////////////////////////////////////////////////////////////////
148 // 400 mV - 0x01, 800 mV - 0x09, 1800 mV - 0x11, 2200 mV - 0x19
149 set_read_req_value = 0x11;
150 send_read_req(set_read_req_value);
151 StartTime = millis();
152
153 do {
154     delay(500);
155     x = read_reg0();
156 } while (x == set_read_req_value);
157
158 if(x != set_read_req_value){
159     limit = read_I2C();
160 }
161 else {Serial.println("XXXXXXXXXXXXX NO SELF CLEAR XXXXXXXXXXXXXXXX");
162 }
163
164 ////////////////////////////////////////////////////////////////////////////////////////////////////////////////// FREEZE (1 SECOND)
165 //////////////////////////////////////////////////////////////////////////////////////////////////////////////////
166 // pinMode(6, OUTPUT);
167 // digitalWrite(6, LOW);
168 // delay(1000);

```

```

169 ////////////////////////////////////////////////////////////////////////////////////////////////////////////////// UNFREEZE
170 //////////////////////////////////////////////////////////////////////////////////////////////////////////////////
171 // pinMode(6, OUTPUT);
172 // digitalWrite(6, HIGH);
173   delay(5000);
174 ////////////////////////////////////////////////////////////////////////////////////////////////////////////////// RESET
175 //////////////////////////////////////////////////////////////////////////////////////////////////////////////////
176 // reset_I2C(set_rst_value);
177 // delay(1000);
178 ////////////////////////////////////////////////////////////////////////////////////////////////////////////////// READ COMMAND
179 //////////////////////////////////////////////////////////////////////////////////////////////////////////////////
180 // 400 mV - 0x01, 800 mV - 0x09, 1800 mV - 0x11, 2200 mV - 0x19
181   set_read_req_value = 0x19;
182   send_read_req(set_read_req_value);
183   StartTime = millis();
184
185   do {
186     delay(500);
187     x = read_reg0();
188   } while (x == set_read_req_value);
189
190   if(x != set_read_req_value){
191     limit = read_I2C();
192   }
193   else {Serial.println("XXXXXXXXXXXXXXXX NO SELF CLEAR XXXXXXXXXXXXXXXXXXXX");}
194 }
195
196 void reset_I2C(int rst){
197   myWire.beginTransmission(0x27); // send a reset request (write)
198   myWire.write(0x00);
199   myWire.write(rst);           // Vctr (reg[4:3]) set Vctrl to 10 for 1.8V (GPIO[0:2]
200   // - z0z)
201   myWire.endTransmission(true);
202 }
203
204 void send_read_req(int read_reg){
205   myWire.beginTransmission(0x27); // start reading data
206   myWire.write(0x00);
207   myWire.write(read_reg);           // Vctrl11 Vctrl10 TEST RST READ set Vctrl to 10 for
208   // 2.2V (GPIO[2:0] - zzz)
209   myWire.endTransmission(true);
210 }
211
212 int read_reg0(){
213   myWire.requestFrom(0x27, 1);
214   int x[1];
215   x[0] = myWire.read();
216   unsigned int reg0 = x[0];
217   return reg0;
218 }
219
220 void test_srams(int test){
221   myWire.beginTransmission(0x27);
222   myWire.write(0x00);
223   myWire.write(test);
224   myWire.endTransmission(true);
225 }
226
227 int read_I2C(){
228   int c[68];
229   int SEU_limit;
230   int i=0;
231   int seu;
232   int ISSI_seu;
233   uint8_t crc;
234
235   myWire.requestFrom(0x27, 68); // request 54 bytes from slave device #27

```

```

235     while(myWire.available())    // slave may send less than requested
236     {
237         c[i] = myWire.read(); // receive a byte as character
238         i++;
239     }
240
241     crc=c[1] ^ c[2] ^ c[3] ^ c[5] ^ c[6] ^ c[8] ^ c[9] ^ c[11] ^ c[12] ^ c[13] ^
242     c[15] ^ c[16] ^ c[17] ^ c[19] ^ c[20] ^ c[21] ^
243     c[22] ^ c[24] ^ c[25] ^ c[27] ^ c[28] ^ c[29] ^ c[31] ^ c[32] ^ c[33] ^
244     c[35] ^ c[37] ^ c[38] ^ c[39] ^ c[41] ^ c[42] ^ c[43] ^
245     c[45] ^ c[47] ^ c[48] ^ c[49] ^ c[51] ^ c[52] ^ c[53] ^ c[55] ^ c[56] ^
246     c[58] ^ c[59] ^ c[61] ^ c[62] ^ c[64] ^ c[65];
247
248     if ( crc == c[67])
249     {
250         int mbu=c[1]*256*256+c[2]*256+c[3];
251         Serial.print(mbu);
252         Serial.print(" ");
253
254         int SRAM180nm_errors=c[5]*256+c[6];
255         Serial.print(SRAM180nm_errors);
256         //Serial.print("0");
257         Serial.print(" ");
258
259         int SRAM180nm_errors2=c[8]*256+c[9];
260         Serial.print(SRAM180nm_errors2);
261         //Serial.print("0");
262         Serial.print(" ");
263
264         seu=c[11]*256*256+c[12]*256+c[13];
265         Serial.print(seu);
266         Serial.print(" ");
267
268         int ISSI_mbu=c[15]*256*256+c[16]*256+c[17];
269         Serial.print(ISSI_mbu);
270         Serial.print(" ");
271
272         ISSI_seu=(c[19]*256*256*256+c[20]*256*256+c[21]*256+c[22]);
273         Serial.print(ISSI_seu);
274         Serial.print(" ");
275
276         double Temperature=((c[24]*256+c[25])*3300/4096);
277         //Temperature=(c[24]*256+c[25]);
278         //int Temperature=(c[24]*256+c[25]);
279         //Serial.print(Temperature);
280         Serial.print(Temperature/10);
281         Serial.print(" ");
282         //
283         int FGD1_freq=(c[27]*256*256+c[28]*256+c[29]);
284         Serial.print(FGD1_freq);
285         Serial.print(" ");
286         //
287         int FGD1_reference_frequency=(c[31]*256*256+c[32]*256+c[33]);
288         Serial.print(FGD1_reference_frequency);
289         Serial.print(" ");
290
291         int FGD1_Recharge_cnt=(c[35]);
292         Serial.print(FGD1_Recharge_cnt);
293         Serial.print(" ");
294
295         int FGD2_freq=(c[37]*256*256+c[38]*256+c[39]);
296         Serial.print(FGD2_freq);
297         Serial.print(" ");
298
299         int FGD2_reference_frequency=(c[41]*256*256+c[42]*256+c[43]);
300         Serial.print(FGD2_reference_frequency);
301         Serial.print(" ");
302
303         int FGD2_Recharge_cnt=(c[45]);
304         Serial.print(FGD2_Recharge_cnt);
305         Serial.print(" ");

```

```

303     int FGD1_target=(c[47]*256*256+c[48]*256+c[49]);
304     Serial.print(FGD1_target);
305     Serial.print(" ");
306
307
308     int FGD2_target=(c[51]*256*256+c[52]*256+c[53]);
309     Serial.print(FGD2_target);
310     Serial.print(" ");
311
312     int V3P3=((c[55]*256+c[56])*2*3300/4096);
313     //int V3P3=(c[55]*256+c[56]);
314     Serial.print(V3P3);
315     Serial.print(" ");
316
317     int V1P8=((c[58]*256+c[59])*2*3300/4096);
318     //int V1P8=(c[58]*256+c[59]);
319     Serial.print(V1P8);
320     Serial.print(" ");
321
322     int Vadj=((c[61]*256+c[62])*2*3300/4096);
323     //int Vadj=(c[61]*256+c[62]);
324     Serial.print(Vadj);
325     Serial.print(" ");
326
327     int V1p2=((c[64]*256+c[65])*2*3300/4096);
328     //int Vadj=(c[61]*256+c[62]);
329     Serial.print(V1p2);
330     Serial.print(" ");
331
332     Serial.print(millis());
333     Serial.println(" ");
334
335     int CRC=(c[67]);
336     //Serial.print(CRC);
337     //Serial.print("          ");
338 }
339 else{
340     Serial.print("Wrong CRC!!");
341     Serial.println(" ");
342     reset_I2C(set_rst_value);
343 }
344 i = 0;
345
346 //delay(10000);
347
348 if(seu > 16000000 || ISSI_seu > 4000000000){
349     SEU_limit = 1;
350 } else SEU_limit = 0;
351
352
353 return SEU_limit;
354 }

```

A.2. Reading FGDOS Chips and Temperature Sensor

A.2.1. read_FGDOS_Temp.ino

```

1 #include "read_FGDOS_Temp.h"
2
3 void setup() {
4     init_spi();
5     delay(500);
6
7     init_temperature(Vin, ADC_resolution);
8     delay(500);
9
10    init_fgdos(SS1);
11    delay(500);
12
13    init_fgdos(SS2);
14    delay(500);

```

```

15
16 // Ambient Temperature reading
17 T_ambient = get_pt100_reading();
18
19 // Print column names
20 delay(5000); // Wait 5 seconds before printing
21
22 Serial.print("T_PT100, ");
23 Serial.print("T_FGDOS_1, ");
24 Serial.print("RECHEV_1, ");
25 Serial.print("RCHCNT_1, ");
26 Serial.print("FREQ_SENS_1, ");
27 Serial.print("FREQ_REF_1, ");
28 Serial.print("TARGET_1, ");
29 Serial.print("THRESHOLD_1, ");
30 Serial.print("CHIPID_1, ");
31 Serial.print("T_FGDOS_2, ");
32 Serial.print("RECHEV_2, ");
33 Serial.print("RCHCNT_2, ");
34 Serial.print("FREQ_SENS_2, ");
35 Serial.print("FREQ_REF_2, ");
36 Serial.print("TARGET_2, ");
37 Serial.print("THRESHOLD_2, ");
38 Serial.print("CHIPID_2, ");
39 // Serial.print("WINDOW_FACTOR, ");
40 Serial.println("");
41
42 // Clean out frequency registers
43 F1S_1 = read_spi(SS1, FS_REG_CTRL); // bit 17:16
44 delay(1);
45 F1S_2 = read_spi(SS1, FS_REG_H); // bit 15:8
46 delay(1);
47 F1S_3 = read_spi(SS1, FS_REG_L); // bit 7:0
48 delay(1);
49 F1R_1 = read_spi(SS1, FR_REG_CTRL); // bit 17:16
50 delay(1);
51 F1R_2 = read_spi(SS1, FR_REG_H); // bit 15:8
52 delay(1);
53 F1R_3 = read_spi(SS1, FR_REG_L); // bit 7:0
54 delay(1);
55 F1S_1 = read_spi(SS2, FS_REG_CTRL); // bit 17:16
56 delay(1);
57 F1S_2 = read_spi(SS2, FS_REG_H); // bit 15:8
58 delay(1);
59 F1S_3 = read_spi(SS2, FS_REG_L); // bit 7:0
60 delay(1);
61 F1R_1 = read_spi(SS2, FR_REG_CTRL); // bit 17:16
62 delay(1);
63 F1R_2 = read_spi(SS2, FR_REG_H); // bit 15:8
64 delay(1);
65 F1R_3 = read_spi(SS2, FR_REG_L); // bit 7:0
66 delay(1);
67 }
68
69 void loop (void) {
70 // Update time
71 millis_now = millis();
72 t = t + (millis_now - millis_previous)/1000;
73
74 // Read sensors and print every read interval
75 if (millis_now - millis_read >= read_interval) {
76 // PT100 Temperature reading and reference temperature
77 T_pt100 = get_pt100_reading();
78
79 // Print temperature reference and reading
80 print_temperatures(T_pt100);
81
82 // FGDOS 1 --> HS mode (change in header)
83 fgdos_readings(SS1);
84 delay(1);
85

```

```

86 // FGDOS 2 --> HS mode (change in header)
87 fgdos_readings(SS2);
88
89 // Print WINDOW_FACTOR
90 // Serial.print(WINDOW_FACTOR);
91 // Serial.print(", ");
92
93 // Update time
94 millis_read = millis_now;
95
96 // Print new line
97 Serial.println(""); // Next line
98 }
99
100 // Update time
101 millis_previous = millis_now;
102 }
103
104 void write_spi(uint8_t CS, uint8_t addr, uint8_t data)
105 {
106     digitalWrite(CS, LOW);
107     delay(1);
108     SPI.transfer(addr | (0b01 << 6));
109     SPI.transfer(data);
110     delay(1);
111     digitalWrite(CS, HIGH);
112 }
113
114 uint8_t read_spi(uint8_t CS, uint8_t addr)
115 {
116     digitalWrite(CS, LOW);
117     delay(1);
118     SPI.transfer(addr | (0b10 << 6));
119     uint8_t data = SPI.transfer(0x00);
120     delay(1);
121     digitalWrite(CS, HIGH);
122
123     return data;
124 }
125
126 void init_spi() {
127     Serial.begin(9600);
128     SPI.begin();
129     SPI.beginTransaction(SPISettings(1000, MSBFIRST, SPI_MODE0));
130
131     // Set chip select pins
132     pinMode(SS1, OUTPUT); // CS pin for FGDOS 1
133     pinMode(SS2, OUTPUT); // CS pin for FGDOS 2
134
135     // Set all to high
136     digitalWrite(SS1, HIGH); // CS HIGH for FGDOS 1 (deactive)
137     digitalWrite(SS2, HIGH); // CS HIGH for FGDOS 2 (deactive)
138 }
139
140 void init_temperature(uint8_t pin_nr, int res) { // ADC settings for oversampling from
141     // 12 bit to 16 bit
142     // Temperature sensor
143     analogReadResolution(res);
144     pinMode(pin_nr, INPUT);
145 }
146
147 void init_fgdos(uint8_t CS) {
148     // Configure FGDOS Z1 (same as Space RadMon-NG settings)
149     // Reg 0x0D
150     write_spi(CS, REGD, REGD_CONFIG); // disconnect recharging system and configure SET
151     // (2:0) to 110 (16.5 V)
152     delay(1);
153
154     // Reg 0x0B
155     write_spi(CS, REGB, REGB_RECHARGE); // automatic recharging, internal charge pump
156     // input at VB, use internal charge pump, measurement window of 32768, target

```

```

    threshold divider 10 LSB bits
154 delay(1);
155
156 // Reg 0x0C
157 write_spi(CS, REGC, REGC_CONFIG); // HS mode
158 delay(1);
159
160 // Reg 0x0E
161 write_spi(CS, REGE, REGE_CONFIG); // NIRQ interruption push-pull and measurement
    window by clk counts
162 delay(1);
163
164 // Set target
165 write_spi(CS, TARGET_REG, TARGET_CONFIG); // configure TARGET(4:0) to 90 kHz
166 // byte reg_target = floor(TARGET_FREQ_SET/WINDOW_FACTOR/BITSHIFT);
167 // write_spi(CS, TARGET_REG, reg_target);
168 delay(1);
169
170 // Set threshold
171 write_spi(CS, THRESHOLD_REG, THRESHOLD_CONFIG); // configure THRESHOLD(4:0) to 49 kHz
172 // byte reg_threshold = floor(THRESHOLD_FREQ_SET/WINDOW_FACTOR/BITSHIFT);
173 // write_spi(CS, THRESHOLD_REG, reg_threshold);
174 delay(1);
175
176 // Reg 0x0D
177 if (CS != 16) {
178     write_spi(CS, REGD, REGD_RECHARGE); // connect recharging system and configure SET
        (2:0) to 100 (16.5 V)
179     delay(1);
180 }
181
182 // Reset recharges
183 write_spi(CS, RECHARGE_REG, RECHARGES_RESET); // reset recharges
184 delay(2200);
185 }
186
187 double get_pt100_reading() {
188     // Bits to voltage with oversampling (12 --> 16 bit accuracy)
189     V_sum = 0;
190     for (int i = 0; i < 255; i++){
191         V_sum += analogRead(Vin);
192     }
193     V = ((V_sum/256) / 4095.0 + V_offset_corr) * V_ref;
194     // Voltage to resistance
195     Rx = R1 * V / (Vcc - V);
196     // Resistance to temperature
197     T_pt100 = (Rx / R0 - 1.0) / alpha;
198
199     return T_pt100;
200 }
201
202 void print_temperatures(double T_board) {
203     Serial.print(T_board);
204     Serial.print(", ");
205     delay(1);
206 }
207
208 bool fgdos_readings(uint8_t CS) {
209     timed_out = freq_construct(CS, &FREQ_SENS, &FREQ_REF);
210     if (!timed_out) {
211         return false;
212     }
213     TEMP = read_spi(CS, TEMP_REG) + T_fgdos_offset;
214     Serial.print(TEMP);
215     Serial.print(", ");
216     delay(1);
217     RECHARGE = read_spi(CS, RECHARGE_REG);
218     Serial.print((RECHARGE & 0x80) >> 7);
219     Serial.print(", ");
220     Serial.print(RECHARGE & 0x7F);
221     Serial.print(", ");

```

```

222 delay(1);
223 // frequencies print
224 Serial.print(FREQ_SENS);
225 Serial.print(", ");
226 Serial.print(FREQ_REF);
227 Serial.print(", ");
228 delay(1);
229 TARGET = read_spi(CS, TARGET_REG);
230 Serial.print(int(((TARGET & 0x1F) * BITSHIFT * WINDOW_FACTOR)));
231 Serial.print(", ");
232 delay(1);
233 THRESHOLD = read_spi(CS, THRESHOLD_REG);
234 Serial.print(int(((THRESHOLD & 0x1F) * BITSHIFT * WINDOW_FACTOR)));
235 Serial.print(", ");
236 delay(1);
237 CHIPID = read_spi(CS, CHIPID_REG);
238 Serial.print(CHIPID);
239 Serial.print(", ");
240
241 return true;
242 }
243
244 bool freq_construct(uint8_t CS, uint32_t *FREQ_SENS, uint32_t *FREQ_REF) {
245     time_start = millis(); // prevent getting stuck
246     x = 1000; // increase amount of time to wait if serial.prints are used! Otherwise set
                to 1
247     have_sens_freq = false;
248     have_ref_freq = false;
249
250     // check to see if no recharge is going on
251     // if((read_spi(CS, 0x01) & 0x80) == 0x80){
252     //     if (CS == 16) {
253     //         Serial.print("recharge in progress for FGDOS1, ");
254     //     }
255     //     else {
256     //         Serial.print("recharge in progress for FGDOS2, ");
257     //     }
258     // }
259
260     while(!have_sens_freq || !have_ref_freq){
261         F1S_1 = read_spi(CS, FS_REG_CTRL);
262         F1R_1 = read_spi(CS, FR_REG_CTRL);
263         DNEWS = F1S_1 & 0x08;
264         F1SOVF = F1S_1 & 0x04;
265         DNEWR = F1R_1 & 0x08;
266         F1ROVF = F1R_1 & 0x04;
267         RECHEV = (read_spi(CS, RECHARGE_REG) & 0x80) >> 7;
268
269         if(RECHEV == 1){
270             // Sensor is recharging
271             if (CS == 16) {
272                 Serial.print("FGDOS1 is recharging, ");
273             }
274             else {
275                 Serial.print("FGDOS2 is recharging, ");
276             }
277             return false;
278         }
279
280         if(!have_sens_freq && DNEWS == 0x08){
281             // sensor frequency
282             // F1S_1 = read_spi(CS, FS_REG_CTRL); // bit 17:16
283             // delay(1);
284             F1S_2 = read_spi(CS, FS_REG_H); // bit 15:8
285             delay(1);
286             F1S_3 = read_spi(CS, FS_REG_L); // bit 7:0
287             delay(1);
288             *FREQ_SENS = (((F1S_1 & 0x03) << 8 | F1S_2) << 8 | F1S_3) * WINDOW_FACTOR;
289             have_sens_freq = true;
290             // if (F1SOVF == 0x04) {
291             //     *FREQ_SENS = 0;

```

```

292 // }
293 }
294 if(!have_ref_freq && DNEWR == 0x08){
295 // reference frequency
296 // F1R_1 = read_spi(CS, FR_REG_CTRL); // bit 17:16
297 // delay(1);
298 F1R_2 = read_spi(CS, FR_REG_H); // bit 15:8
299 delay(1);
300 F1R_3 = read_spi(CS, FR_REG_L); // bit 7:0
301 delay(1);
302 *FREQ_REF = (((F1R_1 & 0x03) << 8 | F1R_2 ) << 8 | F1R_3 )) * WINDOW_FACTOR;
303 have_ref_freq = true;
304 // if (F1ROVF == 0x04) {
305 // *FREQ_REF = 0;
306 // }
307 }
308
309 if ((millis()-time_start>(4*1/WINDOW_FACTOR*x) && !have_ref_freq && !have_sens_freq
310 )){
311 if (CS == 16) {
312 Serial.print("reading failed for FGDOS1, ");
313 }
314 else {
315 Serial.print("reading failed for FGDOS2, ");
316 }
317 return false;
318 }
319 }
320 return true;
321 }

```

A.2.2. read_FGDOS_Temp.h

```

1 // includes
2 #include <SPI.h>
3
4 // constants
5 #define CK_FREQ 32768.0f // clk input frequency
6 // #define WINDOW_PULSES 4096 // 125ms
7 #define WINDOW_PULSES 8192 // 250ms
8 // #define WINDOW_PULSES 16384 // 500ms
9 // #define WINDOW_PULSES 32768 // 1000ms
10 #define WINDOW_FACTOR (CK_FREQ/WINDOW_PULSES)
11
12 // ADC resolution
13 int ADC_resolution = 12;
14
15 // Variables to convert voltage to resistance to temperature
16 double V;
17 double Vcc = 5.0; // Supply voltage
18 double V_ref = 3.27; // Arduino reference voltage (should be 3.3)
19 double V_offset_corr = -0.004; // Arduino reading offset (calibration)
20 double V_sum; // For manual oversampling
21 double Rx;
22 double R0 = 100.0; // Resistance where T = 0 for PT100
23 double R1 = 1000.0; // Resistance used in circuit
24 double alpha = 0.00385; // Google
25 double T_pt100;
26 double T_ambient;
27
28 // Timing for processor
29 double t = 0;
30 double millis_now = 0;
31 double millis_previous;
32 double millis_read = 0;
33 double read_interval = 2200; // reading every 2200 ms
34
35 // FGDOS Temperature offset
36 double T_fgdos_offset = -70;
37

```

```

38 // ports
39 #define Vin AO
40 #define SS1 A2
41 #define SS2 A4
42
43 // Masks
44 #define WR 0x40
45 #define RD 0x80
46 #define FREQ_MASK 0x3FFFF
47 #define BITSHIFT 1024
48
49 // read only registers
50 #define TEMP_REG          0x00
51 #define RECHARGE_REG     0x01 // Can be reset (see REG4)
52 #define DNEWR_REG       0x05
53 #define FR_REG_CTRL     0x05
54 #define FR_REG_H        0x04
55 #define FR_REG_L        0x03
56 #define DNEWS_REG       0x08
57 #define FS_REG_CTRL     0x08
58 #define FS_REG_H        0x07
59 #define FS_REG_L        0x06
60
61 // read-write registers
62 #define TARGET_REG       0x09
63 #define THRESHOLD_REG   0x0A
64 #define CHIPID_REG      0x13
65 #define REGB            0x0B
66 #define REGC            0x0C
67 #define REGD            0x0D
68 #define REGE           0x0E
69
70 // configuration FGDOS
71 #define TARGET_CONFIG    0x16 // Target of around ??? 90 kHz when TDIV = 1
72 #define THRESHOLD_CONFIG 0x0C // Threshold of 49 kHz when TDIV = 1
73 #define THRESHOLD_FREQ_SET 50000
74 #define TARGET_FREQ_SET 90000
75
76 // #define REGB_CONFIG      0xCD // window of 125 ms
77 #define REGB_CONFIG      0x49 // TDIV = 1
78 #define REGB_RECHARGE    0xC9 // window of 250 ms // TDIV = 1
79 #define REGB_RECHARGE_13 0xC8 // window of 250 ms // TDIV = 0
80 // #define REGB_CONFIG      0xC5 // window of 500 ms
81 // #define REGB_CONFIG      0xC1 // window of 1000 ms
82 #define REGC_CONFIG      0x79 // HS
83 #define REGC_FORCE       0xF9 // Force recharge, HS
84 #define REGD_CONFIG      0x01 // Recharge disabled and 001 recharging set
85 #define REGD_RECHARGE    0x41 // Recharge enabled and 001 recharging set
86 #define REGE_CONFIG      0x00
87 #define RECHARGES_RESET  0x00
88
89 // functions
90 double get_pt100_reading();
91 void print_temperatures(double T_pt100);
92 bool fgdos_readings(uint8_t CS);
93 void init_spi();
94 void init_temperature(uint8_t pin_nr);
95 void init_fgdos(uint8_t CS, bool sens_mode);
96 void write_spi(uint8_t CS, uint8_t addr, uint8_t data);
97 uint8_t read_spi(uint8_t CS, uint8_t addr);
98 bool freq_construct(uint8_t CS, uint32_t *FREQ_SENS, uint32_t *FREQ_REF);
99
100 // variables
101 int8_t TEMP;
102 uint8_t RECHEV;
103 uint8_t RECHARGE;
104 uint8_t F1R_1;
105 uint8_t F1R_2;
106 uint8_t F1R_3;
107 uint32_t FREQ_REF; // Combined registers value
108 uint8_t F1S_1;

```

```
109 uint8_t F1S_2;
110 uint8_t F1S_3;
111 uint32_t FREQ_SENS; // Combined registers value
112 uint8_t TARGET;
113 uint8_t THRESHOLD;
114 uint8_t CHIPID;
115
116 // variables for frequency construction
117 unsigned int time_start;
118 int x;
119 int DNEWS;
120 int DNEWR;
121 int F1SOVF;
122 int F1ROVF;
123 bool have_ref_freq;
124 bool have_sens_freq;
125 bool timed_out;
126 int time_out_SENS;
127 int time_out_REF;
128 int FGDOS_nr;
```

B

CELESTA Two-Line Element Sets

CELESTA_TLEs.txt

1	53111U	22080G	22198.10916232	-.00000003	00000-0	00000+0	0	9992
2	53111	70.1471	76.1532	0010630	257.1283	102.9435	6.42553560	106
1	53111U	22080G	22199.04297027	-.00000003	00000-0	00000+0	0	9990
2	53111	70.1436	75.8422	0007664	221.4548	138.3862	6.42534474	168
1	53111U	22080G	22200.91082161	-.00000003	00000-0	00000-0	0	9991
2	53111	70.1474	75.1923	0008827	222.5393	137.4476	6.42532007	285
1	53111U	22080G	22201.22212397	-.00000003	00000-0	00000-0	0	9992
2	53111	70.1472	75.0842	0008017	230.7865	129.1755	6.42529879	302
1	53111U	22080G	22205.26902215	-.00000003	00000-0	00000-0	0	9995
2	53111	70.1549	73.6814	0007962	229.0903	130.8840	6.42529134	568
1	53111U	22080G	22206.20292945	-.00000003	00000-0	00000+0	0	9991
2	53111	70.1541	73.3565	0008228	226.5349	133.4890	6.42529956	625
1	53111U	22080G	22207.29245230	-.00000003	00000-0	00000+0	0	9996
2	53111	70.1542	72.9763	0008990	222.7002	137.3038	6.42530706	690
1	53111U	22080G	22207.60374728	-.00000003	00000-0	00000-0	0	9997
2	53111	70.1552	72.8670	0011076	222.9512	137.0760	6.42531050	719
1	53111U	22080G	22209.16019017	-.00000003	00000-0	00000+0	0	9996
2	53111	70.1517	72.3224	0015664	220.2144	139.7964	6.42532870	816
1	53111U	22080G	22209.16019017	-.00000003	00000-0	00000-0	0	9997
2	53111	70.1517	72.3224	0015664	220.2144	139.7964	6.42532870	816
1	53111U	22080G	22255.16019017	-.00000003	00000-0	00000+0	0	9997
2	53111	70.1086	56.1818	0009300	227.1361	132.8517	6.42544045	3765
